



VNIVERSITAT  
E VALÈNCIA

 Facultat de Química

PROGRAMA DE DOCTORAT  
EN QUÍMICA



## NANOMATERIALS: DEVELOPMENT OF NEW ANALYSIS STRATEGIES

Thesis presented to obtain the PhD degree in Chemistry under the "Doctorado en Química con Mención de Excelencia (R.D. 99/2011)"

**Lorenzo Sanjuan Navarro**

Supervisors:

Prof<sup>a</sup>. Dra. Pilar Campíns Falcó

Prof<sup>a</sup>. Dra. Yolanda Moliner Martínez

Valencia, June 2022



**Departament de Química Analítica**

Pilar Campíns Falcó, Catedrática, y Yolanda Moliner Martínez, Profesora Titular, ambas del Departamento de Química Analítica de la Universidad de Valencia,

**CERTIFICAN**

Que la presente memoria, titulada "*Nanomaterials: development of new analysis strategies*", constituye la Tesis Doctoral de Lorenzo Sanjuan Navarro para optar al grado de Doctora en Química, y que ha sido realizada en los laboratorios del Departamento de Química Analítica de la Universidad de Valencia, bajo su dirección y supervisión.

Y para que así conste a los efectos oportunos, firman el presente certificado en

Valencia, a 23 de junio de 2022.

Fdo. Dra. Pilar Campíns Falcó  
Directora de Tesis

Fdo. Dra. Yolanda Moliner Martínez  
Codirectora de Tesis



This Thesis has been carried out thanks to PhD Research grant FPU (FPU 17/01655) funded by the Ministry of Universities of Spain in the Analytical Chemistry Department of the University of Valencia. A research stay of three month was completed in the Centre for Microbiology and Environmental System Science, Department of Environmental Geosciences of the University of Vienna.





“Aprende como si fueras a vivir toda la vida,  
y vive como si fueras a morir mañana”

**Charles Chaplin**





# AGRAÏMENTS

*Un llarg camí carregat de bons fruits, recompenses i vivències que marcaran la meua vida...* Així podria iniciar la crònica que sintetitza aquesta etapa. Una etapa que ha sigut possible gràcies al recolzament, ajuda i temps que han invertit en mi moltes persones que sempre estaran al meu cor.

En primer lloc, vull agrair a Pilar la oportunitat que em va donar de treballar en aquest grup d'investigació. Un grup que s'ha convertit en la meua segona casa i que m'ha fet sentir de la millor forma possible, treballant amb molt bon ambient i familiaritat. Gràcies Pilar per ensenyar-me tot el que se fins ara, recolzar-me i ajudar-me en tot el que he necessitat, sempre seràs el meu exemple a seguir.

Gràcies Yolanda per estar sempre. En tot allò que he necessitat sempre has estat per a mi. Has sigut professora, consellera, psicòloga, terapeuta i un fum més de coses que sempre recordaré i portaré al meu cor, perquè gràcies a tot això he pogut avançar en aquest camí i aconseguir afrontar diferents reptes que han esdevingut. Gràcies una vegada més per tot el que has fet per mi.

Elles dos han sigut les millor tutores i assessores que qualsevol puga desitjar. I junt a elles, no em puc oblidar de Carmen i Rosa, les quals sempre han estat per a tot el que haja necessitat; formant un gran grup que camina cap al futur segur i consolidat.

Gràcies a Frank i tot el grup d'investigació del "Department of Environmental Geosciences" de la Universitat de Viena per haver-me donat la oportunitat de realitzar amb ells la meua estància doctoral. Allí, a més, també vaig conèixer a quatre persones que es van convertir en essencials per a mi. Gràcies Alba, Joaquín, Blanca i Rafa per aparèixer en la meua vida, espere que aquesta amistat dure per sempre.

I aquesta etapa també ha donat com a fruit moltes altres amistats; els meus companys de laboratori, Maria, Anabel, Pascu, Neus, Rodrigo, Sara, Ana, Lusine, Adri, Henry, Sergio, Héctor, Rocío, Camila, Ivan, Aaron, Carlos, Belen, Juanlu, Lori, Cristian y Víctor; que han compartit amb mi congressos, dinars, sopars i alguna que

altra festa. Gràcies per omplir-me d'alegria en dies tristos. En especial Ana, Adri i Lusine, sabeu que vos porte en el meu cor i que sempre estaré agraït per tot el que m'heu ajudat.

També he de donar les gràcies a Sonia, Enric, Aitor i Pepe. Els cinc vam iniciar aquest camí del doctorat allà pel 2017, sempre hem estat units i sabem que sempre ens tindrem els uns als altres. Moltes gràcies per haver-me deixat compartir amb vosaltres aquesta experiència.

I com no als meus amics del poble, els quals em suporten i m'animen cada dia quan necessite ajuda. Amb els quals, de vegades, passe més hores que en la meua pròpia casa. Ells poden recórrer quilòmetres per visitar-me, encara que siga en 20 metres quadrats, poques hores de sol i apretadets. Moltes gràcies per ser com sou i per estar sempre disponibles per a mi.

I dins d'aquestes línies tenen una part especial i fonamental els meus pares. Gràcies a ells estic on estic i sóc qui sóc. Gràcies pels valors i l'educació que m'heu inculcat, recolzant-me i donant-me el vostre suport en tot allò que m'he proposat. Mai he rebut un NO com a resposta, sempre heu estat disponibles a ajudar-me en tot el que vos he demanat, per això em sent totalment afortunat de tindre uns pares com vosaltres.

I finalment no em puc oblidar de la meu germana, Mila, la meua meitat, sempre estaré per a tot el que necessites, igual que sé que tu sempre estàs i estaràs, gràcies per fer-me la vida més entretinguda, perquè com tu dius, sense tu estaríem massa avorrits.

# RESUMEN

El gran progreso científico y tecnológico vivido en los últimos años se caracteriza por el rápido avance experimentado por la investigación, y en particular por el creciente desarrollo en Nanociencia y Nanotecnología. En este campo, los nanomateriales (NMs), juegan un papel clave debido a sus propiedades físicas y químicas únicas. La definición de NM dada en la 11 Recomendación de la Comisión Europea de 18 de octubre de 2011 (2011/696/UE) ha sido actualizada recientemente en la Recomendación de la Comisión de 10 de junio de 2022 (2022/C 229/01) que establece: *Por «nanomaterial» se entiende un material natural, accidental o fabricado, constituido por partículas sólidas que están presentes individualmente o como partículas constituyentes identificables en agregados o aglomerados, y en el que el 50 % o más de estas partículas en la granulometría numérica cumple al menos una de las condiciones siguientes:*

*a) una o más dimensiones externas de la partícula se hallan en el intervalo de tamaños comprendido entre 1 nm y 100 nm;*

*b) la partícula tiene forma alargada, como la de una varilla, una fibra o un tubo, y dos de sus dimensiones externas son inferiores a 1 nm, mientras que la otra dimensión es superior a 100 nm;*

*c) la partícula tiene forma de placa, y una de sus dimensiones externas es inferior a 1 nm, mientras que las otras dimensiones son superiores a 100 nm.*

*Para determinar la granulometría numérica, no será necesario tener en cuenta las partículas con al menos dos dimensiones externas ortogonales superiores a 100  $\mu\text{m}$ . No obstante, los materiales con una superficie específica por unidad de volumen  $< 6 \text{ m}^2/\text{cm}^3$  no serán considerados nanomateriales. Se aplican las siguientes definiciones:*

*a) «partícula»: una parte diminuta de materia con límites físicos definidos; las moléculas únicas no se consideran «partículas»;*

*b) «agregado»: una partícula compuesta de partículas fuertemente ligadas o fusionadas;*

*c) «aglomerado»: un conjunto de partículas, o de agregados, débilmente ligados en que la extensión de la superficie externa resultante es similar a la suma de las extensiones de las superficies de los distintos componentes.*

Los NMs exhiben propiedades únicas tales como una alta relación área superficial/volumen, características térmicas favorables y facilidad de funcionalización de la superficie, siendo necesaria su caracterización para analizar sus diversas propiedades. Además, las moléculas adsorbidas en la superficie alteran la química superficial y dictan la funcionalidad en muchos contextos. El uso de estos materiales se ha incrementado sustancialmente en los últimos tiempos en una amplia variedad de áreas científicas y en diferentes sectores industriales tales como pinturas, automóviles, productos electrónicos y alimentación. En cuanto a su producción global, se estima alrededor de 11 millones de toneladas por año.

Los NMs se han clasificado según sus dimensiones, forma y origen. De este modo, podemos encontrar NMs 0-, uni-, bi- y tri-dimensionales, así como formas diversas tales como esferas, cilindros, elipses, tubos, racimos, entre otras. Además, los NMs pueden ser sintetizados con el objetivo de realizar una función específica, o presentar un origen natural y obtenerse a partir de ciertos productos presentes en el medio ambiente. La composición es otro parámetro que permite clasificar los NMs en diferentes grupos, de esta forma encontramos:

- Nanopartículas metálicas
- NMs a base de carbono
- NMs a base de sílice
- Quantum Dots
- Dendrímeros
- Composites

Dentro de la Química Analítica, estos materiales, presentan una gran importancia debido a sus propiedades intrínsecas y su gran utilidad. Por este motivo, dichos NMs pueden jugar dos papeles importantes, contribuyendo desde la etapa de muestreo y preparación de muestra, a la separación y detección, de acuerdo a su función y aplicabilidad para mejorar los parámetros analíticos

existentes, pero también han de considerarse propiamente como analitos de interés.

- Es imprescindible la caracterización y determinación de NMs, ya que son **analitos** que se encuentran en una amplia variedad de muestras, como cosméticos, alimentos, matrices clínicas y ambientales. El estudio de diferentes propiedades de estos materiales, tales como tamaños, morfología, estructura, estabilidad e interacciones químicas permite obtener una valiosa información (bio)química proporcionando un importante apoyo al desarrollo y conocimiento integral de la Nanociencia y la Nanotecnología. A pesar de su importancia, el número de estudios de nanomateriales como analitos solo representa el 30-35%. Por este motivo, no hay duda, que la caracterización y determinación de NMs desde una perspectiva analítica ha de abordarse con el objetivo de contribuir a este tipo de estudios para incrementar el conocimiento.
- Por otro lado, los NMs se utilizan como **herramientas analíticas**, desempeñando diferentes funciones con el objetivo de dotar de nuevos parámetros a los procesos analíticos existentes o desarrollar otros nuevos, y dar respuesta a las demandas de distintos campos de aplicación. Alrededor del 65-70% de los artículos publicados en Analytical Nanoscience and Nanotechnology emplean los NMs como herramienta analítica, demostrando su enorme valor, aplicabilidad y adaptabilidad.

En esta Tesis se han estudiado, nanopartículas de oro y plata (AuNPs y AgNPs) como nanopartículas metálicas, carbon black (CB) como NM basado en carbono, y nanopartículas y nanotubos de sílice, así como sílice obtenida a partir de cenizas de paja de arroz y su modificación, abordando la doble perspectiva analítica.

Las NPs metálicas como AuNPs y AgNPs, además de su elevada área superficial, exhiben una banda característica de resonancia de plasmón de superficie (SPR), debida a la excitación de los electrones de conducción superficial de las NPs por medio de radiación electromagnética. Esta banda depende de diferentes parámetros tales como el tamaño, la forma, la constante dieléctrica o el estado de agregación de las nanopartículas, permitiendo el uso de estos NMs como

herramientas analíticas en diferentes aplicaciones y en particular como sensores plasmónicos colorimétricos.

El CB es un material amorfo manufacturado que consiste en un fino polvo negro de carbono casi elemental en forma de partículas esféricas de tamaño coloidal, fusionadas en agregación de partículas y aglomerados. Tamaño, forma, área superficial o cristalinidad son parámetros importantes. Su porosidad, y su conductividad térmica y eléctrica lo convierten en un material muy utilizado en la industria. Además, su elevado uso, provoca su presencia en el medio ambiente durante su ciclo de vida.

Los materiales a base de sílice presentan diferentes rutas de síntesis a partir de reactivos químicos o también residuos, como por ejemplo la paja del arroz. Cristalinidad, tamaño de partícula y forma, morfología, porosidad, solubilidad o la química de la superficie delimitan su empleo en distintos campos. Su uso también está muy extendido en diferentes áreas de aplicación.

El proceso de dispersión de todos estos NMs es crucial tanto para su estudio como para sus usos específicos. Sin embargo, se trata de una etapa crítica ya que diferentes factores tales como el medio, el tiempo de preparación o diferentes condiciones ambientales pueden producir fenómenos de agregación, aglomeración o sedimentación que afectan a sus propiedades y a su estabilidad. Su modificación con diferentes ligandos o agentes superficiales está descrita para su estabilización. Además, el control y el seguimiento de las dispersiones permite evaluar las posibles modificaciones experimentadas, así como evaluar la correcta actuación de estos NMs.

Para el estudio de los NMs se utilizan diferentes técnicas analíticas. Las técnicas de imagen (SEM, TEM y microscopia óptica) y las técnicas espectroscópicas (DLS, UV-vis, FTIR y Raman) proporcionan información basada en sus propiedades intrínsecas, morfología y estructura. Las técnicas de separación, permiten obtener una mayor información sobre la distribución de tamaños. En esta Tesis, se ha empleado la cromatografía líquida capilar (CapLC), la nanocromatografía líquida (NanoLC) y el fraccionamiento de flujo de campo (FFF).

En este contexto, el grupo de investigación MINTOTA ha demostrado la aplicabilidad de CapLC para la caracterización de diferentes NPs metálicas,

observando una respuesta lineal entre la señal cromatográfica y la concentración de NPs, así como también respecto a los tamaños promedio. Además, el acoplamiento de la microextracción en fase sólida en tubo (IT-SPME) a capilar o nano LC con detector de fila de diodos (DAD), permite, por una parte, miniaturizar la etapa de preparación de la muestra y por otra, unificar el procesado de dicha muestra, la extracción, la preconcentración e inyección en una sola etapa. Esta metodología puede llevarse a cabo en diferentes tipos de configuración entre los que destacan, la modalidad de carga – expulsión en un muestreador automático, y la modalidad en válvula, la cual ha sido utilizada en esta Tesis.

Entre las diferentes aplicaciones de IT-SPME-CapLC-DAD, es muy interesante la aplicación centrada en el estudio de las dispersiones de NPs, la cual se caracteriza por la obtención de una respuesta cromatográfica que proporciona dos picos bien definidos, correspondientes a la existencia de diferentes distribuciones de NPs en la dispersión a granel: NPs no polarizadas que interactúan con la fase extractiva IT-SPME por un efecto hidrofóbico, y NPs polarizadas cuya separación viene gobernada por un mecanismo de exclusión por tamaño en la columna analítica. La relación de picos para una dispersión dada permite la estimación del diámetro promedio de las NPs metálicas y el estudio de distintas propiedades, tales con la estabilidad y posibles cambios en el nanoentorno. Desde el punto de vista cuantitativo, se ha demostrado que el área o altura de los picos cromatográficos está relacionada con la concentración de NPs. En esta Tesis se ha demostrado además la posibilidad de seguir un ensayo plasmónicos mediante el uso de IT-SPME acoplado a capilar y nano LC-DAD.

Por otro lado, esta Tesis aborda la técnica FFF como herramienta para la caracterización y determinación de NPs. Esta técnica se caracteriza por la presencia de un flujo en régimen laminar, lo que corresponde a un flujo máximo en el centro del canal y mínimo en las paredes superior e inferior, con un perfil parabólico con la altura del canal. Por tanto, la velocidad de elución de los analitos depende de su posición vertical en dicho canal. Por otro lado, en esta técnica, existe una fuerza externa que se aplica perpendicular a la dirección de elución de los analitos, es decir, en la altura del canal, que determina la posición de dichos analitos. Esto da como resultado un gradiente de concentración en esta pared, lo que permite un transporte neto por difusión desde regiones de mayor concentración a regiones de menor concentración cuando los analitos pueden difundirse significativamente, como es el caso de objetos de tamaño nanométrico o submicrométrico. Así, la

posición media de los analitos en la altura del canal viene gobernada por la fuerza aplicada y la difusión del analito. Esto da como resultado un orden de elución inversamente relacionado con el coeficiente de difusión de los analitos, o directamente relacionado con su tamaño hidrodinámico (DH).

En esta Tesis, FFF de flujo asimétrico (AF4) el cual emplea como fuerza externa una fuerza hidrodinámica generada por un segundo flujo perpendicular al flujo de elución, y FFF sedimentación (SdF3) basado en una fuerza centrífuga generada por la rotación del canal, que presenta una cierta curvatura han sido empleados para establecer y caracterizar las distribuciones de tamaños de las NPs.

Teniendo en cuenta el marco introductorio antes mencionado, los objetivos específicos de esta Tesis, se resumen en los siguientes ítems:

- Desarrollo de nuevas metodologías para la caracterización y determinación de AuNPs, AgNPs, CB y materiales basados en sílice. Para abordar este objetivo, se ha evaluado la señal característica de diferentes NMs obtenida mediante diferentes técnicas de separación como IT-SPME-miniaturizada-LC-DAD, AF4-UV-vis-DLS and SdF3-MALS. Además, se ha estudiado el efecto del tiempo en la estabilidad de la dispersión y la contribución de matrices ambientales como suelos o aguas con el fin de entender las transformaciones que los NMs pueden experimentar a lo largo de su ciclo de vida.
- Propuesta de nuevas herramientas basadas en las propiedades intrínsecas de las NPs metálicas y los materiales de base sílice usados como sensores o adsorbentes con el objetivo de llevar a cabo aplicaciones específicas o mejorar procedimientos analíticos existentes. En este caso, las NPs metálicas se han utilizado como plataformas plasmónicas para determinar y cuantificar ácidos y poliaminas. La sílice extraída de las cenizas de paja de arroz se ha utilizado como material para obtener un nuevo adsorbente iónico patentado que eliminar nitrato de agua, demostrándose útil en su remediación.

Para abordar los objetivos descritos, diferentes metodologías analíticas han sido utilizadas. En primer lugar, se ha llevado a cabo la síntesis de las AuNPs y AgNPs, siguiendo procedimientos establecidos en la bibliografía. Además, se ha



obtenido la sílice de la paja del arroz mediante un proceso sol-gel en el que el silicato aislado mediante tratamiento básico a reflujo, se ha modificado con el grupo amino. Siguiendo con el estudio de los materiales de sílice, también se ha sintetizado un pigmento híbrido con halosita y alizarina que ha sido caracterizado mediante AF4-DLS.

Las dispersiones de los diferentes NMs se han llevado a cabo mediante dilución de la dispersión original (NPs metálicas), o a través de procesos de dispersión asistidos con ultrasonidos (CB) o tratamientos básicos con agitación (materiales de sílice).

En cuanto a los tratamientos de la muestra, diferentes metodologías han sido aplicadas. Para la determinación de espermina mediante el uso de AuNPs, la extracción en fase sólida (SPE) ha sido usada con el objetivo de extraer el analito de interés de muestras de orina. Además, también se ha realizado una adsorción de nitratos sobre la sílice extraída de la paja del arroz y modificada mediante grupos amino por intercambio iónico. Para ello se ha diseñado un sistema en flujo que permite el paso de la muestra de agua a través del material adsorbente. Este mismo estudio también se ha realizado de forma estática mediante agitación.

Se ha evaluado la retención de AgNPs en suelos mediante agitación de una mezcla del analito de interés en la matriz a estudiar y medida del sobrenadante. En el caso del CB, mezclas del NM de carbono con matrices de suelo han sido tratadas con dispersantes poliméricos y biológicos en presencia de ultrasonidos, obteniendo un correcto aislamiento del NM en forma de dispersión, que puede ser posteriormente recuperado mediante una etapa de filtración.

Para el tratamiento de muestra en línea se ha utilizado la configuración de IT-SPME en válvula. Así, la muestra es procesada manualmente mediante la inyección en dicha válvula, de forma que los analitos son adsorbidos en la columna capilar. Posteriormente, al cambiar a la posición de inyección, dichos analitos son desorbidos y arrastrados al sistema cromatográfico mediante la fase móvil. Esta configuración también ha sido utilizada para el tratamiento y análisis de AgNPs fuera de línea, con el objetivo de evaluar la posible interacción de dichas partículas con la fase extractante y realizar el posterior análisis de tamaños mediante AF4.

Finalmente, las distintas condiciones experimentales características de cada técnica analítica han sido optimizadas con el objetivo de conseguir resultados adecuados en cada uno de los análisis realizados. Así, para IT-SPME-miniaturizada-LC-DAD, AF4-UV-vis-DLS y SdF3-MALS, se han ensayado diferentes flujos, volúmenes de inyección y fases móviles con el objetivo de conseguir resultados óptimos.

Teniendo en cuenta la metodología propuesta y los objetivos establecidos, los resultados englobados en esta Tesis se resumen a continuación:

Dispersiones de **AuNPs y AgNPs** han sido caracterizadas y su concentración ha sido determinada empleando la banda SPR característica como señal analítica a partir de las técnicas: IT-SPME acoplado a capilar y nano LC-DAD, y AF4 acoplado a detector UV-vis y DLS. Al caracterizar las dispersiones de AuNPs y AgNPs mediante LC miniaturizada, se observaron dos distribuciones de partículas correspondientes a poblaciones polarizadas y no polarizadas en la dispersión original, cuya separación se explicó mediante la exclusión por tamaño y el efecto hidrofóbico, respectivamente. Este efecto fue observado y estudiado en dispersiones de NPs metálicas comerciales y AuNPs desnudas. El uso de AF4-UV-vis-DLS, resolvió mezclas de diferentes NPs metálicas obteniendo resultados adecuados. Además, mediante el uso de esta técnica, se realizó un estudio de estabilidad con el tiempo y los resultados mostraron que la dependencia de la señal con el tiempo era más importante para las AgNPs que para las AuNPs, lo que se pudo correlacionar con su baja estabilidad. En relación con el tamaño de las partículas, la disminución de la señal fue mayor para los NPs metálicas más grandes. El mecanismo involucrado en este procedimiento de pérdida de señal se atribuyó a la disolución de las NPs metálicas en dispersiones acuosas diluidas, ya que el diámetro hidrodinámico fue constante.

Continuando con el estudio de las AgNPs, se realizó un ensayo de estabilidad en varias matrices acuosas mediante la técnica AF4. Este estudio permitió comprender el posible comportamiento de las AgNPs en el medio ambiente durante tiempos cortos. Los resultados fueron compatibles con la agregación de AgNPs, ya que se observó un cambio en la banda SPR y un crecimiento de tamaño de partícula con el tiempo. Los fractogramas mostraron diferentes huellas de evolución en función de las matrices medioambientales de agua estudiadas. El mayor efecto se observó en un agua del grifo, mientras que el

agua embotellada no proporcionó un cambio destacado en la estabilidad de las NPs. En cuanto al mecanismo de acción involucrado, la concentración salina podría ser uno de los efectos causantes de dicha agregación. Sin embargo, la materia orgánica disuelta y los haluros podrían proporcionar estabilización y pasivación de las NPs, respectivamente. Este hecho se observó al analizar aguas de transición y de mar con concentraciones elevadas de sales, pero que también contenían concentraciones considerables de materia orgánica y haluros. Al usar estas matrices, la agregación de las AgNPs fue menor de lo esperado.

En esta Tesis, también se evaluó cuantitativamente la capacidad de diferentes suelos para capturar AgNPs utilizando la técnica IT-SPME acoplada a CapLC-DAD para su seguimiento. Los resultados mostraron que la adsorción de AgNPs en un suelo se veía afectada principalmente por la cantidad de materia orgánica y secundariamente, por propiedades como el tamaño de partícula del suelo, pH, conductividad (EC) y potencial (Eh). Además, se observó que en los suelos con bajo contenido de materia orgánica, la extracción de diferentes compuestos por la matriz de NPs, tales como los ácidos húmicos, estabilizaban las AgNPs no retenidas, lo que dificultaba su adsorción.

Para completar el estudio de AuNPs y AgNPs, se evaluó la capacidad de éstas como herramienta analítica para la detección y cuantificación de espermina en orina, así como de diferentes ácidos (ácido acético, ácido clorhídrico y ácido fosfórico). La relación de las dos distribuciones de partículas presentes en las NPs metálicas y expuestas anteriormente condicionó su aplicación en estos ensayos plasmónicos. Tanto la técnica IT-SPME acoplada a LC miniaturizada con detector DAD, como AF4-UV-vis-DLS permitieron el seguimiento de dichos ensayos con resultados satisfactorios. Además, esta nueva metodología proporcionó una mejor sensibilidad y selectividad en comparación con la espectroscopia UV-vis.

Como material a base de carbono, se eligió el **CB** debido a su elevada utilidad en un gran número de áreas científicas y campos de ampliación. De este modo, diferentes muestras de CB se caracterizaron por AF4-UV-vis-DLS utilizando dispersantes poliméricos y biológicos. Se evaluó la capacidad dispersiva y se propusieron los mecanismos de dispersión para cada dispersante. Los tamaños hidrodinámicos obtenidos, mostraron diferencias significativas teniendo en cuenta el dispersante utilizado. El dispersante polimérico proporcionó diámetros hidrodinámicos más altos con estabilidades más bajas, sin embargo, al usar

dispersante biológico, el tamaño hidrodinámico fue más bajo y la estabilidad mejoró considerablemente. En ambos casos se realizaron estudios de precisión, obteniendo valores de desviación estándar relativa (RSD) menores al 5% con gráficos de calibración lineal satisfactorios.

Además, se realizó un estudio de estabilidad con el tiempo y los fractogramas mostraron que el dispersante biológico permitió obtener dispersiones con estabilidad adecuada durante una semana, en comparación con la menor estabilidad observada para las dispersiones poliméricas. Asimismo, también se realizó un estudio de estabilidad en diferentes matrices de agua. La dilución de la dispersión polimérica con diferentes matrices de aguas naturales produjo una pérdida drástica de la estabilidad de la dispersión, siendo este efecto despreciable en el caso de las dispersiones biológicas.

Teniendo en cuenta la gran aplicabilidad de este NM y su posible presencia en muestras ambientales durante su ciclo de vida, se desarrolló un procedimiento de pretratamiento de muestras basado en medios dispersivos para evaluar su aislamiento de muestras de suelo. Además, también se aplicó un paso asistido por filtración para evaluar la posible recuperación de dicho CB. De esta forma, se estudiaron muestras de suelo contaminadas con CB, el aislamiento del NM dependió de la composición de la matriz, obteniendo una posible relación entre el porcentaje de materia orgánica y la composición de partículas de los suelos con la eficiencia del procedimiento. Los suelos con mayor cantidad de materia orgánica y menor tamaño de partícula mostraron mejores eficiencias de dispersión utilizando dispersantes biológicos.

En el proceso de recuperación asistida por filtración, se estudiaron diferentes membranas para las dispersiones poliméricas y biológicas de CB. Los resultados obtenidos indicaron que el tamaño de partícula era un parámetro clave, que dependía del dispersante utilizado. Además, la carga superficial también debía ser considerada con el objetivo de obtener recuperaciones adecuadas. De este modo, los filtros de teflón de 0,10  $\mu\text{m}$  proporcionaron mejores resultados para dicho proceso de recuperación. Finalmente, se empleó reflectancia difusa para cuantificar el CB recuperado.

Como aplicación práctica se analizó una muestra de suelo contaminada con una pasta pigmentaria a base de CB, lográndose extracciones cuantitativas usando

el dispersante biológico, demostrando que la metodología propuesta es una herramienta prometedora para muestras ambientales. Como técnicas analíticas se utilizaron AF4-DLS y SdF3-MALS, con resultados satisfactorios en ambos casos.

Finalmente, los **materiales basados en sílice** fueron estudiados por AF4 para completar la información proporcionada por otras técnicas analíticas. Se analizaron diferentes materiales de sílice con distinto tamaño de partícula (desde nanómetros hasta micrómetros). Además, también se caracterizaron diferentes formas, como NPs o nanotubos.

Se llevaron a cabo dispersiones de SiO<sub>2</sub>NPs sólidas y se caracterizaron por AF4-DLS. Se obtuvieron los valores de tamaños hidrodinámicos. Además, también se analizaron diferentes dispersiones comerciales de SiO<sub>2</sub>NPs con diferentes tamaños nanométricos y condiciones de estabilidad. En este caso, los diámetros hidrodinámicos fueron menores confirmando la presencia de posibles estructuras en forma de collar de perlas (agregación de partículas) en las dispersiones de SiO<sub>2</sub>NPs sólidas analizadas en primer lugar. Para los NMs de sílice con otras formas, se seleccionaron nanotubos de halosita (HNT). Para este material también se evaluó su funcionalización con pigmentos.

Por otro lado, la  $\mu$ -SiO<sub>2</sub> obtenida a partir de cenizas de paja de arroz y su modificación con grupos amino se caracterizó como un ejemplo de material de sílice con una distribución de tamaño heterogénea (de nanómetros a micrómetros), obteniendo diámetros hidrodinámicos promedio de hasta 4  $\mu$ m. El uso de este material presenta ciertas ventajas respecto a la sostenibilidad, ya que permite reducir la cantidad de gases nocivos emitidos a la atmósfera debido a la quema indiscriminada de residuos de paja de arroz en los campos. Entre estos gases podemos destacar principalmente dióxido de carbono y metano, y en cantidad de trazas compuestos de nitrógeno y azufre, óxido de carbono y hidrocarburos policíclicos aromáticos. Del mismo modo, y mostrando una doble función sostenible, esta sílice modificada también puede ser usada como adsorbente iónico con el objetivo de reducir la cantidad de nitratos presente en las aguas. En esta Tesis, patrones y muestras reales de agua fueron tratadas con el adsorbente de sílice sintetizado y modificado. Los resultados mostraron reducciones considerables de la concentración del analito estudiado. Además, se evaluó la escalabilidad del método, comparándolo con métodos industriales tradicionales, observando ventajas potenciales.

Por lo tanto, se puede establecer una conclusión general: los NMs pueden presentar dos roles distintos dentro de la Química Analítica, por un lado, el uso de los NMs como herramientas analíticas, y por otro, el estudio de estos NMs como analitos. En la actualidad son muchos los logros analíticos en el uso de NMs como herramientas en el desarrollo de nuevos procesos analíticos, con especial incidencia en el tratamiento de muestras. Sin embargo, la detección y determinación de NMs en muestras complejas (ambientales, biológicas o industriales) es aún muy limitada, y la validación sistemática de los métodos correspondientes para ser incorporados en los laboratorios de rutina/control está lejos de ser una realidad en la actualidad. Por ello, para obtener una comprensión completa de su comportamiento y actividad, es necesario realizar una caracterización, determinación y evaluación de los NM teniendo en cuenta sus propiedades particulares, desarrollando así nuevas metodologías analíticas que complementen a las existentes.

Debido a su creciente aplicabilidad, es necesario hacer hincapié en la posible toxicidad de estos materiales. La conclusión hasta el momento es que, aunque los NMs no son peligrosos por sí mismos, todavía existe incertidumbre científica sobre su seguridad en muchos aspectos y, por lo tanto, la evaluación de esta debe realizarse caso por caso. De este modo, también son necesarias nuevas metodologías para completar el conocimiento de estos materiales desde el punto de vista toxicológico.

Teniendo en cuenta los diferentes resultados obtenidos en esta Tesis, se puede observar que la aplicabilidad de los NMs ha aumentado considerablemente en los últimos años. Además, su presencia en diferentes escenarios y matrices es cada vez mayor, mostrando la necesidad de caracterización.

De esta forma, en esta Tesis, se ha podido profundizar en el estudio de estos NMs como analitos, teniendo en cuenta distintos parámetros que pueden afectar a sus propiedades (tiempo de dispersión, condiciones ambientales, mezclas, presencia en distintas matrices...) con el objetivo de caracterizarlos y evaluarlos para asegurar su correcto desempeño en diferentes herramientas analíticas. Además, las metodologías analíticas desarrolladas, han contribuido a completar el conocimiento existente respecto a estos NMs y pueden servir como preámbulo para futuros estudios que continúen la misma línea de investigación.

# ABSTRACT

Nanoscience and Nanotechnology represent an expanding research area, which involves structures, devices, and systems with novel properties and functions. NMs are a key part in this field which particular properties and performance should be studied and knowledge.

In this Thesis, different analytical methodologies have been carried out in order to determine and characterize NMs as analytes. Moreover, different analytical tools employing this NMs have been evaluated in order to improve the existing and develop new analytical processes, aiming to exploit the unique physicochemical properties of these materials.

Therefore, AuNPs and AgNPs as metallic NPs, CB as carbon based NM and different silica based materials with different sizes and shapes have been studied using different analytical techniques. Image analysis techniques which are necessary to establish the size and shape descriptors have been used. By another hand, spectroscopic techniques have also been proposed to study the structure and presence of different compounds. Finally, separation techniques have also been studied in order to both characterization and determination the nanomaterials studied, and to provide additional information to that obtained with image and spectroscopic techniques.

Focusing in the separation techniques, IT-SPME-miniaturized LC coupled to UV-vis and FFF techniques coupled to UV-vis, DLS and MALS have been used for carry out the determination and characterization of these NMs. By IT-SPME-miniaturized LC, particle distributions of AuNPs and AgNPs were evaluated obtaining two different populations in the bulk dispersion. Moreover, a study of AgNPs retention in soils was performed. Using AF4 technique, the metallic NPs signal was characterized and the effect of different factors such as dilution, dispersion time and effect of environmental matrices was studied. AuNPs and AgNPs were used as analytical tools in this Thesis for carried out plasmonic assays in order to determine and quantify acid compound and spermine in urine samples.

CB was also studied by FFF techniques. In this case, CB dispersion using polymeric and biological dispersants were studied in order to establish the dispersions mechanisms and evaluate their stability with time. Moreover, the effect of water matrices in the dispersion were also tested. A procedure based on a dispersive media for CB isolation from soil samples and recovery of this NM using a filter-aided step were proposed by the first time with suitable results employing biological dispersants.

Silica based materials, such as  $\text{SiO}_2\text{NPs}$ , halloysite NTs and  $\mu\text{-SiO}_2$  obtained from rice straw ashes were characterized by AF4-DLS in order to show an overall vision about the separation mechanisms involved according to the material size and shape. Furthermore, this  $\mu\text{-SiO}_2$  obtained from rice straw ashes was modified with amino group with the aim of use it as adsorbent material for reduce the nitrate concentration in waters. The proposed methodology was tested using standards and real samples, and its scalability was evaluated.

Therefore, in this Thesis, it has been possible to carry out the study of different NMs, taking into account different parameters that can affect their properties with the aim of objective of characterizing and evaluating them to ensure their correct performance in different analytical tools. In addition, the analytical methodologies developed have contributed to enhance and complete the existing knowledge of these NMs and could be useful for future studies.



# INDEX

<b>CHAPTER 1: INTRODUCTION</b> .....	<b>1</b>
<b>1.1 OVERVIEW</b> .....	<b>3</b>
<b>1.2 NANOMATERIALS IN ANALYTICAL CHEMISTRY</b> .....	<b>7</b>
1.2.1 Metallic nanoparticles, MNPs .....	9
1.2.1.1 Gold and silver nanoparticles: AuNPs and AgNPs .....	9
1.2.1.1.1 Interest from the analytical perspective .....	9
1.2.1.1.2 Synthesis and properties .....	11
1.2.2 Carbon nanomaterials .....	20
1.2.2.1 Carbon Black .....	21
1.2.2.1.1 Applications and matrices of interest .....	21
1.2.2.1.2 Synthesis vs properties of CB and functionalized CB .....	26
1.2.3 Silica based nanomaterials .....	31
1.2.3.1 Spherical silica nanoparticles .....	36
1.2.3.2 Silica nanotubes .....	37
1.2.3.3 Other silica based NM shapes .....	39
<b>1.3 ANALYTICAL TECHNIQUES</b> .....	<b>40</b>
1.3.1 Spectroscopic techniques .....	40
1.3.2 Image techniques .....	44
1.3.3 Separation techniques .....	45
1.3.3.1 Liquid chromatography (LC) .....	46
1.3.3.1.1 IT-SPME-LC for NPs characterization .....	47
1.3.3.2 Field flow fractionation .....	50
<b>1.4 STUDIED ANALYTES AND MATRICES OF INTEREST</b> .....	<b>59</b>
1.4.1 MNPs in water and soil samples .....	59
1.4.2 CB in water and soil samples .....	60
1.4.3 Polyamines in urine samples .....	60
1.4.4 Nitrate in aquatic environments .....	61
<b>CHAPTER 2: OBJECTIVES</b> .....	<b>63</b>
<b>CHAPTER 3: METHODOLOGY</b> .....	<b>73</b>
<b>3.1 REAGENTS</b> .....	<b>75</b>

<b>3.2 INSTRUMENTATION .....</b>	<b>77</b>
3.2.1 Spectroscopic techniques .....	77
3.2.1.1 UV-vis spectrophotometry .....	77
3.2.1.2 Diffuse reflectance spectrophotometry (DR) .....	78
3.2.1.3 Infrared spectroscopy (FTIR) .....	78
3.2.1.4 Raman spectroscopy.....	79
3.2.1.5 Dynamic light scattering (DLS).....	79
3.2.2 Separation techniques.....	80
3.2.2.1 Capillary and nano high performance liquid chromatography .....	80
3.2.2.2 Field flow fractionation (FFF).....	81
3.2.2.2.1 Asymmetrical flow field flow fractionation (AF4) .....	81
3.2.2.2.1 Sedimentation field flow fractionation (SdF3) .....	82
3.2.3 Image techniques and others .....	83
3.2.3.1 Optical microscope .....	83
3.2.3.2 Scanning electronic microscope (SEM) .....	83
3.2.3.3 Transmission electronic microscope (TEM).....	84
3.2.3.4 Specific surface area technique (BET) .....	84
<b>3.3 PROCEDURES .....</b>	<b>85</b>
3.3.1 Synthesis of metallic NPs .....	85
3.3.1.1 Naked AuNPs synthesis .....	85
3.3.1.2 AgNPs synthesis .....	85
3.3.2 Synthesis of silica based materials .....	85
3.3.2.1 Silica obtained from rice straw ashes and its modification.....	85
3.3.2.2 Hybrid pigments HNT-alizarine (AZ-HNT) and modified-HNT alizarine (AZ-mod-HNT) synthesis.....	88
3.3.3. Preparation of dispersions.....	88
3.3.3.1 Metallic NPs dispersions.....	88
3.3.3.2 CB dispersions.....	88
3.3.3.3 Silica based materials dispersions .....	89
3.3.4 Sample treatment.....	91
3.3.4.1 Solid phase extraction .....	91
3.3.4.1.1 Spermine extraction .....	91
3.3.4.1.2 Nitrate extraction in batch .....	92
3.3.4.1.3 Nitrate extraction in flow .....	92
3.3.4.2 Solid-liquid extraction.....	95

3.3.4.2.1 AgNPs extraction .....	95
3.3.4.2.2 Dispersive isolation of CB from soil samples and filter-aided recovery .....	95
3.3.4.3 Off-line IT-SPME.....	97
3.3.4.4 On-line IT-SPME .....	98
3.3.5 Measurement conditions .....	99
3.3.5.1 Spectroscopic conditions .....	99
3.3.5.2 Chromatographic conditions .....	100
3.3.5.3 AF4 and SdF3 conditions .....	101
3.3.5.3.1 AF4 experimental conditions.....	101
3.3.5.3.2 SdF3 experimental conditions .....	109
<b>3.4 SAMPLES .....</b>	<b>109</b>
3.4.1 NMs bulk dispersions.....	109
3.4.2 Water samples .....	109
3.4.3 Soil samples .....	110
3.4.4 Urine sample.....	110
3.4.5 Pigment paste sample .....	110
<b>CHAPTER 4: RESULTS AND DISCUSSION .....</b>	<b>111</b>
<b>4.1 METALLIC NANOPARTICLES: AuNPs and AgNPs .....</b>	<b>113</b>
4.1.1 Characterization of MNPs by AF4-UV-vis-DLS .....	113
4.1.1.1 Effect of time in the analytical responses of MNPs.....	116
4.1.1.2 Effect of environmental water matrices in the stability of citrate-capped AgNPs .....	124
4.1.1.2.1 Characterization of selected citrate-capped AgNPs bulk batches used.....	124
4.1.1.2.2 Behavior of the dispersions in function of environmental water used as diluent.....	126
4.1.1.2.3 Characterizing information: AF4 vs Static DLS and UV-vis spectroscopy.....	136
4.1.2 Characterization of MNPs by IT-SPME-miniaturized LC-DAD.....	141
4.1.2.1 Study of the capture of AgNPs by several kinds of soils using IT-SPME-CapLC-DAD .....	144
4.1.2.1.1 Capture percentage (%) of AgNPs in the different soils.....	158

4.1.2.1.2 Capture percentage (%) of AgNPs in different sized-fractions of a given soil .....	161
4.1.2.1.3 SEM microanalysis studies.....	162
4.1.2.1.4 Influence of the properties of different soils on their ability to capture AgNPs .....	165
4.1.3 AuNPs and AgNPs to develop plasmonic assays .....	168
4.1.3.1 Monitoring plasmonic assays by AF4-UV-vis-DLS.....	168
4.1.3.1.1 Nanoparticle assessment.....	168
4.1.3.1.2 Analysis of different acids by AF4-UV-vis-DLS.....	171
4.1.3.2 Monitoring plasmonic assays by IT-SPME-miniaturized LC-DAD.....	175
4.1.3.2.1 Nanoparticle assessment.....	175
4.1.3.2.2 Analysis of spermine and different acids by IT-SPME-miniaturized LC-DAD.....	179
<b>4.2 CARBON NANOMATERIALS: CARBON BLACK.....</b>	<b>189</b>
4.2.1 Characterization of CB .....	189
4.2.1.1 Characterization of CB mixtures by AF4 .....	198
4.2.2 Effect of time on the analytical response of CB dispersions .....	201
4.2.3 Influence of water matrices in CB dispersion stability .....	202
4.2.4 Isolation of CB from soils and its recovery by filter-aided procedure.....	204
4.2.4.1 CB isolation from soils .....	204
4.2.4.2 CB recovery by filter-aided extraction from the dispersion .....	211
<b>4.3 SILICA NANOMATERIALS .....</b>	<b>225</b>
4.3.1 Characterization of silica based materials by SEM and FTIR-ATR. ....	225
4.3.2 Characterization of SiO <sub>2</sub> NPs by AF4-DLS .....	228
4.3.3 Characterization of HNT by AF4-DLS .....	235
4.3.4 $\mu$ -SiO <sub>2</sub> obtained from rice straw ashes. Characterization and applicability as adsorbent material .....	238
4.3.4.1 Optimization of the amino-silica synthesis and scale up possibilities .....	238
4.3.4.2 Characterization of $\mu$ -SiO <sub>2</sub> material and their amino modification .....	241
4.3.4.3 Absorption of nitrate in $\mu$ -SiO <sub>2</sub> from rice straw ashes .....	245

4.3.4.4 In-flow nitrate adsorption in standards and well water samples.....	249
4.3.4.5 Sustainability of the process in comparison with other methods.....	253
<b>CHAPTER 5: CONCLUSIONS .....</b>	<b>257</b>
<b>REFERENCES.....</b>	<b>267</b>
<b>ANNEX.....</b>	<b>307</b>
<b>A1. ABBREVIATIONS .....</b>	<b>309</b>
<b>A2. FIGURE LIST .....</b>	<b>313</b>
<b>A3. TABLE LIST .....</b>	<b>325</b>
<b>A4. PhD CONTRIBUTIONS TO PUBLICATIONS .....</b>	<b>329</b>



# **CHAPTER 1: INTRODUCTION**





## 1.1 OVERVIEW

The **nanomaterial** (NM) definition in the European Commission Recommendation 2011/696/EU Nanomaterial (NM) has been recently updated in the European Commission Recommendation 2022/C229/01 which establish: *'nanomaterial' means a natural, incidental or manufactured material consisting of solid particles that are present, either on their own or as identifiable constituent particles in aggregates or agglomerates, and where 50 % or more of these particles in the number-based size distribution fulfil at least one of the following conditions:*

*(a) one or more external dimensions of the particle are in the size range 1 nm to 100 nm; (b) the particle has an elongated shape, such as a rod, fiber or tube, where two external dimensions are smaller than 1 nm and the other dimension is larger than 100 nm; (c) the particle has a plate-like shape, where one external dimension is smaller than 1 nm and the other dimensions are larger than 100 nm.*

*In the determination of the particle number-based size distribution, particles with at least two orthogonal external dimensions larger than 100  $\mu\text{m}$  need not be considered. However, a material with a specific surface area by volume of  $<6 \text{ m}^2/\text{cm}^3$  shall not be considered a nanomaterial. Moreover, the following definitions apply:*

*(a) 'particle' means a minute piece of matter with defined physical boundaries; single molecules are not considered 'particles'; (b) 'aggregate' means a particle comprising of strongly bound or fused particles; (c) 'agglomerate' means a collection of weakly bound particles or aggregates where the resulting external surface area is similar to the sum of the surface areas of the individual components.*

In the last years, the use of NMs have substantially increased in a wide variety of applications fields and scientific areas since their unique properties have given rise a high number of applications. Figure 1 shows the increased interest of the scientific community in the last ten years.

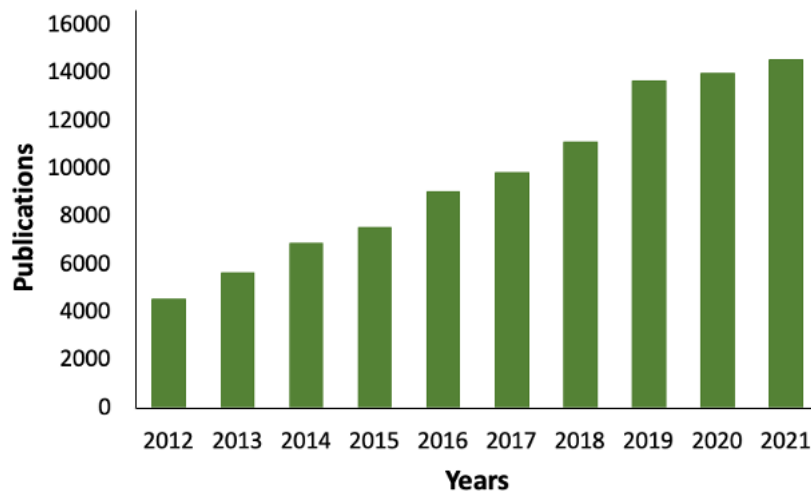


**Figure 1:** Publications from 2012-2021 with the topic “Nanomaterials”. Source: Web of Science, May 2022.

NMs offer great opportunities to improve conventional methods in different novel areas such as nanomedicine [1], environment [2] or analytical chemistry research [3]; and have been increasingly commercialized in several industries including paints, automobiles, clothing, sunscreens and electronic products [4]. Figure 2 shows the percentages of use of the most employed NMs [5].

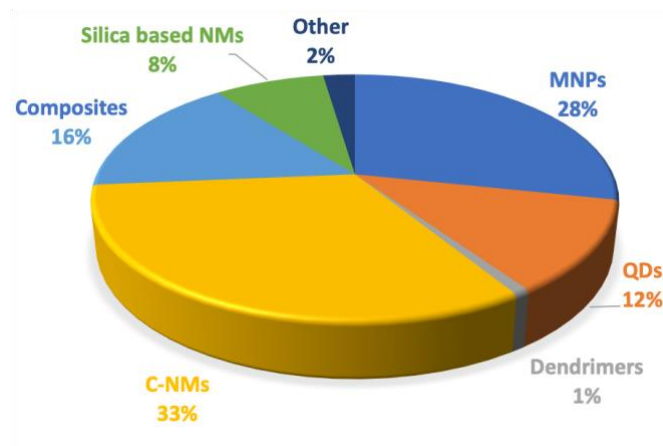


**Figure 2:** Percentages of use of NMs

Among the different types of NMs, the most widely used are (Figure 2) [5]:

- Metallic NPs (MNPs): mainly zero-valent metal nanoparticles (NPs), ionic NPs and metal oxides NPs. They can be synthesized chemically or biologically, but at industrial level, chemical methods are mainly applied. The most explored properties are: optical, thermal, magnetic and electric [6].
- Quantum Dots (QDs): these nanomaterials are semiconductor nanocrystals composed by metallic complexes of selenium and sulphur. QDs exhibit unique optical and electronic properties, so that they can absorb ultraviolet or white light and they have been used for their fluorescence properties [7]
- Carbon based NMs (C-NMs): are carbon compounds with different geometries (spherical, ellipsoidal or tubular), and specific properties such as thermal and electrical conductivity, tensile strength and elasticity. Fullerenes, multiwalled carbon nanotubes (MWCNT), single walled carbon nanotubes (SWCNT) or carbon black (CB), are the C-NMs most widely used [5].
- Dendrimers: dendrimers are multifunctional ramified nanosized polymers with specific functions in their endings. Moreover, their size, flexibility, topology and molecular weight can be modified in order to adjust it to perform different chemical functions in several fields [8].
- Composites: combine one or more NPs with other larger materials. Nanocomposites are integral for several industrial sectors such as automotive, electronic components, biochemistry and medicine [9].
- Silica based NMs: silica is the main component and include silica nanoparticles ( $\text{SiO}_2$ NPs), oxides or silica nanomaterials obtained by natural products, among others. Their unique structures and properties have given rise to a huge number of applications in different areas [10].
- Others: Different zinc, titanium and ceric NPs are used in a wide range of areas [11]. Polymers or organic based NMs such as liposomes, micelles and proteins are also used as ENMs.

Table 1 summarizes the principal properties of the different NMs that determine their applicability. Other properties such as chemical composition, size, shape, surface, crystallinity, and agglomeration/aggregation state should be also take in account in order to have a whole characterization of the NMs [12].

**Table 1:** Principal properties of different NMs.

NANOMATERIAL	PROPERTIES
<b>Metallic nanoparticles</b>	Large surface-to-volume ratio, optical, thermal, magnetic, catalytic and electrochemical
<b>Quantum Dots</b>	Optical and electrical
<b>Carbon based NMs</b>	Thermal conductivity, electrical conductivity, tensile strength, elasticity
<b>Dendrimers</b>	Specific function in their endings
<b>Composites</b>	Tensile strength, better torsion and stiffness, high fatigue endurance limit, and electrical conductivity.
<b>Silica based NMs</b>	Hydrophilic, easy surface functionalization, mechanical and thermal stability and low toxicity.

The success of NMs applicability depends on their full characterization. By another hand, considering that global production is estimated at 11 millions tons [13] and the increasing application of NMs, these play a key role in environmental science during their lifecycle, from synthesis to disposal, due to the direct and indirect emissions and possible human contact, wide obviously, is associated to toxicological studies of NMs in the different areas [14].

Different toxicity studies have demonstrated that NMs up to 10 nm have a similar behaviour than gases, they mainly disrupt the cell normal biochemical environment [15]. Studies with humans and animals have shown that after inhalation through oral exposure, NPs are distributed to the liver, heart, spleen, and brain in addition to lungs and gastrointestinal tract [16]. This fact might lead to changes in the cell viability, alteration mitochondrial function, generation of reactive oxygen species and lactate dehydrogenase leakage [17,18]. Moreover,

NMs could alter protein expression, produce inflammation and disturbing blood coagulation system [19].

The potential harmful effects associated with NMs have been demonstrated to be highly variable depending on multiple factors such as physicochemical characteristics and properties, exposure conditions and evolution processes as a result of chemical and physical transformations that NMs experiment after their synthesis. That is why Analytical Chemistry has address in the last years new challenges based on NMs as analytes and analytical tools [20,21].

## 1.2 NANOMATERIALS IN ANALYTICAL CHEMISTRY

NMs and their applications have a great importance in Analytical Chemistry. The number of reviews focused in “Nanomaterials analytical chemistry”, provided 550 results, whereof 286 belong to the last five years showing the increase interest on this topic [22].

Particles of wide-ranging chemistries are now routinely engineered and synthesized at the nm length scale to provide integral components for systems as diverse as medical therapeutics and diagnostics, energy harvesting and storage, textiles and construction, electronics, optics, and chemical synthesis and purification. Thus, it is not surprising that new methods for chemical analyses take advantage of the unique properties of NMs, as well as new methods for the analysis of NMs themselves, are nowadays intense research areas [23–25].

Hence, in Analytical Chemistry, NMs play two different important roles in the processes according to their different function and applicability (Figure 3):

- The NMs can be characterized and determined as **analytes** in a wide variety of samples, such as cosmetics, foods, clinical and environmental matrices. Different properties such as sizes, morphology, structure, stability and chemistry interactions are studied. The valuable (bio)chemical information obtained by these analyses provides a significant support to the integral development and knowledge of Nanoscience and Nanotechnology. Notwithstanding its importance, the number of analytical studies of nanomaterials as analytes on Nanoscience and Nanotechnology only

accounts for 30–35%. There is no doubt that analysis (both characterization and determination) of nanomatter material should be enforced from an analytical perspective [26].

- On the other hand, NMs can be used as **tools**, playing different roles (sorbents, stationary and pseudo-stationary phases, inert and active supports, sensors, fluorophore probes, and electric conductors) in different research fields to improve the existing and to develop new analytical processes, aiming to exploit the unique physicochemical properties of the nanomatter, thereby enhancing the analytical properties, which are indicators of the quality of the information provided. About 65–70% of the articles published in Analytical Nanoscience and Nanotechnology involve the use of nanomaterials as analytical tools [26].

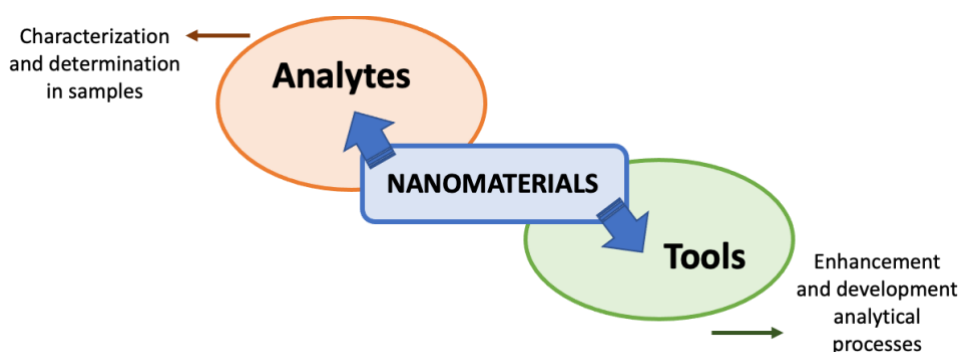


**Figure 3:** Schematic representation of the approaches where NMs are of analytical interest.

The use of the NMs in Analytical Chemistry as analytes and analytical tools involves the need to develop different analytical procedures in order to characterize and determine their presence and corroborate their proper performance in the different applications fields, that means, that the analytical parameters for different NMs must be addressed, considering their stability and potential variations under certain experimental conditions.

### **1.2.1 Metallic nanoparticles, MNPs**

MNPs, have attracted significant interest in a wide variety of research areas and applications fields according to their unique physical and chemical properties at nano-scale [27]. This group include zero-valent MNPs and oxide MNPs.

Among zero-valent MNPs, cobalt (Co) and niquel (Ni) zero-valent MNPs have been used as catalysts for the removal of organic pollutants [28]. In this group, AuNPs and AgNPs exhibit high applicability in medicine, chemical industries and bioanalytical areas [5].

In case of metallic oxide NPs, TiO<sub>2</sub>, ZnO, MoO<sub>3</sub>, Bi<sub>2</sub>O<sub>3</sub>, CeO<sub>2</sub>, CrO<sub>2</sub>, BaTiO<sub>3</sub>, among others are widely used. They are synthesized by several physical, chemical and biological methods. The metallic oxide NPs like TiO<sub>2</sub>, ZnO, Al<sub>2</sub>O<sub>3</sub>, along with MNPs like silver (Ag) and tin (Sn) have applications in paint industry. TiO<sub>2</sub> also have applications in solar cells, sunscreens, cosmetics, bottle coatings due to their unique property to block ultra-violet radiations. In the case of ZnO, NPs are part of fertilizer, cosmetics and coating industries. Iron oxide NPs showing significant promise for environmental remediation due to their purportedly low cost, highly reactive surface sites and high in-situ reactivity [29]. Furthermore, palladium (Pd)NPs and noble MNPs are used as modern diagnostic tools to combat serious diseases [30,31], among other utilities.

Nowadays, the released into the environment through household wastes, waste water treatment plants and industrial wastes of these MNPs and metallic oxide NPs have increased considerably. Moreover, their uses as tools in different analytical systems are also remarkably, making necessary a control of proper performance.

#### **1.2.1.1 Gold and silver nanoparticles: AuNPs and AgNPs**

##### *1.2.1.1.1 Interest from the analytical perspective*

Nowadays, AuNPs and AgNPs are used in many of the fields of science, analytical uses [32], medical applications [33–35], bioimaging [36], construction industry and sensor technologies [37,38]. Moreover, their easy surface

functionalization provides a versatile platform for different novel applications [39,40]. However, recent studies have demonstrated the toxicity of MNPs in model organisms such as *Drosophila melanogaster* [41] and human cells [42,43].

Figure 4.a, shows that Chemistry and Science Technology are most important application areas (32 %). In this field, colorimetric and electrochemical uses are predominant. Among the most notable applications and researches, it can be found the detection of different inorganic compounds in environmental samples, or characterization of different analytes in industrial matrices [44,45].

Biochemistry, biophysics, pharmacy, cell biology and medicine represent other important application areas (23 %), where the characterization and determination of vitamins [46], polyamines [47] and other organic compounds in biological matrices have been carried out by using AuNPs or AgNPs as read-out platforms.

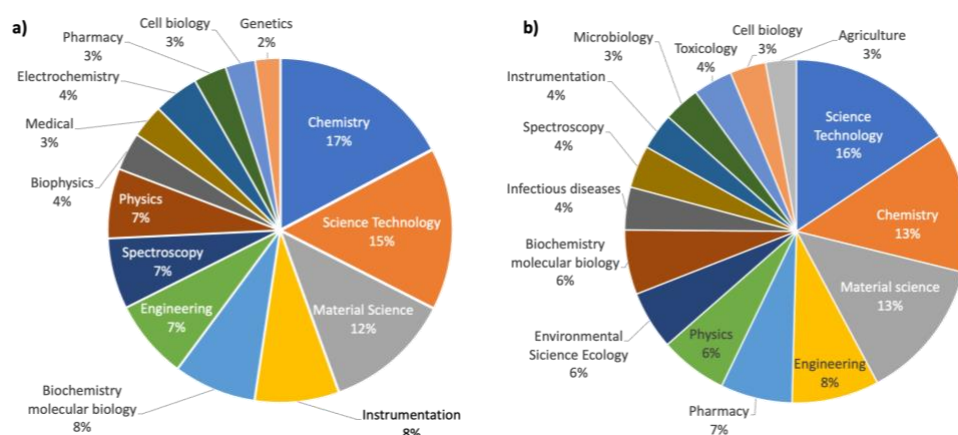


**Figure 4:** Application areas of MNPs with key words a) “Gold nanoparticles applications” 2016-2022. b) “Silver nanoparticles applications” 2016-2022. (Source: Web of Science). May 2022.

In the case of AgNPs, similar applications have been observed (Figure 4.b). Science technology, Chemistry and Material Science involve 42 % of the applications. Different industrial and analytical areas such as textile [48], electronics [49], food [40] and nanosensors [50] are also application areas. Similarly, medical, environmental and biochemical fields encompass a 36 % of



implementation areas with different application in agriculture [51], dentistry [52], toxicity [53], infectious diseases [54], biomedicine [55] and antimicrobial [48].

As can be seen, AuNPs and AgNPs present a broad-spectrum of applications in different research areas with different uses as analytes and tools, showing their versatility, adaptability and their utility.

#### *1.2.1.1.2 Synthesis and properties*

Different synthesis methods have been developed for AuNPs. The most used method was carried out by Turkevitch et al., and involves the reduction of  $\text{HAuCl}_4$  using citrate as a reducing agent [56]. However, the citrate-stabilized capping can produce a AuNPs irreversible aggregation. For this reason, other methods have been established for the preparation of AuNPs, employing different reducing agents [57].

Brust et al. synthesized organic soluble alkanethiol-stabilized AuNPs through a biphasic reduction protocol employing sodium borohydride ( $\text{NaBH}_4$ ) as the reducing agent and tetraethylammonium bromide as the phase transfer reagent [58]. This methodology allowed obtaining high stability NPs with low aggregation rate. Similarly, surfactants and different acid such as thiocetic acid or ascorbic acid have been employed, to prevent the aggregation processes [59,60].

AuNPs can be also synthesized by using laser ablation, obtaining accurate and reproducible results in terms of dimensional and morphological aspects. In this case, the synthesis mechanism required reduction of gold (III) chloride hydrate ( $\text{HAuCl}_4$ ) metallic precursor by considering the photo-induced effects of a 532 nm wavelength laser beam [47].

Recently, Green Chemistry based synthetic procedures have been proposed for AuNPs. The most important benefits of these synthesis are the availability of biological resources in large amount, high density, natural stability and easy solubility in water. Stozhko et al. carried out an effective eco-friendly methodology to obtain AuNPs employing plant extracts (phytosynthesis) as reducing, stabilizing, and capping agent. The main advantages of the AuNPs were a high catalytic ability in the process of organic dye degradation, antibacterial and antioxidant activity [61,62].

Focusing in AgNPs, different synthesis routes have been developed. Physical synthesis, consists in the AgNPs generation by the use of thermal energy. This involves the evaporation condensation reaction to enhance the nucleation reaction by increasing the temperature [63]. Moreover, laser ablation has been also proposed to prepare AgNPs. Using this method, pure and uncontaminated AgNPs colloids can be prepared as in [64] where NPs 9 and 20 nm were obtained by laser ablation in water with continuous and pulsed laser, respectively.

Regarding to chemical synthesis, reduction by organic and inorganic agents is the most common approach. Different reducing agents such as sodium citrate, ascorbate, sodium borohydride, H<sub>2</sub> and different copolymers have been used as reductor of silver ions (Ag<sup>+</sup>) in aqueous or non-aqueous solutions. Furthermore, methods like photoreduction have been described. In this methods the properties of produced NPs were studied as a function of irradiation time [65]; microwave-assisted synthesis which allowed obtaining AgNPs with low reaction times and preventing particle agglomeration [66]; or electrochemical synthetic methods with control particle size by adjusting electrolysis parameters, and improvement of homogeneity by changing the compositions of electrolytic solutions [63], among others.

Green synthesis of AgNPs using different natural compounds present in plants, (*Azadirachta indica*), fungi (*Phaenerochaete*) or algae (*Spirulina platensis*) have been described. AgNPs produced by bacteria (*Klebsiella pneumonia*) acting as reducing and capping agent have also been proposed with the advantage of cost and time-effective results [67–69].

Synthesis of non-spherical AuNPs and AgNPs planar (triangles, 5 or 6 diagonal, round surfaces, etc.) and three dimensional (cubic, pyramid, etc.) have been described [70]. MNPs with non-spherical morphologies have been synthesized in a one-step methodology by using Eosin Methylene Blue agar as reducing agent [71]. Similarly, several AgNPs with non-spherical structures in the presence of polyvinylpyrrolidone as capping compound have been also reported [72].

All the above procedures have given rise to AgNPs and AuNPs dispersions. The dispersion state of MNPs is a critical parameter of these NMs due to their

possible effect in the intrinsic properties of NPs, and consequently in the applicability. Different factors such as media, preparation time or environmental conditions can produce phenomena such as aggregation, agglomeration or precipitation that, obviously, modify the dispersion features [73]. For this reason, the control and monitorization of AuNPs and AgNPs dispersions are decisive to ensure a reliable performance.

The enhancement of dispersibility and biocompatibility MNPs, in particular AgNPs and AuNPs, can be achieved by surface functionalization. In addition, it can prevent aggregation, agglomeration and precipitation. The presence of charged ligands or capping agents in the nanomaterial surface allows the presence of electrostatic and steric repulsions which are responsible for this stability [74]. More specifically, this repulsion process consists in the formation of a tightly bonded layer known as the Stern layer due to the negatively charged surface of the MNPs attracts some of the positive ions (counter ions) in the dispersion. Stern layer gives rise to a diffuse region of positive ions, shielded and solvated negative ions and dispersant molecules, known as the diffuse layer, which extends from the Stern layer to electrostatic equilibrium. All this set of charged species distributed around the NP forms what is known as the electric double layer (Figure 5). This electrostatic layer protects the NPs and prevents them for aggregation. The DLVO theory (from Derjaguin, B.; Landau, L.; Verwey, E.; Overbeek, T.) [75] explains the stability and behavior of colloidal systems as an equilibrium between opposite forces: the attractive van der Waals forces and the electrostatic repulsion of the electric double layer. Consequently, the system stability depends on the resultant force of both, whose magnitude determines the kinetic energy that two NPs must have when colliding to overcome the energy barrier that prevents their aggregation. However, DLVO lacks an atomistic description of the electrical double layer at the surface of NPs, which excludes the examination of the molecular properties of the solvent electrolytes, and eventually aggregating onto the NP [73].

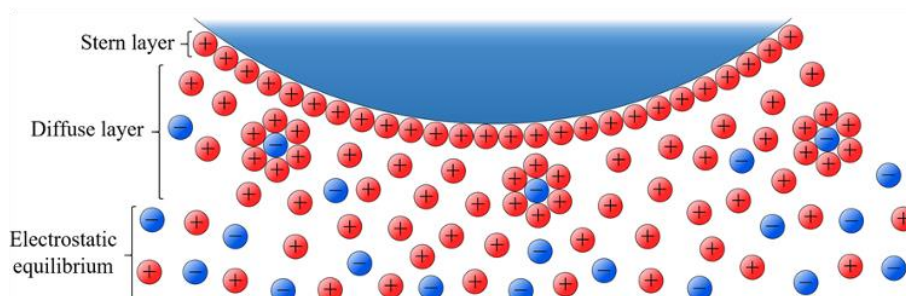


**Figure 5:** Schematic representation of the electrical double layer in a negatively charged NP.

Other studies have showed that the strength of electrostatic repulsion is connected to the degree of the surface charge, which, in turn, depends on the pKa value of the ligands, the pH value, and the ionic strength of the solution and the matrix [76]. Thus, capping agents and ligands, with high surface charges such as citrate and ionic polymers, are generally used as stabilizing agents in AuNPs [77]. Surface modification using long-chain spacers, such as PEGylation or neutral polymers, is another method to preserve and enhance the stability of AuNPs suspensions, depending on steric repulsion [76]. The ligand amounts and direction are two critical factors of the AuNPs properties on the functionalization process, since they play a key role in the strength of the interactions with other molecules. Similarly, the environmental conditions are important. For example, the storage in the dark and cold conditions allows extended the AuNPs stability considerably [78]. In other cases, the different compounds present in the matrix can also affect the dispersibility of AuNPs, as well as to enhance possible transformations that can alter their performance. Following the same approach in order to enhance AuNPs dispersion stability, their encapsulation in polymers, silica and metal organic frameworks can contribute to provide a higher stability combined to more robust protection [79].

As can be seen in Table 2, different method using different capping agents and ligands have been used in order to improve stability of AuNPs dispersions and avoid their aggregation.

**Table 2:** Capping agents used in AuNPs.

Group	Ligand		Size (nm)	Function	Ref.
	Compound				
<b>Thiol</b>	DHLA		3-5 - 6.5	Stabilizing and aggregation prevention. Antioxidant activity.	[80]
<b>DNA</b>	Poly A, G, C and T bases		13	Stability. High ionic strength	[81]
<b>RNA</b>	siRNA		5 - 25	Stability. Cellular delivery	[82]
<b>Protein</b>	BSA		13 - 50	Colloidal stability. Reversible agglomeration / disagglomeration	[83]
<b>Lipids</b>	DOPC, sphingomyelin and cholesterol		13 - 60	Stability. Biomedical diagnostics.	[84]
<b>Salts</b>	Sodium citrate and phosphate (PBS)		3 - 150	Stabilizing	[85,86]
<b>Polymer</b>	Polyethylene glycol		11 -24.5	Stabilizing	[85]
<b>Carbohydrates</b>	Polysaccharides		10	Stabilizing agent. Used for modified of glassy carbon paste electrode	[87]
<b>Natural bioactive</b>	Helichrysum foetidum extract. Helichrysetin and helichrysin		2 -12	Biosafety and avoid toxically effects. Stabilizing	[88]

As in the case of AuNPs, it is important to use capping agents to stabilize and dispersion the AgNPs during of MNPs preparation in order to avoid their aggregation. The presence of different salts and surfactants comprising

functionalities for interactions with particle surface can stabilize particle growth, and protect particles from sedimentation, agglomeration, or losing their surface properties. Similarly, polymeric compounds have been reported to be the effective protective agents to stabilize AgNPs [89]. In the last years, eco-friendly capping in AgNPs green synthesis have also been used [90]. Table 3 shows some representative examples of capping agents used for AgNPs.

**Table 3:** Capping agents used in AgNPs.

Ligand		Size (nm)	Function	Ref.
Group	Compound			
<b>Thiol</b>	5-methyl-1,3,4-thiadiazole-2-thiol	1 - 12	Exceedingly stability. Colorimetric sensor applications	[91]
<b>Surfactants</b>	SDS and CTAB	---	Stabilizers for the preparation of AgNPs	[92]
<b>Salts</b>	Sodium citrate	13 - 30	Stabilizers	[93]
<b>Amino acids</b>	Tyrosine	14	Reductor and capping agent	[94]
<b>DNA</b>	Double-stranded DNA	81	Stabilizers. Allows selective electron transfer	[95]
<b>Polymer</b>	PVP, Chitosan	3 - 132 / 13 - 27	Enhanced the antibacterial activity. Colorimetric sensor	[96–98]
<b>Natural capping</b>	Yerba mate	34 - 144	Stabilizing. Use eco-friendly capping agent	[89]

The high applicability of AuNPs and AgNPs is mainly due to their specific physicochemical and optical properties. On the one hand, surface plasmon resonance (SPR) band is a unique and characteristic property of MNPs, in particular for AuNPs and AgNPs, according to their extraordinary efficiency absorbing and scattering light. SPR takes place when NPs surface conduction electrons are excited by electromagnetic radiation (with higher wavelength than NP size). The excitation produces a oscillation of the free electrons with the electromagnetic wave frequency but confined in the nanometric size, and consequently a scattering of the incident light [99]. Therefore, the sum of absorbed light and scattering light

produce a new absorbance band called SPR band. The characteristics of this band depend on several parameters such as shape, size, dielectric constant and aggregation state. However, the absence of this band in both small nanoparticles ( $d < 2$  nm) and the bulk material must be taken into account [100]. Figure 6.a shows a schematic representation of SPR.

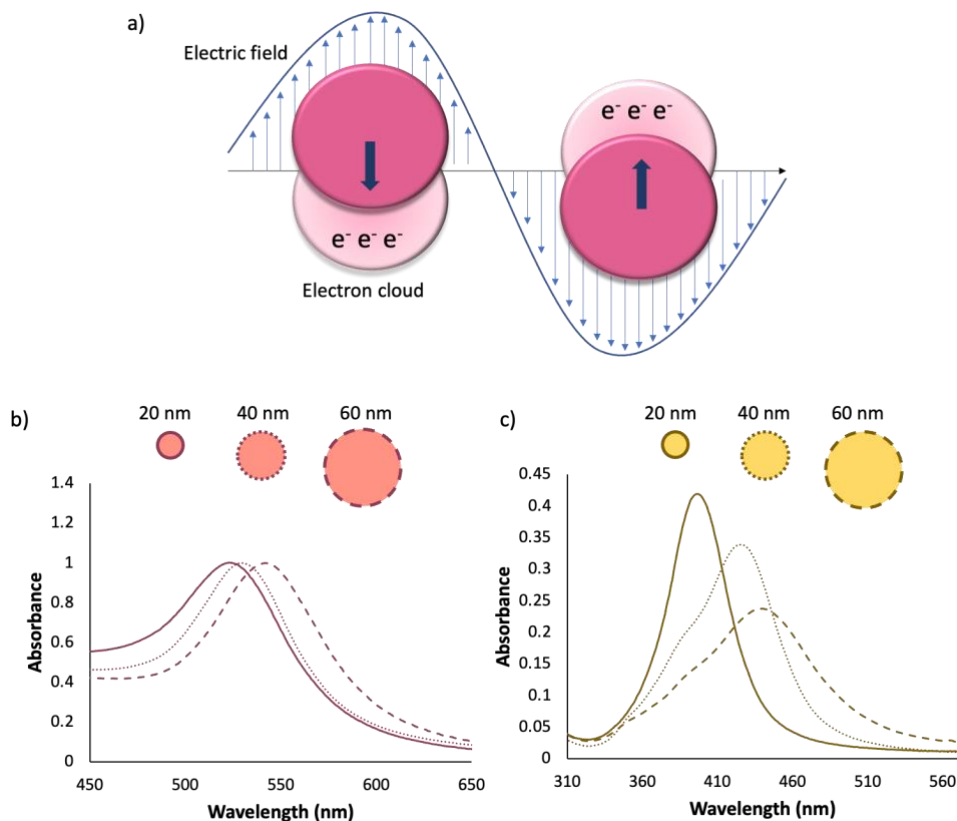






**Figure 6:** a) Schematic representation of localized SPR band. b) Normalized SPR bands of spherical AUNPs of 20, 40 and 60 nm. c) SPR bands of spherical AgNPs of 20, 40 and 60 nm

As can be seen in Figure 6.b and c, SPR band depends on the particle size. An increase of particle core size produces a SPR band shift towards greater wavelength. This effect can be observed in AuNPs and AgNPs with different core sizes.

For AgNPs, SPR band shows a significant correlation with NPs shape. By controlling synthesis methods, reducing and stabilizing factor, NPs sizes and therefore, SPR band can be controlled (see Table 4). These shapes provide different SPRB according to the number of resonant bands which in turn is mainly determined by the number of ways in which its electron density can be polarized. Moreover, the position of SPRB also depends on shape anisotropy and corner sharpness [101].

**Table 4:** Relationship between nanomaterials shape and SPR band.

Shape	SPR band
	A strong SPR band at 410 nm is observed. Moreover, a small shoulder band also appears at 370 nm, which is a quadruple resonance.
	The primary SPR band is observed around 900 nm. With ensemble measurements where light polarization effects are randomized, two SPRB (longitudinal and transverse) should be observed.
	A strong SPR band at 510 – 520 nm with a number of additional peaks at lower wavelength are observed.
	A high dipole resonance at 750 – 800 nm is showed. Different peaks with lower intensity are observed around 450 – 550 nm.

As above mentioned, different environmental conditions can produce SPR band shifts that can be related with aggregate, agglomerate and precipitate NPs process. These phenomena make MNPs a very interesting tool with different applications [102]. This is the case of colorimetric sensor, based on SPR band shift to higher wavelengths and broadened when the analyte is present due to the aggregation or agglomeration processes. The analytical response will be a colour change that can be quantified. As can be seen in Table 5, different examples of the



use of AuNPs and AgNPs as colorimetric sensor have been reported in the bibliography.

**Table 5:** Uses of MNPs as colorimetric sensors in to determine different analytes.

MNPs	Analyte	LOD	Matrix	Ref.
Ag nanoplates	Hydrogen sulfide	520 nM	Cancer cells	[103]
AgNPs	Hydrogen sulfide	45 nL·L <sup>-1</sup>	Breath	[104]
AuNPs-aptamers	MAMP - MDMA	5 mM	Water	[105]
AgNPs-citrate	Creatinine	53.4 nM	Urine	[105]
AuNPs-sucrose	Vitamins B1 and B6	8 ng·mL <sup>-1</sup> for B1 and 15 ng·mL <sup>-1</sup> for B6	Rice	[46]
AuNPs solution	Spermine	15 ng·L <sup>-1</sup>	Urine	[47]

On the other hand, AuNPs and AgNPs show characteristic properties such large surface-to-volume ratio, excellent biocompatibility, low toxicity, electronic characteristics, thermal conductivity and catalytic applicability. These properties also allow the use of NPs as attractive material for electrocatalyst and as carrier in medicine science [106].

These MNPs exhibit an exceptional quenching ability to proximal fluorophores, which is related with the adequate overlap between the emission spectrum of excited fluorophores and the SPRB. This phenomenon is called Fluorescence Resonance Energy Transfer (FRET) and it take place with AuNPs and AgNPs up to 1 nm [100]. Similarly, AuNPs can act as a quenching fluorophore through the electron acceptance in the photoinduced electron transfer process (PET). This process is controlled by charging/discharging of the gold core [107,108].

MNPs have also been used as effective surface-enhanced Raman spectroscopy (SERS) substrates [109]. SERS is a surface sensitive technique that provides high Raman scattering enhancement of molecules adsorbing on a rough metal surface. The NPs allows an electrochemical enhancement which occurs as the surface plasmon gets excited by incident light and amplifies the electromagnetic field of the metal surface. Moreover, a chemical enhancement,

take place when the molecule adsorbs strongly on the surface of the metal, which leads to changes of its polarizability [110–112].

Likewise, AuNPs and AgNPs show antibacterial and immunological properties, which implies a have attracted significant interest as a novel platform in nanobiotechnology and biomedicine [113].

Therefore, considering all the above aspects, the study, analysis and characterization of this metallic nanoparticles are necessary to fully understand and monitor their properties, stability and proper performance [114].

*In this Thesis, the AuNPs and AgNPs determination have been carried out in order to characterize and monitor their stability and possible modifications in different matrices. Moreover, their applicability as analytical tools taking advantage of the SPR band have also been studied.*

### **1.2.2 Carbon nanomaterials**

Carbon nanotube (CNT) are the most used C-based NM. Discovered by Iijima in 1991, it may be regarded as a single graphene layer rolled along an axis aligned along the graphene crystalline directions. As CNTs also carbon fibers (CFs) are unidimensional system. However, CFs are disordered, tangled structures possessing a two-dimensional long-range order of C atoms organized in planar hexagonal networks while in the direction orthogonal to these planes, CFs display only a short range order due to parallel plane stacking [115]. If in unidimensional carbon structures we reduce their length to the nanometer size we will obtain nanocages. Fullerenes is a perfectly spherical nanocage formed by a number of pentagonal and hexagonal rings. Carbon nano-onions (CNOs) are cages with spherical or polyhedral shape formed by several fullerene-like overlapped carbon shells, which are defective and disordered to a certain degree. Another unidimensional carbon nanostructure (CNS) is represented by the carbon dots (CDs) which contain graphitic and amorphous carbon phases [116]. Focusing in the amorphous materials, nowadays, CB is another C-NM with a great applicability in a wide variety of industrial fields and research areas due to their intrinsically properties, and therefore, the development of analytical methods is of great

interest, since, contrary to CNTs, CB are still scarcely explored from the Analytical point of view.

### **1.2.2.1 Carbon Black**

CB is a manufactured amorphous material consisting of a fine black powder of nearly elemental carbon in the form of spherical particles and their aggregates and agglomerates. It is produced mainly by the incomplete combustion of hydrocarbons under reduced presence of oxygen [117,118]. Its excellent ability to color, electrical conductivity and weather, and chemical resistance, make it in a powerfully material used in a wide variety of areas. Similarly, the nature of CB surface and its characteristics with respect to its structural organization, porous structure, surface area and its chemical composition are of outstanding importance according the different uses of CB in specific applications [119]. The main difference with elemental carbon is the lower content of extractable organic and inorganic compounds (lower than 1%). Likewise, it is physically and chemically distinct from black carbon (BC), which is generated as byproduct from incomplete combustion, being the amount of carbon content in its structure lesser than 50% [120].

#### *1.2.2.1.1 Applications and matrices of interest*

As can be seen in Figure 7, materials science, chemistry, science technology and engineering are the subjects where CB-NM exhibits a higher presence. These items cover more than 58% of global applicability. Focusing in material science and chemistry, a revision about the different uses of CB-NM showed that the utility as composites or reinforcing filler in tires and other rubber products [121], electrochemical sensors [122], toxicity studies [123] or pigments [124] are predominant. Furthermore, CB-NM also has an important role in Environmental Science, Ecology, Food and Medicine subjects, which cover a percentage up to 10% of applicability. This is an evidence of the increasing interest of CB-NM in biological samples.

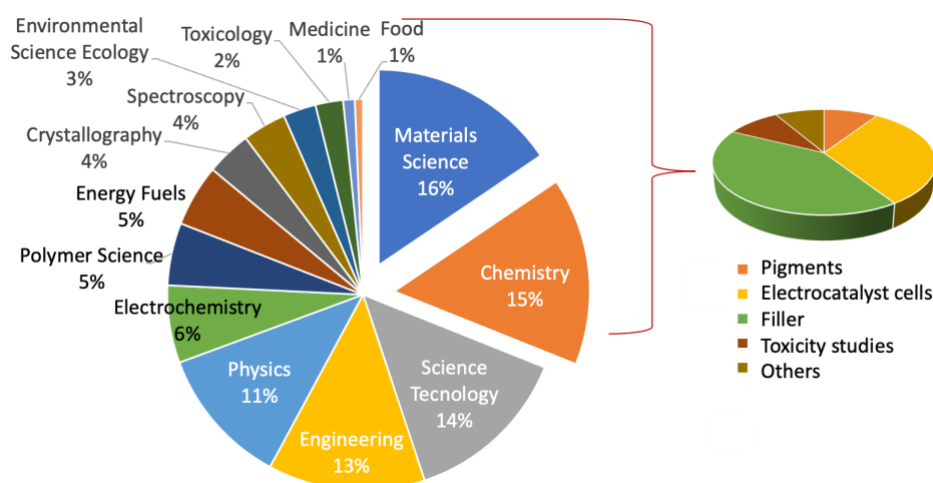


**Figure 7:** Application areas of CB-NMs. Web of Science and keywords “Carbon Black nanoparticles applications” 2016-2022.

The main health concerns associated with CB and other poorly soluble, low-toxicity (PSLT) particles are lung effects resulting from inhalation exposure, besides the overall weight of evidence indicates that CB should not be considered a direct genotoxicant or reproductive toxicant [123]. The International Agency for Research on Cancer (IAARC) has classified CB (airborne, unbound particles of respirable size) as possible carcinogenic to humans (Group 2B) [125]. The sizes of CB primary particles range from 10 nm to 100 nm. A few to many tens of particles immediately form highly branched chains of primary particles called aggregates, which can agglomerate. CB can cause lung tumours, chronic inflammation and epithelial hyperplasia, depending on the particle size, level of aggregation and/or agglomeration. Agglomerates can reach many micrometers in diameter, which decrease cancer risk in humans if their sizes are higher than 10  $\mu\text{m}$ , which is the respirable particle size. Thus, the knowledge of the aggregation/agglomeration stage is useful to evaluate the potential toxicological issues. Other diseases associated with exposure to CB in animals, specifically mice, are the cardiovascular dysfunctions, sexual and neuroinflammatory changes, lower sperm production and disorder male reproductive system [126].

Table 6 summarizes the most studied CB matrices, including their functions for industrial matrices or studies carried out for environmental and health related matrices, used concentrations and CB sizes.

**Table 6:** Characteristics and functions of matrices where CB can be found.

Matrix/Ref.	CB Phase	Function / Studies	Concentration	Size (nm)
Toners / [129]	Solid	Pigment	4 - 20 %	3000 - 10000
Inks / [124]	Solid-Liquid dispersion	Pigment	0.2 - 20 %	70 - 270
Paints / [127]	Solid-Liquid dispersion	Pigment	20 - 25 %	10 - 6800
Electrodes / [130,131]	Solid	Determination of Bisphenol A chloramphenicol	0.1 % 0.5 %	< 510
Nanoclays / [132]	Solid	Filler	3 %	< 2000
Resins / [133]	Solid	Filler	14 - 33 %	< 500
Polymers/ [134]	Solid	Filler	10 - 50 %	40 - 50
Rubber tires/ [136]	Solid	Reinforce and filler	20 - 35 %	15 - 100
Plastics / [135]	Solid	Reinforce and filler	2.5 - 5 %	16, 100 - 200
Air / [138]	Solid-Gas dispersion	Particle size determination and toxicological studies (as model)*	0.12 – 3.24 mg L <sup>-1</sup>	150
Soils / [139]	Solid	Particle size determination and toxicological studies*	10 - 1000 mg Kg <sup>-1</sup> (CB spikes)	20 - 70 (aggregates)
Sea water / [140]	Solid-Liquid dispersion	Particle size determination and toxicological studies*	1 - 10 mg L <sup>-1</sup> In vitro assays of mussel hemocytes	35 - 400
Cell media / [141]	Solid-Liquid dispersion	Characterization and toxicological studies*	10 - 500 mg L <sup>-1</sup> In vitro assays	60 – 270

Considering the high efficiency of CB in radiation absorption of pigment, toners, inks and paints, these matrices were analyzed [124,128,129]. CB was used for modifying working glassy carbon electrodes (GC), for example GC modified by casein-CB (CAS-CB) was applied for improving the detection limit of bisphenol A (BPA) sensing in environmental and milk samples [130]. Functionalized CB nanospheres and MoS<sub>2</sub> nanoclusters were proposed for the effective electrocatalytic reduction of chloramphenicol [131]. Moreover, CB was proposed as filler in nanoclays [132], resins [133], polymers [134,135] and rubber tires [136]. Note that the matrices contained CB are solid, solid-liquid and solid-gas dispersions as Table 6 shows. For CB dispersions, stability is a relevant factor

Environmental and health-related samples are also becoming interesting matrices for toxicological studies [137–141]. However, these matrices are still scarcely explored, and therefore the development of new analytical methodologies for the analysis of CB in water, soil, air and in biological samples, is of great interest from environmental, health and industrial point of views. In vitro toxicity assessment of engineered nanomaterials (ENM) in general, the most common testing platform for ENM, requires prior ENM dispersion, stabilization, and characterization in cell culture media [141]. Accurate characterization of important properties of such polydisperse distributions (size distribution, effective density, charge, mobility, aggregation kinetics, etc.) is critical for understanding differences in the effective dose delivered to cells as a function of time and dispersion conditions, as well as for nano-bio interactions [141]. Table 6 shows that CB concentrations of interest and CB sizes in the several matrices are very different. Those facts are relevant in order to implement analytical procedures together with sample matrix type.

Table 7 shows selected review articles published in the period 2018-2021 about CB nanomaterial. As it can be seen, the interest was focused on previously discussed applications bearing in mind the improving of their performance and the evaluating of the toxicity as main topics treated [119, 125, 142–154]. This table also shows the interest of the scientific community in CB recycling [144,148] and remediation [146]. However, the characterization of CB in different matrices is still unexplored, specifically for environmental and biological samples. A limited number of reviews are focused in this topic which shows the needed of develop new methodologies of determination and characterization of CB in these matrices.

**Table 7:** Reviews of “Carbon Black Nanoparticles / nanomaterials “ (2018-2021)

<b>Title / topic</b>	<b>Ref.</b>
Development of hybrid materials based on carbon black reinforced poly(2-methoxyaniline): preparation, characterization and tailoring optical, thermal and electrochemical properties / <b>Application – reinforcement</b>	[142]
Recent development in nanocarbon materials for gas sensor applications / <b>Application – sensors</b>	[143]
Review; Risk Assessment of Aerosolized SWCNTs, MWCNTs, Fullerenes and Carbon Black / <b>Toxicity</b>	[125]
Wet compounding with pyrolytic carbon black from waste tyre for manufacture of new tyre – A mini review / <b>Application – tyres</b>	[144]
Carbon black as an outstanding and affordable nanomaterial for electrochemical (bio)sensor design / <b>Application – sensors</b>	[119]
Applications of Wet-Functionalized Graphene in Rubber Composites / <b>Application – tyres</b>	[145]
Sustainable Development of Carbon Nanocomposites: Synthesis and Classification for Environmental Remediation / <b>Application – composites</b>	[146]
Nanocomposite and bio-nanocomposite polymeric materials/membranes development in energy and medical sector: A review / <b>Application – fillers</b>	[147]
Challenges and Emerging Trends in Toner Waste Recycling: A Review / <b>Application – toners</b>	[148]
Flexible strain sensors fabricated using carbon-based nanomaterials: A review / <b>Application – sensors</b>	[149]
Current overview and perspectives on carbon-based (bio)sensors for carbamate pesticides electroanalysis / <b>Application – sensor</b>	[150]
The impact of nanomaterial characteristics on inhalation toxicity / <b>Toxicity</b>	[151]
A Systematic Review of the Routes and Forms of Exposure to Engineered Nanomaterials / <b>Toxicity</b>	[152]
Fetotoxicity of Nanoparticles: Causes and Mechanisms / <b>Toxicity</b>	[153]
Polyurethane Composite Foams in High-Performance Applications: A Review / <b>Application – fillers</b>	[154]

### 1.2.2.1.2 Synthesis vs properties of CB and functionalized CB

Carbon Black includes a high variety of materials with different properties, providing a wide diversity of matrices. The properties and performance of CB-NMs depend on the production process carried out. According to the chemical processes, they can be classified, taking into account incomplete combustion, as thermal oxidative decomposition that includes furnace black, lampblack and channel black; thermal decomposition in the absence of oxygen that covers thermal black and acetylene black; and a more environmental friendly method named plasma process [155–157]. In the context of physical-chemical properties, oil furnace provides CB around 80 nm as core particle size, meanwhile channel black and acetylene black provide CB in the range 30-50 nm. Larger particles can be obtained by using thermal black and lampblack, 120-500 nm and 60-200 nm, respectively. Aggregates and agglomerates were reported for all obtained products from the several indicated synthesis. Plasma process was developed in order to reduce the emissions associated with manufacturing methods, however, it shows still some restrictions related to performance and structural quality of CB (see Figure 8) [155].

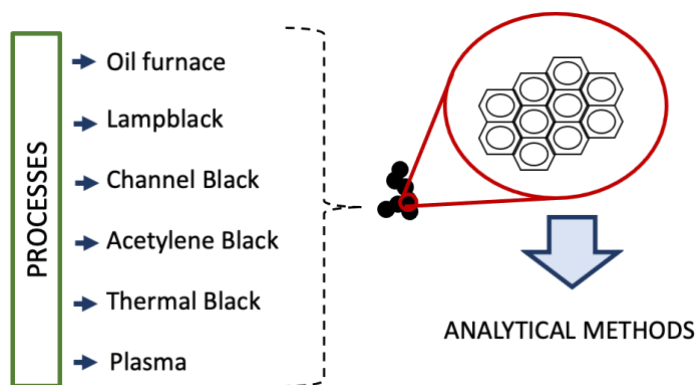


**Figure 8:** Summary of the CB synthetic processes.

Considering the different synthesis processes exposed above several raw materials are available, being surface chemistry, particle size and structure the main parameters that allow CB-NM application, which provided several types of matrices as it can be seen in Table 6. Other factors such as, porosity, density or



thermal and electronic properties have a significant effect in the CB NM successful application too.

Size, graphitic content, shape, and crystallinity are determined by the CB primary particles as first matrix to consider. Monodisperse and polydisperse dispersions of solid raw material were reported [158–161]. CB primary particles combine to form aggregates of different size and structure. Mainly, four basic forms of solid raw material can be defined as spherical, elliptic, linear and ramified, with an increasing degree of aggregation [162]. Figure 9 shows the schematic representation of different CB configurations. Moreover, these aggregates are further associated by van der Waals interactions to finally form agglomerates [163]. The electrical conductivity and oil absorption characteristics increase and the bulk density decreases as a function of the raw material structure complexity [162].

The surface area is one of the most important features influencing CB properties and hence toxicological features. This parameter determines the interfacial area between CB and the medium in which a given volume of NPs are dispersed. Dispersions of different nature provided very varied matrices. For non-porous CB, its surface area exhibits an overall inverse correlation with particle size. Furthermore, several functional groups exist on the surface CB, which their amount and kinds can produce changes in the CB interaction with the medium. However, a satisfactory description of surface properties of CB is still missing, mainly because only a limited number of tools have been available to assess the CB surface in terms of ensemble properties [159]. On the other hand, the incomplete combustion that takes place in the CB synthesis procedure, induces the presence of different functional groups on its surface. Carboxyl, carbonyl, hydroxyl, ether, quinone or lactone groups are some of the most common groups [159]. For example, CB with a large amount of hydroxyl group, has a greatly enhanced affinity to print ink matrices, showing an excellent dispersibility [164].

The covalent modification via in situ generation of a diazonium salt on the CB surface was used to improve the photothermal regeneration of a CO<sub>2</sub> capture nanofluid through decarboxylation [165]. However, the influence of CB functionalization over its properties for electroanalytical applications is still being poorly explored [166]. Leistenschneider et al. used a simple method based on a mechanochemical treatment utilizing a NH<sub>3</sub> solution in order to improve the wettability of these materials [167].

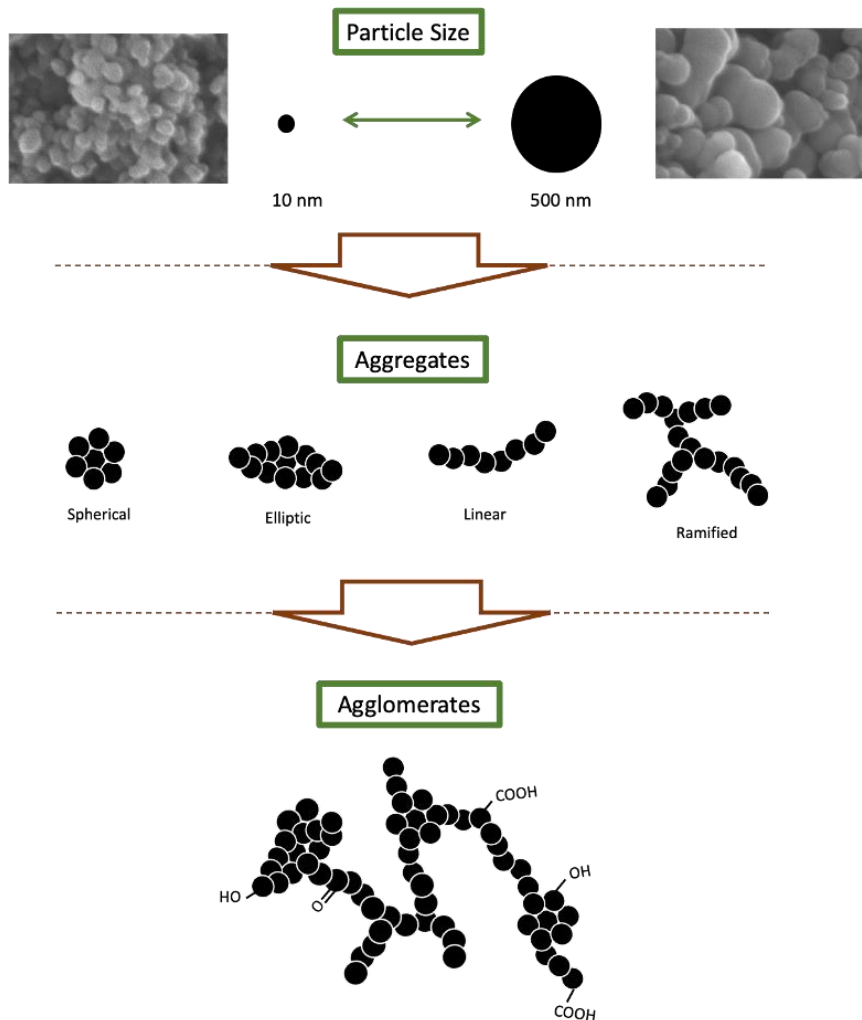


**Figure 9:** Schematic diagram of CB primary particles, different configurations and aggregates/agglomerates.

Other study employed a mixture of sulfuric and nitric acid, and a reflux system for obtaining functionalized CB with enhanced hydrophilicity [131]. By contrast, the hydrophobicity can be also improved, Li et al. developed a CB surface modification with  $-\text{PhF}_5$  groups using an in situ diazonium reduction reaction for improving drying properties without altering the nanostructure [168]. Similarly,

He/SF<sub>6</sub> atmospheric plasma jet source located outside and inserted in alcohol solution was also proposed [169].

Debnath et al. reported an acid method for CB modification in order to enhance thermal stability and tensile strength of fillers that contained this nanomaterial [132]. In the case of electrical properties, Eris et al. [170] applied a CB acidification process using H<sub>2</sub>SO<sub>4</sub> and HNO<sub>3</sub>, that allowed to increase the electrochemical activity of fuel cell catalysts that contained this NM. Figure 10 shows the main examples of surface modified-CB with different functional groups and the effect on the CB chemical and physical behavior. Other characteristics such as storage time, antibacterial activity or chemical properties can be also tuned through functionalization (see Figure 10). Mohan et al. developed a hydrothermal method to integrate SnO<sub>2</sub> nanostructures on CB surface. This study allowed obtaining samples with long term stability, unique fluorescence and poor bacterial activity [171].

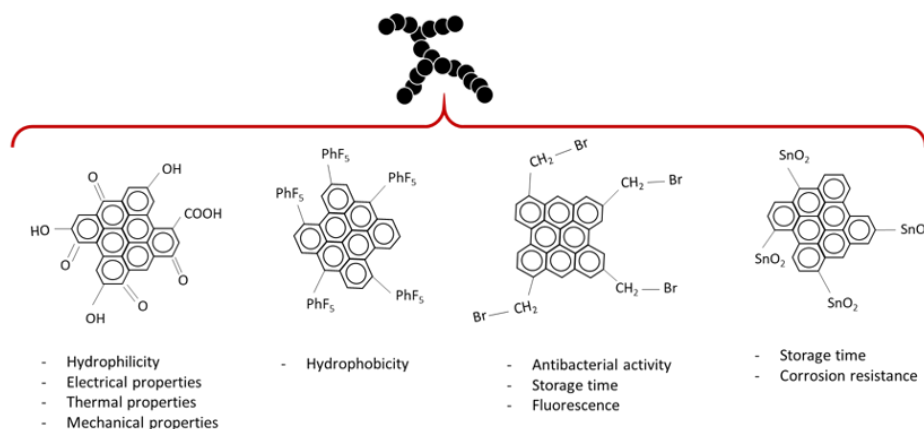


**Figure 10:** Different surface modified-CB and their main properties.

The porosity must be taken into account in surface area measurements and effective CB loading capacity. Additionally, this property has several implications in the microstructure understanding and nanomaterial formation [172]. CB electrical conductivity is due to the electron flow through CB structure achieving a conductive network. In the most accepted theory, electron flow occurs when the CB particles are separated up to 100 Å. At these distances, electrons tunnel through the

resistive medium from particle to particle. The more particles at distances lower than 100 Å, the greater the electrical conductivity. This property is an important factor in polymers and catalysts, among others [173]. Likewise, thermal conductivity of CB, which is related with the ability to facilitate effective heat transfer, has been demonstrated to allow enhance mechanical properties of matrices such as rubbers, silicones and films [174].

Dispersion of these micro and nanoparticles is crucial in order to obtain reliable analytical results. It should be noted that the dispersion medium will determine the surface chemistry of CB and therefore, particle size and microstructure.

Basically, the dispersive media can be classified in polymeric dispersants and cellular media. In addition, these dispersions can be modified with different compounds, organic and inorganic, in order to improve the dispersive behaviour. The efficiency in the dispersion will determine the CB properties and therefore, will be related with their potential application.

In the most recent studies, chloroform, THF and toluene were proposed to disperse CB in polystyrene solution. The presence of these organic solvents provided difference in the macroscopic dispersion state and aggregate structure [175]. Sodium lignosulfonates were also proposed to improve the colloidal stability of CB in aqueous dispersion as Subramanian and Oye reported [176]. Nafion was also used to improve the stability as it has been demonstrated to be a strong stabilizing agent mainly due to the particle zeta potential (Z-potential) achieved. Basically, the use of these compounds in non-aqueous media such as methanol, ethanol and isopropanol decreased the particle size of carbon aggregates [177].

More recently ILs were also reported as dispersing agents in polymeric matrices. The composite properties were improved mainly due to the enhanced dispersion in ILs media [178]. Finally, cell culture medium was also described to establish toxicological effects of CB in biological samples. Cell culture medium supplemented with surfactants such as Tween has also been proposed [179].

Further investigations are still necessary in order to establish the most adequate dispersion procedure for studying CB. Additionally, there is a gap in

extraction and preconcentration strategies of this C-NM, particularly important to develop reliable analytical methodologies in environmental and biological analysis.

All these aspects demonstrate the need to develop reliable separation, determination and characterization techniques allowing the study of the raw material and the different matrices. Morphology, chemical and physical properties and possible transformations of CB NMs require to develop new analytical strategies in order to ensure their proper performance and their toxicological aspects.

*In this Thesis, the characterization of different CB samples in different dispersants have been carried out. Moreover, the stability study in different matrices have been developed and their possible dispersion/extraction from soils have been evaluated.*

### **1.2.3 Silica based nanomaterials**

In the recent years, silica based NMs, also known as silicon dioxide ( $\text{SiO}_2$ ), have been one of the most investigated types of materials in Science and Technology [180]. Their unique structures and properties have given rise to a huge number of applications and innovative tools in different areas [181,182].

Silica based NMs are synthesized using different methods. Chemical and biogenic methods are the most employed. The chemical methods include sol-gel processes involving the development of networks through an arrangement of colloidal suspension (sol) and gelation to form a system in continuous liquid phase (gel) in the presence of a catalyst which can be acid or base [183]. One example of this synthesis is Stöber's method, in which the silica is prepared by controlling hydrolysis and condensation of tetraethylorthosilicate (TEOS) in ethanol to which catalyst amounts of water and ammonia are added. This method can be used to obtain colloidal silica which is transformed in silica gel with ageing and destabilization [184]. A precipitation and/or calcination step can be also included with the aim of obtaining other silica structures [185]. Flame synthesis and micro emulsion are other silica methods used since a long time ago. These routes are easy to follow and modify in terms of parameters but can be costly and difficult to manage in different steps [186]. Chemical vapor condensation (CVC) is another of

the synthetic routes used to obtain silica based NPs. In this route, silicon tetrachloride react with oxygen and hydrogen, obtaining NPs in powder form [187].

The above mentioned methods involve the use of various toxic and hazardous chemicals that are harmful for the biosphere and environment. This paved the way for the development of green nanotechnology that uses environment friendly methods and bioagents to synthesize micro and nano based silica [188]. Among the different strategies to carry out green synthesis, the use of natural products is one of the most attractive approaches. Various natural products (see Table 8) have been investigated as natural silica sources and the silica obtained have showed suitable applicability in a wide variety of fields according to its excellent adsorbent properties, photophysical inertness, chemical stability and facile surface modification. For example, SiO<sub>2</sub>NPs can be synthesized from olive residues exhibiting anticancer properties [189]. Sugarcane bagasse, bamboo leaf, cassava periderm and oil palm ashes exhibit high silica content as well as capable of producing amorphous silica [190]. Moreover, sand is other material used to obtain amorphous silica with a very high purity that can be used as a supporting photocatalyst material to remediate phenol waste [191,192]. Similarly, rice straw is a natural source of silica [193] that allows finding a new utility to the huge amount of rice straw generated per year [194].

**Table 8:** Silica content present in different natural silica sources [189, 190, 191].

Natural Source	SiO <sub>2</sub> content (%)
Olive residue	≥ 20
Sand	20 - 70
Sugarcane bagasse ash	50 - 97
Bamboo leaf ash	60 - 80
Cassava periderm ash	60 - 70
Oil palm ash	40 - 80
Rice straw ash	80 - 97

The properties of silica based NMs considered essentials are crystallinity, particle size and morphology, porosity, chemical purity, surface chemistry and

solubility [185]. Moreover, other properties such as mechanical and thermal stability or low toxicity make silica a promising NM. Regarding to crystallinity, silica structures can be crystalline or amorphous. In crystalline structures such as quartz and zeolites, the arrangement of atoms is ordered in all dimensions with long-range order (at least 10 repeats in all directions) and produce sharp maxima in a diffraction experiment. On the other hand, amorphous silica may present some short-range order but lacks long-range order in 3 dimensions and does not exhibit a sharp XRD pattern [195].

The particle size is determined by the experimental conditions during the synthesis. Amorphous silica particles provide particle size from 10 to 25 nm. Larger primary particles can be prepared from TEOS by Stöber synthesis. Grinding and milling processes reduce particle size. These techniques are most often applied to quartz, silica gel and vitreous silica. The obtained products generally have a broad size distribution. Crystalline particles exhibit crystal planes at the surface, and the morphology of the crystalline nanoparticles depends on the crystal class such as cubic, hexagonal, tetragonal, and orthorhombic. For all nanomaterials, in aqueous environment, the primary nano-sized silica particles tend to form aggregates [196,197].

According to IUPAC [198], pores are classified according to their diameter into micropores (< 2 nm), mesopores (2-50 nm) and macropores (> 50 nm). Amorphous particles can be microporous or non-porous (dense). The porosity of Stöber silica can be tuned by adapting the synthesis parameters: decreasing the ratio of water to TEOS promotes particle growth by aggregating smaller sub-particles, thus leading to rough particle surfaces with micropores. In contrast, smooth particle surfaces are obtained with conditions of high ratio of water to TEOS. Silica gel is a powder with particle size in the micrometer range or larger and is, typically, mesoporous [199].

The hydrophilicity of silica based NMs increases with the number of silanols, or silicon-bonded hydroxyl groups, capable of forming hydrogen bonds with physical water molecules. Colloidal silica, precipitated silica and ordered mesoporous silica and silica gel are hydrophilic because of their high concentration of silanols. Silica gel, for example, can adsorb water in quantities up to 100% of its proper weight. Pure silica zeolites typically are hydrophobic because they lack silanols in the pores of their framework. Silica produced at high temperature, such

as pyrogenic and vitreous silica, or calcined at temperatures exceeding 800 °C, is almost entirely dehydroxylated [185].

By another hand, solubility depends on the surface curvature of the NPs. For micrometer-sized nonporous amorphous silica, the equilibrium concentrations of  $\text{Si}(\text{OH})_4$  at 25 °C in water corresponds to 70  $\text{mg}\cdot\text{L}^{-1}$  at pH 7.  $\text{SiO}_2$ NPs and nanoporous silica show enhanced equilibrium solubility, of 100-130  $\text{mg}\cdot\text{L}^{-1}$ . According to Vogelsberger et al. [200], the solubilization of amorphous  $\text{SiO}_2$ NPs in physiological buffer at 25 °C is accelerated because of the large surface area exposed. The solubility equilibrium is reached only after 24 to 48 h. Crystalline silica such as quartz has a much lower equilibrium solubility, of 6  $\text{mg}\cdot\text{L}^{-1}$  [196].

Considering the high existing variability of silica based NMs, they also can be classified according to their shapes, such as films, spheres, ellipsoids, rods and tubes (Figure 11). The synthetic route is fundamental to obtain the different silica based materials, (i.e., size or shape), which obviously show different physical and chemical properties. This is the case of dispersion ability and stability.

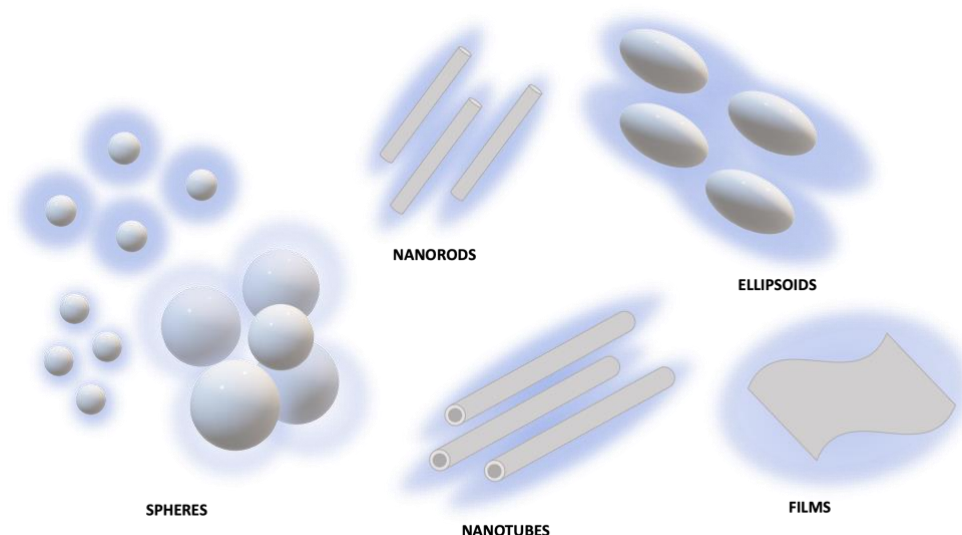


**Figure 11:** Different shapes of silica based NMs.



Silica based NMs dispersions have been of interest in colloidal science because of their anomalous behavior of aggregation may not be predicted by DLVO theory. Moreover, different structural parameters are responsible for the dispersion stability of this NM. The presence of silanol groups (Si–OH) on a silica surface was postulated by Hofmann in 1934. These hydrophilic silanol groups on a silica surface act as binding sites ( $H^+$  bonds) for water. From experimental observations with silica gels, aerosilogels, and porous glasses, Zhuravlev concluded that silanol groups were the most probable groups on the surface of amorphous, fully hydroxylated silica, and that one OH group corresponded to one surface Si atom [201]. The protonation and deprotonation of these silanol groups determine the surface charge of silica nanoparticles and the extent of the repulsive energy to keep them dispersed in the solution [202].

In order to achieved suitable silica based NMs dispersion stability, different procedures are employed through inducing charge in the NPs surface. The easiest method of inducing a charge is by taking advantage of acidic silanol groups on the silica particles surface. By reacting these groups with alkyl, the particles become charged which allow their interaction with dispersant and consequently their suitable stability.

For cationic forms, the silica particles are fully coated with an aluminum hydroxide compound such that the net particle charge is positive. These positive charges allow the electrostatic interactions with the dispersants used (Figure 12).

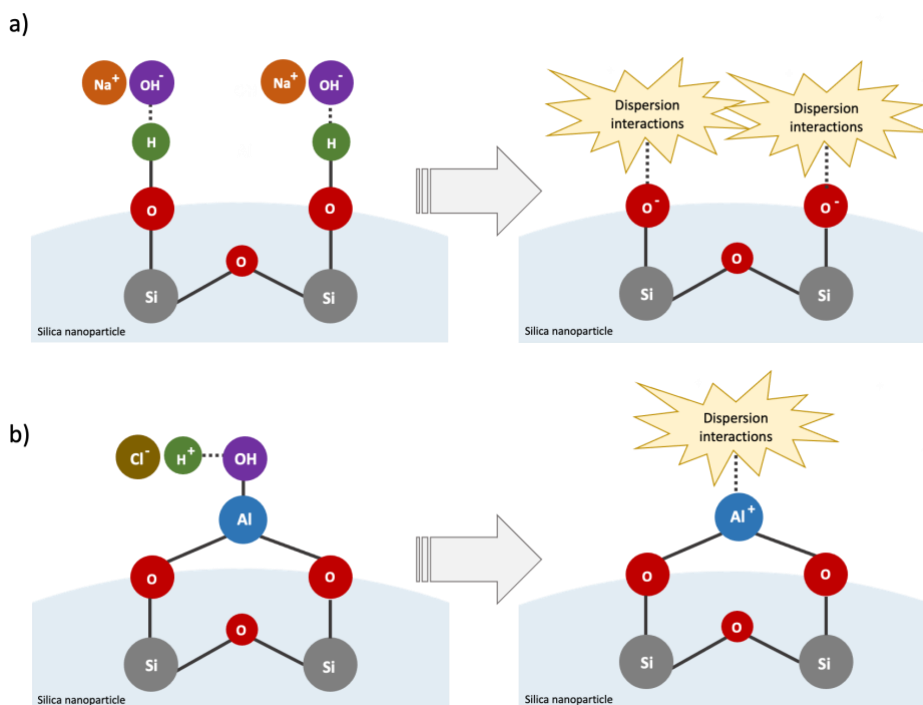


**Figure 12:** Schematic diagram to induce a) negative charge and b) positive charges in the Silica based NMs surface.

### 1.2.3.1 Spherical silica nanoparticles

Spherical silica nanoparticles (S-SiO<sub>2</sub>NPs) have shown great applicability in a high number of fields according to their remarkably instinctive properties like high surface area, tunable pore size/diameter, biocompatibility, modifiability and polymeric hybridizability. These particles are shown to be non-toxic in nature, hence of great interest for biomedical and environmental tool. Moreover, the molecular mobilizability onto the internal and external surface of the particles makes them excellent carriers for biotic and non-biotic compounds. Furthermore, the size of the spherical particles can be varied by altering the surfactants composition during the synthesis [188].

S-SiO<sub>2</sub>NPs with different sizes and capping have been used as model system to study adsorption, catalysis, and size-dependent solid-state properties [203]. Moreover, commercial S-SiO<sub>2</sub>NPs aqueous dispersions are used as inorganic

binders, reinforcing and strengthening agents, refractory bonding agents, and surface modifiers in different products [204,205]. As a binder, it provides excellent strength and adhesion in catalyst wash coats and catalyst structures, precision investment casting molds, insulation boards, and other refractory fiber-based parts [206]. It can also be used as a silica source in flocculating agents, as co-binders in functional coatings, and in paper manufacturing. On the other hand, solid S-SiO<sub>2</sub>NPs have been used in research areas as sensors fillers [207,208]. Similarly, this nanomaterial is employed as additive for the manufacture of rubber, plastics and fibers [209,210]; as an important and useful component in agriculture [211]; and as a stable, non-toxic platform for biomedical applications such as drug delivery and theragnostic [212].

### 1.2.3.2 Silica nanotubes

Silica nanotubes (SiNTs) attract special interest due to their unique optical, electrical, and mechanical properties, their hydrophilic nature and their potential as nanocontainers and nanoreactors. This silica NMs have been demonstrate as a choice for encapsulation of optically-active molecules within their void nanospace, in which the excited state properties of encapsulated molecules can be effectively modified, thus allowing these NT systems be used as optical nanomaterials, (e.g., in photoinduced energy transfer and electron transfer) [213]. All these properties, along with the high robustness of the silica framework and their easy colloidal suspension formation, make silica nanotubes particularly well suited for catalysis (e.g., for enzyme immobilization), separations, sensing, nanofluidic and drug/gene delivery [214].

In particular, halloysite is an example of natural nanoclay aluminosilicate nanotubes. Aluminosilicates clays are formed by the arrangement of two different sheets: one of these sheets consists on tetrahedral SiO<sub>4</sub> units, where each Si atom shares one of its O atoms with the second sheet which in turn consists on aluminum in octahedral co-ordination, represented as AlO<sub>6</sub> [215]. Different sheet structures can be observed. The 1:1 structure consists on a pair of octahedral and tetrahedral sheets, that can be linked or not to other pair of sheets by hydrogen bonding. On the other hand, the 2:1 structure shows one AlO<sub>6</sub> octahedral sheet sandwiched between two SiO<sub>4</sub> tetrahedral sheets by covalent bonding. These three-layer structure can present an expanding or non-expanding lattice. In some clays, there is a considerable substitution of aluminum by silicon in the tetrahedral sheet that

can reach up to 15%. Further, magnesium and iron can also substitute aluminum in the octahedral sheet. These substitutions give rise to an overall negative charge on the layers that is balanced by water molecules and ions, providing the layered aluminosilicates with ion exchange capacity. In order to hold layers together, water and ions allow creating relatively weak force which leads to the expansion of the lattice [216,217].

Halloysite exists in the form of several morphological modifications [218]. The most abundant modification is tubular, which is also termed halloysite nanotubes (HNT). HNT consists of aluminum and silicon oxide layers rolled into tubes. There can be 15 and more layers in the nanotubes. The plates are rolled into tubes because of differences in the size of silicon and aluminum ions. The layers are rolled in such a fashion that the aluminum oxide layer is located on the inner side, and the silicon oxide layer, on the outer side of the tube [219] (Figure 13). Mainly, it can be used as inorganic matrix in hybrid pigments in order to improve the stability and performance of these compounds [220]. Silica structure of this NM can also modify with acidic and alkaline treatments [221], and surface can be altered for the purpose of preserving original properties and providing new such as hydrophobicity or biocompatibility [222].

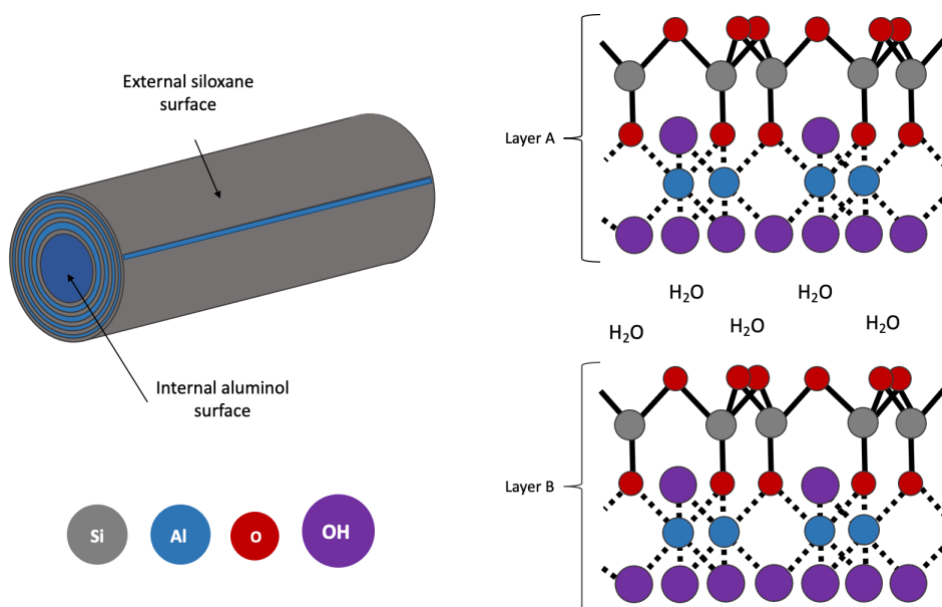


**Figure 13:** Representation of chemical structure of HNT.

### 1.2.3.3 Other silica based NM shapes

Nanorods, ellipsoids or films are other interesting morphologies. Chung-Yuan Mou's [223] and Victor Lin's [224], synthesized and used silica nanorods as nanocarriers for photodynamic therapy combined with drug delivery, or to encapsulate MRI contrast agents. The control of the shape of silica nanorods was achieved through a fine control of the pH or using a structure co-directing agent such as perfluorooctanoic acid most often associated with a cationic surfactant such as cetyltrimethylammonium bromide [225].

Ellipsoids silica NPs have been proposed as drug delivery carriers. This silica based NM shows inability to retain its shape due to minimization of surface free energy leading to spherical particles poses a major. Its synthesis is based on the introduction of a co-surfactant, the addition of potassium chloride and ethanol [226].

Si nanofilms have been mainly used as electrochemical sensors and molecular sieving/separation [227,228]. Synthesis is based on the evaporation induced self-assembly approach (EISA method) which is based in the deposition onto a solid support a homogeneous silica solution of a soluble precursor with a surfactant or copolymer. Then, the evaporation of alcohol leading to the film formation. Other methods such as self-assembly of silica precursors with surfactant templates at air-water or water-oil interfaces allow also obtained silica films. However, the effective use of films in various application fields has some specific requirements that poses synthetic challenges. Firstly, films have to be continuous and free of cracks and secondly, the pores of the film should be accessible, preferably from the film surface. In addition, thin films undergo shrinkage during the calcination step, which induces tension inside the films and thus causes problems with their stability [229].

*In this Thesis, different silica based micro and NMs such as aqueous dispersion SiO<sub>2</sub>NPs, HNTs and  $\mu$ -SiO<sub>2</sub> obtained from rice straw ashes have been studied and characterized in detail.*

## **1.3 ANALYTICAL TECHNIQUES**

The great development and applicability of NMs is directly correlated with the need of analytical methodologies to perform morphological characterization, identification and quantification. Thus, a wide variety of strategies are involved. Particle size distribution is a difficult parameter to analyse mainly due to the lack of homogeneity in the micro and nanostructure. Therefore, image analysis techniques are necessary to establish the size and shape descriptors. By another hand, spectroscopic techniques have also been proposed to study the structure and presence of different compounds. Finally, separation techniques have also been studied in order to both, characterization and determination, the nanomaterials studied, and to provide additional information to that obtained with image and spectroscopic techniques.

### ***1.3.1 Spectroscopic techniques***

NMs have unique optical properties that are sensitive to the size, shape, concentration, aggregation/agglomeration state and refractive index. Indeed, UV-vis spectroscopy has been widely used to characterize NMs [230]. For MNPs, the use of UV-vis is mandatory in order to evaluate and identify their characteristic SPR band. However, it should be taken into account that this band is influenced by a wide variety of factors such as size, shape, concentration, aggregation/agglomeration state, and dielectric and physical-chemical environment [231,232].

CB and silica based NMs can be also characterized by this technique. UV-vis absorption spectra are employed to gain further insight into the characterization of synthesized NMs, their concentration, and also the dispersibility in different solvents [233].

However, one of the limitations of UV-visible spectroscopy is that it cannot accurately quantify different MNPs variables, such as the extent of metal nanoparticle functionalization. The SPR band can be shifted due to changes in the environment that the metal nanoparticles exist in along with changes in morphology. It can be difficult to distinguish the factor that dominates the UV-vis

band shift because it is possible for reaction intermediates, reactants, or other impurities to float around in solution along with the conjugated NPs [234].

Similarly, UV-vis spectroscopy cannot unambiguously account for nanoparticle aggregation, which can occur due to interactions between the nanoparticles, the presence of other compounds in the dispersion or experimental conditions. There are numerous factors that can account for an SPR band shift in UV-vis, so it is not possible to attribute the shift to aggregation without further analysis. Other techniques, such as separation methods are needed for completing the characterization of NMs [235].

In the context of NPs size estimation, dynamic light scattering (DLS) has been widely described to determine the hydrodynamic size of NMs in different matrices and polydispersity. In this technique, the hydrodynamic size of a particle is estimated from its translational diffusion ( $D$ ) within a fluid (both parameters related through the Stokes-Einstein equation). Experimentally, samples are exposed to radiation: light is scattered differently by particles according to their sizes (with the larger ones scattering more light). The rate at which the scattered light fluctuates in time (a function of  $D$ ) is registered, obtaining the DLS correlogram. From the signal profiles, data can be obtained: the time at which the signal starts to significantly decay provides an estimation of the mean size; in addition, a steeper slope corresponds to a more monodisperse sample [236]. Table 9 summarizes some representative methods using DLS for particle size characterization. As it can be seen, there is a high variability in terms of sizes as a function of the matrix and dispersants used. As it is expected, this technique has been used for characterization purposes, however, size distribution separation and quantification are not addressed.

**Table 9:** Revision studies using DLS techniques for NMs characterization.

Dispersant / Capping agent	Sample	Laser (nm)	Size (nm)	Relative error (%)	Ref.
Eucalyptus Camaldulensis aqueous extracts	AgNPs	---	68	---	[237]
Prosopis juliflora bark extract	AgNPs	633	54	---	[238]
Folic acid, cysteine in aqueous dispersion	AuNPs and FA-Cys-AuNPs	---	22.4 and 33.8	---	[239]
Styrene maleic anhydride	Commercial CB	660	110 - 1070	25 - 50	[128]
Methyl methacrylate, maleic anhydride and diallyl phthalate	Commercial CB (pigment black)	633	178 - 233	---	[240]
Styrene: acrylic acid	CB in Ink	632.8	76	25.5	[124]
Water + glycerine or isopropyl alcohol	CB in ink	633	<100	---	[241]
Cell culture medium (RPMI + 10% FBS)	Commercial CB	633	270	3	[141]
Amino functionalized silica and hyaluronic acid	Mesoporous silica functionalized	---	151 and 508.4	0.9 and 0.4	[242]
Carboxy and amino-terminated polyethylene glycol functionalized silica	Mesoporous silica NPs functionalized	---	155.5 and 211.3	---	[243]
Aqueous silica dispersion with surface modification	Silica gel NPs	---	10.8 – 237.7	---	[244]

As can be seen in Table 9, the biosynthesis of silver nanoparticles using different extracts as reducing and capping agent is monitored by DLS technique in order to obtain the average hydrodynamic diameter (DH) of NPs synthesized [237,238]. Moreover, for AuNPs, DLS allowing corroborated the proper performance of these NMs in different applications, such as their utility as contrast media in dual-energy computed tomography [239].



Regarding CB, Kim et al. [128] focused its work in the direct study of commercial CB. The results indicated that DLS measurements were affected by a high uncertainty compared with other techniques, however, it showed acceptable results in terms of characterization, Bo et al. [240] studied grafted commercial CB on the surface through grafting polymerization, obtaining DLS values around 200 nm with polydispersity index of 0.166 to 0.280. The grafted CB had a smaller average size and better dispersibility than CB ethanolic dispersions.

By another hand ink matrices represent one of the most important samples. Mainly, DLS has been proposed for CB characterization as a function of time for stability studies [124]. DLS technique has also been successfully used as a complementary technique to establish the CB source in black pigments [241]. For biological matrices, cell culture medium has used as suitable dispersant and DLS has allowed the characterization of dispersion formed [141].

In the case of silica based NMs, DLS technique is used to characterize the functionalization of these NMs for their applicability in a wide variety of research areas, such as drug delivery system [242,243]. Moreover, it has been used to evaluate the effect of particle size in different approaches, for example on the inhibition of formation damage caused by asphaltene precipitation/deposition in oil reservoirs [244].

In the context of structural information, X-ray diffraction (XRD) and X-ray photoelectron spectroscopy (XPS) have been described to determine composition or crystalline structure of catalyst composed by NMs such as PtCu-CB [245], Fe<sub>3</sub>O<sub>4</sub>-CB [246], AuNPs/TiO<sub>2</sub> [247] or CuO/SiO<sub>2</sub> [248], among others. Elemental composition has been established by energy dispersive X-ray spectroscopy (EDS) in composites [249] and NPs synthesis evaluation [250].

Fourier transform infrared spectroscopy (FTIR) and Raman spectroscopy have also been employed for chemical and structural identification. Particularly relevant is the use of Raman spectroscopy to determine CB evidences in forensic samples [129]. Moreover, these techniques are also used in MNPs to establish possible interaction between NPs and other compounds [251], as well as characterize the capping agents of NPs surface [252].

Other spectroscopic techniques, such as electrochemical impedance spectroscopy (EIS) are employed to establish the relative effectiveness of dispersants used in non-aqueous CB dispersions based on their ability to suspend particles in oil mediums [253]. Similarly, this technique has been applied in silica based NMs for evaluating the time-dependent corrosion protection ability [254].

### **1.3.2 Image techniques**

Electronic microscopic techniques have been mainly proposed to obtain morphological information about micro and NMs, either in thin sections or in samples isolated by sieving, density separation and/or chemical extraction. NMs characterization has been mainly carried out by scanning electron microscope (SEM) and transmission electron microscope (TEM). However, atomic force microscope (AFM) has also employed to obtain structural information.

SEM is based on an electron beam interacts with NP surfaces, and secondary electrons, backscattered electrons or X-ray photons are measured. Sample preparation is simple, but sometimes Au or Au/Pd coating is required to assure conductivity, resulting in the loss of part of the surface information. SEM is more suited for bulk level analysis and when coupled to EDS, the resulting SEM-EDS method can provide some semi-quantitative information. Morphology, shape and size distribution has been assessed by SEM in different NMs such as catalysts and composites in order to determine the relationship of the nano- or microstructures with the performance properties [255]. Moreover, interparticle distances, porous structure and orientation have been established by this technique. From an analytical point of view, morphology studies allow the understanding of potential binding or active sites where other target analytes can be trapped.

TEM has been also proposed to determine and characterize the sizes, shapes and aggregates of different NMs [256]. This is performed by transmitting a high energy electron beam through a very thin layer of the specimen. Then non adsorbed electrons are focused onto an imaging detector producing a direct image of the target NP [257]. Nonetheless, samples need to be dehydrated and immobilized on a solid support (e.g., placing a drop of the suspension onto a carbon-coated copper grid), a procedure which may require long time periods. In other words, “dried NPs” are measured and core sizes obtained. Consequently,

TEM by itself is not appropriate for assessing the effect produced by nano-environmental changes [258]. In some cases, TEM measurements are suitable for visualization of the surroundings of particles like the protein corona. In addition, sample dehydration can lead to structural distortions when compared to the solvent-swollen NP state [259].

Furthermore, in TEM analysis only a part of the studied sample is considered by means of counting a well-defined number of particles (e.g., 500). Counting all of the NPs on the grid is very difficult. It is rather a statistical approach in which the obtained data is extended to characterize the complete sample. Going further, for diluted samples, the task of counting particles becomes even more difficult, tedious and time-consuming because sometimes replicates are needed. This limits the ability to detect lower NP concentrations. Regardless of this, TEM remains one of the most used methods for contrasting results in this field [260]

AFM combined with force spectroscopy consists of a scanning microscope probe designed to measure local properties such as friction, height or magnetism, among others. This technique has also been proposed in order to investigate interactions between NMs and matrices. The mechanisms have been established as a function of the surface charges and Z-potential measurements, which is fundamental to understand the behaviour of NMs in different dispersive media [261].

Despite their limitations, microscope related techniques provide the most direct information on shapes, sizes and distributions of the initial NMs, and together with spectroscopic and separation techniques a full knowledge of micro and NPs can be achieved.

### ***1.3.3 Separation techniques***

As can be seen in the above sections, detection techniques such as electronic microscope analysis or spectroscopic methods such as UV-vis or DLS, among other, only provide partial information. However, the increase on the use and the need to fully understand the performance of micro and NMs, has led to the development of separation techniques, mainly liquid chromatography and field flow fractionation which provide a complete characteristic information of them.

### 1.3.3.1 Liquid chromatography (LC)

LC is an important and well-known technique commonly used for estimating a wide variety of compounds. According to flow rates used and chromatographic column intern diameter, different sub-techniques are defined which are employed in a wide variety of applications.

**Table 10:** Column dimensions and Flow of principal LC systems.

	Analytical column i.d (μm)	Mobil phase flow (μl·min <sup>-1</sup> )
Conventional LC	3200 - 4600	500 - 2000
Microbore LC	1500 - 3200	100 - 500
Micro-LC	500 - 1500	20 - 100
Capillary LC	150 - 500	1 -20
Nano-LC	10 - 150	0.2 -1

When comparing capillary-LC, and nano-LC to conventional LC and microbore LC (Table 10), a primary benefit to analytical science includes applicability to sample limited situations. Additional advantages include improving limit of detection and lowered mobile phase volumes leading to reduced costs related to both analysis and waste. Furthermore, the use of low id columns in miniaturized LC units systems allows samples that degrade rapidly or require rapid results to potentially be analyzed at point-of-care [262]. For this reason, these capillary and nano-LC techniques show excellent potential for NMs characterization.

Recently, MINTOTA research group has demonstrated the applicability of miniaturized LC in coupled to in-tube SPME the study of different NMs, specifically MNPs, such as AgNPs and AuNPs. As report in [258], chromatographic signal response linearly to concentration of NPs and also to average sizes using the equation (A), with the employ of a unique standard with a known NPs size for the calibration.

$$d_{XNPs} = \left( \frac{[X^+] \cdot d_x^3}{[XNPs]} \right)^{1/3}, \quad (A)$$

where  $d_{\text{XNPs}}$ ,  $d_x$ ,  $[\text{XNPs}]$ , and  $[\text{X}^+]$  correspond to the average particle diameter of noble NPs, the diameter of atomic element (0.289 nm), noble NPs concentration, and initial element (as  $\text{X}^+$  from  $\text{XNO}$ ) concentration, respectively. As it can be seen both XNPs parameters ( $d_{\text{XNPs}}$  and  $[\text{XNPs}]$ ) vary inversely.

This phenomenon is due to that the flow in miniaturized LC and the diffusion through the pores (on the same order of magnitude as the diameters of the studied NPs), condition the particle interaction through the system in a dynamic process.

#### *1.3.3.1.1 IT-SPME-LC for NPs characterization*

In 1990, Pawliszyn et al. [263] develop an attractive technique in terms of sample preparation, solid phase microextraction (SPME) based on the interaction of analytes presents in a liquid or gas with a solid sorbent. Thus, components of sample are separated according their affinity with the sorbent. SPME is a green-chemistry technique since it respects its basic principles.

In this context, the term "microextraction" refers to the volume or mass of extractive phase used in the sample preparation procedure (in the microliter or microgram range). This phase can be immobilized on different devices such as fibers, filters or other surfaces, or even placed in direct contact with the sample. The volume of sample processed is usually high compared to the amount of extractive phase.

On the one hand, this technique allows miniaturizing the sample preparation stage and, on the other hand, combining sample processing, extraction and pre-concentration in a single stage (minimizing the use of solvents). Taking into account the different variants of SPME, those that use capillary columns for extraction have additional advantages, such as, for example, automation and online coupling with the separation and/or detection method used. In-tube solid phase microextraction (IT-SPME) was first introduced in 1997 by R. Eisert and J. Pawliszyn.

IT-SPME can be combined with capillary and nano chromatography as proposed by MINTOTA. Two different work methods have been proposed for this combined technique: draw/eject IT-SPME and in flow-through IT-SPME. In the first one, the capillary with the extractive phase is connected between the needle and

the loop of a programmable automatic injector. The analytes are extracted by cycles where sample is aspirated and expelled through the extractive capillary. Then, they are desorbed and transferred to the analytical column by using an appropriate mobile phase [264].

In flow-through IT-SPME is the modality where the capillary column is used as a loop of an injection valve. Figure 14 shows a simple scheme of this configuration, where capillary column is coupled to the injection valve. The analytes are extracted in the sample loading process. Subsequently, when the valve is changed, they are transferred to the analytical column [265]. There are two modalities of perform the desorption process: static and dynamic. In the first one, the analytes are desorbed by injecting a suitable solvent and then they are transported by the mobile phase to the chromatographic system. On the other hand, in the dynamic mode, it is the mobile phase itself that is responsible for desorbing the analytes. In general, the static mode is used when the analytes are strongly retained in the adsorbent material. Another setup is based on the use of two valves. In this case, in a first step, the analytes are desorbed from the first capillary and transfer to the injection loop of the second valve. Then, the change of the valve position from load to inject allows sending the desorbed analytes to the chromatographic column [266].

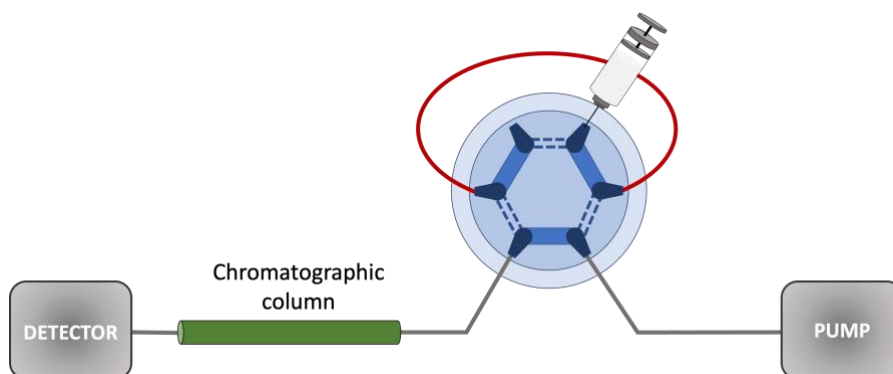


**Figure 14:** In flow-through IT-SPME configuration.

IT-SPME-LC have been used in the last years for analysis of a wide variety of compounds and NMs using different extractive capillaries. Table 11 shows some examples reported during the last 5 years, where its use in NMs determination is demonstrated.

**Table 11:** Applications of IT-SPME described in the literature between 2017 – 2022.

Technique	Capillary	Analyte	Sample	Ref.
IT-SPME-HPLC-DAD	Basalt fiber functionalized with AuNPs	PAHs	Water	[383]
IT-SPME-HPLC-UV-Fluorescence	Cotton thread modified with organic polymer	Nonsteroidal anti-inflammatory drugs	Human plasma	[384]
IT-SPME-HPLC-UV	Polyhedral oligomeric silsesquioxane-based hybrid monolith	Bisphenols	Milk	[385]
IT-SPME-HPLC-DAD	Ionic-liquid-modified melamine-formaldehyde aerogel	Estrogens	Plastic bottle, tap and surface water	[386]
IT-SPME-LC-MS/MS	Supel-Q Plot	Tobacco-specific nitrosamines	Hair	[387]
IT-SPME-LC-DAD	Polyaniline/titanium dioxide nanorods functionalized carbon fibers	Phthalate esters	Water	[388]
IT-SPME-CapLC-DAD	Commercial capillary GC coated with ZB-FFAP	Caffeine and its metabolites	Serum, Saliva and urine	[389]
IT-SPME-HPLC-DAD	Graphene oxide-functionalized mesoporous silica	Polycyclic aromatic hydrocarbons	Honey	[390]
IT-SPME-HPLC-DAD	Monolithic capillary microextraction columns embedded modified Fe <sub>3</sub> O <sub>4</sub> magnetic NPs	Heavy metal ions	Environmental waters and seafood	[391]
IT-SPME-HPLC-UV	Amide group modified polysaccharide-silica hybrid monolith	Ractopamine	Pork muscle	[392]
IT-SPME-MinLC-DAD	PDMS columns and columns functionalized with single-walled carbon nano-tubes	MNPs	MNPs bulk dispersions	[260]
IT-SPME-CapLC-DAD	PDMS columns and columns functionalized with single-walled carbon nano-tubes	AgNPs	AgNPs synthesized	[258]

Among the different applications of IT-SPME-LC, the application in the characterization of NPs dispersion is very interesting. In this approach, the chromatographic response of noble nanoparticle dispersions provides two chromatographic peaks, which respond to the existence of different NPs distributions in the bulk dispersion: non-polarized NPs which interact with the IT-SPME extractive phase by a hydrophobic effect, and water polarized NPs governed by a size exclusion mechanism in the analytical column. Thereby, the peak ratio for a given dispersion allows the estimation of the average diameter of noble NPs and permits to study stability and functionality related properties. For quantitative purposes, it has been demonstrated that the area or height of the chromatographic peaks are related with the NP concentration [258].

### **1.3.3.2 Field flow fractionation**

In the context of micro and NMs separation, field flow fractionation techniques have attracted the attention of Analytical Chemistry in the recent years, since isolate and characterizes NPs distributions in bulk dispersions according to particles properties, such as size, composition or electrophoretic mobility. In addition, the technique can be coupled to different detectors (UV-vis, DLS or MALS among others) that obviously provide a wide information of the target micro and nanoanalytes. These techniques are based on the application of a perpendicular force field to the main flow of a suspension or solution of fluid pumped along a channel [267]. The force field can be a perpendicular asymmetric flow through a semi-permeable membrane (AF4), gravitational (GF3), or it can arise from a sedimentation process (SdF3), a thermal gradient (TF3) and an electric (EIF3) or magnetic field (MgF3) [268].

In FFF, the separation system is a parallelepipedal channel. In this configuration two points are important. On the one hand, the rate of elution of the carrier liquid is generally of the order of milliliters per minute. Under these conditions, the flow regime is laminar, which corresponds to a maximum flow at the center of the channel, minimum at the upper and lower walls, with a parabolic profile in the height of the channel. Therefore, the rate of elution of analytes depends on their position in the height of the channel. On the other hand, the force is applied perpendicular to the direction of elution of the analytes, that is, in the height of the channel. It is, therefore, the force application that determines the



position of the analytes in the height of the channel. The most commonly form to apply this force is from top to bottom [268].

This force leads to the accumulation of analytes on the lower wall of the channel, which is then called the accumulation wall. This accumulation is promoted during the injection of the sample, by a focusing step carried out without an elution flow. This results in a concentration gradient at this wall, which results in a net transport by diffusion from regions of higher concentration to regions of lower concentration when the analytes are able to diffuse significantly, which is the case for objects of nanometric/submicrometric sizes (<1000 nm). The elution mode is called normal mode or Brownian mode. The applied force and the opposing diffusion then govern the mean position of the analytes in the height of the channel. This results in an order of elution inversely related to the diffusion coefficient of the analytes, or also directly related to their hydrodynamic size (typically expressed by the DH). The formalization of the retention in this mode leads to express the retention time according to (B):

$$t_R = \frac{w \cdot U_x \cdot t_0}{6D}, \quad (\text{B})$$

where  $t_0$  is the void time,  $w$  the height of the channel,  $D$  the diffusion coefficient of the analyte and  $U_x$  the speed of the analyte in the height of the channel. This expression shows the dependence of the retention time in particular on the diffusion coefficient and the speed of the analytes in the height of the channel, this speed being induced by the applied force. Knowing that the diffusion coefficient is related to the hydrodynamic size by the Stokes–Einstein relation (C):

$$D = \frac{k \cdot T}{3 \cdot \pi \cdot \eta \cdot DH}, \quad (\text{C})$$

where  $DH$  is the hydrodynamic diameter,  $k$  the Boltzmann constant,  $T$  the temperature, and  $\eta$  the viscosity of the carrier liquid. Thus, it may be relevant, from an analytical point of view to express the retention time either as a function of  $DH$  (D). Moreover, it is important to remark that when the diffusion opposing the applied force is negligible, the position of the analytes in the height of the channel is determined by their size: larger objects are eluted first, smaller ones last. The mode of elution is then called steric mode. This mode occurs for sizes generally

beyond the micrometer. Therefore, NPs are not eluted in steric mode, which will not be detailed below.

$$t_R = \frac{\pi \cdot \eta \cdot DH \cdot w \cdot U_x \cdot t_0}{2 \cdot K \cdot T}, \quad (D)$$

Regarding the analysis of NMs, the field generated by a perpendicular asymmetric flow (AF4) is the one with the greatest applicability in different areas and allows characterizing a wide variety of analytes including synthetic polymers, proteins, viruses, antibodies and nanoparticles both in aqueous and organic solvents. This sub-technique uses the hydrodynamic force generated by a second flow perpendicular to the elution flow, called cross-flow. In AF4, a second pump generates the crossflow through the porous frit made of stainless steel or ceramics in bottom of channel. Meanwhile the other side of the channel is solid. This setup provides greater separation efficiency and less dilution; controlling pressure at the outlet generates the cross-flow. The presence of ultrafiltration membrane helps retain the NPs within the channel [267] (see Figure 15.a).

Similarly, sedimentation field flow fractionation (SdF4) is applied to characterize particle size distributions. In this case a centrifugal force is applied on the particles suspended in a mobile phase. This force is generated by rotation of the channel, which is curved and located on the circumference of a spinning wheel. Because centrifugal force can be generated over a wide range and is more efficient than that generated by gravity, centrifugal force is well suited and so used for the NM characterization. The retention in SdF4 is a function of the effective mass of the analytes, which depends on the volume, and therefore, on the size of the analytes; it is linked to the physical diameter for spherical NPs. The density of the analytes is also involved in their retention; this is important to note because a size-based separation will only be effective at equal density of the constitute materials of all of the analytes in a sample. (see Figure 15.b) [269].

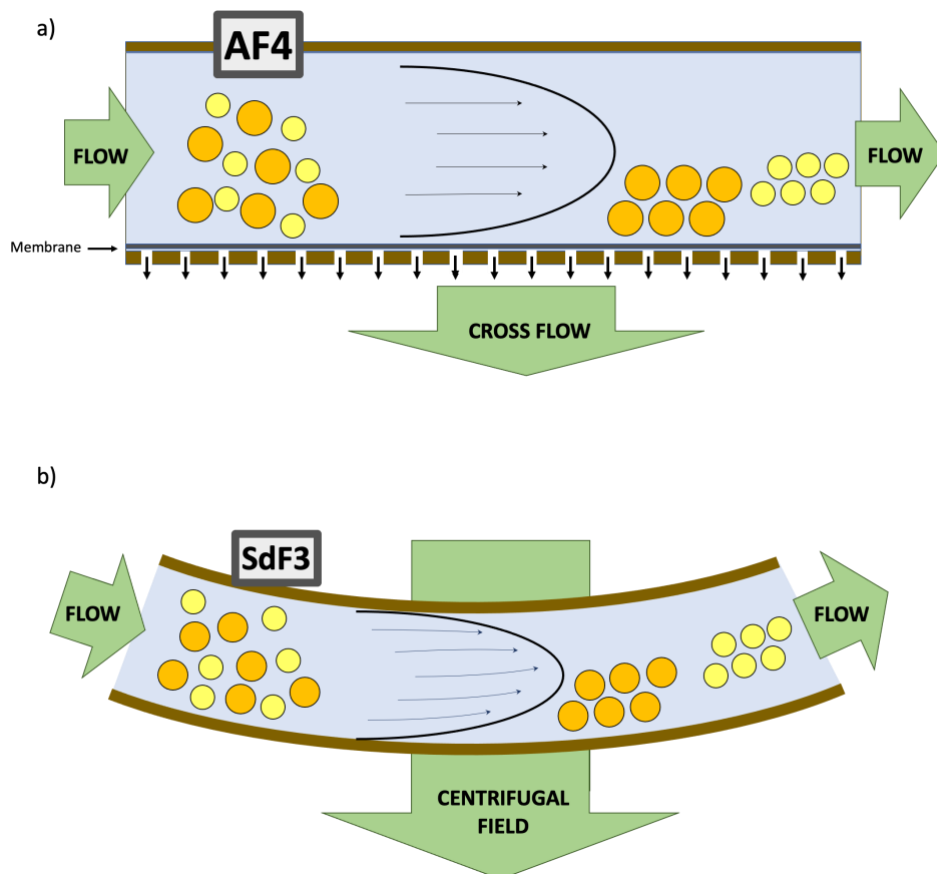


**Figure 15:** a) Principle of asymmetric flow field flow fractionation (AF4). b) Principle of sedimentation field flow fractionation (SdF3)

For MNPS, different FFF methodologies have been employed in order to characterize and analyse these NPs in bulk dispersion, as well as in different matrices. Table 12 shows selected representative works.

**Table 12:** Some representative studies using FFF techniques for AuNPs and AgNPs characterization.

MNPs	FFF technique - Chanel flow (mL·min <sup>-1</sup> )	Cross-flow (mL·min <sup>-1</sup> )	Sample	Detector	Size (nm)	Ref.
AgNPs nanospheres	SdF3 ---	---	Commercial AgNPs	UV-vis	30, 60, 75 and 100	[270]
Three AgNPs	AF4 1.00	1.00	Synthesized and commercial AuNPs in juvenile clams	ICP-MS	11.3 – 49.8	[271]
AgNPs	AF4 ---	3.00	AgNPs in mollusks	UV-ICP-MS	---	[272]
AgNPs sphere and plates	AF4 1.00	3.00	Commercial AgNPs	ICP-MS	26.09 – 54.05	[273]
AuNPs nanospheres, nanotriangle and nanorods	AF4 0.94	0.5	Synthesized AuNPs	UV	35, 47 and 51	[274]
AuNPs	AF4 1.00	1.50	Commercial AuNPs	UV-vis	20 -100	[275]
AuNPs	AF4 1.00	2.50	Human urine, blood and serum	MALS-UV-ICP-MS	5, 20, 40 and 60	[276]
Phosphate and citrate AuNPs	AF4 0.50	1.00	Cell culture medium	ICP-MS	10 - 80	[277]
Citrate AuNPs	AF4 0.50	1.50	Commercial AuNPs	UV-vis and DLS	40 - 60	[278]

A particular methodology has been developed to measure AgNPs mass and density, by combining SdF3 with other techniques, providing a straightforward and reproducible means for these measurements [270]. Similarly, AF4 technique has been employed to evaluate the effects of particle shape for two types of AgNPs (sphere and plates). In this case, the results showed that the broadening coefficient for plate-NPs apparently became smaller than that for sphere-NPs.

Jassim et al. have focused their work in the toxicological study of three types of AgNPs (chemically synthesized, biological synthesized and commercial) in juvenile clams. Moreover, the characterization of physicochemical properties of MNPs is carried out focusing in their separation and fractionation by AF4 [271]. Following the study of AgNPs in seafoods, Taboada-Lopez et al. have developed an strategy based on AF4-UV-ICP-MS analysis following enzymatic digestion for the detection and quantification of AgNPs at environmental levels in mollusks [272].

For AuNPs, different reports show the potential utility of FFF techniques. As an example, three different types of AuNPs with different morphologies have been synthesized and analyzed using AF4 to characterize the size and to compare the elution mechanism of the particles having different shapes [274]. The results indicated that non-spherical particles moved down the FFF channel by different mechanism from that of the spherical particles showing lower elution time for last ones. Similarly, the development and in-house validation of a standard operating procedure for sizing of an unknown AuNPs sample by AF4 coupled with UV-vis detection using external size calibration with gold nanoparticle standards in the size range of 20–100 nm have been proposed in [275]. Moreover, the dependence of initial AuNPs concentration with the size measurement uncertainties has been evaluated for this technique. The results demonstrated that at low concentration of nanoparticles, the AF4-DLS combined technique failed to evaluate the real size of nanoparticles in suspension, detecting an apparent and progressive size increase as a function of the elution time and of the concentration of MNPs [278].

Considering the potential toxicity of MNPs, different works have applied FFF techniques for the assessment of human exposure to these NPs both in the general population and in exposed workers, to implement adequate risk management and mitigation strategies for the sustainable use these NMs [276,277].

Focusing in CB materials, FFF techniques have also been reported to separate organic C-NPs by size and shape, and several methods have been developed to characterize subpopulations of particles in different matrices. Remarkably, most of them are based on flow field flow fractionation. Table 13 shows some significative methods using FFF based techniques for the separation and characterization of CB in different matrices.

**Table 13:** Reviews published in the last 5 years using FFF techniques for CB separation and characterization

Dispersant	FFF technique - Chanel flow (mL·min <sup>-1</sup> )	Cross-flow (mL·min <sup>-1</sup> )	Sample	Detector	Size (nm)	Ref.
Aqueous styrene: acrylic acid (1:1, 2:1, 3:1)	AF4 0.75	0.75	Ink	UV-vis and DLS	83	[124]
Styrene maleic anhydride	AF4 0.8	0.3	Commercial Carbon Black	UV-vis	~300	[128]
Water + glycerin or isopropyl alcohol	AF4 ---	---	Black ink	MALS and (off-line) ICP-MS	<100	[241]
Aqueous dispersion	AF4 0.5	1 to 0	Latex suspension	UV-vis and ICP-MS	---	[279]
EtOH 95% and aqueous surfactant dispersant (SDS and Novachem)	AF4 0.7	2.5 to 0	Carbon Black in plastic matrices	MALS	100 - 200	[135]
Salt solutions, styrene acrylate and styrene maleic anhydride	AF4 0.75	0.75	Ink	UV-vis	80 - 257	[280]
Triton X-100, tween 20 and FL-70	SdF3 1.26	---	Commercial Carbon Black	UV-vis	78 - 300	[281]

Bae et al. [124] developed an AF4-based method to determine CB particles in ink samples using a cross flow and channel flow of 0.75 mL·min<sup>-1</sup>. CB dispersions were carried out employing different copolymeric dispersing agents of hydrophobic and hydrophilic monomers. The results indicated that CB was better dispersed, mainly, in hydrophobic medium. The different values obtained suggested that AF4 was more reliable than other techniques. Furthermore, sensitivity was satisfactory to differentiate CB size distributions. Bocca et al. [241] applied different analytical

techniques for the size characterization and determination of nano and micro-sized particles among which CB. Different inks were analyzed including red, ice blue, bright orange, deep violet, black outlining, dark chocolate or true black. As it is expected, the results obtained by AF4-MALS indicated that black pigments contained the major amount of CB particles with size distributions up to 100 nm. Surface modified CB have also been separated. Kim et al. [280] have developed a surface modification method of CB particles to improve thermal stability of CB inks and their dispersibility. Size distributions obtained by different analytical techniques were compared and results showed that AF4 provided reliable particle size distributions.

In other studies, authors focused their research in matrices with different nature such as latex or plastics. Nischwitz et al. [279] provided a method to determine CB content in latex via AF4-ICP-MS, which allows allowed element selective detection of CB in latex and charcoal particles. On the other hand, Bott et al. [135] have focused their research in the study of CB migration in plastic packaging towards foodstuffs. AF4-MALS results indicate that CB particles not migrate towards the food sample.

Characterization of direct bulk carbon black dispersion has also been carried out. Kim et al. [128] studied the storage stability and the effect of milling time in CB dispersions using three different dispersants. AF4 measurements showed a tendency of gradual decrease in the particle size according to an increase in milling time using a channel flow of  $0.8 \text{ mL}\cdot\text{min}^{-1}$  and cross flow of  $0.3 \text{ mL}\cdot\text{min}^{-1}$ . Moreover, the precision of results was more consistent compared with other techniques.

Related with SdF4, Park et al. [281] carried out a research using commercial CB in order to study the effect of different dispersion factors (surfactant, pH or ionic strength) in the separation and determination of size particle distribution. For dispersion tests, different dispersants were employed, such as Triton X-100, tween 20 or FL-70. The rotor radius of SdF3 equipment was 15.1 cm and the channel volume was 4.42 mL. UV-visible fractograms provided particle sizes between 78 and 300 nm with relative errors around 20 %, and results indicated that well dispersion was obtained with a nonionic surfactant with a pH of around 8 due to this pH provided the higher z-potential which can be related with a maximum repulsion between the samples and high dispersion effectively.

SiO<sub>2</sub> samples have also been studied by FFF techniques. Table 14 summarized different reports in this topic.

**Table 14:** Reports using FFF techniques for silica NMs separation and characterization

Silica NM	FFF technique - Chanel flow (mL·min <sup>-1</sup> )	Cross-flow (mL·min <sup>-1</sup> )	Sample	Detector	Size (nm)	Ref.
SiO <sub>2</sub> NPs	AF4 1.06	0.31	Synthesized SiO <sub>2</sub> NPs	UV-vis	27 - 358	[282]
S-SiO <sub>2</sub> NPs	SdF3 1.00	---	Aqueous suspensions	MALS	150	[283]
Amorphous silica	SdF3 2.00	---	Additives in food	UV-vis	30 - 400	[284]
SiO <sub>2</sub> NPs	AF4 0.50	0.75	A reference material and two silica samples	MALS	29 - 110	[285]
SiO <sub>2</sub> NPs	AF4 0.50	1.00	Coffee creamer	ICP-MS	22 - 201	[286]

Different authors used FFF techniques for size monitoring of wide variety of SiO<sub>2</sub>NPs obtained by different synthesis methods optimizing different parameters such as concentrations of the reactants, reaction time or agitation [282,285].

As practical applications, silica based NMs used in different areas such as food industry. Different works characterized by AF4 and SdF3 the SiO<sub>2</sub>NPs used as additives in food samples, and analyzed the potential toxic effects in human cells [284,286].

The proposed methodologies have demonstrated to be promising tool to determine and characterize different mainly NMs in industrial matrices, environmental and biological samples providing suitable information about their proper performance and adequate applicability in different areas.



## 1.4 STUDIED ANALYTES AND MATRICES OF INTEREST

In this Thesis, metallic NPs such as AuNPs and AgNPs, carbon nanomaterials (CB) and silica nanomaterials has been studied as analytes. Moreover, other analytes as polyamines or nitrates have been also determined in different matrices.

### 1.4.1 MNPs in water and soil samples

The environment is highly exposed to MNPs. They can release different ions, such as  $\text{Ag}^+$ , the toxic species per se responsible for the antimicrobial behavior [287]. Although silver toxicity in humans is relatively low, damage on other species (e.g., aquatic organisms) could have an impact on all trophic levels of the food chain [288]. Moreover, understanding the fate of AgNPs, considered as emerging pollutants, in such environmental matrices is of primary importance. Few systematic studies have been performed to model retention of NPs in soils. Various reports have been published mainly on column experiments, based on inductively coupled mass spectroscopy (ICP-MS) [289]. In this way, the specific nature of the soil could induce a unique way to interact with AgNPs due to the large number of factors involved. Besides, NP aggregation and silver speciation may occur [290].

Recently, the stability of citrate AgNPs in natural brackish aquatic environments was studied in [258], employing different analytical technics. The authors established that the potential environmental risks induced by AgNPs were reduced with increasing salinity by their sedimentation and dissolution, suggesting that the order of potential risk in different natural aquatic systems probably varied as follows: freshwater > brackish water > seawater.

Regarding with AuNPs, their behavior within different environmental matrices is of particular interest for three reasons. First, AuNPs are easier to track through environmental media than other NPs, being relatively stable against oxidation, easy to characterize, and gold occurs at an extremely low background level in most environments [291]. Second, the physiochemical properties (size, shape, and surface chemistry) of AuNPs can be controlled in exquisite detail. This allows the fate and transport of AuNPs in the environment to be closely correlated with material properties [292]. Finally, because AuNPs are being investigated for use in biomedical applications, it can expect an increase in the prevalence of AuNPs

in the environment. For this reason, their characterization and monitorization in environmental samples is necessary to understand their completely behaviour [293].

#### **1.4.2 CB in water and soil samples**

The presence of CB in water and soil environments could potentially lead to unexpected harmful effects since their behaviour in these ecosystems is largely unknown [294]. As an example, CB aggregates reduce fertilization success of marine seaweed [295]. Moreover, impact studies of CB materials in marine microcrustacean, revealed their toxicity in filter-feeding organisms [296]. On the other hand, in the terrestrial environments, CB produce an increase risk to the pristine nature of agricultural ecosystems, threatening terrestrial organism habitats and faunal biodiversity. Earthworm, whose biochemical responses are regarded as an early warning of soil heavy metal and pesticide pollution, may be considerably affected by the presence of this nanomaterial [137]. In the same way, potential transition of CB of soil to atmosphere could be induce harmful effects on human health such as, cytotoxicity to cell and possible carcinogenic tumours [125]. For these reasons, its necessary the development of CB extraction and characterization procedures in order to analyse, remove and recover CB from the environment.

According to the CB expected concentrations in environmental samples, a wide range between 0 – 1000 mg L<sup>-1</sup> is observed with different particles sizes which stablish the presence of single particles, aggregates and agglomerates [139,140].

#### **1.4.3 Polyamines in urine samples**

Polyamines are small molecules, metabolically derived from certain amino acids. These molecules exhibit polycation behaviour with positive charges due to the protonation at physiology pH of the amino primary and secondary groups.

Biogenic polyamines, such as spermine (Figure 16) are key compounds in the cell regulation steps like the growth, the proliferation and the cell differentiation [297]. They are implicated in replication, transcription, translation, post-translation modifications, ionic channel, membrane stability, cellular proliferation, transformation, differentiation, apoptosis and carcinogenesis

biological processes [298]. Due to their participation in a wide variety of cellular processes, it is complex determine their specific function in cells and their action mechanisms.

Different recently studies have exposed that rapid cell growth that takes place in cancerous tissues is associated with a high production of polyamines that are transferred to the bloodstream to the kidney where they are excreted in the urine. When tumor tissue is completely eradicated by surgery or radiotherapy and chemotherapy treatments, there is a decrease in polyamine levels over time [299]. Thus, concentration monitoring of polyamines could be used to follow the evolution of a tumor and to know the efficacy of the therapeutic treatments applied to the patient in an easy and fast way.

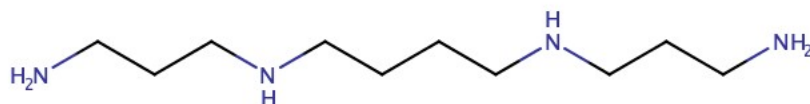


**Figure 16:** Spermine chemistry structure.

Polyamines determination in human urine samples is not easy process due to the large number of interfering components presents in this sample and the low concentration levels. Selective and sensitive determination methods are needed. The most used methods for the detection of polyamines in urine are chromatographic, electrophoretic or fluorimetric methods as well as immunoassays. However, most of them require complex sample treatments and relatively high analysis times.

*In this Thesis, polyamines have been studied by taking advantage of SPR of AuNPs to develop a colorimetric assay.*

#### **1.4.4 Nitrate in aquatic environments**

Nitrate (NO<sub>3</sub><sup>-</sup>) is a polyatomic ion which are common component of fertilizers and explosives. Their uses and applicability have increased in the last years. For this reason, their possible toxicity and presence in different environments should be monitored.

Specifically, the use of fertilizers has experienced substantial growth causing harmful effects in the environmental, such as water resource pollution. European Directive 98/83/EC on the quality of water intended for human consumption stipulates that nitrate concentration in water must not be higher than 50 mg per liter. High levels of nitrate in water can be dangerous to human health as well as to freshwater- and marine ecosystems [300,301].

Usually, nitrate can be converted to nitrite, which has the potential to change the hemoglobin in red blood cells into methemoglobin [300,301]. This process can lead to red blood cells losing the ability to transport oxygen. Moreover, nitrosamines are formed from nitrite by a nitration reaction that can potentially cause cancer of the digestive system. On the other hand, pregnant women may suffer from abortion, intrauterine growth retardation, and central nervous system defects if exposed to a high nitrate environment for a long period [302].

Thus, within the framework of a suitable circular economy applied to environmental field [303], the need of removing the pollution present in the environment such as nitrates, has allowed proposing in this Thesis the use of silica nanomaterials obtained from natural sources as powerful tools employed for these purposes.

## **CHAPTER 2: OBJECTIVES**



The rapid progress of research and development on Nanoscience and Nanotechnology is one of the global features of the modern scientific and technological progress. In this field, NMs play a key role due to their unique chemical and physical properties. NMs are categorized depending on their size, shape and origin. Moreover, the composition is another classification which include MNPs, C-NMs or silica based materials among others.

In the last years, the use of NMs has increased substantially in a wide variety of scientific areas and application fields including paints, automobiles, electronic products and food industries. For this reason, their characterization and determination are necessary in order to ensure their correct performance.

Different analytical techniques are used for NMs study. Image and spectroscopic techniques only provide partial information focusing in the morphology, structure and intrinsic properties. For this reason, the development of new methodologies based on separation techniques such as liquid chromatography and field flow fractionation are necessary in order to fully understand the performance of NMs.

The different objectives that encompass this Thesis can be summarized in the following two items:

- Development of new methodologies for assessment, characterization and determination of AuNPs, AgNPs, CB and silica based materials. To address this objective, the characteristic signal of different NMs obtained by different separation techniques such as IT-SPME-miniaturized LC-DAD, AF4-UV-vis-DLS and SdF3-MALS have been evaluated. Moreover, the effect of time in the dispersion stability and the influence of environmental matrices such as soils or waters in order to understand the transformations that NMs can be experimented along their life cycle, have been studied.
- Development of new analytical tools based on MNPs and silica based materials intrinsically properties and used as sensors or adsorbents in order to carry out different applications or enhance analytical procedures. In this case, MNPs have been used as plasmonic platforms in order to determine and quantify acid compounds and polyamines. Meanwhile, silica extracted from rice straw ashes has been used as adsorbent materials for removing

nitrate from waters in order to remediate the pollution that agriculture activities can cause.

The PhD Thesis has been carried out thanks to the finance obtained by pre-doctoral scholarships:

- FPU 17/01655: Ayudas para la formación de profesorado universitario, Spanish Ministry of Universities. 4 years.
- EST 21/00250: Ayudas complementarias de movilidad destinadas a beneficiarios del programa de Formación del Profesorado Universitario (FPU). Spanish Ministry of Universities. Research stay in the Department of Environmental Geosciences of University of Vienna. 3 months.

Moreover, different projects granted to “*Miniaturización y Métodos Totales de Análisis*” (MINTOTA) research group, which belongs to the Analytical Chemistry Department of the University of Valencia, have allowed the develop of this Thesis. These projects are:

- Project PROMETEO2016/109, granted by Generalitat Valenciana – Prometeo program for excellent research groups; Development of new strategies for the design of in situ analysis devices: nano and biomaterials (4 years).
- Project CTQ2017-90082-P, granted by Spanish Ministry of Science and Innovation, and EU-FEDER; In-tube solid phase microextraction coupled online to liquid nanochromatography: new opportunities for/from the nanoscale and chromatography (4 years).
- LIFE16 ENV/ES/000419 (LIFE LIBERNITRATE), granted by EC-EASME LIFE and CIP-ECO-Innovation; Responsible reduction of nitrate in the comprehensive water cycle (4 years).
- INNEST/2021/15, granted by Agencia Valenciana de la Innovación (AVI); Treatment of waste water from a reversible electro dialysis plant using electrochemical processes - ELEKTRA (2 years).



- PDC2021-121604-100, granted by Spanish Ministry of Science and Innovation, and EU-FEDER; Resilient ammonia solid chemisensor for controlling atmospheres of poultry farms - NH3ControlFarm (2 years).
- OTRI2021-218441NIVES; To characterize BBMV vesicles by asymmetrical flow field-flow fractionation (AF4) - BASF Corporation (2 years).

The development of this PhD Thesis has allowed the publication of eight scientific papers and one patent. Moreover, there are two papers submitted, and another one drafted and waiting for sending. Following, each of them are detailed:

- Campíns-Falcó, P., González-Fuenzalida, R.A., **Sanjuan-Navarro, L.**, Moliner-Martínez, Y., Verdú-Andrés, J., Molins-Legua, C., Herráez-Hernández, R. Capillary LC of metallic nanoparticles coupled on line to IT-SPME: application to plasmonic assays. *Actualidad Analítica*. 60, 36-37 (2017).
- González-Fuenzalida, R.A., **Sanjuan-Navarro, L.**, Moliner-Martínez, Y., Campíns-Falcó, P. Quantitative study of the capture of silver nanoparticles by several kinds of soils. *Science of the Total Environment*. 630, 1226-1236 (2018). Impact factor (JCR 2020): 7.963.
- Moliner, C., Teruel-Juanes, R., Primaz, C.T., Badia, J.D., Bosio, B., Campíns-Falcó, P., Molins-Legua, C., Hernandez, F., **Sanjuan-Navarro, L.**, Madramany, P., Moran, J., Castro, J., Sanchis, F.J., Martinez, J.D., Hiddink, F., Ribes-Greus, A., Arato, E. Reduction of Nitrates in waste water through the valorization of rice straw: LIFE LIBERNITRATE Project. *Sustainability*. 10, 3007 (2018). Impact factor (JCR 2020): 3.251.
- **Sanjuan-Navarro, L.**, Boughbina-Portolés, A., Moliner-Martínez, Y., Campíns-Falcó, P. Aqueous dilution of noble NPs bulk dispersions: modelling instability due to dissolution by AF4 and stablishing considerations for plasmonic assays. *Nanomaterials*. 10, 1802 (2020). Impact factor (JCR 2020): 5.076.
- Boughbina-Portolés, A., **Sanjuan-Navarro, L.**, Moliner-Martínez, Y., Campíns-Falcó, P. Study of the stability of citrate capped AgNPs in several

- environmental water matrices by asymmetrical flow field flow fractionation. *Nanomaterials*. 11, 926 (2021). Impact factor (JCR 2020): 5.076.
- **Sanjuan-Navarro, L.**, Cortés-Bautista, S., Moliner-Martínez, Y., Campíns-Falcó, P. In-tube solid phase microextraction coupled to miniaturized liquid chromatography for both, noble metal nanoparticles assessment and sensitive plasmonic assay development. *Analytica Chimica Acta*. 1171, 338665 (2021). Impact factor (JCR 2020): 6.558.
  - Robles-Jimarez, H.R., **Sanjuan-Navarro, L.**, Jornet-Martínez, N., Primaz, C.T., Teruel-Juanes, R., Molins-Legua, C., Ribes-Greus, A., Campíns-Falcó, P. New silica based adsorbent material from rice straw and its in-flow applications to nitrate reduction in waters: Process sustainability and scale-up possibilities. *Science of the Total Environment*. 805, 150317 (2022). Impact factor (JCR 2020): 7.963.
  - **Sanjuan-Navarro, L.**, Moliner-Martínez, Y., Campíns-Falcó, P. Characterization and Quantitation of Carbon Black Nanomaterials in Polymeric and Biological Aqueous Dispersants by Asymmetrical Flow Field Flow Fractionation. *ACS Omega*. 6(47), 31822-31830 (2021). Impact factor (JCR 2020): 3.512.
  - **Sanjuan-Navarro, L.**, Moliner-Martínez, Y., Campíns-Falcó, P. The State of Art of Nanocarbon Black as Analyte of Interest in Several Matrices: A Review. *Trends in Analytical Chemistry*. (Minor revision). Impact factor (JCR 2020): 12.296.
  - **Sanjuan-Navarro, L.**, Moliner-Martínez, Y., Campíns-Falcó, P. Isolation of Carbon Black from soils employing a biological dispersant and its recovery by filter-aided procedure: characterization by field flow fractionation techniques. (submitted).
  - **Sanjuan-Navarro, L.**, Moliner-Martínez, Y., Campíns-Falcó, P. Asymmetrical flow field flow fractionation for the analysis of different silica materials: from nanometers to micrometers (draft).

- Primaz, C.T., Jornet-Martínez, N., **Sanjuan-Navarro, L.**, Moliner-Estopiñán, C.E., Campíns-Falcó, P., Molins-Legua, C., Ribes-Greus, A., Badía-Valiente, J.D., Teruel-Juanes, R., Gil-Castell, O., Bosio, B., Arato, E. Patent 2727673. Procedimiento de adsorción de nitratos mediante sílice modificada activa a partir de cenizas de paja de arroz. ES2727673A1 --- WO 2020/169862A1. Concession data: 24.02.2021.

The results obtained in this PhD Thesis have been showed in different national and international congress, which are detailed in the next lines:

- Campíns-Falcó, P., González-Fuenzalida, R.A., **Sanjuan-Navarro, L.**, Moliner-Martínez, Y., Verdú-Andrés, J., Molins-Legua, C., Herráez-Hernández, R. Capillary LC of Metallic Nanoparticles coupled on line to IT-SPME: uses and utilities. 19<sup>th</sup> International Symposium on Advances in Extraction Technologies (ExTech). Santiago de Compostela, Spain. June 2017. International congress. Oral contribution.
- **Sanjuan-Navarro, L.**, González-Fuenzalida, R.A., Muñoz-Ortuño, M., Jornet-Martínez, N., Moliner-Martínez, Y., Campíns-Falcó, P. Capillary LC of metallic nanoparticles coupled on line to IT-SPME: application to plasmonic assays. XXI Reunión de la Sociedad Española de Química Analítica (SEQA). Valencia, Spain. September 2017. National congress. Poster contribution. Award for the best poster contribution.
- **Sanjuan-Navarro, L.**, Jornet-Martínez, N., Ballester-Caudet, A., Moliner-Martínez, Y., Campíns-Falcó, P. Chromatographic Characterization of AuNPs Used in Plasmonic Assays. 32<sup>nd</sup> International Symposium on Chromatography (ISC). Cannes-Mandelieu, France. September 2018. International congress. Poster contribution. Oral presentation of the poster.
- **Sanjuan-Navarro, L.**, Moliner-Martínez, Y., Campíns-Falcó, P. Evaluation of asymmetrical flow field flow fractionation for study the stability of silver nanoparticles. XXII Reunión de la Sociedad Española de Química Analítica (SEQA). Valladolid, Spain. July 2019. National congress. Poster contribution.

- Robles-Jimarez, H.R., **Sanjuan-Navarro, L.**, Jornet-Martínez, N., Molins-Legua, C., Campíns-Falcó, P. Active silica from rice straw for avoiding nitrates of the comprehensive water cycle: a proof of concept. XXII Reunión de la Sociedad Española de Química Analítica (SEQA). Valladolid, Spain. July 2019. National congress. Poster contribution.
- **Sanjuan-Navarro, L.**, Moliner-Martínez, Y., Campíns-Falcó, P. Asymmetrical flow field flow fractionation for studying the stability of aqueous AuNPs dispersions. IX International Congress on Analytical Nanoscience and Nanotechnology (NyNa). Zaragoza, Spain. July 2019. International congress. Poster contribution.
- Moliner-Martínez, Y., Prieto-Blanco, M.C., **Sanjuan-Navarro, L.**, Pardo-Puñal, M., Campíns-Falcó, P. In-situ generation of AgNPs: determination of chlorogenic acid in dietary products by In-Tube SPME capillary liquid chromatography with DAD detection. IX International Congress on Analytical Nanoscience and Nanotechnology (NyNa). Zaragoza, Spain. July 2019. International congress. Poster contribution.
- Campíns-Falcó, P., González-Fuenzalida, R.A., **Sanjuan-Navarro, L.**, Moliner-Martínez, Y. Combining information given by IT-SPME-miniaturized LC-DAD and AF4-UV-Vis DLS for Au and Ag nanoparticles studies. IX International Congress on Analytical Nanoscience and Nanotechnology (NyNa). Zaragoza, Spain. July 2019. International congress. Oral contribution.
- Moliner-Martínez, Y., **Sanjuan-Navarro, L.**, Campíns-Falcó, P. Monitorization of localized surface plasmon resonance responses by in-tube SPME coupled to capillary liquid chromatography and DAD detection. 25<sup>th</sup> International Symposium on Separation Sciences (ISSS). Łódź, Poland. September 2019. International congress. Oral contribution.
- **Sanjuan-Navarro, L.**, Moliner-Martínez, Y., Campíns-Falcó, P. Study of the dilution effect in AuNPs and AgNPs aqueous dispersions. 25<sup>th</sup> International Symposium on Separation Sciences (ISSS). Łódź, Poland. September 2019. International congress. Poster contribution.

- **Sanjuan-Navarro, L.**, Moliner-Martínez, Y., Campíns-Falcó, P. Analytical performance of asymmetrical flow field flow fractionation coupled to UV-Vis and DLS detection to evaluate the effect of dilution in aqueous silver nanoparticles dispersion stability. 20<sup>th</sup> International Symposium on Field- and Flow-Based Separations (FFF). Vienna, Austria. February 2020. International congress. Oral contribution.
- Campíns-Falcó, P., González-Fuenzalida, R., **Sanjuan-Navarro, L.**, Moliner-Martínez, Y. Merging results from AF4-UV-Vis-DLS and IT-SPME-Miniaturized LC-DAD for Au and Ag nanoparticles studies. 20<sup>th</sup> International Symposium on Field- and Flow-Based Separations (FFF). Vienna, Austria. February 2020. International congress. Oral contribution.
- Moliner-Martínez, Y., **Sanjuan-Navarro, L.**, Campíns-Falcó, P. Effect of dilution on aqueous dispersion stability of gold nanoparticles by using asymmetrical flow field flow fractionation coupled with UV-Vis and DLS detection. 20<sup>th</sup> International Symposium on Field- and Flow-Based Separations (FFF). Vienna, Austria. February 2020. International congress. Oral contribution.
- **Sanjuan-Navarro, L.**, Moliner-Martínez, Y., Campíns-Falcó, P. Study of filter based extraction of carbon black nanoparticles by using AF4-DLS. 23<sup>rd</sup> International Symposium on Advances in Extraction Technologies (ExTech). Online Event. June-July 2021. International congress. Poster contribution.
- Robles-Jimarez, H.R., **Sanjuan-Navarro, L.**, Jornet-Martínez, N., Molins-Legua, C., Campíns-Falcó, P. Amino-functionalized silica from rice straw: nitrate adsorption. 23<sup>rd</sup> International Symposium on Advances in Extraction Technologies (ExTech). Online Event. June-July 2021. International congress. Poster contribution.



## **CHAPTER 3: METHODOLOGY**

















### 3.1 REAGENTS

Table 15 summarizes the reagents, chemicals and commercial suppliers employed in this Thesis. The hazard pictograms are also included, considering the Regulation R (CE) n° 1272/2008 of the Parliament and Council about classification, labelling and packing of substances and mixtures (January 20<sup>th</sup>, 2009).

**Table 15:** Summary of reagents used in this Thesis, with their hazard pictograms, where

 = Flammable (GHS02);  = Corrosive (GHS05);  = Toxic (GHS06);  = Harmful (GHS07);  = Health hazard (GHS08);  = Environmental hazard (GHS09).

REAGENT	SUPPLIER						
1-butyl-3-methyl imidazoliumoctylsulphate	Sigma <sup>a</sup>				X		
1-butyl-4-methyl pyridiniumhexafluoro phosphate	Sigma				X		
1-methyl-3-octyl imidazoliumhexafluoro phosphate	Sigma						
3-aminopropyl triethoxysilane	Merck		X		X		
3,3',5,5'-tetramethyl benzidine (TMB)	Sigma						
Acetic acid (HAc)	VWR	X	X		X	X	
Acetonitrile	VWR	X		X		X	
Acrylic acid	Sigma	X	X		X		X
AgNPs (20, 40 and 60 nm) <sup>b</sup>	Sigma						
Alizarin	Sigma		X		X		X
Ammonia	Scharlau		X	X			X
Ammonium acetate	Sigma						
AuNPs (20 nm) <sup>c</sup>	Sigma						
AuNPs (20, 40 60 and 80 nm) <sup>d</sup>	Sigma						
Carbon Black (N326, N550 and N772)	Birla Carbon						

Chelex 100	Sigma				
DMEM/F-12	Merck				
DMEM/F-12 modified <sup>e</sup>	Merck				
Ethanol	VWR	x			
Gold (III) chloride trihydrate	Sigma		x		x
Gold (III) tetrachloroauric acid trihydrate	Sigma		x		x
Halloysite nanotubes (HNTs)	Sigma				
Hydrochloric acid	Sigma		x	x	
Hydrogen peroxide	Panreac		x		x
Ludox SiO <sub>2</sub> NPs dispersions	Merck				x
Manganese oxide	Sigma				x
Methanol	VWR	x		x	x
Nousperse FX 365	Elements GmbH				
O-phosphoric acid	Sigma		x		x
Potassium hydroxide	Sigma		x		x
Potassium nitrate	Merck				
Potassium sulphate	Sigma				
Rice straw ash	LIFE project <sup>f</sup>				
SiO <sub>2</sub> NPs (5 - 15 nm)	Sigma				x
Silver nitrate	Sigma		x		x
Sodium acetate anhydrous	Panreac				
Sodium azide	Panreac			x	x
Sodium bicarbonate	Scharlau				
Sodium borohydride	Fluka	x	x	x	x
Sodium chloride	Sigma				
Sodium dodecyl sulphate	Merck			x	x
Sodium hydrogen carbonate	Panreac				
Sodium hydroxide	Panreac		x		
Sodium thiosulfate	Merck				x
Spermine tetrahydrochloride	Sigma				x
Styrene	Sigma	x			x

Tetraortosilicate (TEOS)	Sigma	x	x	x
Trisodium citrate	Guinama			
Triton X-100	Sigma	x	x	x
Tween 20	Sigma			
Tween 80	Sigma			
Ultrapure Water	Barnstead system			

<sup>a</sup> Sigma = Sigma-Aldrich

<sup>b</sup> AgNPs stabilized in citrate buffer solution

<sup>c</sup> AuNPs stabilized in 0.1 mM PBS

<sup>d</sup> AuNPs stabilized in citrate buffer solution

<sup>e</sup> DMEM/F-12 supplemented with L-alanyl-L-glutamine dipeptide

<sup>f</sup> LIFE project = LIFE-Libernitrate project

## 3.2 INSTRUMENTATION

Spectroscopic, image and separation techniques have been employed for the development of the present Thesis. The use of these techniques involves the operation of a wide variety of equipment and instruments, which are detailed below.

### 3.2.1 Spectroscopic techniques

#### 3.2.1.1 UV-vis spectrophotometry

UV-vis measurements were performed with a Variant Cary 60 Fiber Optic UV-vis spectrophotometer (Agilent Technologies, USA). Spectra were recorded in the range 190 - 1000 nm.

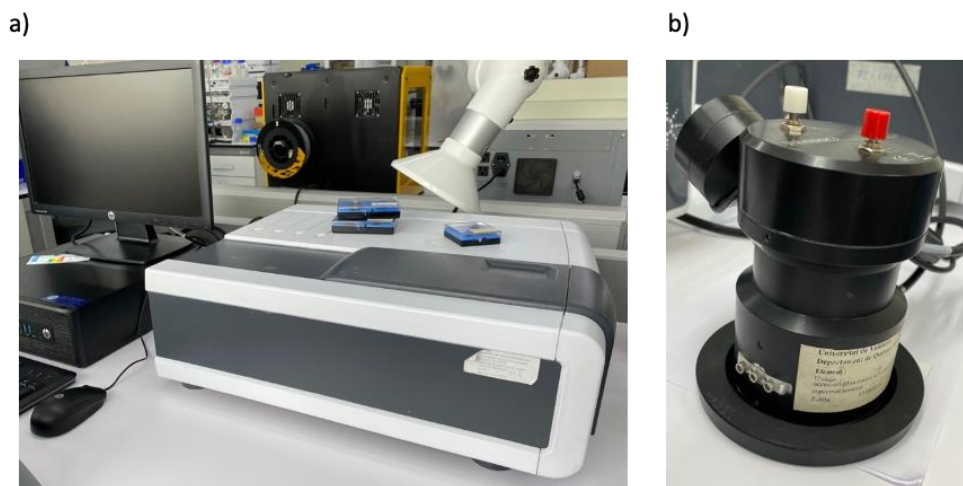


**Figure 17:** a) UV-vis spectrophotometer. b) Diffuse reflection probe with integral video camera.

### 3.2.1.2 Diffuse reflectance spectrophotometry (DR)

The diffuse reflectance (DR) measurements were performed using a Cary 60 UV-vis spectrophotometer (Agilent Technologies, USA) equipped with a diffuse reflection probe from Harrick Scientific Products (USA). The diffuse reflection probe has an integral video camera, which provides a visual image to select the sample spot to be analyzed. Spectra were recorded from 200 to 800 nm (see Figure 17).

### 3.2.1.3 Infrared spectroscopy (FTIR)

FTIR measurements were carried out with a Cary 630 FTIR-ATR spectrophotometer (Agilent Technologies, USA). For data collection and processing, MicroLab FTIR and Resolution Pro software's (Agilent Technologies, USA) were used, respectively.

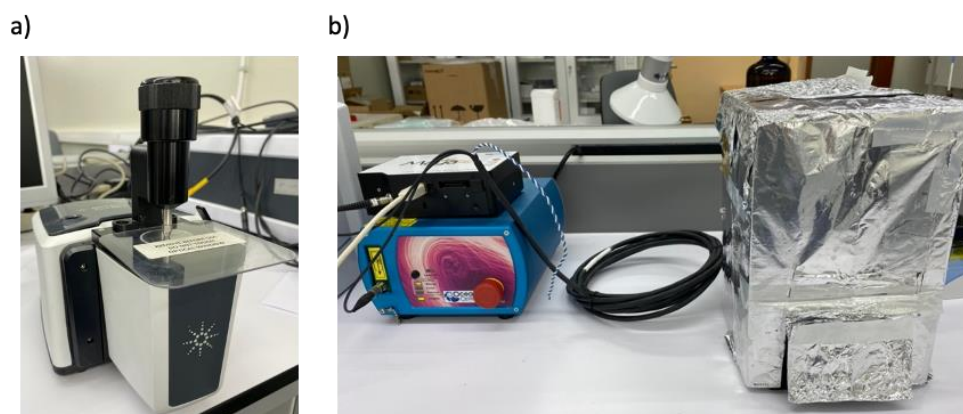


**Figure 18:** a) FTIR-ATR spectrophotometer. b) Raman fiber optic probe coupled to Raman spectrophotometer.

#### 3.2.1.4 Raman spectroscopy

Raman studies were carried out with a Raman fiber optic probe coupled to a Raman spectrophotometer (EEUU) and a laser source from Ocean Optics. The working wavelength was 532 nm, and the spectra were recorded between 1000 and 3500  $\text{cm}^{-1}$  (see Figure 18).

#### 3.2.1.5 Dynamic light scattering (DLS)

DLS directly measurements were performed using a Nano-Zetasizer system (Malvern, UK) with temperature control.



*Figure 19:* DLS system

### **3.2.2 Separation techniques**

#### **3.2.2.1 Capillary and nano high performance liquid chromatography**

The chromatographic studies were carried out using an Agilent Technologies high performance capillary liquid chromatography system equipped with a LC capillary binary gradient pump (Agilent 1200 Series, Agilent Technologies, USA) coupled to a diode array detector (DAD). The DAD detector registered UV-Vis spectra in the range 300 - 800 nm. The analytical column was a Jupiter C18 column (5  $\mu\text{m}$ , 300  $\text{\AA}$ , 0.5 mm i.d x 5 cm).



**Figure 20:** IT-SPME CapLC system with binary capillary pump.

Moreover, an Agilent Technologies high performance liquid chromatography system equipped with a LC nano binary gradient pump (Agilent 1200 series, Agilent Technologies, USA) coupled DAD was also employed. DAD detector registered the spectra between 300 and 800 nm. A Zorbax 300SB-C18 (3.5  $\mu\text{m}$ , 300  $\text{\AA}$ , 0.075 mm i.d x 50 mm) was used as analytical column.

### **3.2.2.2 Field flow fractionation (FFF)**

#### *3.2.2.2.1 Asymmetrical flow field flow fractionation (AF4)*

In this Thesis, an AF4 system (AF200 Postnova Analytics, Germany) was used. The channel was 29 cm long with 10 kDa regenerated cellulose membrane and a 350  $\mu\text{m}$  channel spacer. The flows were provided by two separate pumps and the cross-flow was applied by a separate piston pump which was continuously adjustable. The output of the channel was connected to an on-line UV-vis spectrometer (SPD-20AV, Postnova, Germany) and a DLS detector (Nano ZS, Malvern, UK) with a temperature control.



**Figure 21:** AF4 system equipped with UV-vis and DLS detectors.

#### 3.2.2.2.1 Sedimentation field flow fractionation (SdF3)

The SdF3 system (CF2000 model, Postnova Analytics Inc, Germany) was equipped with a MALS detector Astra V (Wyatt Technology, Germany). The SdF3 channel was 57.6 cm long, 2.0 cm wide, and 0.0250 cm thick, with a rotor radius of 15.1 cm. The channel volume was calculated to be 2.7 mL.



**Figure 22:** SdF3 system equipped with a MALS detector.



### **3.2.3 Image techniques and others**

#### **3.2.3.1 Optical microscope**

In this Thesis a optical microscope ECLIPSE E200 (Nikon Corporation, Japan) equipped with three objective lenses (10x, 50x and 100x), working under bright field illumination, was used. The data obtained were processed using the Nis-Elements software (version 4.20.02, Nikon).



**Figure 23:** Optical microscope.

#### **3.2.3.2 Scanning electronic microscope (SEM)**

A Hitachi S-4100 scanning electron microscope (SEM; Nipon Hitachi, Germany) operating at 10 kV was used in order to characterize the surface of nanomaterials. Samples were sputter-coated with gold-palladium.

Microanalysis was also performed by using the EDAX detector.

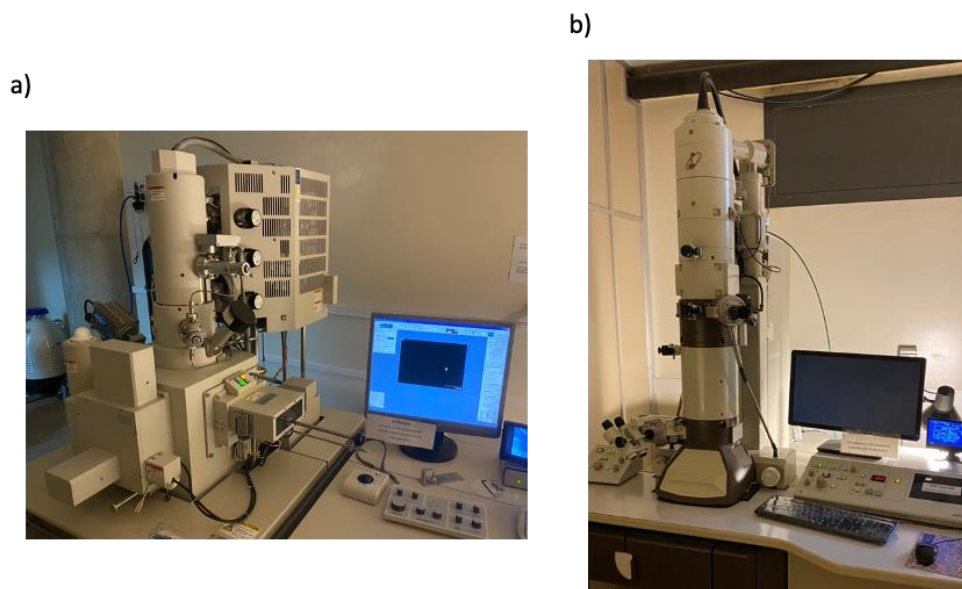


**Figure 24:** a) Hitachi S-4100 scanning electron microscope. b) Jeol 1010 transmission electron microscope.

### 3.2.3.3 Transmission electronic microscope (TEM)

Transmission electron microscope JEM-1010 (Jeol) was used in this Thesis, operating at 100 kV. Samples were prepared by depositing a drop of NPs dispersion (10  $\mu$ l) on a carbon-coated copper grid (300 mesh), which was subsequently dried overnight at room temperature.

### 3.2.3.4 Specific surface area technique (BET)

The specific surface of solids was assessed utilizing the Brunauer-Emmett-Teller (BET) technique, and the pore size distribution was estimated from desorption branches of nitrogen isotherms using the Porosimeter Micromeritics ASAP 2010 02 (Micromeritics, USA).

### 3.3 PROCEDURES

In this Thesis, commercial AuNPs and AgNPs, CB and silica based nanomaterials have been employed. In addition, naked AuNPs, AgNPs, silica  $\mu$ -material and hybrid pigment alizarine-HNTs were synthesized following the procedures describe below:

#### 3.3.1 *Synthesis of metallic NPs*

##### 3.3.1.1 Naked AuNPs synthesis

Naked AuNPs were synthesized using the procedure described in [47], following a laser ablation synthesis.

##### 3.3.1.2 AgNPs synthesis

Citrate-capped AgNPs were synthesized using Frank's approach. In this method, AgNPs are prepared by reducing  $\text{Ag}^+$  with  $\text{NaBH}_4$  in the presence of citrate anions [304]. For controlling both sizes and shapes of the resulting particles, hydrogen peroxide can be added to the mixture [305]. Briefly, trisodium citrate (1.3 mL, 1% w/v),  $\text{AgNO}_3$  (0.064 mL, 1% w/v),  $\text{H}_2\text{O}_2$  (0.1 mL, 30% v/v) and  $\text{NaBH}_4$  (0.94 mL, 0.1% w/v) were subsequently added in a 20 mL flask and then, diluted with water to obtain a final volume of 5 mL. The reaction mixture was stirred for 15 min at room temperature. Finally, the samples were stored and kept in the dark after being adequately diluted with water. For the synthesis blank, the same procedure was followed but no  $\text{AgNO}_3$  was added to the mixture.

#### 3.3.2 *Synthesis of silica based materials*

##### 3.3.2.1 Silica obtained from rice straw ashes and its modification

Two procedures were tested to obtain amino-modified silica from rice straw ashes by thermal decomposition. At lab scale 100 g of ashes were treated with 500 mL of 4 M NaOH under refluxing at 95°C and stirring for 6 h. The resulted mixture was filtered by gravity to obtain a clear yellow solution of silicate.

- Procedure 1: Sulfuric acid 4 M was added to silicate solution until pH 7 to obtain silica gel ( $\text{SiO}_2$ ). The gel was dried obtaining crystals and an amount of silica of  $62 \pm 8$  g ( $n = 10$ ) or  $0.12 \pm 0.02$  g·mL<sup>-1</sup> was obtained. Then, the silica (between 1 and 4 g at lab scale and 100 – 300 g for scaling-up) was modified with amino groups by being rehydrated into hydroalcoholic medium containing APTES and ammonia as a catalyst to obtain the amino-modified silica gel. Table 16 summarized the parameters for the optimization of the synthesis of modified silica: amounts of water, ammonia, APTES and ethanol, all of them express per g of silica and the time required for the synthesis.
- Procedure 2: Precipitation and amino-modification of the silica were done simultaneously in one step. The sodium silicate solution (between 8 and 33 mL at lab scale and 830 and 2500 mL for scaling-up) was dispersed in a solution of water, sulfuric acid, ammonia and APTES. After that, ethanol was added in a controlled rate to form the amino-modified silica gel. The amino-modified silica gel was filtrated, washed and dried to obtain the solid adsorbent material. In order to stablish the amount of silica for the synthesis obtained from silicate, 1 mL of obtained solution is taken, which was acidified with  $\text{H}_2\text{SO}_4$  until pH =7 and the obtained silica was centrifuged and dried at room temperature and weighed. See Table 16 for the amounts of reagents assayed. Successive modification on the amino-modified silica layer by layer was also carried out.

Table 16 shows the conditions tested at lab and the experimental conditions to scale-up for proposed synthetic route.

**Table 16:** Parameters for the optimization of the amino-silica synthesis.

Assay	Proc.	Scale <sup>a</sup>	Reagents (g / g silica) <sup>b</sup>				Time (h)	Layers <sup>c</sup>
			H <sub>2</sub> O	NH <sub>3</sub>	APTES	EtOH		
A1	1	lab	10	1.25	3.1	50	6.5	1
A2	1	lab	10	1.25	0.7	50	6.5	1
A3	1	lab	10	0.16	0.4	6.25	6.5	1
A4	1	lab	2	0.15	0.5	12.5	6.5	1
A5	1	lab	5	0.6	3.0	25	6.5	1
A6	1	lab	20	1.25	5.1	100	13	2
A7	1	lab	30	2.5	9.2	150	19.5	3
A8	1	lab	40	3.75	12.3	200	26	4
A9	1	lab	50	5	15.4	250	32.5	5
A10	2	lab	75	2.5	3.2	22.5	1.5	1
A11	2	lab	75	2.5	3.2	22.5	1.5	1
A12	2	lab	75	2.5	3.2	22.5	1.5	1
A13	2	lab	75	2.5	3.2	22.5	1.5	1
A14	2	lab	75	2.5	1.2	22.5	1.5	1
A15	2	lab	75	0	3.2	22.5	1.5	1
A16	2	lab	75	0	1.6	22.5	1.5	1
A17	2	lab	0	0	0	0	1.5	1
A18	2	lab	150	5	6.5	45	3	2
A19	2	lab	150	5	6.5	45	3	2
A20	2	lab	75	5	3.2	22.5	3	2
A21	2	lab	150	0	6.5	45	3	2
A22	1	scale-up	9.6	1.25	1	45	3	1
A23	1	scale-up	0	0	0	0	12	1
A24	1	scale-up	9.6	1.25	1	45	8	1
A25	1	scale-up	9.6	1.25	0.5	45	8	1
A26	1	scale-up	6.4	0.8	1	30	3	1
A27	2	scale-up	30	3	1.5	27	12	1
A28	2	scale-up	10	1.2	1	45	6	1
A29	2	scale-up	75	2.5	3.2	22.5	2	1
A30	2	scale-up	75	2.5	3.2	22.5	2	1
A31	2	scale-up	75	2.5	3.2	22.5	2	1
A32	2	Scale-up	75	2.5	3.2	22.5	2	2

<sup>a</sup> Lab: 1 - 4 g silica obtained from rice straw in 100-500 ml, scale-up: 100-150 g silica in  $\approx$  6 L. <sup>b</sup> Relative concentration of reagents calculated per g of silica. <sup>c</sup> Layers; number of successive functionalizations, more than one layers appears in shading.

### **3.3.2.2 Hybrid pigments HNT-alizarine (AZ-HNT) and modified-HNT alizarine (AZ-mod-HNT) synthesis**

Synthesis of hybrid pigments was carried out using an adsorption process described in [220]. In this case,  $100 \text{ mg}\cdot\text{L}^{-1}$  of alizarine (AZ) solution was basified using NaOH 0.1 M until obtaining deep-red colour (pH 9). 50 mL of this solution was mixture with 0.5 g of HNT, stirred for 4 hours. After centrifugation, heating the resulting solid at  $50 \text{ }^\circ\text{C}$  for 24 h and grinding, AZ-HNT hybrid pigment was obtained. Moreover, an AZ-mod-HNT (see Section 3.3.3.3) was also synthesised following the same procedure.

### **3.3.3. Preparation of dispersions**

#### **3.3.3.1 Metallic NPs dispersions**

Metallic NPs dispersions were prepared by dilution of bulk dispersion using ultrapure water as dispersant. Diluted dispersions (1/2 to 1/10) were prepared by mixing the adequate amount with the dispersant.

Water matrices were also studied as dilution media. Dilutions 1/4 were prepared with given environmental water was prepared in all cases.

#### **3.3.3.2 CB dispersions**

Three different CB samples (N326, N550, and N722) were studied. According to the specification of the manufacturer, properties such as SSA and OAN were varied as a function of the CB sample. N326 had an SSA of  $78 \text{ m}^2\cdot\text{g}^{-1}$  and an OAN of  $72 \text{ mL}\cdot(100 \text{ g})^{-1}$ ; N550 had an SSA of  $40 \text{ m}^2\cdot\text{g}^{-1}$  and an OAN of  $121 \text{ mL}\cdot(100 \text{ g})^{-1}$ , and N722 had an SSA of  $32 \text{ m}^2\cdot\text{g}^{-1}$  and an OAN of  $65 \text{ mL}\cdot(100 \text{ g})^{-1}$ .

Polymeric and biological dispersants were evaluated in this case. Polymeric dispersant was a mixture of styrene and acrylic acid (3:1). Then, a solution of 0.025% of this mixture in water was prepared. The CB dispersion was carried out after 5 days of dispersant preparation in order to avoid undesirable responses from the dispersant (see Figure 25). A CB dispersion ( $300 \text{ mg}\cdot\text{L}^{-1}$ ) was prepared for each CB sample. For this aim, the diluted dispersant and adequate amounts of CB were

mixed and agitated for 5 min. After, the dispersion was sonicated for 2 h. The working dispersion was prepared by adequate dilution with the dispersant and sonication for 30 min.

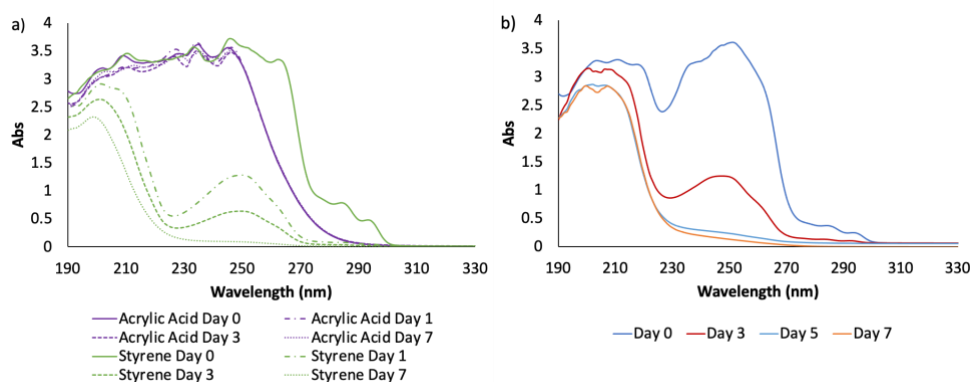


**Figure 25:** a) UV-vis spectra of styrene (green) and acrylic acid (purple) diluted in water at different preparation time. b) UV-vis spectra of polymer mixture (styrene and acrylic acid diluted in water) at different preparation time.

Biological dispersant was an aqueous solution containing Tween 80 (0.02%) and DMEM/F-12 (10%) or DMEM/F-12 supplemented. CB dispersions ( $300 \text{ mg}\cdot\text{L}^{-1}$ ) of each CB sample were prepared following the same procedure described for polymeric dispersions. Different dilutions of these bulk dispersions were prepared using the biological dispersant. In this case, dilution with ultrapure water was also studied by preparing the dispersion at the same concentration level.

Analysis with SdF3-MALS was performed with CB dispersions of  $100 \text{ mg}\cdot\text{L}^{-1}$  employing the biological dispersant.

### 3.3.3.3 Silica based materials dispersions

Regarding solid  $\text{SiO}_2$ NPs, their dispersion was performed employing the following procedure. 0.5 g of  $\text{SiO}_2$ NPs was added to 25 mL of KOH 14.5 mM. Then, the dispersion was stirred during 48 hours. For this  $\text{SiO}_2$  NM, Tween 20 and Triton X-100 were also assayed as dispersants. In these cases, the samples prepared were: 0.2 g of  $\text{SiO}_2$ NPs with 20 mL Triton X-100 0.10 %, 0.2 g of  $\text{SiO}_2$ NPs with 20 mL Triton

X-100 0.01 % and 0.2 g of SiO<sub>2</sub>NPs with 20 mL Tween 20 0.10 %. These dispersions were sonicated for 2 hours.

Commercial SiO<sub>2</sub>NPs dispersions were diluted with ultrapure water in order to obtain a final concentration of 1.25%.

Likewise, μ-SiO<sub>2</sub> obtained from rice straw ashes was dispersed using the following procedure: 0.2 g of extracted SiO<sub>2</sub> or amino modified extracted SiO<sub>2</sub> were mixed with 20 mL of KOH 14.5 mM. Then, the dispersion was stirred during 48 hours.

The modification of HNTs was performed following the procedure described in [306]: silica based material was dispersed at a concentration of 20 g·L<sup>-1</sup> in a 14.5 mM KOH solution under magnetic stirring for 24 h. The hydroxylated HNTs were then washed several times with ultrapure water by centrifugation at 10000 rpm for 10 min. The supernatant was removed, and the slurry was dried in an oven at 110 °C for 15 h.

Different dispersants were tested for obtaining HNTs dispersions. Salts, ionic liquids and surfactants were employed (Table 17). Manual stirring (10 min), ultrasounds (1 hour) and Ultra-Turrax (5 min at 8000 rpm) were the procedures employed for obtaining dispersions.

The dispersions of hybrid pigments AZ-HNT (0.02 %) and AZ-mod-HNT (0.02 %) were carried out using Tween 20 0.1 % as a dispersant and the procedure of Ultra-Turrax equipment described above.



**Table 17:** Dispersant compositions and techniques used in the preparation of HNTs and HNTs modified dispersions.

DISPERSANT		DISPERSION	
	Concentration (%)	HNT (0.2 %)	Modified HNT (0.2 %)
NaCl (Manual)	1.00	✓	
Triton X-100 (Manual)	0.20	✓	
NaCl + Triton X-100 (Manual)	NaCl: 1.00 / Triton: 0.20	✓	
Triton X-100 (Ultrasounds)	0.20	✓	
NaCl + Triton X-100 (Ultrasounds)	NaCl: 1.00 / Triton: 0.20	✓	
NaCl (Ultra-Turrax)	1.00		✓
Triton X-100 (Ultra-Turrax)	0.20	✓	✓
Tween 20 (Ultra-Turrax)	0.20	✓	✓
1-butyl-4-methylimidazoliumoctyl sulphate (Ultra-Turrax)	1.00		✓
1-butyl-4-methylpyridinium hexafluorophosphate (Ultra-Turrax)	1.00		✓
1-methyl-3-octylimidazolium hexafluorophosphate (Ultra-Turrax)	1.00		✓

### 3.3.4 Sample treatment

#### 3.3.4.1 Solid phase extraction

##### 3.3.4.1.1 Spermine extraction

SPE was used to carry out urine samples pretreatment. Thus, C18 silica cartridges (100 mg, Phenomenex, EEUU) were conditioned with methanol (1 mL) and hydrogen carbonate solution (1 mL, 0.5 M) at pH 12. Then, 1 mL of standards or urine was passed through the cartridge. After, a clean-up step with hydrogen carbonate solution (2 mL), acetonitrile (1 mL) and ultrapure water (2 mL) was carried out. The elution was carried out by using HAc 5% in two fractions of 0.25 mL each. Finally, aliquots of the elution with AuNPs solution (300  $\mu$ L AuNPs + 300

μL ultrapure water) were injected in the chromatographic system or analyzed by using spectroscopy measurements.

#### 3.3.4.1.2 Nitrate extraction in batch

Silica obtained from rice straw ashes was modified and used as solid phase extractive material for adsorption of nitrates. An amount of 0.1 g of modified silica of synthesis A10 (see Table 16) was placed into a 4 mL vial and 3 mL of 0.1 M HCl was added and stirred for 3 h to activate the silica. Then, it was centrifuged and washed with water. The activated silica was dispersed in 3 mL of a solution of 25 μg·mL<sup>-1</sup> of nitrate and stirred for 10, 30, 60 and 1440 min and after centrifuged at 6000 rpm, 1 mL of the supernatant was collected, and the spectrum was registered between 200 and 400 nm in a quartz cuvette of 1 cm of path length. A nitrate linear calibration up to 50 mg·L<sup>-1</sup> at 220 nm was used for nitrate quantifying purposes. The nitrate removal was obtained using (E):

$$\%R = \frac{C_o - C_t}{C_o} \cdot 100, \quad (E)$$

where, %R is the percent of removal nitrate, C<sub>o</sub> is the initial concentration in μg·mL<sup>-1</sup> and C<sub>t</sub> is the concentration of the nitrate anions at t time in μg·mL<sup>-1</sup>.

#### 3.3.4.1.3 Nitrate extraction in flow

- Adsorption isotherms

0.25 g of modified silica (A10, see Table 16) was placed in a liquid chromatography column Sigma with a length of 10 cm and 0.7 cm of diameter and connected with FIA connections to a peristaltic pump (Figure 26.a). The modified silica was activated by recirculating a solution of 1 M HCl at flow rate of 5 mL·min<sup>-1</sup> for 1 h. Once the silica was activated, a solution containing nitrate was recirculated for 30 min through the system and after the spectrum was obtained between 200 and 400 nm in order to quantify the adsorbed nitrate concentration. Several concentrations of 0, 25, 50, 75, 100 and 120 μg·mL<sup>-1</sup> were tested. Equation (F) and (G) for studying Langmuir [307] and Freundlich [308] models were obtained.

$$q_e = \frac{q_m \cdot b \cdot C_e}{1 + b \cdot C_e} = \frac{(C_o - C_e) \cdot V}{m}, \quad (F)$$

where  $q_e$  is the equilibrium sorption capacity of sorbent in mg of nitrate per gram of sorbent,  $C_0$  is initial concentration in  $\mu\text{g}\cdot\text{mL}^{-1}$ ,  $C_e$  is the equilibrium concentration of nitrate anion in  $\mu\text{g}\cdot\text{mL}^{-1}$  after nitrate adsorption,  $q_m$  is the maximum amount of anion adsorbed in mg of nitrate per gram of sorbent,  $b$  is the factor related with the bonding energy of adsorption in  $\text{l}\cdot\text{mg}^{-1}$ ,  $V$  is the treated volume of standard and  $m$  is silica mass.

$$q_e = K_f \cdot C_e^{1/n}, \quad (\text{G})$$

where  $q_e$  is the equilibrium sorption capacity of sorbent in mg of nitrate per gram of sorbent),  $C_e$  is the equilibrium concentration of nitrate anion in  $\text{mg}\cdot\text{L}^{-1}$  after nitrate adsorption,  $K_f$  is the adsorption capacity in mg of nitrate per gram of adsorbent and  $n$  is the adsorption intensity of the sorbent.

- Fixed-bed column experiments

Different bed heights of 1.25, 2.3, 3.7 and 7.3 cm, obtained with amounts of modified silica (A13, see Table 16) of 0.25, 0.45, 0.75 and 1.47 g, respectively and various flow rates (5, 5.5, 8, 10, 15 and 22  $\text{mL}\cdot\text{min}^{-1}$ ) for a fixed amount of 0.25 g of modified silica were tested for nitrate removal efficiencies by the device shown in Figure 26.b, and by employing a nitrate solution of 26  $\text{mg}\cdot\text{L}^{-1}$ .

A quantity of 0.25 g of silica was weighed and activated, and a solution of 50  $\mu\text{g}\cdot\text{mL}^{-1}$  of nitrate was passed until achieving the initial nitrate concentration, using the device of Figure 26.b and the Thomas [309] and Yan [310] models (equations (H) and (I), respectively) were tested. Non-linear fits were obtained from software SOLVER for Microsoft Excel 2021.

$$\frac{C_t}{C_0} = \frac{1}{1 + \left[ \frac{K_{Th}}{Q} (q_0 \cdot m - C_0 \cdot V) \right]}, \quad (\text{H})$$

where  $C_t$  is the effluent concentration in  $\mu\text{g}\cdot\text{mL}^{-1}$ ,  $C_0$  is the influent concentration in  $\mu\text{g}\cdot\text{mL}^{-1}$ ,  $Q$  is the flow rate in  $\text{mL}\cdot\text{min}^{-1}$ ,  $V$  is the effluent volume in mL,  $m$  is the mass of the adsorbent in grams,  $t$  is time in min,  $k_{Th}$  is the Thomas rate constant in  $\text{mL}\cdot\text{min}^{-1}\cdot\text{mg}^{-1}$  and  $q_0$  is the maximum adsorption capacity in  $\text{mg}\cdot\text{g}^{-1}$ .

$$\frac{C_t}{C_o} = 1 - \frac{1}{1 + \left(\frac{Q \cdot C_o \cdot t}{q_y \cdot m}\right)^a} \quad (I)$$

where  $C_o$  is the initial solution concentration in  $\mu\text{g}\cdot\text{mL}^{-1}$ ,  $Q$  is the flow rate in  $\text{mL}\cdot\text{min}^{-1}$ ,  $q_y$  is the maximum adsorption capacity in  $\text{mg}\cdot\text{g}^{-1}$ ,  $m$  is the amount of adsorbent in grams and  $a$  is the Yan model constant.

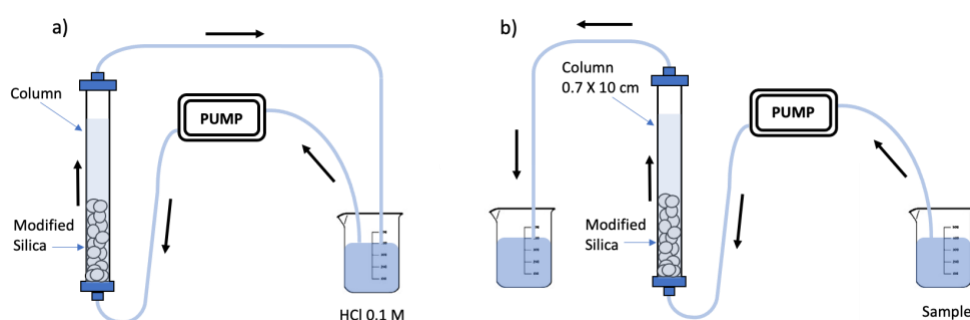


**Figure 26:** Lab manifolds for testing nitrate adsorption: a) for silica activation and establishing of adsorption isotherms and b) for in flow nitrate adsorption studies and breakthrough curves.

- *In-flow nitrate adsorption in standards and well water samples*

Several quantities of 0.25 g of silica were weighed and activated, and well samples, nitrate standards and a multicomponent standard (containing 45, 120, 20 and 30  $\mu\text{g}\cdot\text{mL}^{-1}$  of nitrate, bicarbonate, chloride and sulphate, respectively) were processed using the device of Figure 26.b, an UV-vis probe was interfaced in order to monitor the concentration continuously. The same experience was realized by using 0.25 g of commercial resin in the form of chloride. Flow rate of  $5\text{ mL}\cdot\text{min}^{-1}$  and a bed height of 2.3 cm were employed for both, silica and resin. A silica sample of 0.25 g previously saturated with well water was processed with sodium hydroxide 0.1 M for 60 min at a flow rate of  $5\text{ mL}\cdot\text{min}^{-1}$  by using the device of Figure 26.a, an aliquot was taken every 5 min and nitrate concentration was measured. Regenerated silica was activated and reused for nitrate adsorption by using the lab manifold of Figure 26.b as mentioned above. These steps were repeated three times.

### 3.3.4.2 Solid-liquid extraction

#### 3.3.4.2.1 AgNPs extraction

A quantity of soil sample (0.1 g) was mixed with AgNPs, synthesis blanks of AgNPs or water (1 mL) resulting in three types of working samples named A, SB and W, respectively. SB samples were conducted as control to evaluate the influence of the synthesis matrix in the procedure. Then and after stirring for 5 min, aliquots of the supernatants of each working sample were taken from time to time (depending on the experiment and constituting a series referred in the same manner as the working samples), centrifuged (5 min at 3000 rpm, with an EBA 200 Hettich centrifuge) and passed through 0.45  $\mu\text{m}$  PTFE syringe filters obtaining the final samples. All experiments were carried out at least in duplicate ( $n = 2$ ). These parameters were properly optimized.

#### 3.3.4.2.2 Dispersive isolation of CB from soil samples and filter-aided recovery

- Dispersion isolation

Two orchard (A and B) and two mountain (A and B) soils were used and 2 mg of CB was mixture with 1 g of soil. Then, the dispersions were performed following the procedure above mentioned (5 min agitated + 2 hours sonicated). Supernatant was collected and injected in the AF4 system in order to study the isolation capacity and the potential interferents present in soil samples with the corresponding dilutions (1/2 for polymeric dispersions and 1/8 for biological dispersions).

As a practical application, a soil sample contaminated with a 20 % CB based-pigment paste supplied by PINTURAS ISAVAL SL was analyzed. For this aim, 1 mL of the pigment was mixed with 1 mL of the dispersive agents. Then, 25  $\mu\text{L}$  of that dispersion was added to 1 g of soil. Hereafter, CB was isolated and detected following the procedure described in the previous sections.

- Filter-aided CB recovery and re-dispersion

Once CB was isolated by using the dispersive media, 1.5 mL of each bulk dispersion ( $300 \text{ mg}\cdot\text{L}^{-1}$ ) were passed through the different filter membranes using a syringe of 2.5 mL and a Swinnex filter holder from Merck. The supernatant was collected and injected in the AF4 system diluted 1/2 for polymeric dispersion and 1/8 for biological dispersion. For SdF3-MALS analysis, samples were directly injected after the filtering step. Recoveries were calculated by comparing the AF4-DLS response of a CB standard with the response of CB filtered solution. Figure 27 shows the complete filter-aided recovery procedure.

CB isolated from soil samples was also filtered using membranes of fiberglass  $2.00 \mu\text{m}$ , nylon  $0.45 \mu\text{m}$  and teflon  $0.10 \mu\text{m}$ . The filtered solution was collected and injected in the AF4 system diluted 1/2 for polymeric dispersion and 1/8 for biological dispersion. For SdF3-MALS analysis, samples were directly injected after the filtering step.

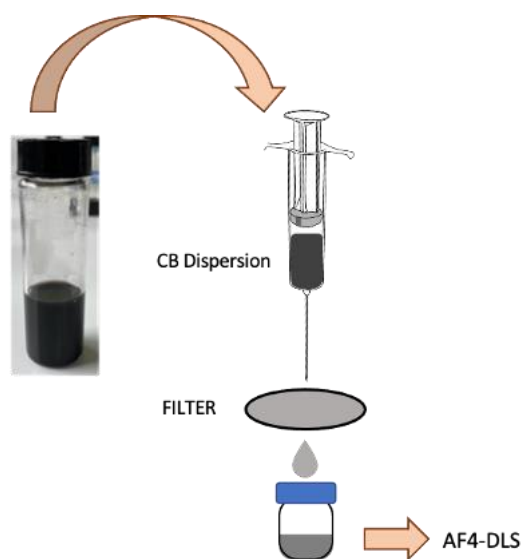


**Figure 27:** Filter-aided recovery procedure.

Re-dispersion of CB recovered in the filter was carried out using a shaking procedure for 4 hours using 1.5 mL of the corresponding dispersant. Then, an aliquot of the dispersion was injected in the AF4-DLS system.

For diffuse reflectance analysis, 400  $\mu\text{l}$  of CB or pigment paste dispersions obtained with dilution 1/8 with the biological dispersant, were recovered using 0.10  $\mu\text{m}$  teflon membrane. Then, the filter sample was measured using a Cary 60 UV-Vis spectrophotometer equipped with a diffuse reflection probe.

### **3.3.4.3 Off-line IT-SPME**

For IT-SPME procedures, the stainless-steel loop of the conventional six port injection valve was replaced by a GC capillary with specific length. In the case of off-line IT-SPME for AgNPs dispersions, a capillary column of polydimethylsiloxane (PDMS) with 35% of polydiphenylsiloxane (TRB%, Teknokroma), (24.3 cm length, 0.32 mm i.d and 3  $\mu\text{m}$  thickness; 20  $\mu\text{l}$ ) was employed. The desorption solvent consisted of a mixture of 10 mM ammonium acetate, 10 mM SDS and 1 mM sodium thiosulfate prepared in water previously filtered with nylon filters (0.45  $\mu\text{m}$ ) (mobile phase in miniaturized LC). The desorption solvent was ultrasonicated for 45 min previous to use it.

First, 20  $\mu\text{l}$  of AgNPs bulk dispersion (20 nm core) was injected in IT-SPME capillary column (20  $\mu\text{L}$ ), after 20  $\mu\text{L}$  of desorption solvent was injected and collected (see Figure 28). Then, 140  $\mu\text{L}$  of ultrapure water was added to the solution (1:8 dilution) and 20  $\mu\text{L}$  was injected in the AF4-UV-vis-DLS system, obtaining the corresponding signal named "First Extraction". The second step, consisted in injecting another 20  $\mu\text{L}$  of desorption solvent in the IT-SPME capillary column, the solution was recollected and diluted with 140  $\mu\text{L}$  of ultrapure water, then 20  $\mu\text{L}$  was injected in the AF4 system. This step was repeated 4 times, obtaining successive extractions. The results were compared with a direct injection of AgNPs (dilution 1/8) with ultrapure water directly injected in the stainless loop of the AF4 system.

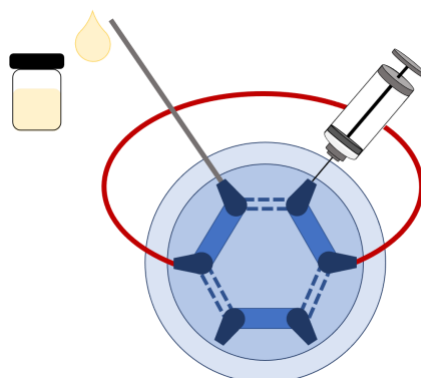


**Figure 28:** Off-line IT-SPME system

#### 3.3.4.4 On-line IT-SPME

On-line pretreatment using IT-SPME was performed by coupling the capillary extraction phase with the capillary and nano LC. Typically, the sample was passed through the IT-SPME capillary for its clean-up, extraction and preconcentration of analytes. Then, the valve was rotated to injection position and the analytes were transferred to the analytical column for their separation and detection (see Figure 29).

IT-SPME-CapLC was used for the extraction of AuNPs and AgNPs in the presence of SPN and acid compounds as target analytes. For this aim, capillary column of PDMS with 35% of polydiphenilsiloxane (20 cm length, 0.32 mm i.d and 3  $\mu\text{m}$  thickness; 16.08  $\mu\text{l}$ ) was connected to a conventional 6-port injection valve (Rheodyne, 7725 mode) and used as injection loop.

IT-SPME-NanoLC was also employed, but in this case using a synthesized capillary column of TEOS- tetramethyl orthosilicate (MTEOS)-  $\text{SiO}_2\text{NPs}$  (15 cm length and 0.075 mm i.d; 0.66  $\mu\text{l}$ ), which was synthesized by using the procedure proposed in Ref [311]. The capillary column was also connected to a conventional 6-port injection valve.

The extraction of AgNPs from soils samples was performed by using a capillary column of PDMS with 35% of polydiphenilsiloxane (70 cm length, 0.32 mm i.d and 3  $\mu\text{m}$  thickness; 56.27  $\mu\text{l}$ ).



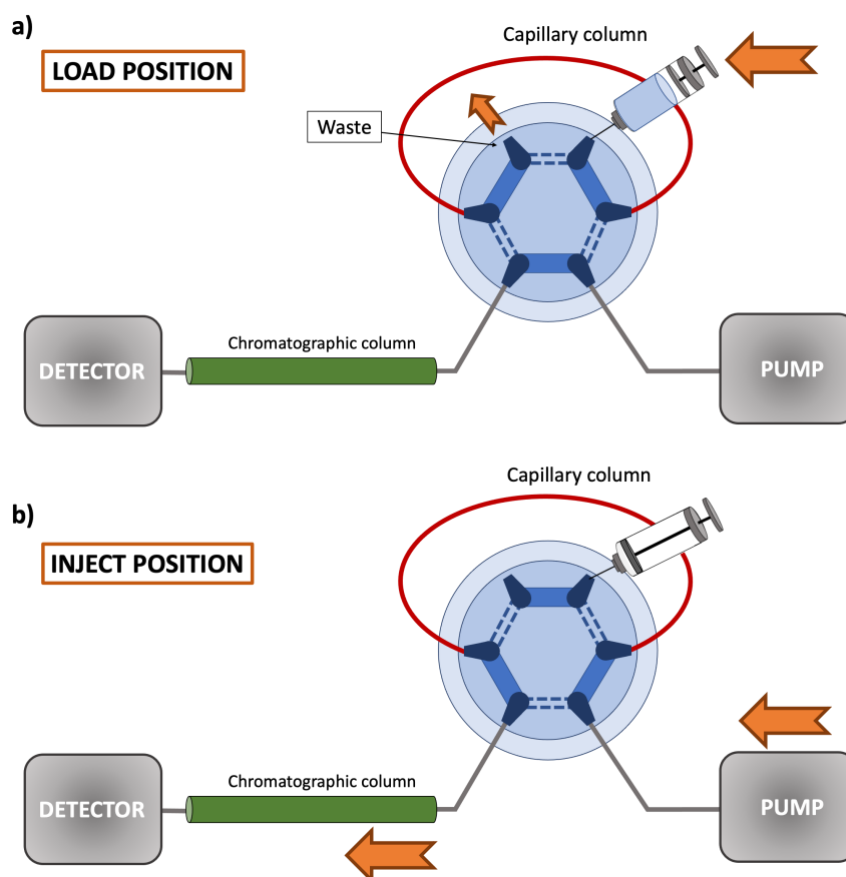


**Figure 29:** In-valve IT-SPME-miniaturized LC with six port valve a) in load position, b) in inject position.

### 3.3.5 Measurement conditions

#### 3.3.5.1 Spectroscopic conditions

SPR band of MNPs was registered using UV-vis spectroscopy. The analytical signal of bulk dispersion and their dilutions using ultrapure water and other water matrices were recorded between 300 and 800 nm. Mixture preparation was assigned to  $t = 0$  min.

For acid aggregation assays using spectrophotometric technique, MNPs dispersions were prepared mixing different volumes of naked and commercial MNPs with ultrapure water and then adding the adequate amount of HAc solutions. Naked AuNPs dispersions were prepared by mixing 300  $\mu\text{l}$  of ultrapure  $\text{H}_2\text{O}$  and 300  $\mu\text{l}$  of NPs with different volumes of acid standards. Citrate and phosphate capped AuNPs diluted at 25% (v/v) containing HAc 10% (v/v) were obtained by mixing: 250  $\mu\text{l}$  of AuNPs, 250  $\mu\text{l}$  of water, then 500  $\mu\text{l}$  of HAc 20% (v/v) was added reaching a final volume of 1 mL. Citrate capped AgNPs diluted at 50% (v/v) in HAc 0.2% (v/v) were prepared by mixing: 500  $\mu\text{l}$  of AgNPs with 300  $\mu\text{l}$  of water, then 200  $\mu\text{l}$  of HAc 1% (v/v) was added to a final volume of 1 mL. Citrate capped AgNPs and AuNPs mixtures diluted at 25% (v/v) in HAc 0.7% (v/v) were prepared by mixing: 150  $\mu\text{l}$  of AgNPs and 150  $\mu\text{l}$  of AuNPs with 220  $\mu\text{l}$  of water, then 80  $\mu\text{l}$  of HAc 1% (v/v) was added to a final volume of 600  $\mu\text{l}$  (HAc 20% and 1% (v/v) solutions were prepared taking 20 and 1 mL, respectively, of HAc glacial and making up to 100 mL with water). Spectroscopic measurements were carried out by registering the spectra between 300 and 800 nm. kinetic study was performed by measuring the spectra during 10 min in intervals of 20 s.

In the case of nitrate adsorption, spectroscopic measurements were carried out in the range 200 and 400 nm, using 220 nm as wavelength to obtain the calibration curve with a reference wavelength at 700 nm.

### 3.3.5.2 Chromatographic conditions

Studies of  $[\text{H}^+]$ -induced aggregation by IT-SPME-CapLC were performed using different additions of acid taking the adequate amount of the standard (HAc 5%, HCl 0.2% and  $\text{H}_3\text{PO}_4$  0.2%) to 300  $\mu\text{l}$  of ultrapure water and 300  $\mu\text{l}$  of AuNPs. Naked AuNPs and commercial MNPs were assayed.

In order to carry out acid aggregation assay by IT-SPME-NanoLC, commercial NPs dispersions were prepared mixing different volumes of commercial NPs with water and then adding the adequate amount of HAc solution. Citrate and phosphate capped AuNPs diluted at 25% (v/v) in HAc 10% (v/v) were obtained from 250  $\mu\text{l}$  of bulk AuNPs, 250  $\mu\text{l}$  of water and 500  $\mu\text{l}$  of HAc 20% (v/v) reaching a final volume of 1 mL. Citrate capped AgNPs diluted at 50% (v/v) in HAc 0.2% (v/v) were prepared by mixing: 500  $\mu\text{l}$  of AgNPs with 300  $\mu\text{l}$  of water, then 200  $\mu\text{l}$  of HAc 1% (v/v) was added to a final volume of 1 mL. Citrate capped AgNPs and

AuNPs mixtures diluted at 25 % (v/v) in HAc 0.7 % (v/v) were prepared by mixing: 150  $\mu\text{l}$  of AgNPs and 150  $\mu\text{l}$  of AuNPs with 280  $\mu\text{l}$  of water, then 20  $\mu\text{l}$  of HAc 20% (v/v) was added to a final volume of 600  $\mu\text{l}$ .

In both cases, a mixture of 10 mM ammonium acetate, 10 mM SDS and 1 mM sodium thiosulfate prepared in water previously filtered with nylon filters (0.45  $\mu\text{m}$ ) and sonicated for 45 min was used as mobile phase for IT-SPME-miniaturized LC. Working flow rate was 12  $\mu\text{l}\cdot\text{min}^{-1}$  for CapLC and 0.5  $\mu\text{l}\cdot\text{min}^{-1}$  for NanoLC. Then, 20  $\mu\text{l}$  or 10  $\mu\text{l}$  of standard or samples were processed into CapLC or NanoLC, respectively. DAD detector registered the spectra between 300 and 800 nm. After each session, the chromatographic system was conditioned with mobile phase (15 min), water (15 min) and EtOH (30 min).

In the case of AgNPs capture by soils using IT-SPME-CapLC, the mobile phase was the same that employed in the before assay. Flow rate used was 20  $\mu\text{l}\cdot\text{min}^{-1}$ . All solvents were filtered through 0.45  $\mu\text{m}$  nylon membranes and sonicated before use. The DAD was coupled to a data processing and acquisition system. UV-vis spectrum of AgNPs was used for identification. Chromatograms were obtained at 400 nm.

### **3.3.5.3 AF4 and SdF3 conditions**

#### *3.3.5.3.1 AF4 experimental conditions*

Table 18 summarizes the experimental conditions and programs used to determine and characterize the different analytes.

**Table 18:** AF4 experimental conditions used in several works of this Thesis. (Df: detector flow rate; If: injection flow rate; Ff: focus flow rate; Cf: cross flow rate; It: injection time; Tt: transition time)

<b>Analyte:</b> AuNPs	<b>Eluent:</b> Ultrapure water + 0.02% NaN <sub>3</sub> , pH:7	<b>DAD:</b> 530 nm
<b>General conditions:</b>		
<b>Df</b> (mL·min <sup>-1</sup> ): 0.50	<b>If</b> (mL·min <sup>-1</sup> ): 0.20	<b>Ff</b> (mL·min <sup>-1</sup> ): 1.30
<b>Cf</b> (mL·min <sup>-1</sup> ): 1.00	<b>It</b> (min): 3.0	<b>Tt</b> (min): 1.0
<b>1<sup>st</sup> elution step</b>		
○ Elution time (min): 30.0	○ Elution time (min): 10.0	
○ Elution type: linear	○ Elution type: constant	
○ Exponent: 1	○ Exponent: 0	
○ Initial cross flow (mL·min <sup>-1</sup> ): 1.00	○ Initial cross flow (mL·min <sup>-1</sup> ): 0.00	
<b>2<sup>nd</sup> elution step</b>		
<b>Analyte:</b> AgNPs		
<b>Eluent:</b> Ultrapure water + 0.02% NaN <sub>3</sub> , pH:9.2		
<b>DAD:</b> 390-410 nm		
<b>General conditions:</b>		
<b>Df</b> (mL·min <sup>-1</sup> ): 0.50	<b>If</b> (mL·min <sup>-1</sup> ): 0.20	<b>Ff</b> (mL·min <sup>-1</sup> ): 1.30
<b>Cf</b> (mL·min <sup>-1</sup> ): 1.00	<b>It</b> (min): 7.0	<b>Tt</b> (min): 0.5
<b>1<sup>st</sup> elution step</b>		
○ Elution time (min): 35.0	○ Elution time (min): 10.0	
○ Elution type: linear	○ Elution type: constant	
○ Exponent: 1	○ Exponent: 0	
○ Initial cross flow (mL·min <sup>-1</sup> ): 1.00	○ Initial cross flow (mL·min <sup>-1</sup> ): 0.00	
<b>2<sup>nd</sup> elution step</b>		

<b>Analyte: Aggregates of AgNPs</b>	<b>Eluent:</b> Ultrapure water + 0.02% NaN <sub>3</sub> , pH:9.2	<b>DAD:</b> 395 and 750 nm
<b>General conditions:</b>		
○ <b>Df</b> (mL·min <sup>-1</sup> ): 0.50	○ <b>If</b> (mL·min <sup>-1</sup> ): 0.20	○ <b>Ff</b> (mL·min <sup>-1</sup> ): 1.30
○ <b>Cf</b> (mL·min <sup>-1</sup> ): 1.00	○ <b>It</b> (min): 7.0	○ <b>Tt</b> (min): 0.5
<b>1<sup>st</sup> elution step</b>		
○ Elution time (min): 35.0	○ Elution type: linear	○ Elution time (min): 10.0
○ Exponent: 1	○ Initial cross flow (mL·min <sup>-1</sup> ): 0.20	○ Elution type: constant
		○ Exponent: 0
		○ Initial cross flow (mL·min <sup>-1</sup> ): 0.00
<b>2<sup>nd</sup> elution step</b>		
		○ Elution time (min): 10.0
		○ Elution type: constant
		○ Exponent: 0
		○ Initial cross flow (mL·min <sup>-1</sup> ): 0.00
<b>Analyte: CB</b>		
<b>Eluent:</b> Ultrapure water + 0.02% NaN <sub>3</sub> , pH:7		
<b>DAD:</b> 254 nm		
<b>General conditions:</b>		
○ <b>Df</b> (mL·min <sup>-1</sup> ): 0.50	○ <b>If</b> (mL·min <sup>-1</sup> ): 0.50	○ <b>Ff</b> (mL·min <sup>-1</sup> ): 0.50 or 1.00
○ <b>Cf</b> (mL·min <sup>-1</sup> ): 0.50	○ <b>It</b> (min): 3.0	○ <b>Tt</b> (min): 1.0
<b>1<sup>st</sup> elution step</b>		
○ Elution time (min): 30.0	○ Elution type: linear	○ Elution time (min): 10.0
○ Exponent: 1	○ Initial cross flow (mL·min <sup>-1</sup> ): 0.50 or 1.00	○ Elution type: constant
		○ Exponent: 0
		○ Initial cross flow (mL·min <sup>-1</sup> ): 0.00
<b>2<sup>nd</sup> elution step</b>		
		○ Elution time (min): 10.0
		○ Elution type: constant
		○ Exponent: 0
		○ Initial cross flow (mL·min <sup>-1</sup> ): 0.00

<b>Analyte: Silica – Program 1</b>		<b>Eluent: Ultrapure water + 0.02% NaN<sub>3</sub>, pH:7</b>		<b>DAD: 254 nm</b>	
<b>General conditions:</b>					
<b>Df</b> (mL·min <sup>-1</sup> ): 0.50	<b>If</b> (mL·min <sup>-1</sup> ): 0.50	<b>Ff</b> (mL·min <sup>-1</sup> ): 1.00	<b>Cf</b> (mL·min <sup>-1</sup> ): 1.00	<b>It</b> (min): 1.5	<b>Tt</b> (min): 1.0
<b>1<sup>st</sup> elution step</b>		<b>2<sup>nd</sup> elution step</b>		<b>3<sup>rd</sup> elution step</b>	
○ Elution time (min): 7.0	○ Elution time (min): 7.0	○ Elution time (min): 2.0	○ Elution time (min): 14.0	○ Elution time (min): 7.0	○ Elution time (min): 7.0
○ Elution type: constant	○ Elution type: linear	○ Elution type: constant	○ Elution type: constant	○ Elution type: constant	○ Elution type: constant
○ Exponent: 0	○ Exponent: 1	○ Exponent: 0	○ Exponent: 0	○ Exponent: 0	○ Exponent: 0
○ Initial cross flow (mL·min <sup>-1</sup> ): 1.00	○ Initial cross flow (mL·min <sup>-1</sup> ): 1.00	○ Initial cross flow (mL·min <sup>-1</sup> ): 1.00	○ Initial cross flow (mL·min <sup>-1</sup> ): 0.10	○ Initial cross flow (mL·min <sup>-1</sup> ): 0.00	○ Initial cross flow (mL·min <sup>-1</sup> ): 0.00
<b>Analyte: Silica – Program 2</b>		<b>Eluent: Ultrapure water + 0.02% NaN<sub>3</sub>, pH:7</b>		<b>DAD: 254 nm</b>	
<b>General conditions:</b>					
<b>Df</b> (mL·min <sup>-1</sup> ): 0.50	<b>If</b> (mL·min <sup>-1</sup> ): 0.50	<b>Ff</b> (mL·min <sup>-1</sup> ): 0.50	<b>Cf</b> (mL·min <sup>-1</sup> ): 0.50	<b>It</b> (min): 1.5	<b>Tt</b> (min): 1.0
<b>1<sup>st</sup> elution step</b>		<b>2<sup>nd</sup> elution step</b>		<b>3<sup>rd</sup> elution step</b>	
○ Elution time (min): 4.0	○ Elution time (min): 4.0	○ Elution time (min): 2.0	○ Elution time (min): 20.0	○ Elution time (min): 5.0	○ Elution time (min): 5.0
○ Elution type: power	○ Elution type: power	○ Elution type: power	○ Elution type: power	○ Elution type: constant	○ Elution type: constant
○ Exponent: 4.8	○ Exponent: 0.1	○ Exponent: 0.5	○ Exponent: 0.5	○ Exponent: 0	○ Exponent: 0
○ Initial cross flow (mL·min <sup>-1</sup> ): 0.50	○ Initial cross flow (mL·min <sup>-1</sup> ): 0.45	○ Initial cross flow (mL·min <sup>-1</sup> ): 0.05	○ Initial cross flow (mL·min <sup>-1</sup> ): 0.05	○ Initial cross flow (mL·min <sup>-1</sup> ): 0.00	○ Initial cross flow (mL·min <sup>-1</sup> ): 0.00

<b>Analyte: Silica – Program 3</b>		<b>Eluent: Ultrapure water + 0.02% NaN<sub>3</sub>, pH:7</b>		<b>DAD: 254nm</b>	
<b>General conditions:</b>					
<b>Df</b> (mL·min <sup>-1</sup> ): 0.50	<b>If</b> (mL·min <sup>-1</sup> ): 0.50	<b>Ff</b> (mL·min <sup>-1</sup> ): 0.75	<b>Cf</b> (mL·min <sup>-1</sup> ): 0.75	<b>It</b> (min): 1.5	<b>Tt</b> (min): 1.0
<b>1<sup>st</sup> elution step</b>					
○ Elution time (min): 2.0	○ Elution time (min): 2.0	○ Elution time (min): 2.0	○ Elution time (min): 2.0	○ Elution time (min): 20.0	○ Elution time (min): 5.0
○ Elution type: power	○ Elution type: power	○ Elution type: power	○ Elution type: power	○ Elution type: power	○ Elution type: constant
○ Exponent: 1.5	○ Exponent: 0.4	○ Exponent: 0.8	○ Exponent: 0.8	○ Exponent: 0.8	○ Exponent: 0
○ Initial cross flow (mL·min <sup>-1</sup> ): 0.75	○ Initial cross flow (mL·min <sup>-1</sup> ): 0.65	○ Initial cross flow (mL·min <sup>-1</sup> ): 0.25	○ Initial cross flow (mL·min <sup>-1</sup> ): 0.25	○ Initial cross flow (mL·min <sup>-1</sup> ): 0.10	○ Initial cross flow (mL·min <sup>-1</sup> ): 0.00
<b>2<sup>nd</sup> elution step</b>					
○ Elution time (min): 2.0					
○ Elution type: power					
○ Exponent: 0.4					
○ Initial cross flow (mL·min <sup>-1</sup> ): 0.65					
<b>3<sup>rd</sup> elution step</b>					
○ Elution time (min): 2.0					
○ Elution type: power					
○ Exponent: 0.8					
○ Initial cross flow (mL·min <sup>-1</sup> ): 0.25					
<b>4<sup>th</sup> elution step</b>					
○ Elution time (min): 20.0					
○ Elution type: power					
○ Exponent: 0.8					
○ Initial cross flow (mL·min <sup>-1</sup> ): 0.10					
<b>5<sup>th</sup> elution step</b>					
○ Elution time (min): 5.0					
○ Elution type: constant					
○ Exponent: 0					
○ Initial cross flow (mL·min <sup>-1</sup> ): 0.00					
<b>Analyte: Silica – Program 4</b>					
<b>Eluent: Ultrapure water + 0.02% NaN<sub>3</sub>, pH:7</b>		<b>DAD: 254 nm</b>			
<b>General conditions:</b>					
<b>Df</b> (mL·min <sup>-1</sup> ): 0.50	<b>If</b> (mL·min <sup>-1</sup> ): 0.50	<b>Ff</b> (mL·min <sup>-1</sup> ): 0.75	<b>Cf</b> (mL·min <sup>-1</sup> ): 0.75	<b>It</b> (min): 1.5	<b>Tt</b> (min): 1.0
<b>1<sup>st</sup> elution step</b>					
○ Elution time (min): 4.0	○ Elution time (min): 2.0	○ Elution time (min): 2.0	○ Elution time (min): 20.0	○ Elution time (min): 20.0	○ Elution time (min): 5.0
○ Elution type: power	○ Elution type: power	○ Elution type: power	○ Elution type: power	○ Elution type: power	○ Elution type: constant
○ Exponent: 0.7	○ Exponent: 0.3	○ Exponent: 0.5	○ Exponent: 0.5	○ Exponent: 0	○ Exponent: 0
○ Initial cross flow (mL·min <sup>-1</sup> ): 0.75	○ Initial cross flow (mL·min <sup>-1</sup> ): 0.75	○ Initial cross flow (mL·min <sup>-1</sup> ): 0.75	○ Initial cross flow (mL·min <sup>-1</sup> ): 0.10	○ Initial cross flow (mL·min <sup>-1</sup> ): 0.10	○ Initial cross flow (mL·min <sup>-1</sup> ): 0.00
<b>2<sup>nd</sup> elution step</b>					
○ Elution time (min): 4.0					
○ Elution type: power					
○ Exponent: 0.3					
○ Initial cross flow (mL·min <sup>-1</sup> ): 0.75					
<b>3<sup>rd</sup> elution step</b>					
○ Elution time (min): 2.0					
○ Elution type: power					
○ Exponent: 0.5					
○ Initial cross flow (mL·min <sup>-1</sup> ): 0.75					
<b>4<sup>th</sup> elution step</b>					
○ Elution time (min): 20.0					
○ Elution type: power					
○ Exponent: 0.5					
○ Initial cross flow (mL·min <sup>-1</sup> ): 0.10					

<b>Analyte: Silica – Program 5</b>	<b>Eluent:</b> Ultrapure water + 0.02% NaN <sub>3</sub> , pH:7	<b>DAD:</b> 254 nm
<b>General conditions:</b>		
<b>Df</b> (mL·min <sup>-1</sup> ): 0.50	<b>If</b> (mL·min <sup>-1</sup> ): 0.50	<b>Ff</b> (mL·min <sup>-1</sup> ): 0.50
<b>Cf</b> (mL·min <sup>-1</sup> ): 0.50	<b>It</b> (min): 1.5	<b>Tt</b> (min): 1.0

**1<sup>st</sup> elution step**

- Elution time (min): 15.0
- Elution type: constant
- Exponent: 0
- Initial cross flow (mL·min<sup>-1</sup>): 0.50

**2<sup>nd</sup> elution step**

- Elution time (min): 10.0
- Elution type: constant
- Exponent: 0
- Initial cross flow (mL·min<sup>-1</sup>): 0.00

<b>Analyte: Silica – Program 6</b>	<b>Eluent:</b> Ultrapure water + 0.02% NaN <sub>3</sub> , pH:7	<b>DAD:</b> 254 nm
<b>General conditions:</b>		
<b>Df</b> (mL·min <sup>-1</sup> ): 0.50	<b>If</b> (mL·min <sup>-1</sup> ): 0.50	<b>Ff</b> (mL·min <sup>-1</sup> ): 1.00
<b>Cf</b> (mL·min <sup>-1</sup> ): 1.00	<b>It</b> (min): 1.5	<b>Tt</b> (min): 1.0

**1<sup>st</sup> elution step**

- Elution time (min): 15.0
- Elution type: constant
- Exponent: 0
- Initial cross flow (mL·min<sup>-1</sup>): 1.00

**2<sup>nd</sup> elution step**

- Elution time (min): 10.0
- Elution type: constant
- Exponent: 0
- Initial cross flow (mL·min<sup>-1</sup>): 0.00



<b>Analyte: Silica – Program 7</b>	<b>Eluent:</b> Ultrapure water + 0.02% NaN <sub>3</sub> , pH:7	<b>DAD:</b> 254 nm
<b>General conditions:</b>		
<b>Df</b> (mL·min <sup>-1</sup> ): 0.50	<b>If</b> (mL·min <sup>-1</sup> ): 0.50	<b>Ff</b> (mL·min <sup>-1</sup> ): 2.00
<b>Cf</b> (mL·min <sup>-1</sup> ): 2.00	<b>It</b> (min): 1.5	<b>Tt</b> (min): 1.0
<b>1<sup>st</sup> elution step</b>		
<input type="radio"/>	Elution time (min): 15.0	<input type="radio"/>
<input type="radio"/>	Elution type: constant	<input type="radio"/>
<input type="radio"/>	Exponent: 0	<input type="radio"/>
<input type="radio"/>	Initial cross flow (mL·min <sup>-1</sup> ): 2.00	<input type="radio"/>
<b>2<sup>nd</sup> elution step</b>		
<input type="radio"/>	Elution time (min): 10.0	<input type="radio"/>
<input type="radio"/>	Elution type: constant	<input type="radio"/>
<input type="radio"/>	Exponent: 0	<input type="radio"/>
<input type="radio"/>	Initial cross flow (mL·min <sup>-1</sup> ): 0.00	<input type="radio"/>
<b>Analyte: Silica – Program 8</b>		
<b>Eluent:</b> Ultrapure water + 0.02% NaN <sub>3</sub> , pH:7	<b>DAD:</b> 254 nm	
<b>General conditions:</b>		
<b>Df</b> (mL·min <sup>-1</sup> ): 0.50	<b>If</b> (mL·min <sup>-1</sup> ): 0.50	<b>Ff</b> (mL·min <sup>-1</sup> ): 3.00
<b>Cf</b> (mL·min <sup>-1</sup> ): 3.00	<b>It</b> (min): 1.5	<b>Tt</b> (min): 1.0
<b>1<sup>st</sup> elution step</b>		
<input type="radio"/>	Elution time (min): 15.0	<input type="radio"/>
<input type="radio"/>	Elution type: constant	<input type="radio"/>
<input type="radio"/>	Exponent: 0	<input type="radio"/>
<input type="radio"/>	Initial cross flow (mL·min <sup>-1</sup> ): 3.00	<input type="radio"/>
<b>2<sup>nd</sup> elution step</b>		
<input type="radio"/>	Elution time (min): 5.0	<input type="radio"/>
<input type="radio"/>	Elution type: linear	<input type="radio"/>
<input type="radio"/>	Exponent: 1	<input type="radio"/>
<input type="radio"/>	Initial cross flow (mL·min <sup>-1</sup> ): 3.00	<input type="radio"/>
<b>3<sup>rd</sup> elution step</b>		
<input type="radio"/>	Elution time (min): 5.0	<input type="radio"/>
<input type="radio"/>	Elution type: constant	<input type="radio"/>
<input type="radio"/>	Exponent: 0	<input type="radio"/>
<input type="radio"/>	Initial cross flow (mL·min <sup>-1</sup> ): 0.00	<input type="radio"/>

<b>Analyte: Silica – Program 9</b>		<b>Eluent: Ultrapure water + 0.02% NaN<sub>3</sub>, pH:7</b>		<b>DAD: 254 nm</b>	
<b>General conditions:</b>					
<b>Df</b> (mL·min <sup>-1</sup> ):	0.50	<b>If</b> (mL·min <sup>-1</sup> ):	0.50	<b>Ff</b> (mL·min <sup>-1</sup> ):	1.50
		<b>Cf</b> (mL·min <sup>-1</sup> ):	1.50	<b>It</b> (min):	1.5
				<b>Tt</b> (min):	1.0
<b>1<sup>st</sup> elution step</b>					
<input type="radio"/>	Elution time (min):	15.0			
<input type="radio"/>	Elution type:	constant			
<input type="radio"/>	Exponent:	0			
<input type="radio"/>	Initial cross flow (mL·min <sup>-1</sup> ):	1.50			
<b>2<sup>nd</sup> elution step</b>					
<input type="radio"/>	Elution time (min):	2.0			
<input type="radio"/>	Elution type:	linear			
<input type="radio"/>	Exponent:	1			
<input type="radio"/>	Initial cross flow (mL·min <sup>-1</sup> ):	1.50			
<b>3<sup>rd</sup> elution step</b>					
<input type="radio"/>	Elution time (min):	8.0			
<input type="radio"/>	Elution type:	constant			
<input type="radio"/>	Exponent:	0			
<input type="radio"/>	Initial cross flow (mL·min <sup>-1</sup> ):	0.00			
<b>Analyte: Silica – Program 10</b>					
<b>Eluent: Ultrapure water + 0.02% NaN<sub>3</sub>, pH:7</b>		<b>DAD: 254 nm</b>			
<b>General conditions:</b>					
<b>Df</b> (mL·min <sup>-1</sup> ):	0.50	<b>If</b> (mL·min <sup>-1</sup> ):	0.50	<b>Ff</b> (mL·min <sup>-1</sup> ):	2.00
		<b>Cf</b> (mL·min <sup>-1</sup> ):	2.00	<b>It</b> (min):	1.5
				<b>Tt</b> (min):	1.0
<b>1<sup>st</sup> elution step</b>					
<input type="radio"/>	Elution time (min):	15.0			
<input type="radio"/>	Elution type:	constant			
<input type="radio"/>	Exponent:	0			
<input type="radio"/>	Initial cross flow (mL·min <sup>-1</sup> ):	2.00			
<b>2<sup>nd</sup> elution step</b>					
<input type="radio"/>	Elution time (min):	5.0			
<input type="radio"/>	Elution type:	linear			
<input type="radio"/>	Exponent:	1			
<input type="radio"/>	Initial cross flow (mL·min <sup>-1</sup> ):	2.00			
<b>3<sup>rd</sup> elution step</b>					
<input type="radio"/>	Elution time (min):	5.0			
<input type="radio"/>	Elution type:	constant			
<input type="radio"/>	Exponent:	0			
<input type="radio"/>	Initial cross flow (mL·min <sup>-1</sup> ):	0.00			

### 3.3.5.3.2 SdF3 experimental conditions

The experimental conditions for characterize the CB dispersions and their extractions from soils are shown in Table 19.

**Table 19:** SdF3 experimental conditions used for study CB dispersions and their extractions from soils.

Flow rate (mL·min <sup>-1</sup> )	Spacer (μm)	Injection Time (s)	Relaxation Time (min)
1.00	250	12	10

	Elution	Time (min)	Speed (rpm)	Type	Exponent
Program CB	Step 1	5	2250	power	0.00
	Step 2	50	2250	constant	0.17
	Step 3	20	50	power	0.00

## 3.4 SAMPLES

### 3.4.1 NMs bulk dispersions

MNPs, CB and silica bulk dispersions were used in this Thesis as samples. Stability with time and particle size studies were carried out in order to perform characterization and determination.

### 3.4.2 Water samples

In this Thesis, different water samples were used. Particularly, to study the effect of water matrices in AgNPs, ultrapure, bottled, tap, transitional and sea water were employed. In the case of monitoring CB dispersion stability tap, well and waste water were analysed.

Transitional and sea waters were collected in different areas of Valencia. Well and waste waters were obtained from Alginet.

In the case of well water, which fulfilled European Directive 98/83/EC, showed an exception in the nitrate concentration which was higher than  $50 \mu\text{g}\cdot\text{mL}^{-1}$  several times during the experimental period. For this reason, this sample was used for nitrate adsorption assays.

All samples were collected in amber glass bottles (250 mL), which were completely filled and kept at  $4^{\circ}\text{C}$  until analysis. Before analysis, the samples were filtered or centrifuged.

### ***3.4.3 Soil samples***

Six different soil samples (one compost, two mountains, two orchards and one urban soils) were used as environmental matrices. For evaluating the efficiency of CB isolation (Section 3.3.4.2.2), two mountains and two orchards soils were employed. The capacity of soils to capture AgNPs was also studied (Section 3.3.4.2.1).

These samples were collected from different points of the Valencia Community, Spain. They were stored in glass bottles at room temperature.

### ***3.4.4 Urine sample***

The urine samples used in this Thesis were from healthy volunteers, men and women aged between 22-30 years. In the case of cancer patients, the samples were from men aged between 40-70 years. All samples were treated by SPE in order to extract the spermine compound present (Section 3.3.4.1.1). This compound was determined using a plasmonic assay.

### ***3.4.5 Pigment paste sample***

Pigment paste dispersion was used as CB sample and potential pollutant present in soils. This sample was obtained from "Pinturas Isaval SL" and stored in a plastic bottle at room temperature. Extraction was performed following the procedure describe in Section 3.3.4.2.2.

# **CHAPTER 4: RESULTS AND DISCUSSION**



## 4.1 METALLIC NANOPARTICLES: AuNPs and AgNPs

In this section, AuNPs and AgNPs were studied as analytes and analytical tools to develop plasmonic assays. In the first approach, separation techniques such as AF4 and IT-SPME-miniaturized-LC have been demonstrated to be powerful tools to characterize these MNPs. The performance of the proposed separation techniques in real matrices have been studied in environmental samples.

In the second approach, plasmonic assays based on MNPs have been developed for its application in biological analysis.

### 4.1.1 Characterization of MNPs by AF4-UV-vis-DLS

AuNPs and AgNPs were characterized by AF4-UV-vis-DLS. First, a study of the mass response of the AF4 was carried out for the both types of MNPs, the same peak areas were obtained by processing 5, 10 and 20  $\mu\text{L}$  of diluted dispersions 1/2, 1/4 and 1/8 in ultrapure water, respectively; the area values were  $2.5 \pm 0.3$  ( $n = 10$ ) and  $8.0 \pm 0.2$  ( $n = 8$ ) V. for AuNPs and AgNPs, respectively. The injection volume selected for processing samples in AF4 was 20  $\mu\text{L}$ .

Aqueous dilution of commercial citrate-capped AuNPs (20, 40, 60 and 80 nm) and AgNPs (20, 40 and 60 nm) of different sizes and at different dilution ratios were studied. Figure 30 shows the fractograms obtained for AuNPs with different sizes at the same dilution ratio (1/4), injected just after its preparation. It should be noted that the retention time is directly related with the nanoparticle size, larger nanoparticles experimented a greater retention into the channel as result of their minor diffusion coefficient compared with small nanoparticles [312]. The peak at  $\approx 5$  min corresponded to the void peak.

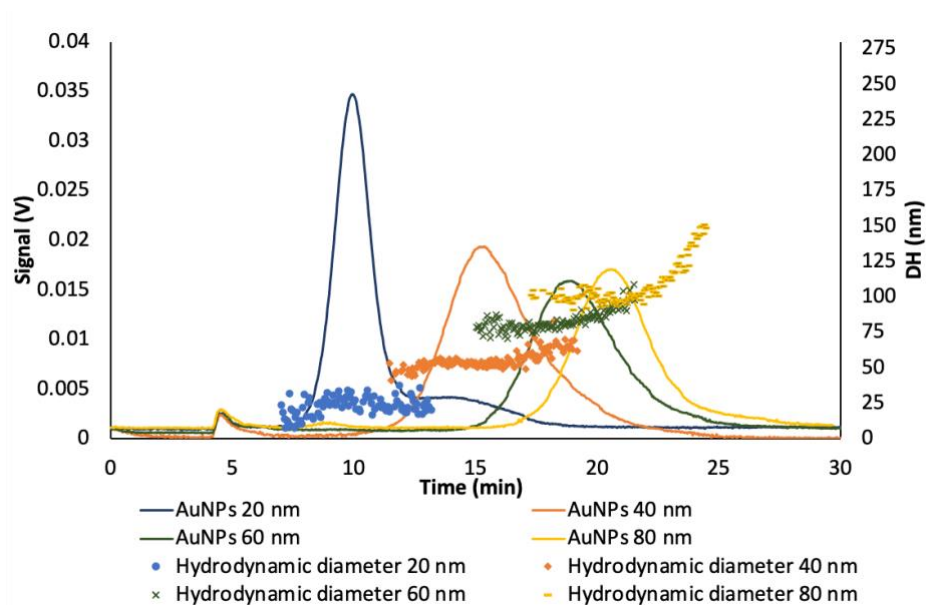


**Figure 30:** Fractograms for 20, 40, 60 and 80 nm citrate-capped AuNPs aqueous dispersions (dilution 1/4).

The correlation between the peak area and dilution ratio (between 1/2 to 1/10) for each size was studied. Table 20 depicts the relationship between the response obtained with the UV-vis detector and the dilution ratio. As it was expected, a lineal correlation was observed for all AuNPs sizes with satisfactory regression coefficients ( $R^2 = 0.999 - 0.991$ ). Moreover, the slope, and thereof the sensitivity was higher for the smaller AuNPs at the working wavelength (520 nm).



**Table 20:** Values of RSD (%) and correlation between peak area and dilution ratio for AuNPs (20, 40, 60 and 80 nm) and AgNPs (20, 40 and 60 nm). A: ordinate and B: slope of the straight lines.

	Dilution Ratio	Concentration $10^2$ (mg·mL <sup>-1</sup> )	A ± SA	B ± SB (% <sup>-1</sup> )	R <sup>2</sup>	RSD (%)
AuNPs 20 nm	1/2 to 1/10	2.66 to 0.53	0.002 ± 0.004	0.409 ± 0.015	0.9961	2.2
AuNPs 40 nm	1/2 to 1/8	2.33 to 0.58	0.002 ± 0.003	0.338 ± 0.008	0.9988	5.3
AuNPs 60 nm	1/2 to 1/8	2.15 to 0.54	0.002 ± 0.005	0.262 ± 0.014	0.9942	6.3
AuNPs 80 nm	1/2 to 1/8	2.03 to 0.51	0.000 ± 0.005	0.233 ± 0.016	0.9911	6.4
AgNPs 20 nm	1/2 to 1/8	1.00 to 0.25	0.001 ± 0.005	0.339 ± 0.019	0.9904	3.1
AgNPs 40 nm	1/2 to 1/6	1.00 to 0.33	0.001 ± 0.004	0.171 ± 0.013	0.9883	9.9
AgNPs 60 nm	1/2 to 1/6	1.00 to 0.33	0.002 ± 0.003	0.119 ± 0.009	0.9890	10.1

Precision studies were also performed, for this aim relative standard deviation (%RSD) was calculated in order to determine the stability of bulk dispersion for each NPs size. In this assay, four different AuNPs dispersions were prepared following the same procedure and immediately analyzed in the AF4 system. The results showed that RSD values were lower than 6.5%, and therefore, intraday precision was suitable in aqueous diluted dispersions.

The same study was carried out for AgNPs (20, 40, 60 nm). Figure 31 shows the fractograms of these NPs. The peak areas as a function of the particle size and RSD values for citrate-capped AgNPs were also calculated (Table 20). Precision was lower than that achieved with AuNPs since the RSD values were higher, near 10%. These values showed the lower AgNPs stability compared with AuNPs, however, the RSD values were suitable for general applications.

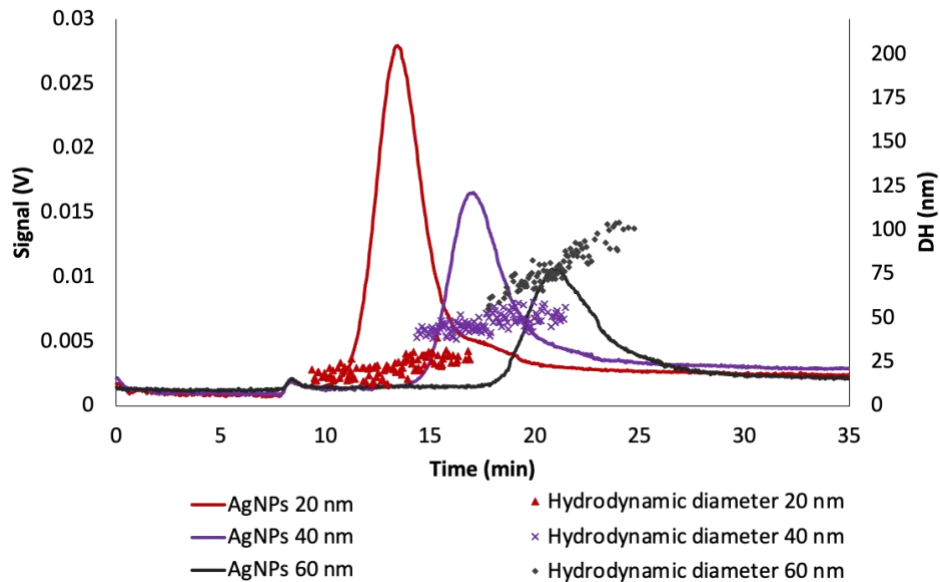


**Figure 31:** Fractograms for 20, 40 and 60 nm citrate-capped AgNPs aqueous dispersions (dilution 1/4).

AuNPs and AgNPs recoveries from the AF4 channel were also calculated. Values between 10.3 and 29.4 % for AuNPs, and between 31.6 and 65.8 % for AgNPs were found. These results were in agreement with previous reports and demonstrated that the interactions between the membrane and NPs have a high probability of undergoing irreversible interactions [313,314].

#### 4.1.1.1 Effect of time in the analytical responses of MNPs

The environment of MNPs is a key parameter for their practical application, since their performance will depend on their stability. In a wide variety of applications, dilution of these NPs is needed; however, dilution induces changes, mainly on the surface interactions, that may affect the performance of this NPs. These changes depend on the kinetic of individual NPs subject to local variations and thereof, the time is an important parameter. To prove this, citrate-capped AuNPs diluted dispersions (1/4) of different sizes were measured at different times after their dilution. Figure 32 shows the fractograms obtained at different times after dispersion preparation ( $t = 0, 24, 48$  and  $72$  h). As can be seen in Figure 32.a –

d and Figure 33.a, there was a decrease in the absorbance signal with time, and that decrease, depended on the particle size.

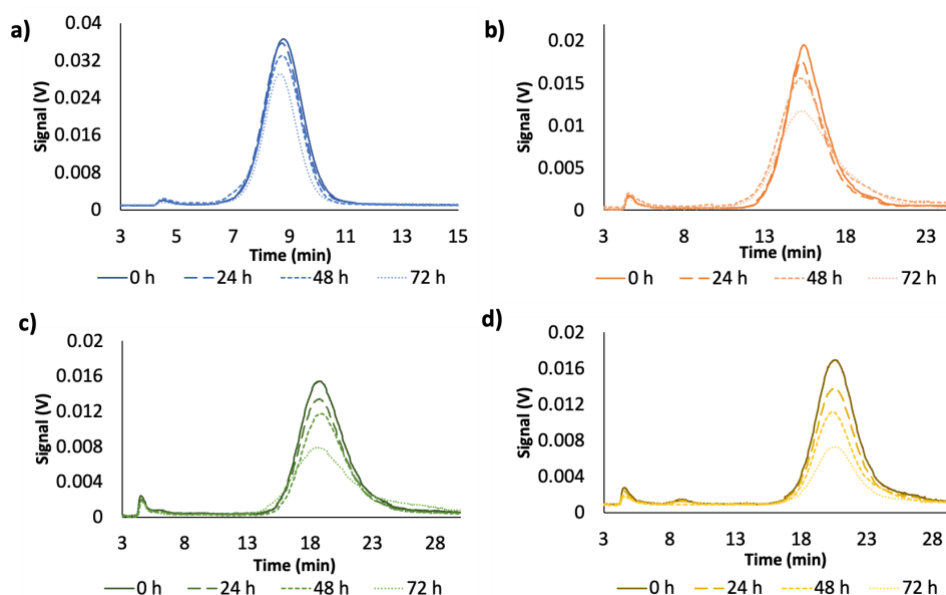


**Figure 32:** Fractograms of the evolution of nanoparticles dispersions over dilution preparation time for different NPs sizes a) AuNPs 20 nm, b) AuNPs 40 nm, c) AuNPs 60 nm, d) AuNPs 80 nm.

The DH of the different AuNPs was measured as a function of time with the DLS detector coupled on-line with the UV-vis detector. Figure 33.b shows the results obtained for the different sized NPs. As can be seen, the DH was constant over the dilution, in addition it was constant with the time and this effect was observed for all NPs sizes.

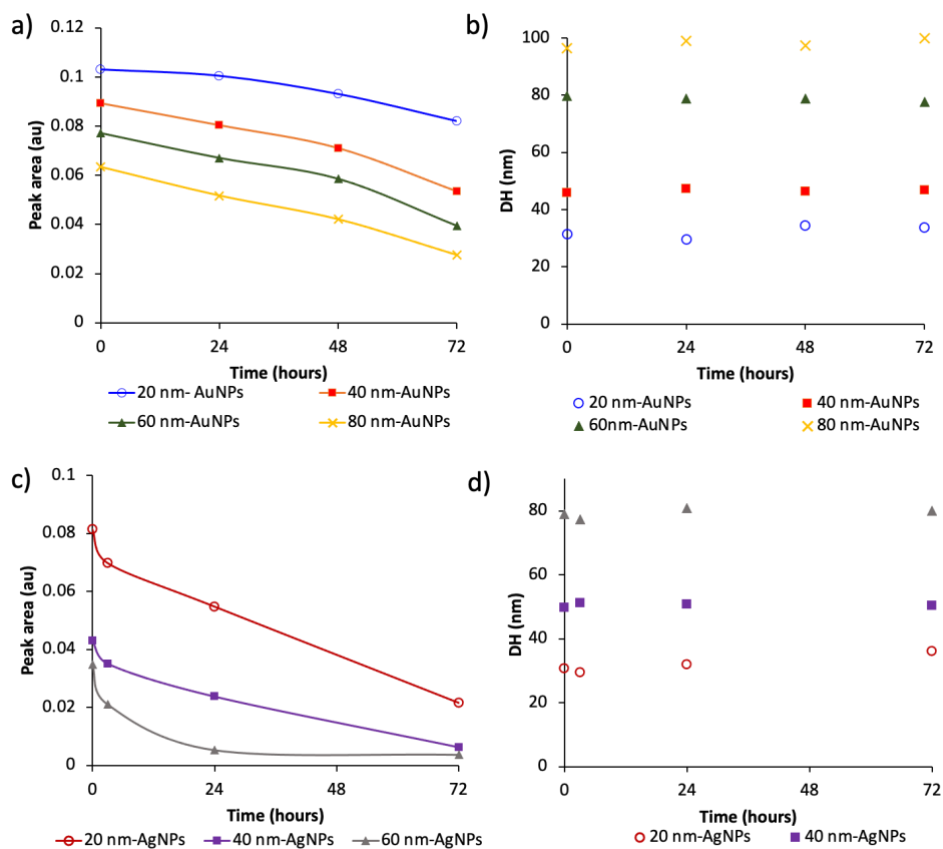


**Figure 33:** a) Variation of the peak area as a function of time for citrate-capped AuNPs. b) Variation of the DH as a function of time for citrate-capped AuNPs. c) Variation of the peak area as a function of time for citrate-capped AuNPs. d) Variation of the DH as a function of time for citrate-capped AuNPs.

The same study was carried out for citrate-capped AgNPs in order to check whether the nature of NPs had some influence on the previous results. Figure 34.a - c represents the signal variation for dispersions with different sizes (20, 40 and 60 nm). As in the case of citrate-capped AuNPs, there was a decrease on the signal with time, and that decrease was a function of the particle size. Indeed, the analytical response for 60 nm AgNPs at 24 h was negligible.

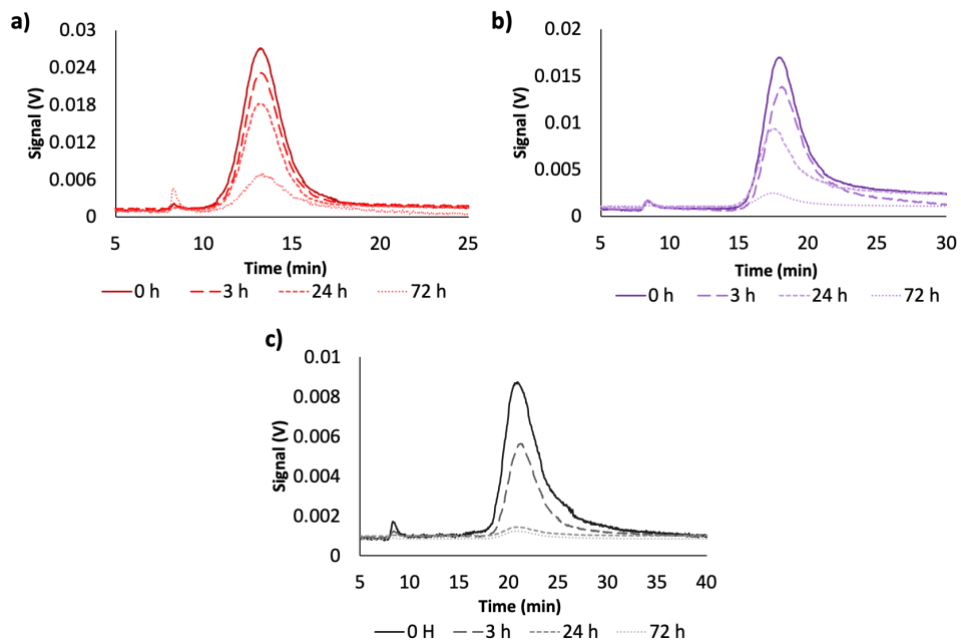


**Figure 34:** Fractograms of the evolution of nanoparticles dispersions as function of dilution preparation time for different sizes a) AgNPs 20 nm, b) AgNPs 40 nm, c) AgNPs 60 nm.

However, compared with AuNPs, the increment of that decrease was higher for AgNPs (see Figure 33.c), that was consistent with the higher stability of AuNPs than that given by AgNPs [315,316]. Figure 33.b and d show the variation of the DH for both NPs being constant with time for both of them. A diluted aqueous dispersion of AuNPs in PBS (dilution 1/8) was measured as a function of time. As can be noted in Figure 35, it was observed the same effect that in previous assays for citrate-capped NPs.

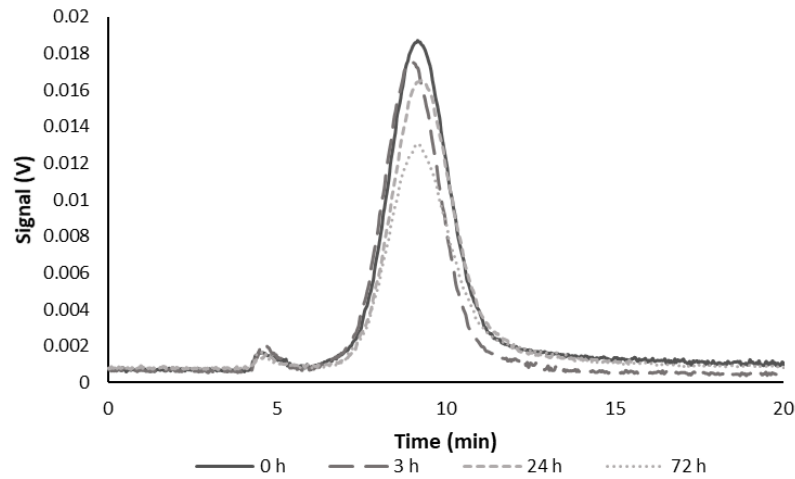


**Figure 35:** Study of AuNPs-PBS dispersions as function of dilution preparation time.

Figure 36 shows the evolution of signal as function of dilution preparation time for mixtures of different sizes of AuNPs with dilution (1/8) and AgNPs with dilution (1/4). As it was expected, fractograms of citrate-capped AuNPs mixture (20, 40 and 80 nm) were resolved, and three peaks were obtained corresponding to 20, 40 and 80 nm AuNPs. As above mentioned, 24 h after the dilution preparation, the UV-vis signal changed as a function of the particle size, in accordance with the results obtained for individual NPs; NPs with higher diameter experienced a decrease on the peak area higher than that provided by smaller NPs. This effect was more drastic after 48 h as it can be seen in Figure 36.a.

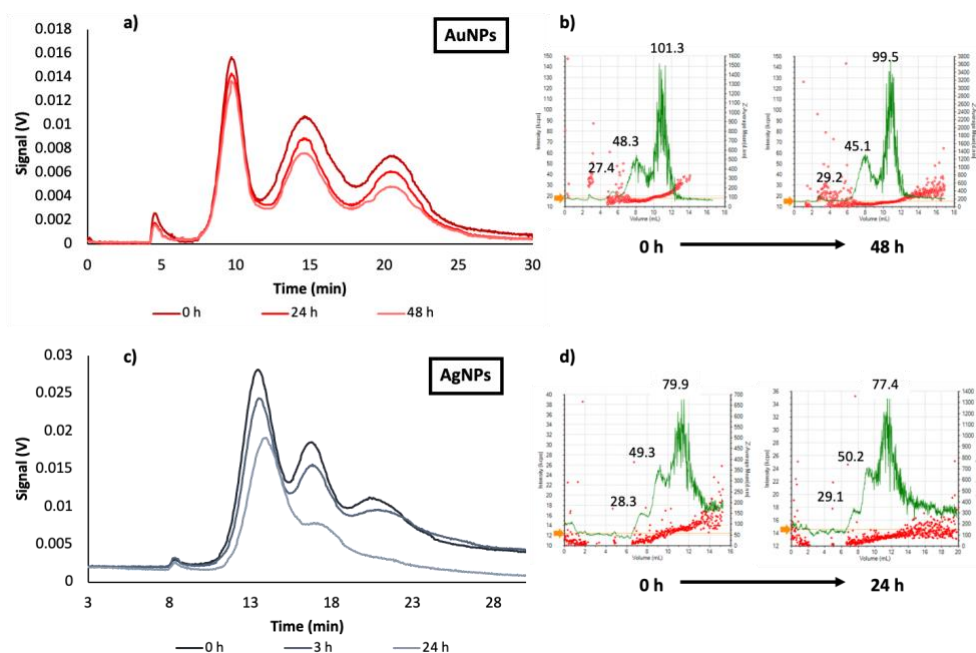


**Figure 36:** Mixtures of different sizes of AuNPs (dilution 1/8) and AgNPs (dilution 1/4). a) Fractograms of the evolution of 20, 40 and 80 nm AuNPs mixture; b) DLS values of AuNPs sizes, DLS spectra in green and DH distribution in red; c) fractograms of the evolution of 20, 40 and 60 nm AgNPs evolution mixture; d) DLS values of AgNPs sizes, DLS spectra in green and DH distribution in red.

In the case of the AgNPs mixture (20, 40, and 60 nm) a similar behaviour was observed (Figure 36.c). However, the lower stability of AgNPs due to interactions with medium, produced a more pronounced signal reduction, since dissolution in this case was more favored than for AuNPs. Indeed, the peak for 60 nm citrate-AgNPs was not detected after 24 h. The average DH of dispersed NPs were stable during the whole analysis (see Figure 36.b and d), as previously stated for individual particles. These results could support the hypothesis that dissolution is the mechanism by which the stability of dispersed NPs in diluted dispersions varied as a function of time.

Figure 37 summarizes the changes for 60 nm AuNPs as an example. As can be seen, there is a decrease on the signal, and after 72 h, the dilution ratio varied from 1/4 to 1/7, in the case of this NPs (Figure 37.a), but its size was constant

(Figure 37.c). TEM analysis showed that the NPs core size did not vary (Figure 37.b). Similar considerations can be done for the other NPs analyzed.

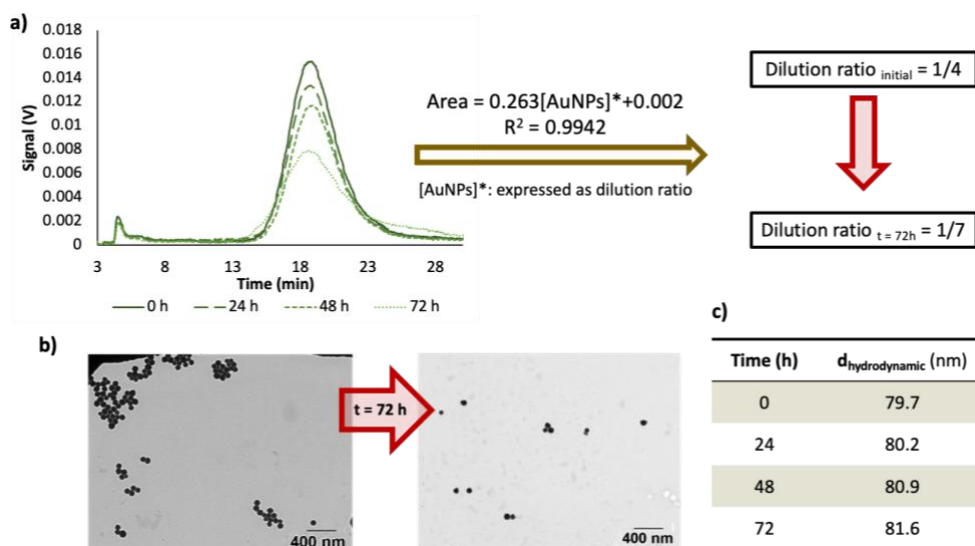


**Figure 37:** a) Effect in the dilution ratio for AuNPs 60 nm with time. b) TEM micrographs for diluted dispersions of citrate-capped AuNPs (60 nm) just after their preparation and after 72 h. c) DH of AuNPs at different dilution times (0, 24, 48 and 72 h).

A TMB assay [317] was applied in order to corroborate the instability by dissolution of the dispersions. In this assay, Au and Ag ions can be detected in NPs dispersions, since the cationic species reacts with TMB to form a blue colour compound ( $\lambda_{\text{max}} = 650 \text{ nm}$ ). To carry out it, 1.2 mL of AuNPs or AgNPs dilution dispersion was mixed with 100  $\mu\text{L}$  of TMB 10 mM in EtOH and 200  $\mu\text{L}$  of NaAc/HAc buffer 1 M, pH = 4. After 15 min, the mixture changed a blue colour complex that indicated the presence of these ions. Figure 38.a and b show the spectra obtained for just prepared diluted dispersion of AuNPs and AgNPs before and after the reaction with TMB, respectively. These spectra were compared with the spectra obtained for  $\text{Au}^{3+}$  and  $\text{Ag}^+$  standard after TMB derivatization as control experiments and blank solution of the TMB assay. As can be seen, cationic species were not detected for recently diluted dispersions, since there was not band at 650 nm, and only their plasmon bands were observed. Several diluted dispersions of NPs were prepared from the batch NPs, and processed by the TMB assay after different preparation times (see Figure 38.a and b). The absorbance at 650 nm increased



with the dispersion dilution time, which is correlated with the presence of  $\text{Au}^{3+}$  and  $\text{Ag}^+$ , indicative of dissolution of NPs.

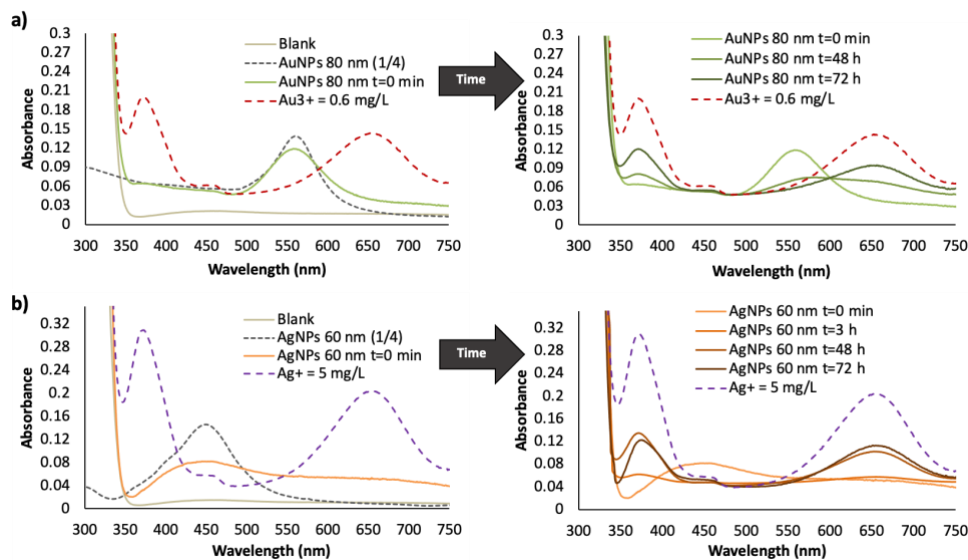


**Figure 38:** AuNPs and AgNPs dissolution TMB assay for several times of preparation of diluted dispersions from batch NPs: a) AuNPs for 0, 48 and 72 h; and b) 0, 3, 48 and 72 h. For more explanation see text.

Figure 38.b shows the spectra for AgNPs. It can be seen that the dissolution of this type of NPs is bigger than that achieved by AuNPs (see Figure 38.a). This assay supported also dissolution as the reason of the loss of NPs with time for diluted dispersions.

From these results, changes of AuNPs and AgNPs with time must be taken into account since the dispersed fraction of NPs available in diluted dispersions varies with time, therefore practical application of NPs in general must consider this effect in order to obtain reliable results. Besides, the main analytical parameters in particular, can be wrong if diluted dispersions are not deeply understood. If the fraction of NPs in diluted dispersions changes, for example limit of detection (LOD) will vary as a function of time, and this must be taken into account in order to characterize an analytical method. To demonstrate this, Table 21 shows the variation in the detection limits calculated for the diluted dispersions used after 72 h of its preparation, and these values were compared with the LOD

calculated for diluted dispersions just prepared from the batch material. LOD was calculated by establishing the dilution ratio of a dispersion providing a signal corresponding to three times the instrumental noise from the equation signal vs. dilution ratio for each size, and taking into account the initial concentration.

**Table 21:** Detection limits calculated for each diluted dispersion of citrate-capped AuNPs and AgNPs.

		Co (mg·mL <sup>-1</sup> )	LOD (µg·mL <sup>-1</sup> )	LOD (µg·mL <sup>-1</sup> )
			t = 0 min	t = 72
AuNPs	20 nm	0.053	0.22	0.26
AuNPs	40 nm	0.047	0.12	0.17
AuNPs	60 nm	0.043	0.14	0.21
AuNPs	80 nm	0.041	0.06	0.09
AgNPs	20 nm	0.020	0.10	0.18
AgNPs	40 nm	0.020	0.23	0.43
AgNPs	60 nm	0.020	0.47	0.89

#### 4.1.1.2 Effect of environmental water matrices in the stability of citrate-capped AgNPs

##### 4.1.1.2.1 Characterization of selected citrate-capped AgNPs bulk batches used

Four different batches of commercial AgNPs with the same nominal concentration given by the supplier and different caducity data (March and October 2020; named M and O, respectively) were studied. The spectra obtained for diluted dispersion with ultrapure water before 2 h of preparation were the same for each batch assayed. Figure 39 includes the fractograms and UV-vis spectra corresponding to fresh dispersions diluted 1/4 with ultrapure water. Fractograms recorded using UV-vis detector (Figure 39.a) show a clear difference in batch M1 in reference to the others, in which a displacement of the maximum peak is observed up to 16 min, which is consistent with the presence of larger NPs, as well as a decrease in the signal at  $\lambda = 395$  nm, which can respond to an SPB sift to higher wavelengths than those corresponding to the other dispersions as Table 2 shows, but also due to lower mass of AgNPs. The peak areas were 27.9, 25.9, 23.3 and 22.9 vs for batches O2, O1, M2 and M1, respectively.

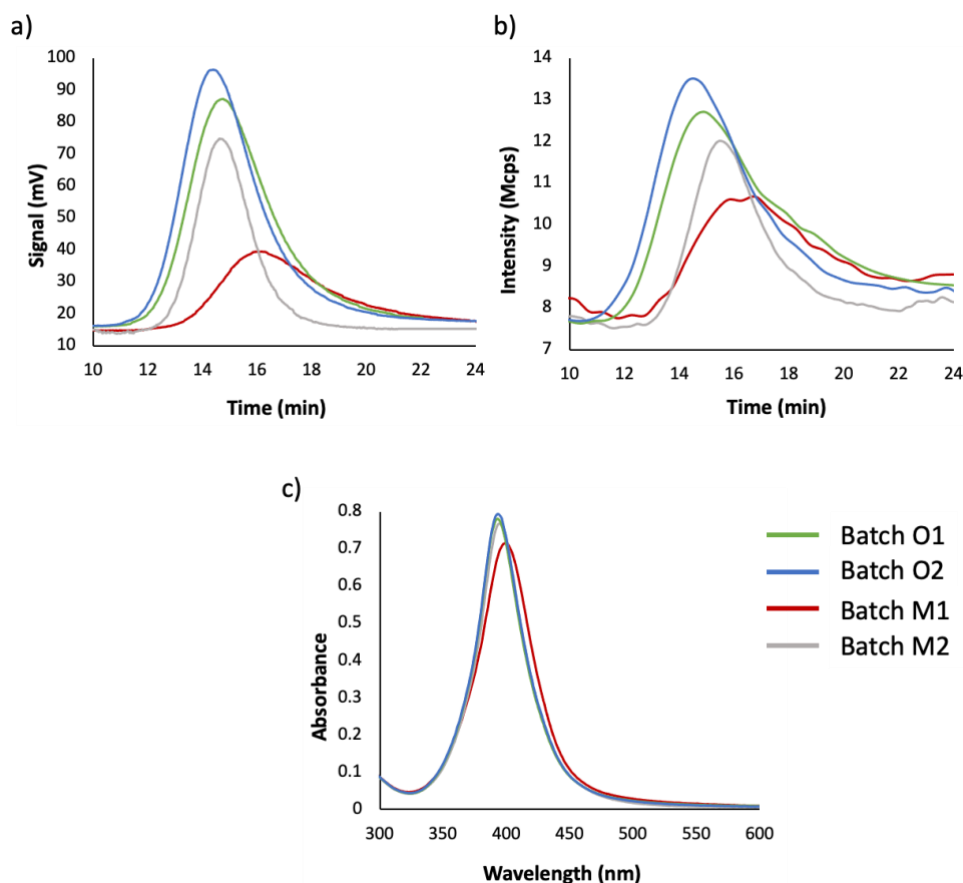


**Figure 39:** Fractograms obtained with a) UV-vis, b) DLS detectors, and c) UV-vis spectra of dispersions diluted 1/4 with ultrapure water ( $5 \text{ mg}\cdot\text{L}^{-1}$ ) of various commercial batches of AgNPs.

The fractograms recorded using the DLS detector indicate less monodispersity for batch M1 with respect to the rest (see Figure 39.b). In addition, batch mode DLS data show a mean DH around 2 nm larger than the others, as shown in Table 22. All batches have a similar SPB by means of UV-vis spectroscopy, although batch M1 shows some differences, since it provides a somewhat lower absorption and a slight bathochromic shift, which can be due to AgNPs with a slightly larger size (Figure 39.c).

**Table 22:** Wavelength values ( $\lambda$ ) of SPB, width of the peak at half the maximum, extinction coefficient ( $\epsilon_{\text{max}}$ ) obtained by UV-vis spectroscopy and DH for different commercial batches of AgNPs.

Batch	$\lambda$ SPB (nm)	Width SPB <sub>1/2</sub> (nm)	$\epsilon_{\text{max}}$ (mM <sup>-1</sup> ·cm <sup>-1</sup> )	DH (nm)
M1	398 ± 2	50.2 ± 0.1	15.43 ± 0.02	22 ± 2
M2	396 ± 1	42.9 ± 0.1	16.58 ± 0.02	22 ± 3
O1	393 ± 2	42.7 ± 0.2	16.83 ± 0.05	21 ± 3
O2	393 ± 2	42.8 ± 0.2	17.05 ± 0.03	20 ± 3

Phenomena such as dissolution and/or passivation can be considered as a consequence of prolonged exposure to atmospheric conditions of the batch dispersion M1 [318,319]. So that a part of AgNPs of the dispersion can be dissolved and released into the environment as Ag<sup>+</sup>, or it can be oxidized, generating an Ag<sub>2</sub>O surface film, which was indicated in other studies by means of a bathochromic shift of the plasmonic band, as well as a broadening and a lower height (see Table 22 and Figure 39.c). If AF4 records are compared with those obtained by UV-vis spectroscopy, it should be noted that AF4 technique showed more differences besides giving their size. From the characterization results of the several batches, we selected O1 and O2 for studying the performance of the bulk NPs by diluting with several environmental water samples.

#### 4.1.1.2.2 Behavior of the dispersions in function of environmental water used as diluent

The behaviour of AgNPs in matrices such as ultrapure, bottled, tap, transitional and sea waters were studied. Table 23 indicates pH, electrical conductivity and redox potential values of the several water matrices, showing significant variations in the measured parameters as expected. Besides the Z-potentials measured by off-line DLS of 1/4 diluted dispersions of citrate capped AgNPs in the water matrices after 1 min of their mixtures are given. Similar Z-potential values were obtained for both batches, M and O. The most negative Z-potentials were achieved by dilution with ultrapure water (the most stable dispersions) and the least one with sea water. Drinking waters presented values between - 14.06 and - 17.67 mV. Transitional and sea waters gave the lesser values.

**Table 23:** pH, electrical conductivity (EC) and redox potential for each aqueous matrices used. Z-potentials for M and O batches of AgNPs diluted 1/4 with several water matrices.

Water Matrix	Abbrviat.	pH	CE ( $\mu\text{S}\cdot\text{cm}^{-1}$ )	Potential (mV)	Z-potential of AgNPs: M/O (mV)
Ultrapure water	UPW	$6.0 \pm 0.2$	$6.2 \pm 0.1$	$250 \pm 10$	-41.27/ -42.97
Bottled water	BW2	$7.37 \pm 0.15$	$272 \pm 4$	$190 \pm 30$	-15.87/ -17.67
Bottled water	BW1	$7.52 \pm 0.04$	$570 \pm 30$	$300 \pm 60$	-14.06/ -14.83
Tap water	TW	$7.39 \pm 0.18$	$10903 \pm 40$	$630 \pm 30$	-14.36/ - 14.76
Transitional water	TrW	$7.67 \pm 0.17$	$(13.4 \pm 0.2) \times 10^3$	$220 \pm 60$	-8.86/ -10.41
Sea water	SW	$7.99 \pm 0.07$	$(58 \pm 3) \times 10^3$	$150 \pm 30$	-5.42/ -5.92

Figure 40.a and b compare the spectra measured up to 15 min of two diluted dispersions (O1 and O2) with bottled water (BW2) and the fingerprint was different to that obtained with ultrapure water, for this last matrix stability at the assayed times was observed. Note that the Z-potential for ultrapure water-diluted dispersions is more negative than the value achieved with BW2 as Table 23 shows. The obtained registers are compatible with the aggregation of AgNPs in BW2. Fractograms obtained by using the DLS detector given in Figure 40.c and d for these dispersions show an increase in the size with respect to that obtained with ultrapure water injected in the AF4 at 1 min of their mixture. For longer times (up to 75 min) the sizes increased markedly as Figure 40.c and d indicated for both dispersions, although the evolution fingerprints were different between both dispersions.

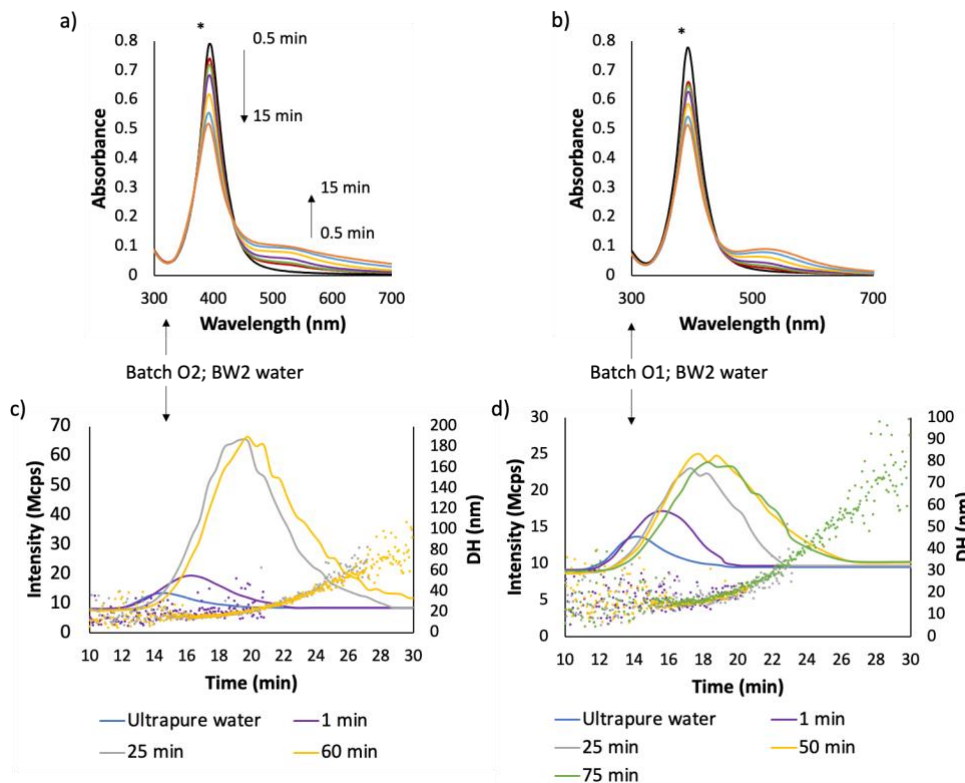


**Figure 40:** Spectra of batches a) O2 and b) O1 diluted  $\frac{1}{4}$  with bottled mineral water measured at several times (0.5, 1, 2, 5, 10, 15 min, the SPR band for the dilution with ultrapure water was also include, marked with \*) and their fractograms (solid lines) c) and d), respectively, by using dynamic light scattering (DLS) and DH (points) measured at different times.

Decreasing of the SPR band can be attributed to a concentration decrease of the initial AgNPs as a consequence of changes in their electrostatic environment, which lead to processes like aggregation causing structural, morphological and surface alterations. In this sense, as can be seen in Figure 41, a higher degradation rate is observed when BW1 and TW waters were employed for diluting batches O instead of BW2 water (see Figure 40). The profiles obtained were similar for the batches with the same caducity data. Those waters presented higher conductivity than BW2 as can be seen in Table 23, and then, higher ionic strength. The aggregation was more severe for O1 and O2 batches than that obtained for M1 and M2 batches in BW1 and TW waters, although their Z-potentials were somewhat

greater in absolute values for O than for M batches (Figure 41 and Figure 42). The electrostatic interactions between a charged NP and an electrolytic solvent fall within one of three regimes as proposed in [73] for citrate capped AuNPs, according to the net charge of the sphere: (i) depolarized ( $\sigma =$  surface charge density  $< \sim 0.6 \text{ e nm}^{-2}$ ), where the thermal motion of the sodium counterions overcomes the electrostatic attraction toward the NP; (ii) mildly polarized ( $\sim 0.6 < \sigma < \sim 4.1 \text{ e nm}^{-2}$ ), in which the Coulomb forces attract enough ions into the Stern layer to screen out the charge load of the NP, and (iii) hyperpolarized ( $\sigma > \sim 4.1 \text{ e nm}^{-2}$ ), the situation at which the counterions' steric and electrostatic hindrance, as well as their loss of translational degrees of freedom, limit their binding onto the NP. The chemisorption of citrate onto the assembled metallic surfaces critically depends on variables such as the particle size, the surface charge density, and the ionic strength of the medium in which the NPs are dispersed [73].

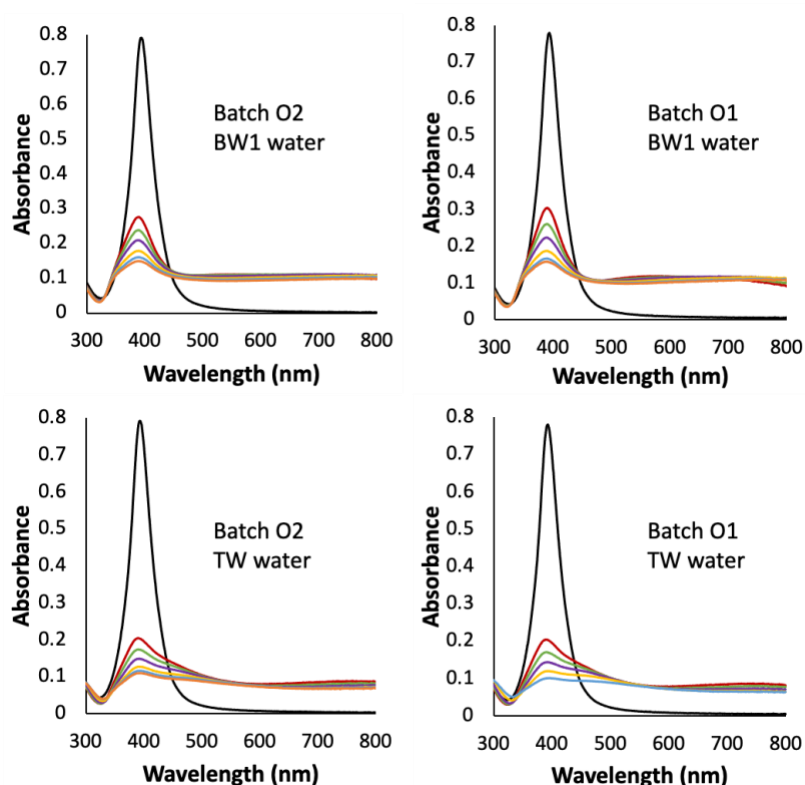


**Figure 41:** Spectra of AgNPs batches O1 and O2 diluted 1/4 with bottled mineral water 1 and tap water measured at several times (0.5, 1, 2, 5, 10, 15 min). The SPR band for the dilution with ultrapure water was also included.

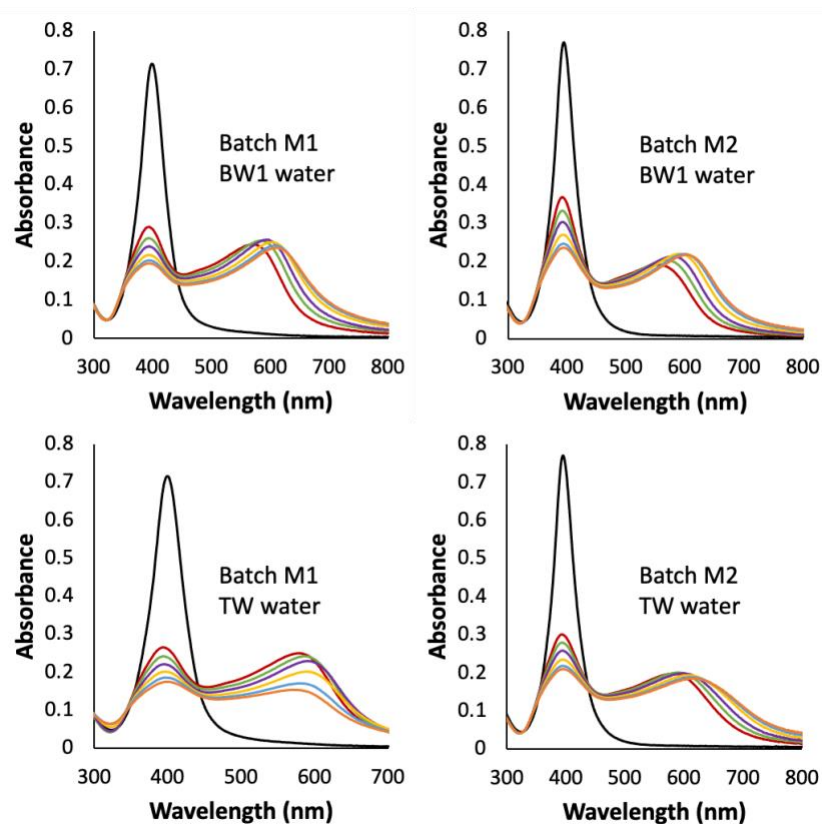


**Figure 42:** Spectra of AgNPs batches M1 and M2 diluted 1/4 with bottled mineral water 1 and tap water measured at several times (0.5, 1, 2, 5, 10, 15 min). The SPR band for the dilution with ultrapure water was also included.

Figure 43 shows the fractograms obtained by using UV-vis and DLS detectors in series for suspensions of studied batches diluted with BW2, BW1 and TW water matrices. Profiles for O1 and O2 batches and BW2 were in accordance with those obtained by DLS detection given in Figure 40.c and d for this matrix, more likely due to changes of AgNPs size because of aggregation, a bathochromic shift can generate an absorbance decrease at the observed wavelength (395 nm). An increase in retention times and a peak broadening were also observed indicating the formation of larger AgNPs. AF4 also shows that the kinetics of the process was bigger for batch O2; batch O1 for 1 min gave a similar signal to UPW dilution. Those results were in accordance with spectra obtained at 1 min (see Figure 40.a and b). Fractograms for higher times for batch O1, show polydispersity too, but in less extension than that provided by batch O2.



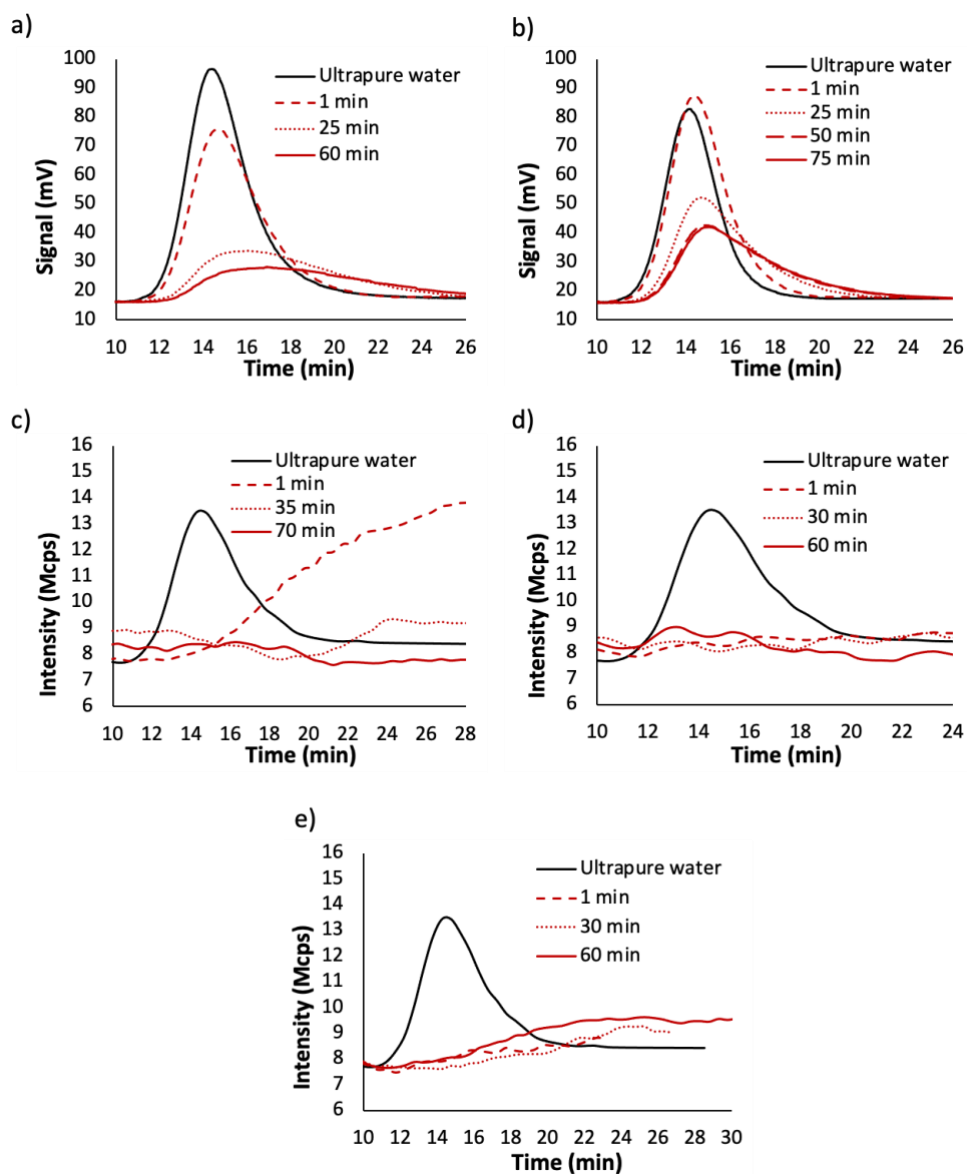


**Figure 43:** Fractograms ( $\lambda = 395$  nm) obtained for suspensions diluted 1/4 of batches a) O2 and b) O1 with BW2 water at different times and batch O2 with water c) bottled water (BW1), d) tap water (TW), and e) sea water (SW) at different time using the DLS detector.

Batch O2 diluted in BW1 water, with a higher electrolyte content than BW2, measured after 1 min of preparation by using DLS detector showed a distribution of NPs in a wide range of sizes; besides no significant UV-vis signal was obtained

at 395 nm, probably due to aggregation of almost all of the initial AgNPs (see Figure 43.c). These results were in accordance with those shown in Figure 41, obtained by UV-vis spectroscopy. Suspensions with a high fraction of aggregated AgNPs give rise to fractograms in which the UV-vis signal is very weak, being indistinguishable from the baseline working at a cross-flow of  $1 \text{ mL}\cdot\text{min}^{-1}$ .

Suspensions prepared with waters with higher ionic strength (BW1 and TW) show no significant signal with respect to baseline for both detectors at assayed times, as can be seen in Figure 43.c and d for the DLS detector. The loss of signal can be related to the aggregation of AgNPs with higher sizes than those presented by BW2. All of this seems to show a trend of size transformation of AgNPs with the ionic strength of the medium. NP aggregation can be induced by increasing the salt concentration of the medium, in [73] it is found that alterations in the aggregation state of the NPs arise mostly from the screening of the NP charge by the sodium counterions in solution. These ions can rest at the interface of the metallic bodies and form salt bridges that stabilize NP–NP dimer.

Figure 44 includes the DH estimated by the DLS detector along the fractograms using AF4-UV-Vis-DLS for BW1 and BW2 dilutions. It can be observed that for batch O2, the use of bottled water of lower hardness (BW2, 13 and 28  $\text{mg}\cdot\text{L}^{-1}$  of Mg and Ca, respectively) for dilution, Figure 44.a, provided less variation in NP sizes than in the case of harder bottled water (BW1, 35 and 55  $\text{mg}\cdot\text{L}^{-1}$  of Mg and Ca, respectively), Figure 44.c, a trend that has also been observed in various studies using other analytical techniques [93,320,321]. Batch O1, Figure 44.b, provided less variation of sizes than batch O2 when BW2 water was used.

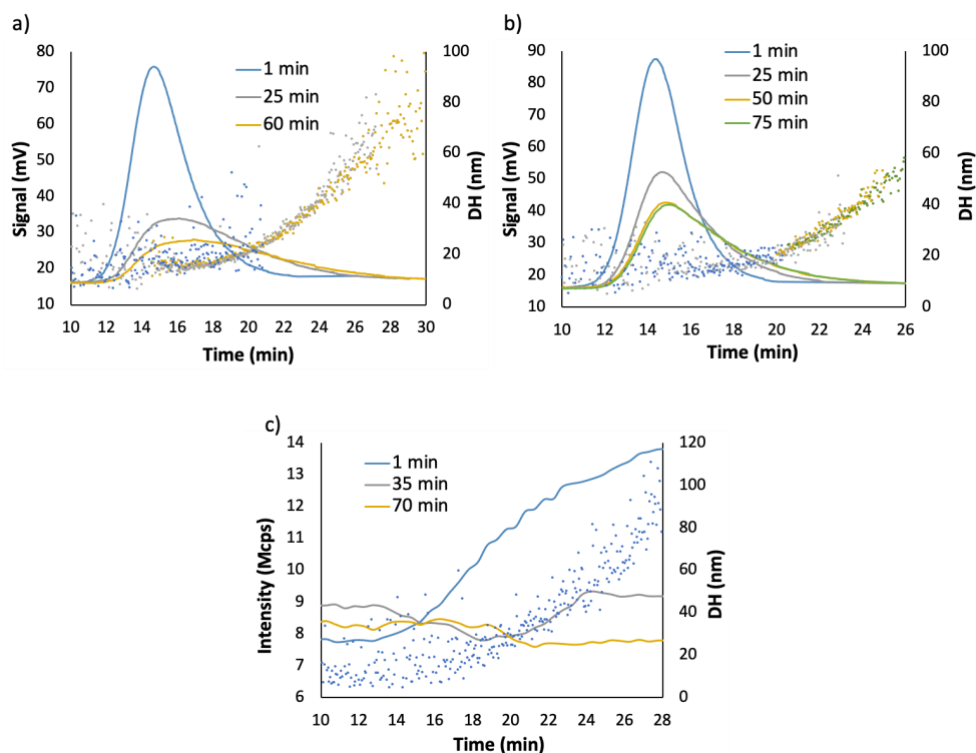


**Figure 44:** Fractograms (solid line) and DH (points) obtained for suspension of batches a) O2 and b) O1 diluted 1/4 with BW2 water at different times using UV-vis detector. (c) Fractograms and DH for suspension of batch O2 diluted 1/4 with BW1 water at different times using the DLS signal.

AF4-UV-vis-DLS aids to understand the magnitude and nature of changes that aqueous dispersant composition can produce in colloidal systems. All these phenomena are characteristic of DLVO-type behaviour [93,319,321]. According to this theory, there is a minimum concentration of each of the saline species from which there is a regime of rapid aggregation or diffusion-controlled aggregation, which is called critical coagulation concentration (CCC) [322,323].

In this sense, the electrolytic substances present in the bulk of AgNPs aqueous dispersions produce a shielding of the charge that covers them, reducing their protection against aggregation processes. If the concentration of these species is below the CCC, aggregation takes place through slow kinetics, a situation known as reaction-limited aggregation regime, in which NPs are partially kinetically

stabilized by the repulsion of the electrical double layer, as seems to be observed in suspensions prepared with BW2 water. Conversely, if electrolyte concentration is higher than the CCC, aggregation occurs more quickly as for BW1 and TW (43 and 115 mg·L<sup>-1</sup> of Mg and Ca, respectively), a situation known as diffusion-controlled aggregation regime, in which the charge that covers the NPs is sufficiently shielded and the energy barrier is insufficient to prevent the aggregation process [93,319,321].

Since the mechanism through which electrolytes facilitate aggregation consists in the shielding of the charge that covers the NPs, some factors such as ion charge are directly related to their shielding capacity, and consequently, induce the aggregation process. In this sense, there is an inverse dependence of the CCC with the sixth power of the ion charge [93] giving rise to a greater influence of divalent ions compared to monovalent ions between 50–83 times [321] in the aggregation process. Their stability depends to a great extent on the stabilizing agent that is part of their coating. In this sense, the characteristics and behaviors observed are attributable to the electrostatic stabilization mechanism, since AgNPs stabilized by steric effect by coating such as PVP, PEG, or branched polyethyleneimine (BPEI) do not show DLVO-type behaviour and are stable in suspensions in the presence of electrolytes with various units of molar concentration [93,320]. Therefore, in drinking water, the aggregation process should be modulated mainly by concentration of Ca<sup>2+</sup> and Mg<sup>2+</sup>, and definitely, by water hardness. On the other hand, in transitional and sea waters (see Figure 45), given the highest concentration of dissolved ionic substances, the stability of AgNPs should be strongly restricted. However, Figure 45 shows that the aggregation kinetics was faster for TrW than for SW (see also Figure 43.e). Moreover, for batches O the rate order corresponded to BW2, SW, TrW, BW1 and TW, being BW2 the lowest and TW the highest. The same order was established for batch M, but with slower kinetics. AF4 results supported the data obtained by spectroscopy.

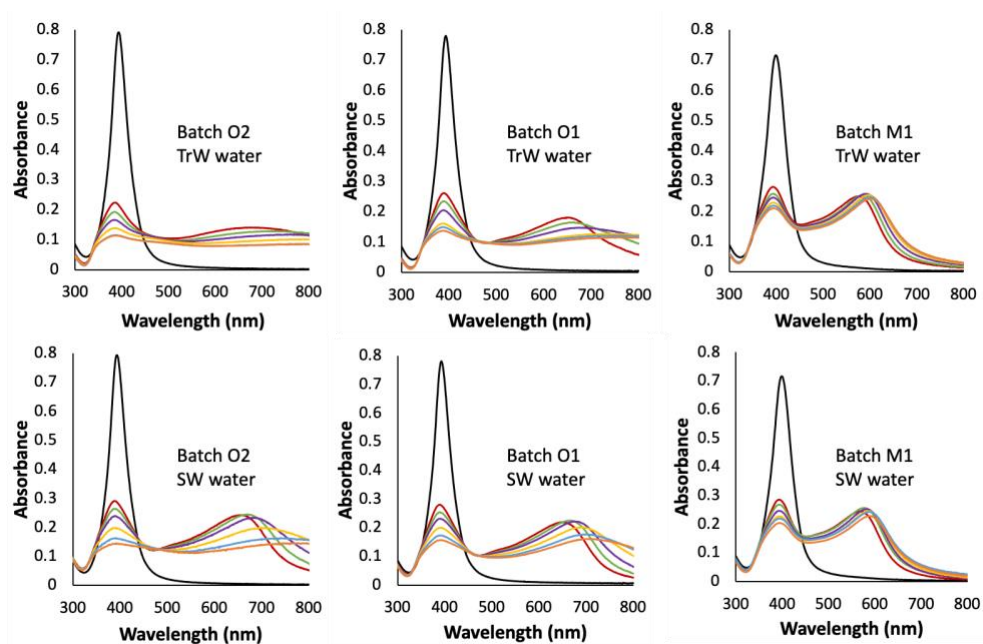


**Figure 45:** Spectra of the several batches diluted 1/4 with transitional and sea waters measured at several times (9.5, 1, 2, 5, 10, 15 min). The SPR band for the dilution ultrapure water was also included.

TrW and SW presented a lower speed with respect to the expected one in comparison with other aqueous matrices with much lower ionic strength (BW1 and TW, Figure 41 and Figure 42) and higher Z-potentials in absolute values (see Table 23), which does not seem to be in agreement with the dependence of this speed with the ionic strength of the medium previously observed and the Z-potentials. These environmental waters are complex media in which other factors can also play a role in AgNPs stability. In this sense, various works show the stabilizing effect of dissolved organic matter (DOM), mainly fulvic and humic acids, which seems to form AgNPs–OM complexes that provide a new external coating in the form of an adsorbed layer that acts as a stabilizer by steric effect [321,324]. Additionally, the high concentration of halides, mainly chlorides, can cause the passivation of AgNPs forming a superficial layer of AgX [318,321].

Definitely, AgNPs behaviour in aqueous matrices and the processes and transformations in which they intervene depends on a large number of factors, especially in natural waters. Some such as ionic strength, the effect of different

cations and anions, organic matter and dissolved O<sub>2</sub> were discussed. However, natural aquatic environments are much more complex, and many other factors such as interaction with natural colloids, heteroaggregation or the presence of large particulate matter are still poorly understood and require great difficulty in undertaking their study.

#### 4.1.1.2.3 Characterizing information: AF4 vs Static DLS and UV-vis spectroscopy

This section was focused in the determination of the information given by AF4 compared with batch DLS measurements and UV-vis spectroscopy. TW and SW waters were selected taking into account their different fingerprints as can be seen in the previous section. Figure 46 and Figure 47 summarize the results given by off-line DLS and UV-vis spectroscopy for batch O2. These off-line DLS results (Figure 46) show that the size of the aggregated AgNPs increased with time for both types of waters and also their polydispersity, more markedly for TW in accordance with that established in the previous section. The aggregation fingerprint was faster for TW than for SW, this last water presented different colors as can be seen in Figure 47.c in the function of time. However, TW dispersions were colorless.

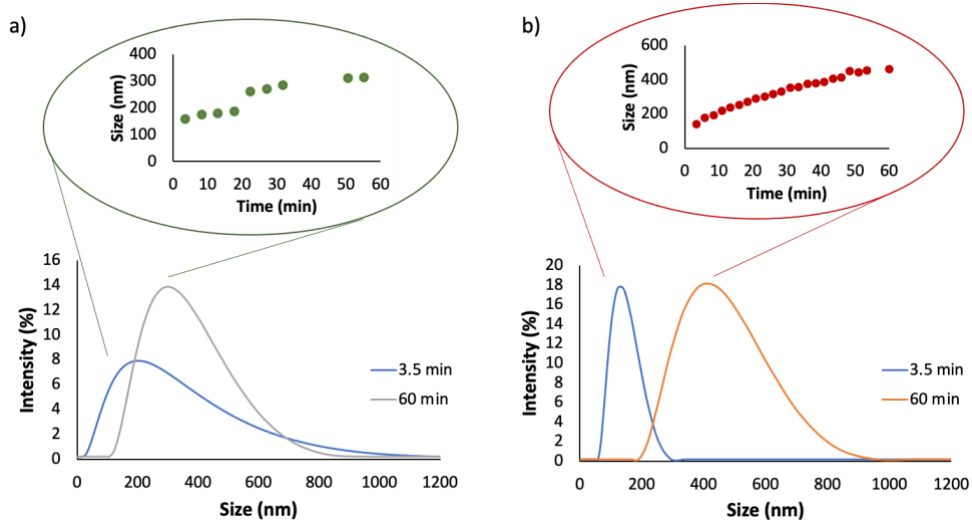


**Figure 46:** Static DLS registers for batch O2 diluted 1/4 with a) sea water (SW) and b) tap water (TW) measured at several times. Insert shows the changes in size of AgNPs with time.

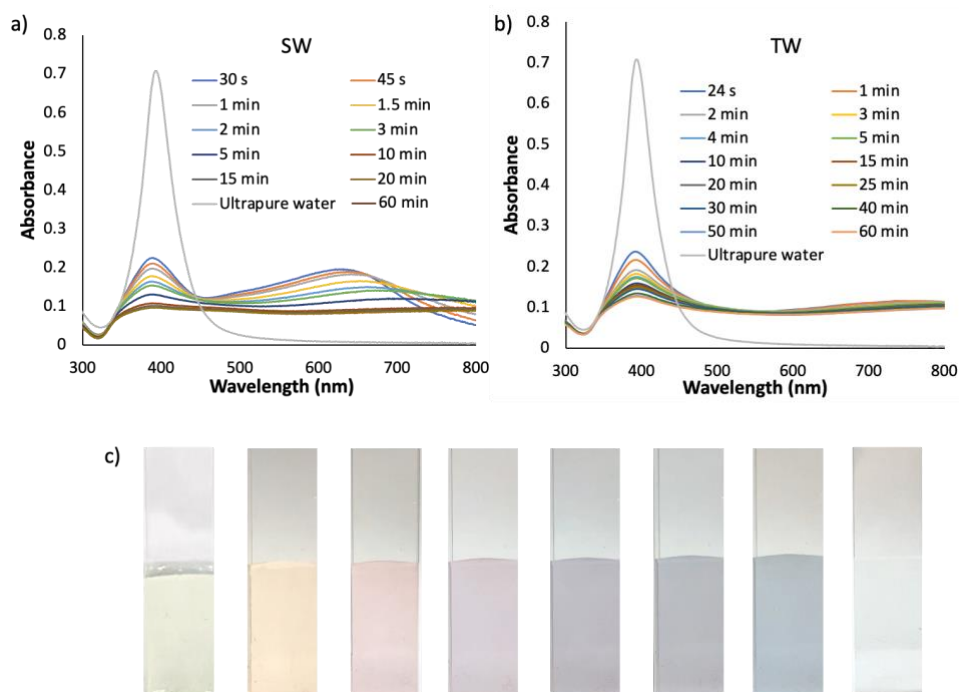


**Figure 47:** Uv-vis spectra for batch O2 diluted 1/4 with a) sea water (SW) and b) tap water (TW) measured at several times. The SPR band for the dilution with ultrapure water was also included. c) Color of the suspension in SW with time.

In order to study the polydispersity of the aggregated AgNPs, a slow crossflow was assayed ( $0.2$  instead  $1.0 \text{ mL}\cdot\text{min}^{-1}$  given in Table 18) for AF4. When lower crossflow was employed the retention times for bigger aggregates diminished. Fractograms obtained for dispersions in SW and TW waters are given in Figure 48 and Figure 49, respectively. AF4 with UV-vis and DLS in series showed two populations of NPs with different sizes for both dispersants. Dispersions in SW at 30 and 180 min measuring at 395 nm presented two peaks indicating two populations with different sizes (Figure 48.a). Images obtained by optical microscope showed the greater size of both aggregates at 180 min than those obtained at 30 min (Figure 48.b). DLS detector permits the evaluation of the sizes as it can be seen in Figure 48.c, fractograms indicate that the aggregates were bigger at 180 min than those obtained at 30 min. Figure 48.d shows the fractograms at 750 nm giving the two populations. A baseline signal was obtained for UPW

dispersion at 750 nm, which was in accordance with its color (see Figure 47.c) indicating no aggregation.

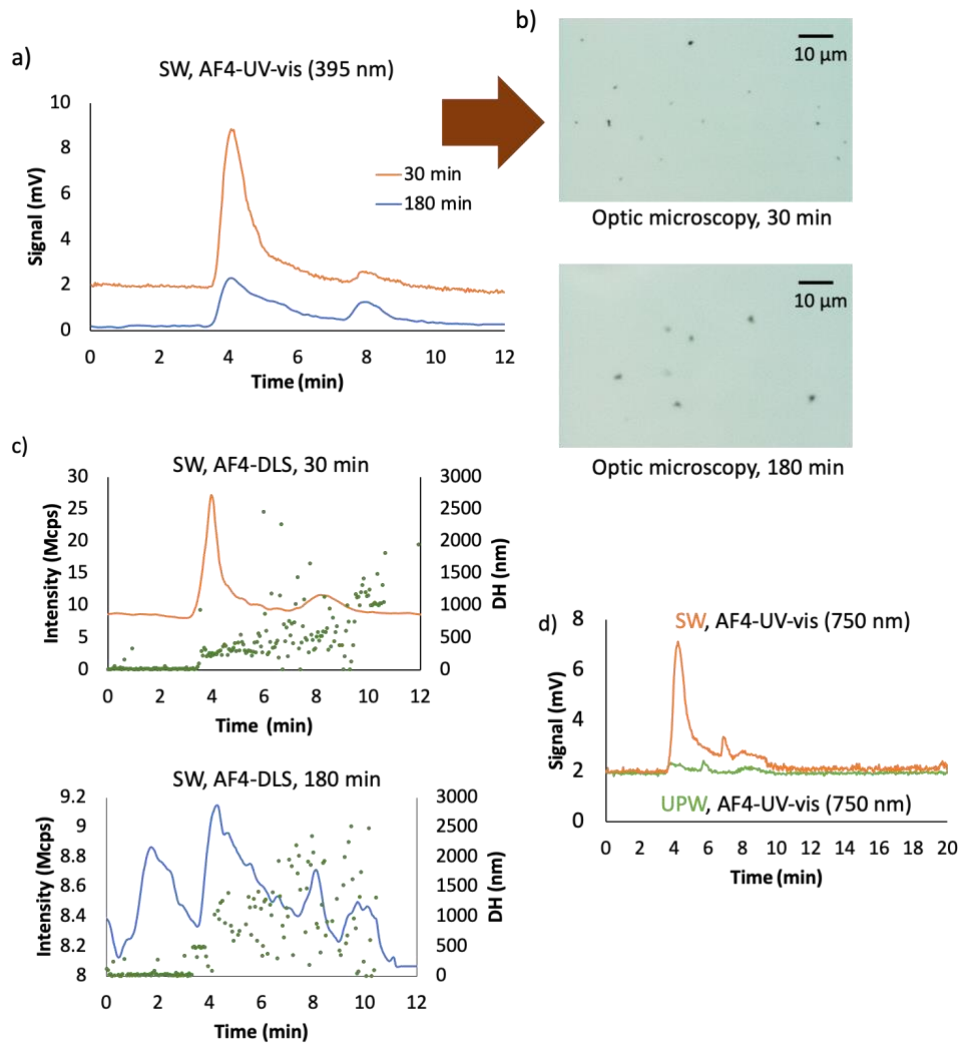


**Figure 48:** AF4 coupled in series with UV-vis and DLS detectors for batch O2 diluted 1/4 with sea (SW) water measured at several times: a) fractograms at 395 nm; b) optic images at 30 and 180 min; c) DLS fractograms at 30 and 180 min; d) fractograms at 750 nm of SW and UPW at 30 min. Cross-flow was  $0.2 \text{ mL}\cdot\text{min}^{-1}$ .

Considering the behavior of AgNPs in TW, two populations were also obtained by AF4 (see Figure 48). The sizes of the two colorless aggregates at 30 min



were higher than those obtained in SW (see Figure 49). These results were in agreement with the aggregation rate described in the previous section and observed by UV-vis spectroscopy in Figure 47.

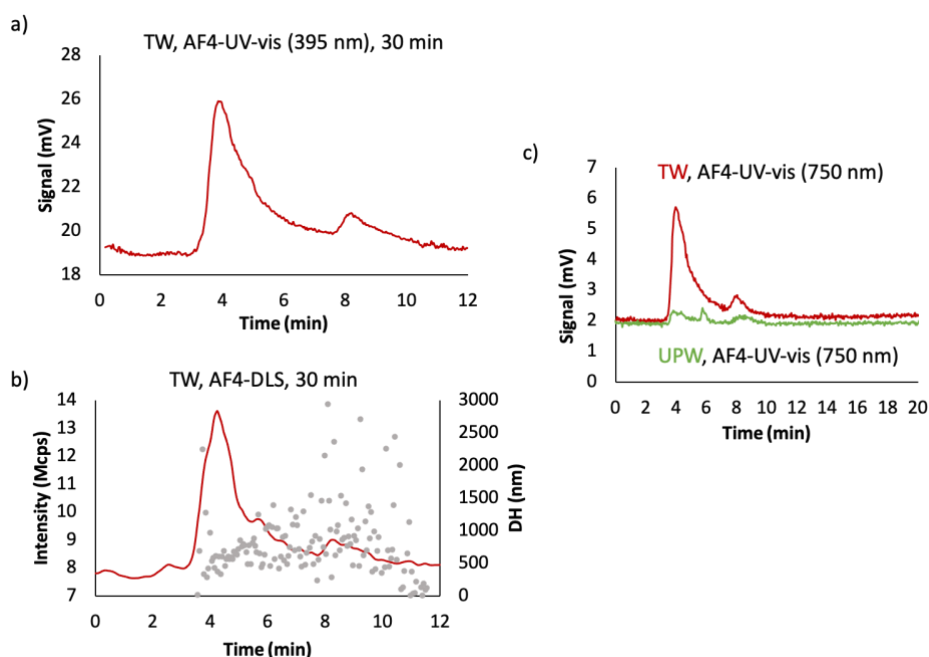


**Figure 49:** AF4 coupled in series with UV-vis and DLS detectors for batch O2 diluted 1/4 with tap (TW) water measured at 30 min: a) fractograms at 395 nm; b) DLS fractograms; c) fractograms at 750 nm of TW and UPW. Cross flow was 0.2 mL·min<sup>-1</sup>.

It has been demonstrated that AF4 coupled online with UV-vis and DLS in series gives relevant information for characterizing the aggregation processes of AgNPs in different water matrices with respect to static DLS and UV-vis spectroscopy.

- Conclusions

In this study, AF4 on-line coupled with UV-vis and DLS detector was used to evaluate the impact of aqueous dilution on analytical response of AuNPs and AgNPs dispersions. Different size dispersions were analyzed and the evolution of the fractograms profiles have been studied. The results demonstrated that for citrate-

capped AuNPs and AgNPs, there was a decrease in the absorbance signal with time that depended on the particle size, this decrease was higher for bigger NPs. By another hand. Hydrodynamic diameter was constant over dilution. AF4-UV-vis-DLS showed that there is an effective variation in the number of NPs is more favored due to their lower stability, and the decrease on the absorbance signal as a function of time was more drastic. Hence, it can be concluded that AuNPs and AgNPs stability varied in diluted aqueous dispersions, and therefore their stability must be guarantee in order to obtain reliable results.

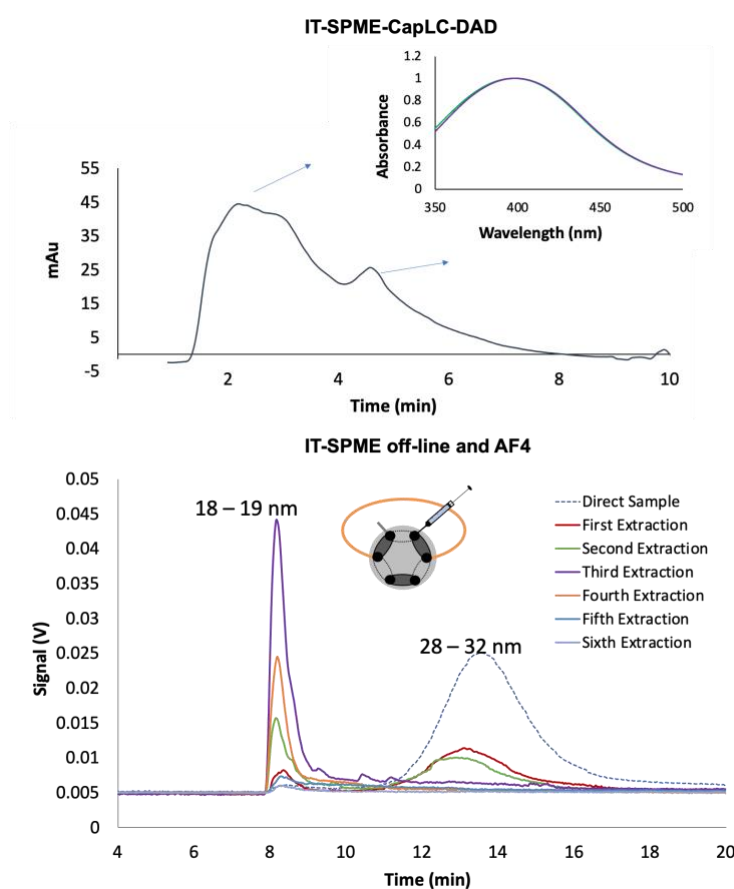
Taking into account the previous results, a study about stability of citrate AgNPs in different environmental water was also carried out. Diluted-dispersions of citrate capped AgNPs with ultrapure, several drinking, transitional and sea waters were studied for short times (up to 180 min). The water matrix influenced AgNPs stability and it was demonstrated that aggregation was the process involved. Aggregation kinetics depended on the type of water. Several sizes were obtained in the function of the water, which determined the color of AgNPs.

Definitely, AgNPs behavior in aqueous matrices and the processes and transformations in which they intervene depends on a large number of factors. Some such as ionic strength, the effect of different cations and anions, organic matter, natural colloids, heteroaggregation, among others, can justify their different performance. Ultrapure water conserved citrate capping to a great extent and then, stability of NPs. Drinking waters with similar Z-potentials, responded to ionic strength in the aggregation process. Transitional and sea waters presented more stability than expected, probably due to steric effects of dissolved organic matter or passivation due to the high level of chloride.

It was demonstrated that AF4 coupled online with UV-vis and DLS in series provides relevant information for characterizing the aggregation processes of AgNPs in the different water matrices studied with respect to static DLS and UV-vis spectroscopy. Several populations of aggregates were obtained by AF4, which provides new information and also permits the interpretation of the results achieved by static DLS and UV-vis spectroscopy. The use of the proposed technique provides valuable information for NPs performance in the environment.

#### 4.1.2 Characterization of MNPs by IT-SPME-miniaturized LC-DAD

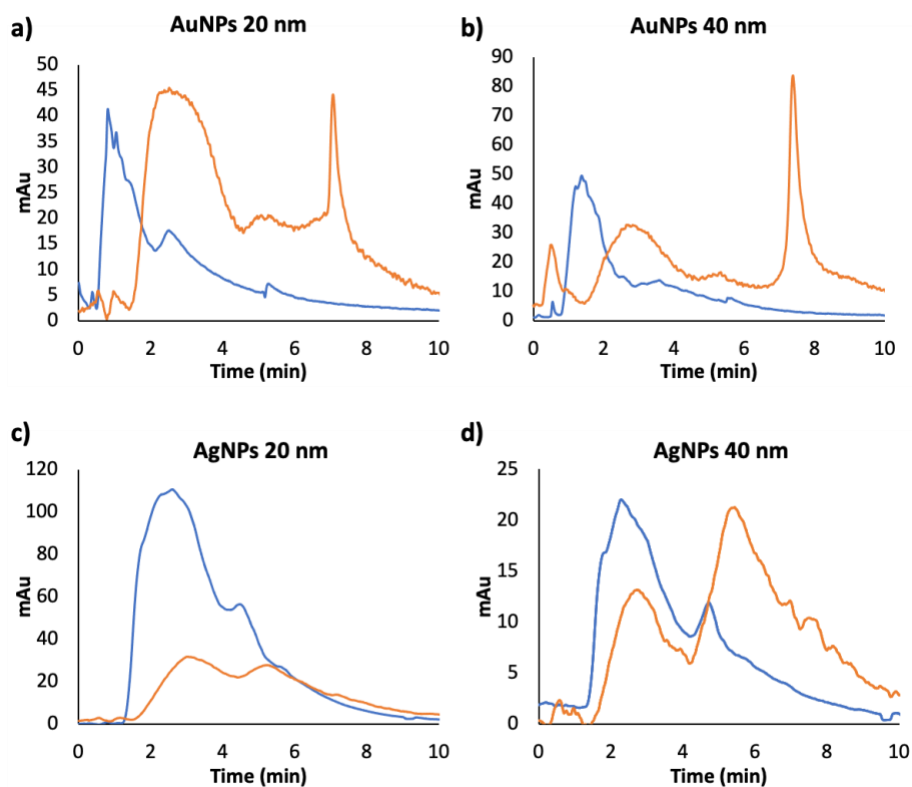
The IT-SPME step, which influenced the chromatogram fingerprint, was studied by AF4. Figure 50 shows two groups in the fractogram in function of the processed LC-mobile phase volume for (1/8) water diluted AgNPs (20 nm core and citrate capping). This figure also shows the chromatogram obtained by coupling on-line IT-SPME and CapLC with DAD detection.



**Figure 50:** On-line IT-SPME-CapLC-DAD (inset: normalized spectra obtained at the maximum of the two chromatographic peaks) and off-line IT-SPME and AF4 results for (1/8) ultrapure water diluted dispersion of AgNPs (20 nm core; citrate capping).

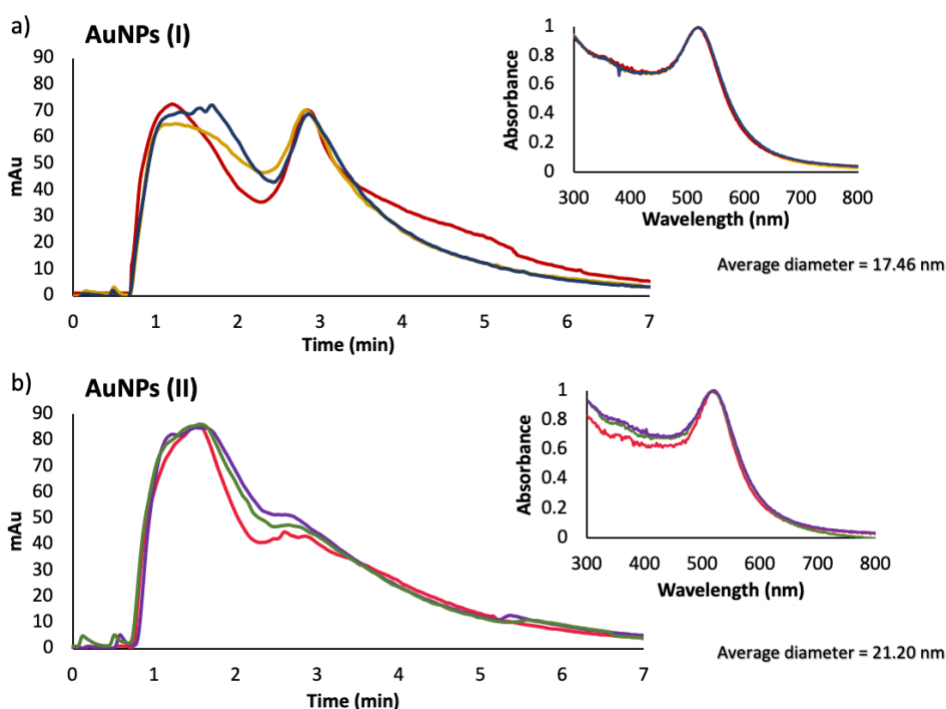
The non-polarized group of NPs (second chromatographic peak) required higher volumes of mobile phase to be extracted from the IT-SPME capillary and provided smaller DH than the water polarized NPs (first chromatographic peak). These results were in accordance with the separation mechanisms established in [258] for IT-SPME-CapLC-DAD (see Figure 50). Only one population was observed if direct injection with a stainless loop was carried out, similar to the signal obtained in [258] by CapLC-DAD without coupling IT-SPME. Polarized population eluted first from the IT-SPME capillary because their interaction was weak with the extractive phase, meanwhile non-polarized population interacted with the IT-SPME extractive phase eluting at high retention times as AF4 demonstrated.

Figure 51 shows the chromatographic profiles of commercial citrate capped NPs of different size, which were dependent of size and metal. The miniaturized LC systems improved sensitivity and resolution, less sample dilution and diffusion effects are achieved in reference to conventional LC and IT-SPME coupling permits to detect differences in the distribution of polarized and nonpolarized noble NPs in the bulk dispersion. The peak at lower retention time ( $t_r$ ), was characterized by a minimal interaction with the IT-SPME extractive phase; and thereof the separation mechanism was attributed to size exclusion interactions in the analytical column [258]. The identification of a second peak at higher  $t_r$ , demonstrated the presence of a stronger interaction between the noble NPs distribution and the IT-SPME extractive phase. Taking into account the apolar nature of the coating, this separation can be explained by means of hydrophobic effect [258]. Based on these results, the differences in the distribution of polarized and non-polarized noble NPs in the bulk dispersion can be used to differentiate them.



**Figure 51:** Chromatographic profiles of commercial citrate capped MNPs. In blue: signal obtained by capillary LC; and in orange: signal obtained by nanoLC.

Naked AuNPs have also been characterized. Figure 52 shows the profiles obtained for six batches of synthesized naked AuNPs. The profiles for the different batches of AuNPs (dilution 1:1 of the bulk dispersion) showed differences in the distribution of polarized and non-polarized AuNPs in bulk dispersions. Attending to these differences, the naked AuNPs were classified into two groups: Group I: similar polarized and non-polarized distribution in the bulk dispersion [AuNPs(I)] (Figure 52.a), and Group II: predominant polarized NPs distribution in the bulk dispersion [AuNPs(II)] (Figure 52.b) as for commercial AuNPs (see Figure 51). It should be noted that the DH were 17.46 nm and 21.20 nm for AuNPs(I) and AuNPs(II) bulk dispersion estimated by static DLS measurements, respectively, showing low differences in the NPs sizes and similar to commercial AuNPs 20 nm. Figure 52 shows that UV-vis spectroscopy provides similar spectra for both, AuNPs(I) and AuNPs(II) and then, any discrimination can be done by this technique.



**Figure 52:** a) Chromatographic profiles obtained for three batches of naked AuNPs corresponding to AuNPs(I). b) Chromatographic profiles obtained for three batches of naked AuNPs corresponding to AuNPs(II). Inserts: UV-vis spectra for both types of naked AuNPs.

#### 4.1.2.1 Study of the capture of AgNPs by several kinds of soils using IT-SPME-CapLC-DAD

Four different soils were used for evaluated the capture of AgNPs. Their characterization was carried out and results are showed in this section.

FTIR-ATR spectroscopy was selected for characterizing the soil samples in terms of SOM content. No sample preparation was required as a small amount of a particular soil was directly measured. Figure 53 shows the obtained IR spectra for each sample. Two groups could be established: in the first one consisting of compost and mountain soils in which in addition to C - O and Si - O bands (at 1430 and 1030  $\text{cm}^{-1}$  respectively), vibrations compatible with organic matter could be

distinguished (O - H, C - H and C - O vibrations in the zones around 3200 and 1700  $\text{cm}^{-1}$ ) due to the presence of SOM; in the second one, consisting of orchard and urban soils, the above-mentioned C - O and Si - O bands (commonly associated to the presence of carbonates and clays) could also be found, whereas less organic matter was present.

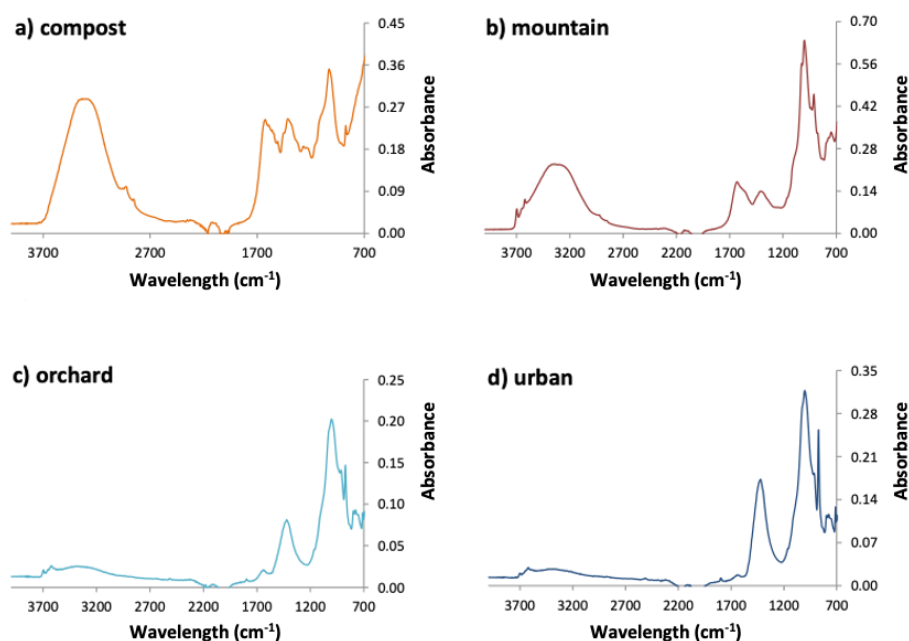


**Figure 53:** IR spectra for the four studied soils obtained by FTIR-ATR.

For compost, this result is not surprising since this soil consists of decomposed/recycled organic matter. At the other end, agricultural soils such as orchard have been documented to have a lower content of clay [290], described to be directly related with the SOM amount [325]. Henceforth, these groups will be distinguished as high-containing and low-containing SOM, namely HSOM and LSOM respectively. Additional information about relations of IR bands and the vibrations of characteristic organic functional groups can be found in Table 24.

**Table 24:** IR bands and functional groups.

Absorption band (cm <sup>-1</sup> )	Functional group
~3400	Alcohol/Phenol O-H stretch
~2900	Alkyl stretch
~1700	Carboxylic acid C=O stretch, Aromatic C=C bending, Alkenyl stretch
~1400	Alcohol/Phenol/Carboxylic acid O-H bending Alkyl bending
~1000	Alcohol C-O bending
~900	Aromatic C-H bending

Organic matter was estimated by a gravimetric method. A quantity of each sample (between 0.45–0.65 g) was weighed in porcelain bowls. Then, they were placed in furnace where they were heated at 550 degrees for 14 hours. When it finished, the samples were hydrated, and then, dried overnight in a stove. Finally, the obtained residue was weighed and by computing the difference with the first measure, the organic content was estimated. The results for n = 3 were: Compost, (62.5 ± 1.2) %; Mountain, (23.13 ± 0.16) %; Orchard; (8.32 ± 0.10) % and Urban, (4.61 ± 0.1) %. The results were in good agreement with the ones obtained by FTIR-ATR.

On the other hand, soils (1.0 g) were sieved several times for controlling the PSD of each sample. The average composition in terms of 5 fractions (below 100 µm, 100 to 200 µm, 200 to 300 µm, 300 to 400 µm and coarse fraction) for the 4 studied soils are displayed in Table 25. Microscope characterization can be found in Figure 54 and Figure 55.



**Table 25:** Soil particle size composition. Percentages (%) of each fraction for the four studied soils and estimated average size.

Fraction	Compost	Mountain	Orchard	Urban
< 100 $\mu\text{m}$	8.95	3.94	17.80	18.67
100-200 $\mu\text{m}$	75.26	15.92	22.68	21.59
200-300 $\mu\text{m}$	14.27	14.02	14.55	19.58
300-400 $\mu\text{m}$	0.79	16.13	13.36	11.59
> 400 $\mu\text{m}$	0.73	49.99	31.61	28.57
average size ( $\mu\text{m}$ )	160	310	230	210

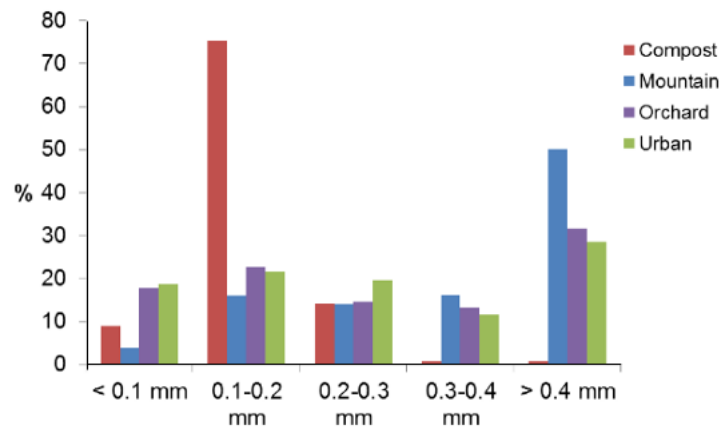


**Figure 54:** Chart showing the distribution of particle size in the 4 studied soils.

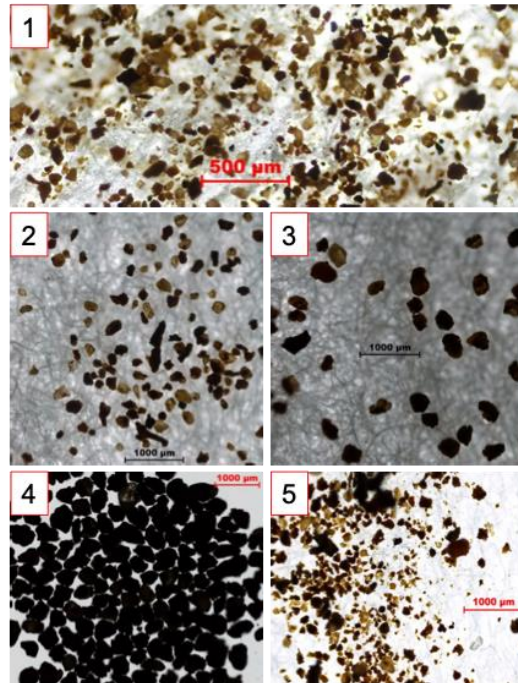


**Figure 55:** Eclipse microscope pictures for each fraction of the orchard soil after being sieved: (1) below 100  $\mu\text{m}$ , (2) 100-200  $\mu\text{m}$ , (3) 200-300  $\mu\text{m}$ , (4) 300-400  $\mu\text{m}$  and (5) above 400  $\mu\text{m}$ .

Alternatively, by using only optic microscope the PSD can also be estimated. The procedure involves obtaining a picture by optic microscope (the microscope allows one to process a large surface by superimposing images). Using the software of the equipment, a histogram of the particle size distribution (i.e., the PSD) could be obtained (similar to ImageJ analysis) (see Figure 56).

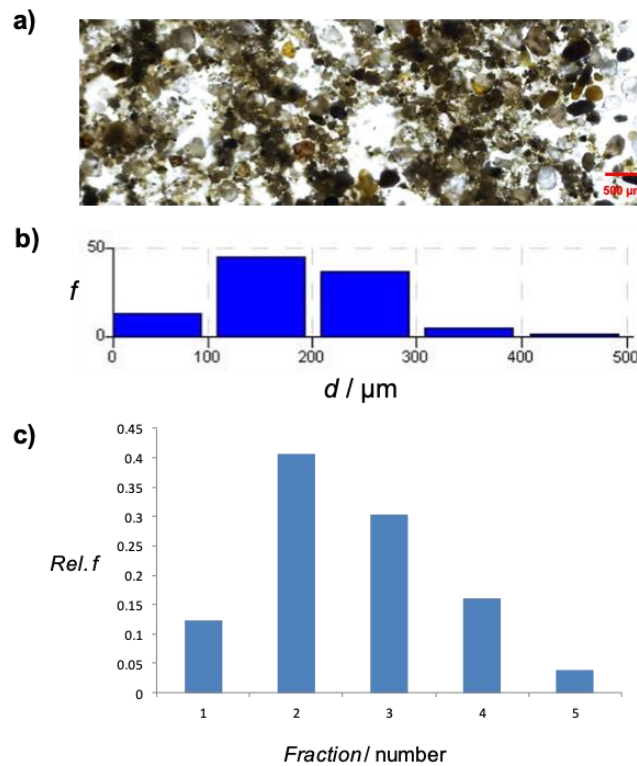


**Figure 56:** Characterization of the soils by optic microscope. a) Eclipse microscope image of the soil mixture sample (500 μm). Histogram of the particle size distribution obtained by: b) optic microscope ( $f$ : frequency) and c) after sieving resulting in different fractions: (1) under 100 μm, (2) 100-200 μm, (3) 200-300 μm, (4) 300-400 μm and (5) over 400 μm.

Results of both methods were contrasted using a linear regression ( $y = (0.92 \pm 0.10)x - (0.02 \pm 0.03)$ ;  $R^2 = 0.99$ ;  $x$  = sieved method and  $y$  = microscope) and thereby, validated. If the two groups established after FTIR-ATR analysis are considered, it can be stated that for the first one, compost had smaller particles than mountain soil; as for the second group, both orchard and urban soils were very similar in PSDs. The estimated average sizes shown in Table 25 confirmed this observation.

Finally, pH, conductivity (EC) and oxidation/reduction potential (Eh) for the four soils were measured in situ. Results are shown in Table 26. From pH values, it can be stated that the four soils are neutral/alkaline and therefore humic acid (HA)

is expected to be one of the main components of SOM, with the higher values obtained for the LSOM group. The measured EC exhibit greater variation: for the LSOM group, values were comparable; conversely for the HSOM group, higher values were obtained, with compost having 10 times more EC than the mountain soil. This parameter is important because it can be linearly related to IS [326,327], parameter described to have great influence in NP-soil interactions [289,328,329].

**Table 26:** Estimations of pH, EC and Eh for the 4 kinds of studied soils.

Parameter	Compost	Mountain	Orchard	Urban
pH	7.4 ± 0.1	7.10 ± 0.04	8.16 ± 0.04	8.30 ± 0.04
EC ( $\mu\text{S}\cdot\text{cm}^{-1}$ )	5575 ± 7	538 ± 4	187.3 ± 0.9	137.9 ± 0.1
Eh (mv)	175 ± 10	200 ± 10	170 ± 10	157 ± 3

The characterization of AgNPs used in this assay can be found below. The average particle diameter obtained by TEM was 17.3 nm and the histogram of size distribution as well as a TEM picture of the synthesis can be seen in Figure 57.a. On the other hand, the UV-vis spectrum for the 17.3 nm AgNPs is also shown in Figure 57.b. As expected, the maximum of absorbance was around 400 nm corresponding to the maximum wavelength of the AgNPs SPRB.

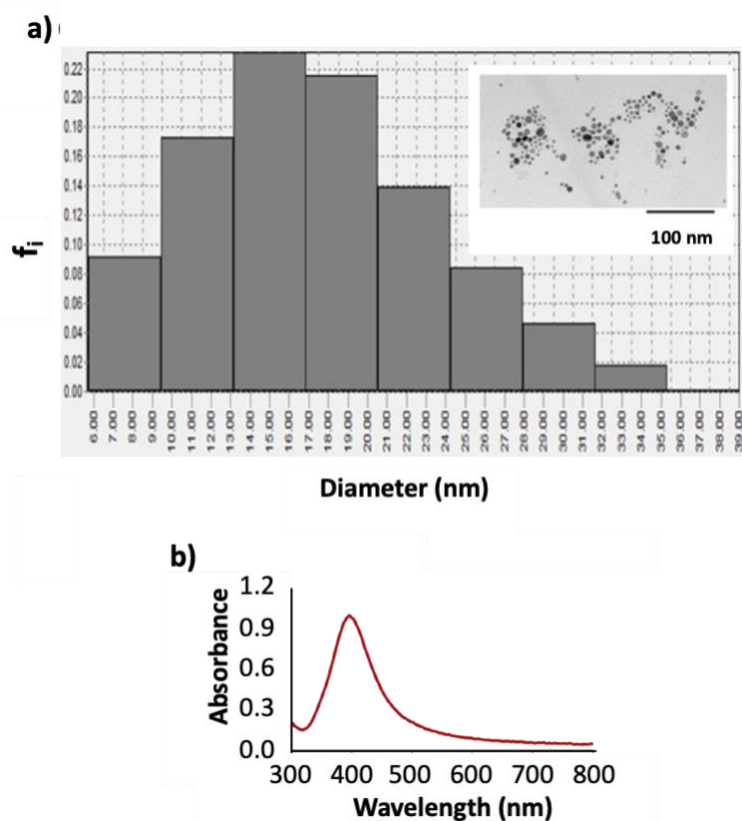


**Figure 57:** TEM histogram of 17.3 nm AgNPs showing their size distribution and TEM picture (upper-right corner). b) UV-vis spectrum of 1:8 17.3 nm AgNPs.

Thus, in preliminary studies, three samples of orchard soil were processed according to procedure discussed in Section 3.3.4.2.1 with AgNPs dispersion (A), the AgNPs synthesis blank (SB) and water (W). After 60 min, an aliquot of the supernatant from each sample was measured by UV-vis spectrophotometry. As it can be seen in Figure 58.a, for SB and W, samples absorbed at 400 nm (yellow-colored supernatants). Thus, an interfering compound was extracted when water or aqueous synthesis blank of AgNPs was added to the soil, at a higher rate for the latter. On the other hand, for A, the SPRB was altered as the unknown interference was also extracted when AgNPs dispersions were added to the soil (Figure 58.a). Considering the resulting spectral profile, it must be confirmed that the obtained UV-vis signal corresponds to the absorption sum of AgNPs and the interfering compound, and not the spectrum of a new species formed in the process.

Successive additions of AgNPs were done on a SB aliquot. The resulting spectra matched in terms of signal profile to the one obtained for the A aliquot. Consequently, both NPs and the unknown interference were present in the A supernatant and their absorptions were additive. TEM pictures of this supernatant were taken and dispersed AgNPs were found as Figure 58.b shows. The spectra of the performed study and the AgNPs SPRB of the used synthesis are displayed in Figure 58.c and d, respectively.

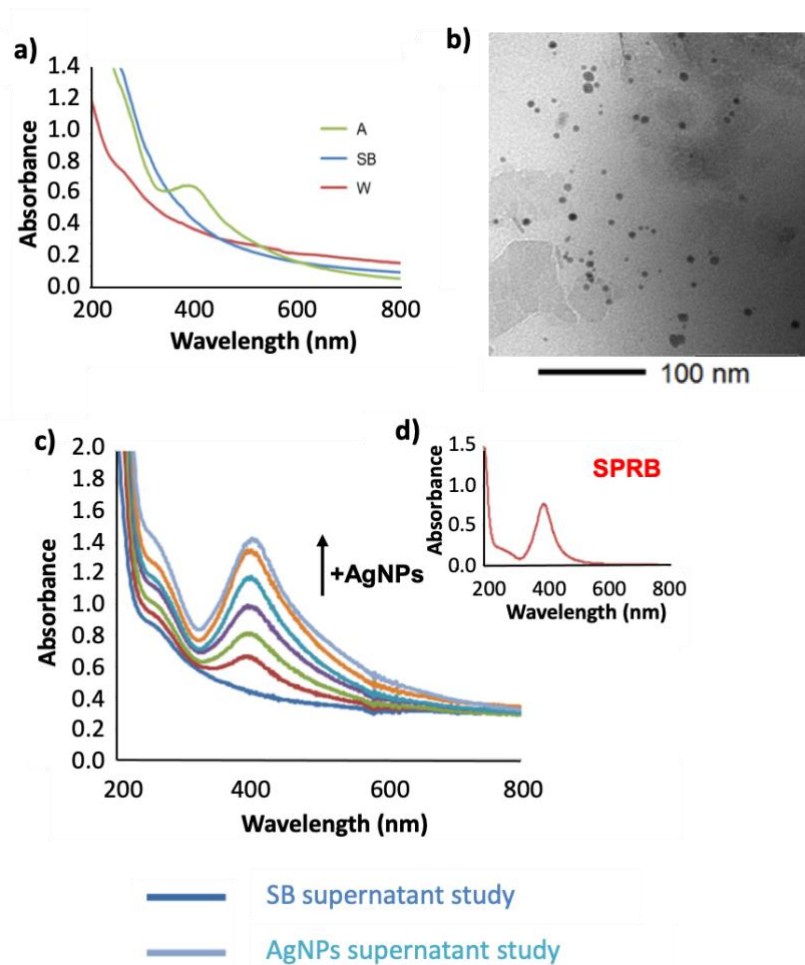


**Figure 58:** a) UV-vis spectrum of the supernatant after contaminating soil samples with: (A) AgNPs, (SB) synthesis blank and (W) water. b) TEM picture of the supernatant contaminated with AgNPs. c) UV-vis spectra of the successive additions of AgNPs on the SB supernatant. d) UV-vis spectrum showing the SPRB of the used AgNPs synthesis.

Additionally, and considering that the major reagent involved in AgNPs syntheses is sodium citrate, a quantity of soil was mixed with a citrate solution. After 1 hour, an aliquot of the supernatant was measured by UV-vis spectrophotometry. Compared to the spectrum obtained when the soil was mixed with the synthesis blank, it can be stated that citrate promotes the extraction of the interfering compound. The results are displayed in Figure 59.

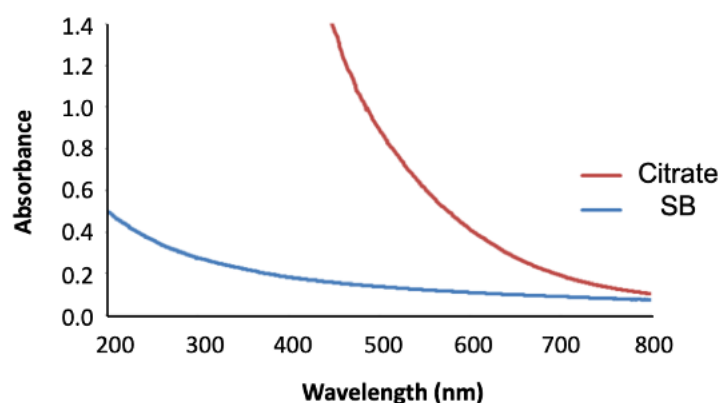


**Figure 59:** UV-vis spectra of the supernatants of: (SB) soil-synthesis blank and (Citrate) soil-sodium citrate solution mixtures.

In this situation, and confirmed the presence of an interfered compound, the CapLC-DAD method permitted to study the extraction rate of this unknown compound in time for the four studied soils obtaining temporal series. Prior to the analysis, the parameters of the procedure were optimized in order to obtain an adequate analytical signal by ensuring that the particles remained unchanged after the sample processing in terms of their response in the chromatographic system. Figure 60.a shows the chromatograms for processed and unprocessed (i.e., directly injected) 1/8 diluted samples of AgNPs. As it can be seen, nearly identical profiles were obtained. Consequently, particles remained unchanged after being processed by the optimized procedure.

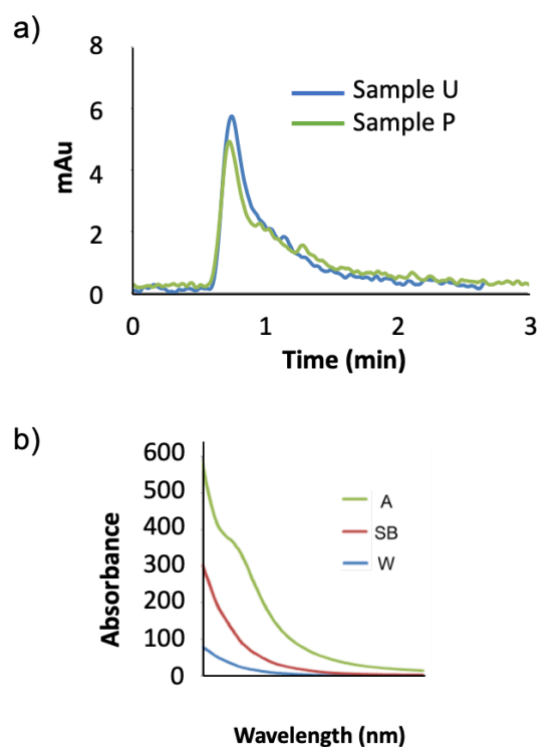


**Figure 60:** a) CapLC chromatograms for samples of 1/8 AgNPs: (sample U) unprocessed and (sample P) processed. b) DAD spectra for the peaks obtained in the 3 series (A, SB and W) for the 4 soils (in this case, measured in the chromatograms of the orchard soil samples).

The next step was the study of methodology interferences. Three series for each soil in presence of AgNPs dispersion (A), blank of the AgNPs synthesis (SB) and water (W) consisting of aliquots taken at different times in a 0–80 min span were processed in the CapLC system without dilution. In this approach, only one chromatographic peak is obtained, thus no separation between AgNPs and the unknown interference is expected. Spectral profiles obtained for the chromatographic peak, presented in the Figure 60.b, were comparable to the ones obtained by UV–vis spectrophotometry (Figure 58.a) and for series A, the DAD spectrum corresponded also to the sum of the involved compounds. Figure 61 shows the temporal variation of the analytical signal for the three series in each soil. Several aspects have to be discussed. In the four soils, the highest and lowest signal values were obtained for A and W, respectively, as the extraction of the



unknown interference was promoted by the synthesis matrix and, notably, the NP presence in A. The magnitude of this extraction is different depending on the nature of the soil, being in increasing order: urban, orchard, mountain and compost. Here, a relation can be made as the two soils where the extraction took place in higher proportion (compost and mountain) were the ones containing more SOM. Hence, the nature of the interfering compound might be organic and presumably related to HAs, whose affinity for AgNPs has been documented [330–333]. Moreover, if series A is analyzed, two groups can be distinguished according of whether signal saturation due to the complete extraction of the interference was reached (urban and mountain) or not (orchard and compost).

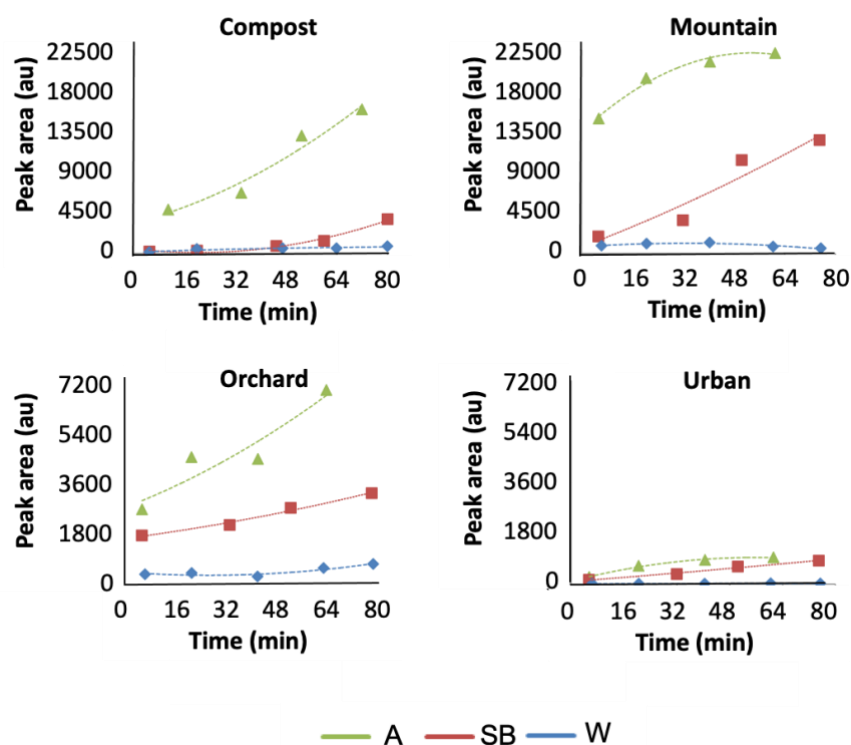


**Figure 61:** Variation of the CapLC signals in time (0-80 min range) for the 3 series (A, SB and W) in each of the 4 soils (compost, mountain, orchard and urban). (n=2)

When IT-SPME was coupled to CapLC, not only sensitivity was increased as more sample can be processed, but the particles dispersed in water and are

separated by polarity into two groups by a dual separation mechanism while keeping the signal response to AgNPs concentration [258] (see Figure 62.a). Firstly, the response of the used synthesis of AgNPs was evaluated by ITSPME-CapLC for testing linearity. 30  $\mu\text{L}$  of sample were injected and a 70 cm long PDMS-TRB35 capillary column was selected. For each run, as expected, two peaks were obtained. The calibration curve was carried out and linearity obtained was excellent ( $R^2$  of 0.9998). Considering the estimated LOD 9  $\mu\text{M}$ , quantitative captures can be assured by this method. This limit is equal to  $\sim 10 \mu\text{g}\cdot\text{L}^{-1}$  in terms of Ag amount. Note that the obtained LOD were comparable to the ones reported in the literature for other different studies and matrices [258,334–336].

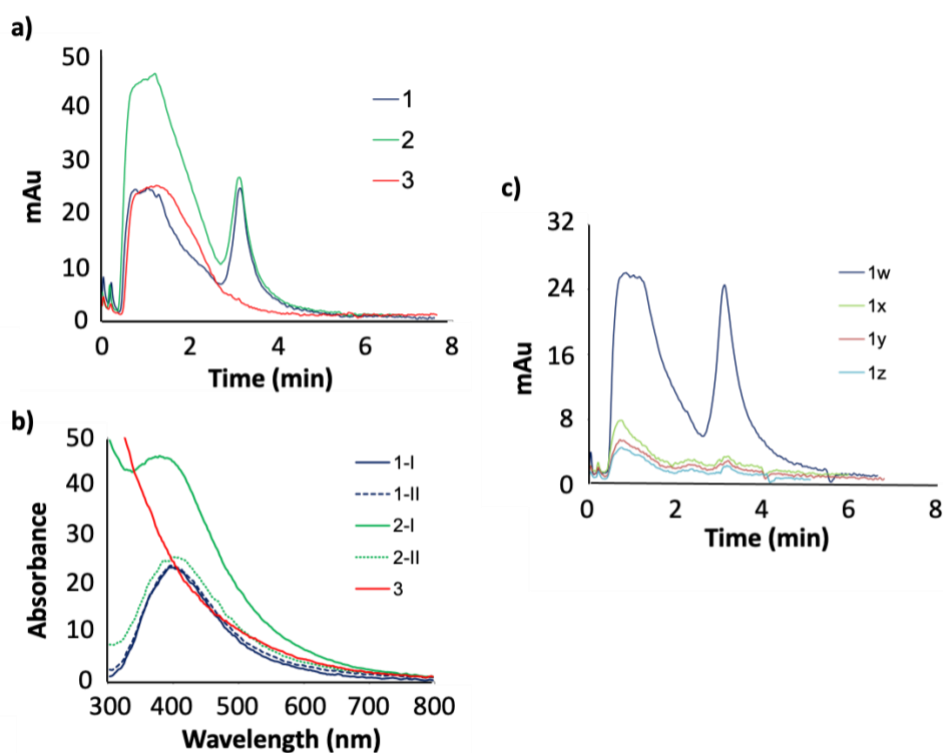


**Figure 62:** a) Chromatograms for: (1) 1/16 AgNPs standard, (2) 1/16 Sample A of the orchard soil and (3) a HA standard ( $10 \text{ mg}\cdot\text{L}^{-1}$ ). b) DAD spectra for: (1-I) 1st and (1-II) 2nd chromatographic peaks of 1/16 AgNPs, (2-I) 1st and (2-II) 2nd peaks of 1/16 Sample A and (3) 1st peak of the HAs standard. c) Chromatograms obtained for AgNPs: (1w) without, and in the presence of 1% sodium thiosulfate after (1x) 40, (1y) 45 and (1z) 50 minutes of reaction.

When samples A of the four soils were processed, two peaks were obtained too. The 1st peak corresponded to a group containing both the interfering compound and AgNPs and the 2nd peak, only AgNPs (see spectra from DAD in Figure 62.b). If only the 2nd peak, corresponding to the particles which interact with the IT-SPME adsorbent, is considered for the analysis, quantitative observations can be made.

At the same time, experiments were performed with HA standards believed to be responsible for the interferences. The complete study is showed in Figure 63. The HAs response was linear in a wide range of concentrations and the chromatograms presented only one peak with a DAD spectrum that matched the ones obtained for the CapLC signals of series SB. If the chromatograms and DAD spectra (Figure 62.a and b) of sample A (for instance, working with the orchard soil), processed AgNPs and a HA standard were compared, results showed that there is a high probability that the main component of the interfering compound was HAs: the signal of sample A can be seen as the sum of contributions of these compounds and AgNPs. This result corroborates the fact that in neutral/alkaline soils HAs represent an important fraction of the SOM composition.

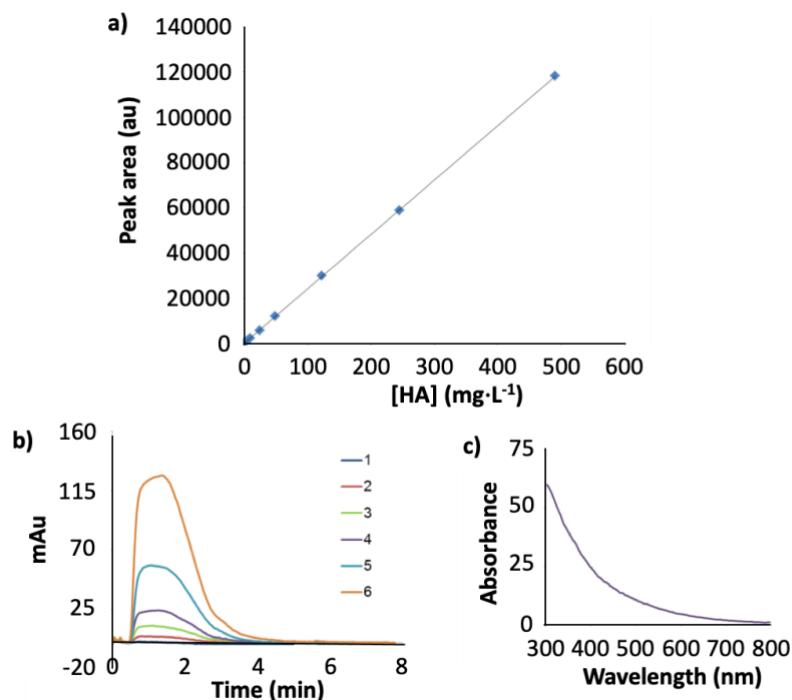


**Figure 63:** a) IT-SPME-CapLC Calibration curve for HAs from 0 to 500 mg·L<sup>-1</sup>. b) Chromatograms obtained for [HAs] standards of: (1) 0.5, (2) 2, (3) 5, (4) 10, (5) 25 and (6) 50 mg·L<sup>-1</sup>. c) DAD spectrum for (4).

#### 4.1.2.1.1 Capture percentage (%) of AgNPs in the different soils

Experimentally, it was found that a high concentration of sodium thiosulfate (1%) quickly disrupted the absorption of the AgNPs (i.e., the SPRB) as Figure 62.c shows. Even more, sodium thiosulfate did not affect the absorption of the interfering compound in samples SB (Figure 64). First, an IT-SPME-CapLC kinetic study of the SPRB disruption by sodium thiosulfate in AgNPs dispersions had to be made for knowing the time at which the NPs are destroyed or a known % of them; second, samples A of the four soils had to be measured before and after adding 1% sodium thiosulfate at the time estimated in the first step, to the suspensions in order to quantify the amount of AgNPs that are in the supernatants and by computing the difference, the ones retained in each soil. The same procedure was

repeated for samples SB in order to confirm that the signal of the interfering compound did not change.

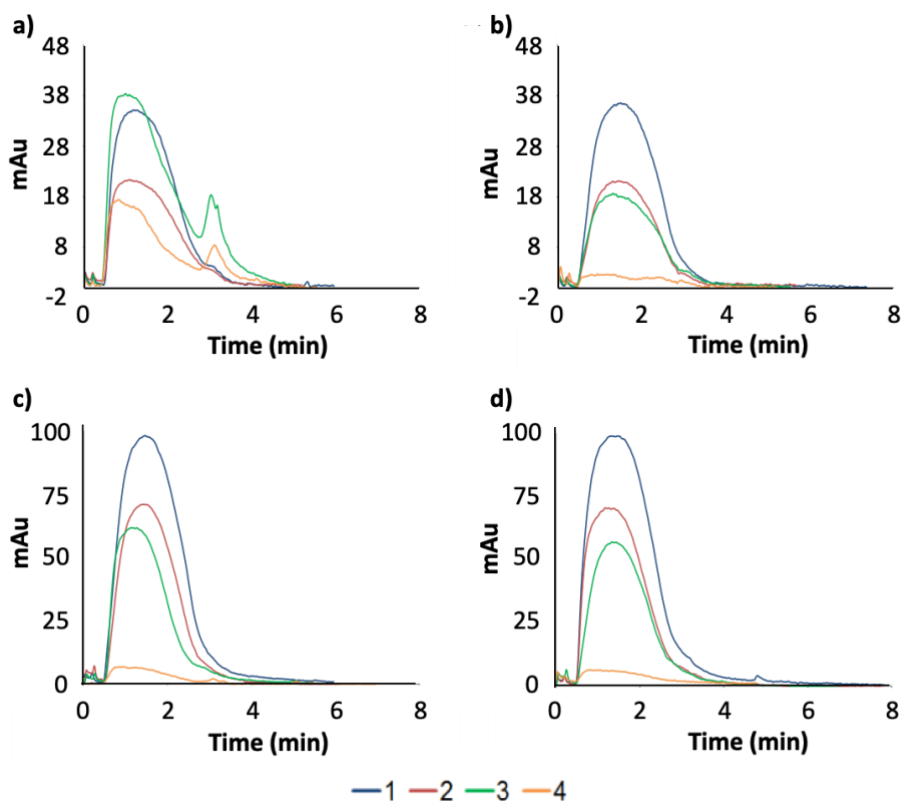


**Figure 64:** Chromatograms for (1) compost, (2) mountain, (3) orchard and (4) urban soils corresponding to: for samples A, injections a) without and b) in the presence of 1% sodium thiosulfate; for samples SB, injections c) without and d) in the presence of 1% sodium thiosulfate (note, exposure time of the samples to sodium thiosulfate: 50 min, 1/16 sample A dilutions).

For the IT-SPME-CapLC kinetic study, the AgNPs were injected directly and in the presence of 1% sodium thiosulfate at different controlled times. Figure 62.c shows the chromatograms after 40, 45 and 50 min of reaction in which the estimated disruption of the absorption was 86, 89 and 90%, respectively (RSD of 4%). Note that after this time, the signal did not decrease significantly. Accordingly, samples A (and SB) can be measured 50 min after being mixed with sodium thiosulfate and if there is a decrease of NP absorption, it will represent 90% of the

former signal. The results of this study are shown in Figure 64. Comparing the chromatograms obtained for samples A without and in the presence of sodium thiosulfate (Figure 64.a and b respectively), it can be observed that the signals remained unchanged for compost and mountain soils and that they decreased in the presence of sodium thiosulfate for orchard and urban soils. For these two samples presented the 2nd peak in the chromatograms of samples A, indicative of the AgNPs presence in their dispersions. For orchard soil, signals were higher. As for samples SB, the peak areas without (Figure 64.c) and in the presence of sodium thiosulfate (Figure 64.d) did not change significantly, <3%, satisfactory considering the method RSD of 7%.

The retention values can be quantified by IT-SPME-CapLC from the 2nd peaks obtained for sample A and the used AgNPs standard. Hence, the unretained particles are estimated and by computing the difference, the capture %. On the other hand, after performing the experiment of using sodium thiosulfate in samples A, quantification of AgNPs retention in each soil can be made indirectly: by calculating the total peak area variation caused by the sodium thiosulfate and comparing to the response obtained for the equivalent dilution of a AgNPs dispersion (i.e., a processed standard), the amount of NPs in the supernatant can be obtained and thereby, the AgNPs retained in each soil.

Both methods, namely “2nd peak” and “disrupting agent”, provided similar results (see Table 27) as it was confirmed through a linear regression of the obtained values ( $y = (1.006 \pm 0.016) x + (0.1 \pm 1.2)$ ;  $R^2$  of 0.999;  $x$  = disrupting agent and  $y$  = 2nd peak). Additionally, a paired t-test showed that these results were comparable at 95% confidence level ( $t$ -value = 1;  $p$ -value = 0.391). AgNPs were poorly retained in orchard soil ( $15 \pm 1\%$ ), moderately in urban soil ( $48 \pm 1\%$ ) and highly in both compost and mountain soils (over 99%). In this case, the standard deviation between two sample determinations was estimated [ISO 5725-1:6, 1994]. Therefore, in soils where the amount of SOM was higher, so was the AgNPs retention. In consequence, SOM is the determining factor in NPs capture as for instance, both NP retentions in compost and mountain soils were almost quantitative, although having the smallest and largest soil particles in proportion respectively (see Table 25). However, further tests will be made in order to estimate the influence of soil particle size in AgNPs retention, as well as relating the previously estimated parameters with the obtained results.

**Table 27:** Retention % of AgNPs quantified by IT-SPME-CapLC-DAD in the different spiked soils from both, the second peak of the chromatogram and by using the disrupting agent.

SOIL	AgNPs (%) 2 <sup>nd</sup> chromatographic peak	AgNPs (%) Disrupting agent
Compost	>99	>99
Mountain	>99	>99
Orchard	14	15
Urban	49	48

#### 4.1.2.1.2 Capture percentage (%) of AgNPs in different sized-fractions of a given soil

For studying the effect of the soil particle sizes on NPs capture, urban soil was selected as the interaction between the matrix and AgNPs was intermediate and after sieving the soil, 5 different sized fractions in a similar proportion were obtained (values in Table 25). Thus, urban soil was sieved and the same experiment, previously performed for samples A, was repeated (i.e., the 2<sup>nd</sup> peak method), but this time on each of the 5 size fractions: below 100  $\mu\text{m}$ , 100 to 200  $\mu\text{m}$ , 200 to 300  $\mu\text{m}$ , 300 to 400  $\mu\text{m}$  and coarse fraction. The chromatograms of this experiment are presented in Figure 65. Table 28 shows the results. For the 3 larger fractions, the amount of retained NPs was comparable (the highest for the fraction with particle sizes from 300 to 400  $\mu\text{m}$ ) and slightly higher than the ones obtained for the two smaller ones. If total AgNPs retention was calculated considering these values and the proportion of each fraction in the soil, a 47% was obtained. This value is in agreement with the 48% obtained in the previous section (Table 27) and the estimation error is only 1.3. To determine statistically significant difference between means of two samples student's t-test ( $p$ -value  $< 0.05$ ) was performed and no difference was found. The effect of the soil particle size is secondary compared to the one caused by SOM.

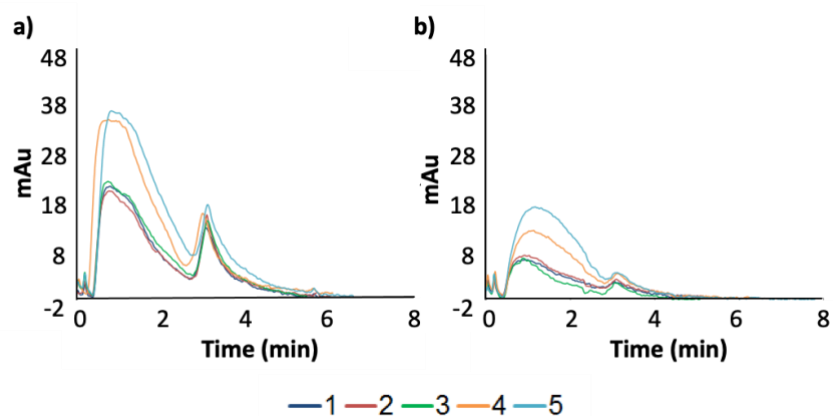


**Figure 65:** Chromatograms obtained from measuring samples: a) without and b) in the presence of 1% sodium thiosulfate for different fractions of urban soil: (1) coarse fraction, (2) 300 to 400  $\mu\text{m}$ , (3) 200 to 300  $\mu\text{m}$ , (4) 100 to 200  $\mu\text{m}$  and (5) below 100  $\mu\text{m}$  (note, exposure time of the samples to sodium thiosulfate of 50 min, 1/16 sample dilutions).

**Table 28:** Retention % of AgNPs in urban soil fractions quantified by IT-SPME-CapLC-DAD.

Fraction	Fraction (%)	AgNPs (%)
< 100 $\mu\text{m}$	18.7	39
100-200 $\mu\text{m}$	21.6	41
200-300 $\mu\text{m}$	19.6	53
300-400 $\mu\text{m}$	11.6	55
> 400 $\mu\text{m}$	28.6	50
Total	100	47

#### 4.1.2.1.3 SEM microanalysis studies

Having worked with the supernatants put in contact with a given soil, but not the soil itself, the final step consisted of estimating the amount of silver in the four studied soils by SEM microanalysis.



As AgNPs in soils could suffer different reactions [337,338], it was decided to determine the amount of total silver. The estimated elementary compositions for each soil as well as the SEM pictures can be found in Table 29 (silver values are highlighted) and Figure 66, respectively. The amounts of silver estimated by SEM for compost (0.69%), mountain (0.66%), orchard (0.35%) and urban (0.44%) soils correlated well with the calculated retention % of each soil as Figure 67 shows (with a  $R^2$  of 0.98, RSD of 3%). Though these are relative values, one can emphasize that SEM results can come at handy for quickly conceiving the amount of remaining silver in a soil after NP-contact. Note that for all the soils, amounts of Fe and Al (related to mineral oxides/hydroxides presence) were quantified, standing out the high Al% found in the mountain sample. Hydrous Fe and Al oxides were described to induce fast heteroaggregation of net negatively charged AgNPs in soils, favoring the particle deposition [339].

**Table 29:** SEM microanalysis. Elementary composition of the different soils.

	Compost	Mountain	Orchard	Urban
Element	Mass (%)			
O K	67.83	50.64	57.82	59.13
Mg K	1.30	0.37	0.91	0.99
Al K	2.69	14.98	6.86	4.82
Si K	9.83	26.76	20.14	16.42
<b>Ag L</b>	<b>0.69</b>	<b>0.66</b>	<b>0.35</b>	<b>0.44</b>
K K	2.28	2.24	2.69	1.95
Ca K	12.72	1.84	7.28	13.25
Fe K	2.66	2.51	3.96	3.01

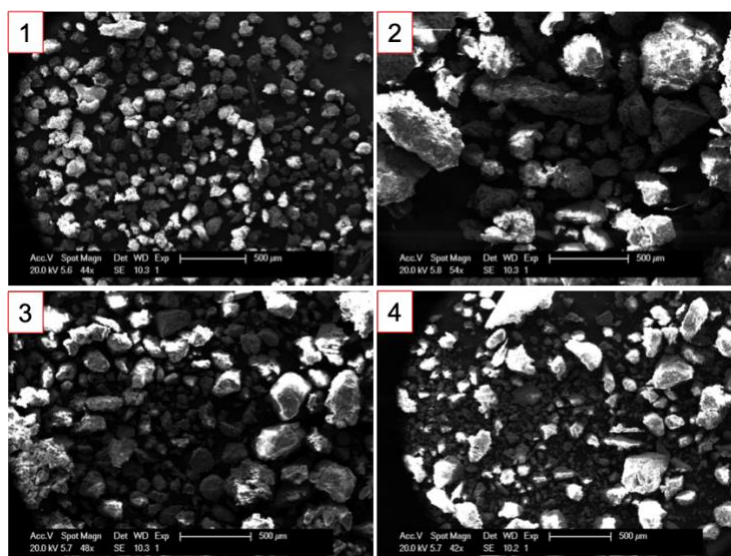


**Figure 66:** a) SEM pictures of the 4 studied soils: (1) compost, (2) mountain, (3) orchard and (4) urban.

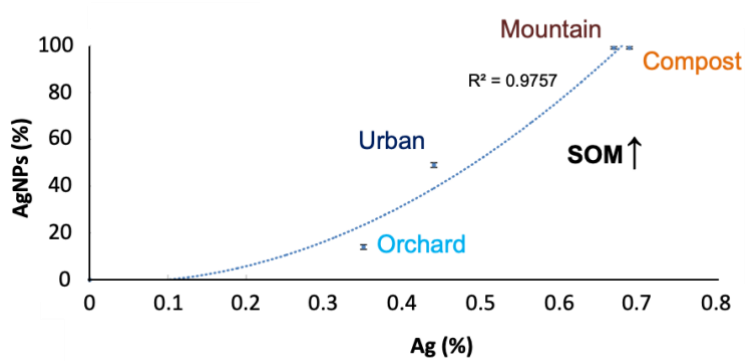


**Figure 67:** Representation of Ag amount (estimated by SEM microanalysis) vs retained AgNPs amount (estimated by the IT-SPME-CapLC-DAD method) in each soil. (n=2)

#### 4.1.2.1.4 Influence of the properties of different soils on their ability to capture AgNPs

After performing the chromatographic analysis for estimating the capture % of AgNPs for the four soils, as well as the SEM microanalysis results suggest that SOM content correlated positively with NP capture ( $r = 0.728$ ,  $p$ -value  $<0.05$ ), prevailing over other soil properties except pH, which correlated negatively ( $r = -0.879$ ,  $p$ -value  $<0.05$ ). For the HSOM group, particle retentions were quantitative. This result is in good agreement with other studies found in the literature where SOM was found to be crucial in the AgNPs retention by reducing the NP mobility in natural soils through aggregation/agglomeration induction [331] or by inhibiting the release of dissolved Ag from the soil matrix [340]. Also, SOM was described as a major binding agent of NPs through the formation of heteroaggregates [341], like Al/Fe mineral species induce [339]. For the LSOM group, orchard soil, was the most inefficient one for capturing AgNPs. In this context, the role of HAs remains to be elucidated as they were described to prevent AgNPs deposition onto soils [330] and as facilitators of the particle mobility and transport [333]. These two factors could explain the behavior of orchard vs urban soil in reference to NP capture.

Mean soil grain size affected the particle retention in a lesser extent ( $r = 0,085$ ,  $p$ -value  $>0.05$ ). However, some documented results in which the more fine the soil particle is, the greater the surface-area-to-volume ratio for interactions are and so, the inhibition of the NP transport [289]. Again, this effect is secondary to the SOM content: compost and mountain exhibited quantitative AgNPs retention although having the smallest and largest average grain sizes. The explanation of the results obtained for the different-sized fractions of the urban soil lies in the fact that as the grain size diminished the extraction of the interfering compound, identified as HAs by the proposed method, increased. The same observation can be made when comparing the soils of the LSOM group: they had similar IR spectrum, PSD, pH, EC and Eh; however, in orchard soils (which was found to have more organic content than the urban samples) the amount of HAs extracted were higher (see Figure 61 and Figure 64).

To this matter, capture % of AgNPs vs the extracted interfering compound (as  $\text{mg}\cdot\text{L}^{-1}$  of HAs) are represented for the four soils (Figure 68.a) and the different sized fractions of urban soil (Figure 68.b). It can be stated that the effect of the amount of extracted compounds is secondary for the HSOM soils, but for LSOM is

important being this amount indirectly proportional to AgNPs retention. In turn, the amount of the discussed extraction was found to be inversely related to the soil grain size in a lower degree. Therefore, extracted HAs stabilized unretained NPs in the supernatant, impeding their adsorption. As previous reports concluded, an increasing colloid stability hinders the NP adsorption onto soils [290].

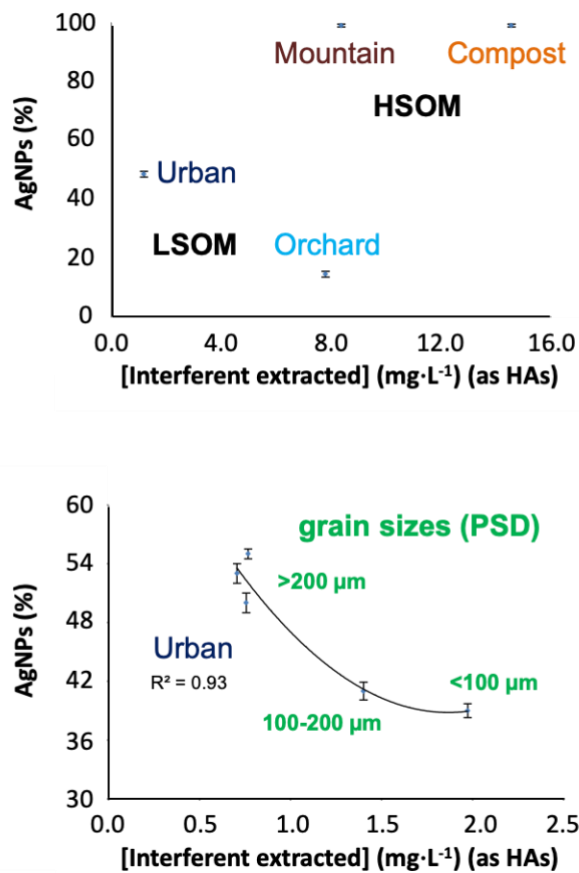


**Figure 68:** Capture % of AgNPs vs the extracted interfering compound (as mg·L<sup>-1</sup> of HAs): a) for the 4 studied soils (LSOM: low-containing SOM; HSOM: high-containing SOM); b) for different-sized fractions of the urban soil. (n=2)

Finally, the effect of other soil properties was assessed. For pH and Eh, results corroborate the literature findings [290,340]: pH > 7 and lower Eh values which inhibit the Ag release from the soil matrix enabled NP retention. EC values,

proportional to the IS of the medium [326,327], were higher for the HSOM soils, as well as lower and similar for the LSOM ones. It was described that a high IS allows the compression of the double layer of AgNPs and soil surfaces resulting in deposition, matching the obtained results.

- Conclusions

In this study, IT-SPME-miniaturized LC-DAD has been proposed as a powerful tool to characterize MNPs. The miniaturized LC systems improved sensitivity and resolution, meanwhile IT-SPME coupling permitted to detect differences in the distribution of polarized and nonpolarized noble MNPs in the bulk dispersion. As a result, two different peaks are obtained, the first one with minimal interaction with the IT-SPME extractive phase (size exclusion separation mechanism), and second with stronger interaction between the noble NPs distribution and the extractive phase (hydrophobic effect separation mechanism).

In order to evaluate the effect of MNPs in environmental samples, estimations of AgNPs capture in different soils by combining on-line IT-SPME, miniaturized LC and measuring the change of SPRB were done for the first time. Studies were carried out by mixing an amount of soil with AgNPs dispersions and after performing the corresponding procedure, quantification of the NP adsorption % was possible.

Through the signal loss at 400 nm (SPRB maximum), capture % of AgNPs were calculated in compost (N99%), mountain (N99%), orchard (15%) and urban (48%) soils. For the latter and after sieving, retention % of AgNPs were obtained in the resulting fractions being slightly higher for the larger-sized ones. So, AgNPs capture on a given soil is mainly affected by the amount of SOM and secondary, by properties such as the soil particle size pH, EC and Eh. In soils with lower content of organic matter, it was found that compounds (including HAs) extracted by the NP matrix stabilize unretained AgNPs, hindering their adsorption. SEM microanalysis in each soil supported the obtained results.

Considering that each soil retained NPs differently, the proposed methodology made it possible to characterize and quantify the AgNPs-soil interaction by measuring the variation of the SPRB, characteristic property of the NPs, opposed to mass detection. The particle retention in different soils could be

assessed in a simple and cost-effective way, allowing one to quickly evaluate the soil potential for adsorbing NPs considering its properties, which can be useful for their administration, characterization or even remediation. The present work represents a step forward in understanding the behavior of AgNPs when exposed to complex environmental scenarios and a valuable one taking into account the reduced number of studies of NPs in solid matrices.

### ***4.1.3 AuNPs and AgNPs to develop plasmonic assays***

#### **4.1.3.1 Monitoring plasmonic assays by AF4-UV-vis-DLS**

##### *4.1.3.1.1 Nanoparticle assessment*

For studying plasmonic assays by AF4 technique. Three different batches of AgNPs 20 nm selected as a use case were assayed. Figure 69 shows the fractograms and their spectra, as it can be seen two of them (batches 1, 2) were similar, but the responses of the other (batch 3) were so different by AF4 with both UV-Vis and DLS detectors. A displacement of the retention time of the maximum of the peak is seen up to 16 min for batch 3, compatible with the presence of larger NPs, as well as a considerable decrease in their signal at  $\lambda = 395$  nm, which can respond to a lower mass of AgNPs. In addition, the DLS data determine a mean DH around 2 nm greater than those of the rest of the batches, as shown in Table 30. By UV-vis spectroscopy, all batches present a similar surface plasmon band (SPR band), although batch 3 shows certain differences, since it provides somewhat lower absorption and a slight bathochromic shift, which could be consistent with slightly larger AgNPs.

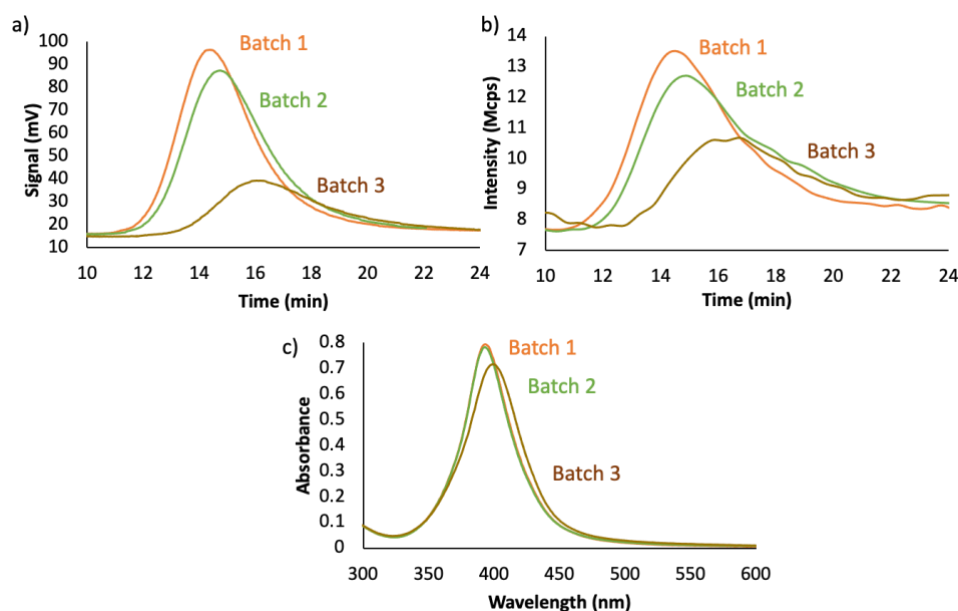


**Figure 69:** Fractograms of three different batches of AgNPs 20 nm diluted 1/4 with ultrapure water ( $5 \mu\text{g}\cdot\text{mL}^{-1}$ ) with a) UV-vis detection, b) DLS detection, and c) their spectra.

**Table 30:** Wavelength values ( $\lambda$ ) of the plasmon maximum, width of the peak at half the maximum, extinction coefficient ( $\epsilon_{\text{max}}$ ) obtained by UV-vis spectroscopy and DH by DLS for three different commercial batches of AgNPs.

Batch	$\lambda$ (nm)	Width <sub>1/2</sub> (nm)	$\epsilon_{\text{max}}$ ( $\text{mM}^{-1}\cdot\text{cm}^{-1}$ )	DH <sup>a</sup> (nm)
3	$397.6 \pm 2.4$	$50.2 \pm 0.1$	$15.43 \pm 0.02$	$22.3 \pm 2.4$
2	$393.4 \pm 2.0$	$42.7 \pm 0.2$	$16.83 \pm 0.05$	$20.5 \pm 3.1$
1	$393.1 \pm 2.2$	$42.8 \pm 0.2$	$17.05 \pm 0.03$	$20.1 \pm 3.0$

<sup>a</sup> Confidence interval  $\alpha = 0.01$

The fractogram recorded using the DLS detector signal indicates a decrease in the intensity of the scattered light for batch 3 with respect to the rest (see Figure 69.b), which signifies the presence of a smaller quantity of AgNPs. Phenomena such as dissolution and/or passivation could be considered to be a consequence of prolonged exposure to atmospheric conditions of batch 3 [318]. A part of the AgNPs could be dissolved and released in the form of  $\text{Ag}^+$ , or it could be oxidized, generating a surface film of  $\text{Ag}_2\text{O}$ , whose formation can be compatible by a bathochromic shift, as well as a lower height and broadening of the plasmon by UV-

vis spectroscopy (see Table 30 and Figure 69.c) [318,342]. In this case, the main differences between batches could be related with the time that each of them has been exposed to the atmosphere, and consequently, with the renewal of dissolved oxygen in the suspension. If the AF4 records are compared with those obtained by UV-Vis spectroscopy, it should be noted that the AF4 technique shows a greater discrimination capacity in the characterization of aqueous dispersions of AgNPs, providing besides more information about mass and size.

We selected batch 1 for plasmonic assays involving hydrochloric acid and HAc. Figure 70 shows the spectra obtained by UV-vis spectrometry corresponding to these assays at 10 min, which are compatible with aggregation processes. By decreasing the pH of the medium, a reduction in the height of the plasmon can be observed accompanied by an increase in the absorption at higher wavelengths until the formation of a second peak whose wavelength undergoes a bathochromic shift with time and with the concentration of acid used. For hydrochloric assay, the disappearance of this second peak is observed to give rise to a continuous band of absorption related with the formation of large-sized NPs that can be part of a polydisperse suspension of AgNPs of a wide range of sizes capable of scattering light from the visible spectrum and near-infrared range (NIR). The footprints of two acids were different, the changes for HAc are slower than those shown for hydrochloric acid by assaying the same concentrations (between 1.5 and 15 mM), which can be related by its acid-base strength.



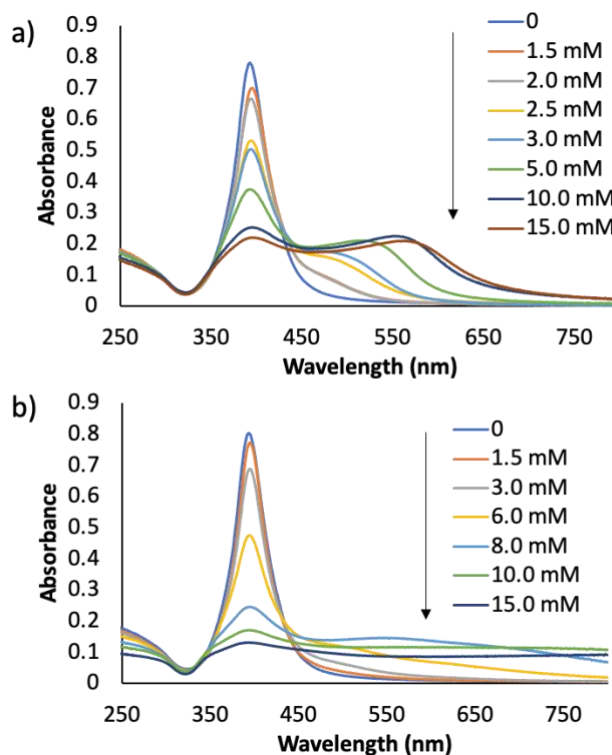


**Figure 70:** UV-vis spectra recorded after 10 min. corresponding to the suspension of AgNPs in a 1/4 dilution ( $5 \mu\text{g}\cdot\text{mL}^{-1}$ ) in the presence of different concentrations of a) HAc and b) hydrochloric acid.

#### 4.1.3.1.2 Analysis of different acids by AF4-UV-vis-DLS

The kinetics of the acid aggregation was monitored by AF4-UV-vis-DLS. Figure 71 shows the fractograms corresponding to the dispersion of AgNPs in 1.5 and 3.0 mM of HAc at several times since their preparations. The signal variation at 3.0 mM HAc was higher than the signal variation in presence of 1.5 mM HAc. By reducing the pH, a decrease in the height of the peak with time was observed in the fractograms recorded using the UV-vis detector (Figure 71.a and c). In addition, a slight in the retention times was observed. The fractograms recorded using the DLS detector (Figure 71.b and d) show a significant increase in retention time with time, as well as a slight increase in peak intensity, which indicate a shift in the size distribution of the AgNPs toward greater dimensions. These observations were compatible with aggregation of AgNPs, since there was a decrease in the intensity

of the plasmon wavelength and a growth with time in the size of the NPs, as it can be seen in the DH data in Figure 71.b and d. Likewise, a higher speed was observed, as well as a larger size of the aggregates when the pH decreases [343,344].

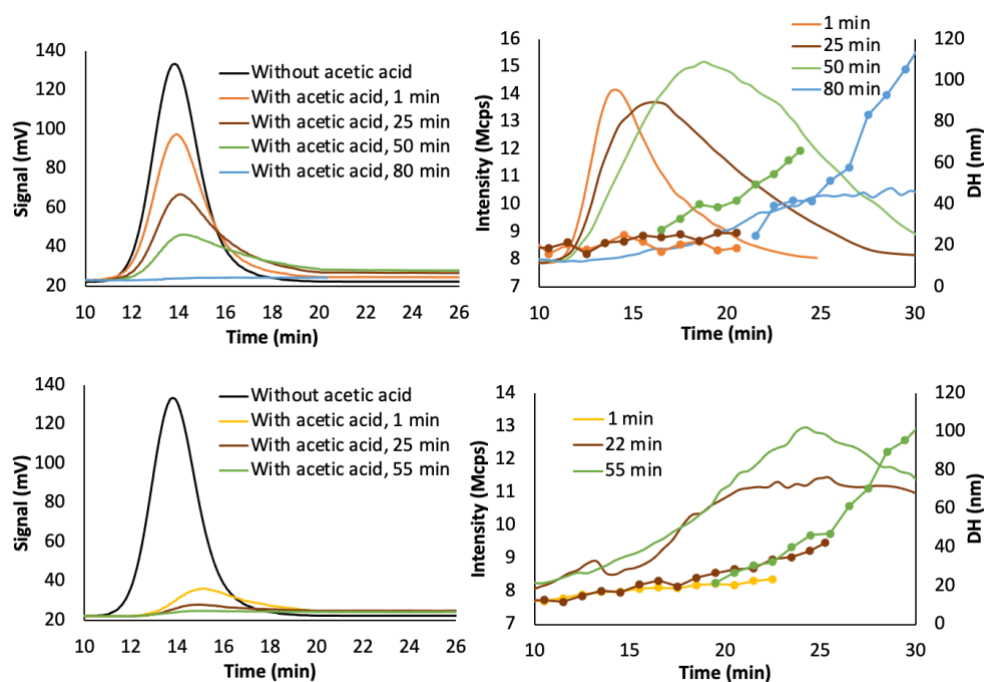


**Figure 71:** Fractograms with UV-vis detection corresponding to suspensions of AgNPs in a 1/4 dilution ( $5 \mu\text{g}\cdot\text{mL}^{-1}$ ) and a) 1.5 mM or c) 3 mM HAC at different times. Fractograms with DLS detection and DH corresponding to the same suspensions at different times (b and d) respectively.

Under acidic pH conditions, the citrate capping, which provides stability to AgNPs, progressively lost its effectiveness by decreasing the surface negative charge density; the Z-potential in the interface that separates the Stern layer and the diffuse layer was less negative by reducing the pH of the medium [345]. NPs lost the repulsive forces that counteract the attractive van der Waals forces by removing the surface coating that protects them, thus facilitated their aggregation. It was observed with the exposure time that fractograms with a lower intensity of light scattering were recorded by the DLS detector as it can be seen in Figure 71.b, which occurred more rapidly at lower pH (see Figure 71.d). A greater tendency to oxidation of the NPs and release to the environment in the form of  $\text{Ag}^+$  as the pH

decreases has also been described [346]. However, it must also be taken into account that the aggregation process implies the formation of sets of NPs from others of a smaller size, which can lead to a significant reduction in their total number. Specifically, for the formation of 100 nm NPs dozens of 20 nm NPs may be necessary depending on the morphology of the final aggregates. This fact can also cause a decrease in the intensity of scattered light registered by the DLS detector when aggregates of size much larger than the initial NPs are formed. Thus, these aggregates can cause a greater scattering of light, but there are much fewer of them.

In this sense, the response of the AgNPs to the action of different acids, consisted of the loss of protection against the aggregation process, which could be observed by the decrease and the bathochromic shift in the plasmon (SPR band) using UV-vis spectroscopy, related with the increase in retention times, loss of area and higher DH values showed by AF4-UV-vis-DLS. Likewise, reducing the pH of the suspensions increased the aggregation speed, as well as it could facilitate the oxidation and/or dissolution of the AgNPs surface. These statements should be considered for developing plasmonic assays for quantifying analytes properly.

Figure 72 shows the normalized absorbance values obtained by UV-vis spectrometry at different times for each of assayed suspension against the concentration of HAc (Figure 72.a) and hydrochloric acid (Figure 72.d). A sinusoidal response was observed which for a certain range of concentrations, offers linearity in the change trend of absorbance with the acid concentration at a given time. This trend constitutes the basis on which plasmonic assays for the detection and/or quantification of substances are based [47,104]. Other possibilities are transforming the concentrations in their logs (see Figure 72.b) or employing the maximum wavelength of the aggregated NPs for quantifying as it is done for HAc calibration (see Figure 72.c). For all types of calibration graphs, the time influenced their equation and also the linear interval of concentrations (see Figure 72.b and e), sensitivity and accuracy of the assay as can be reflected in Figure 72. Those aspects should be considered when the plasmonic assay is carried out.

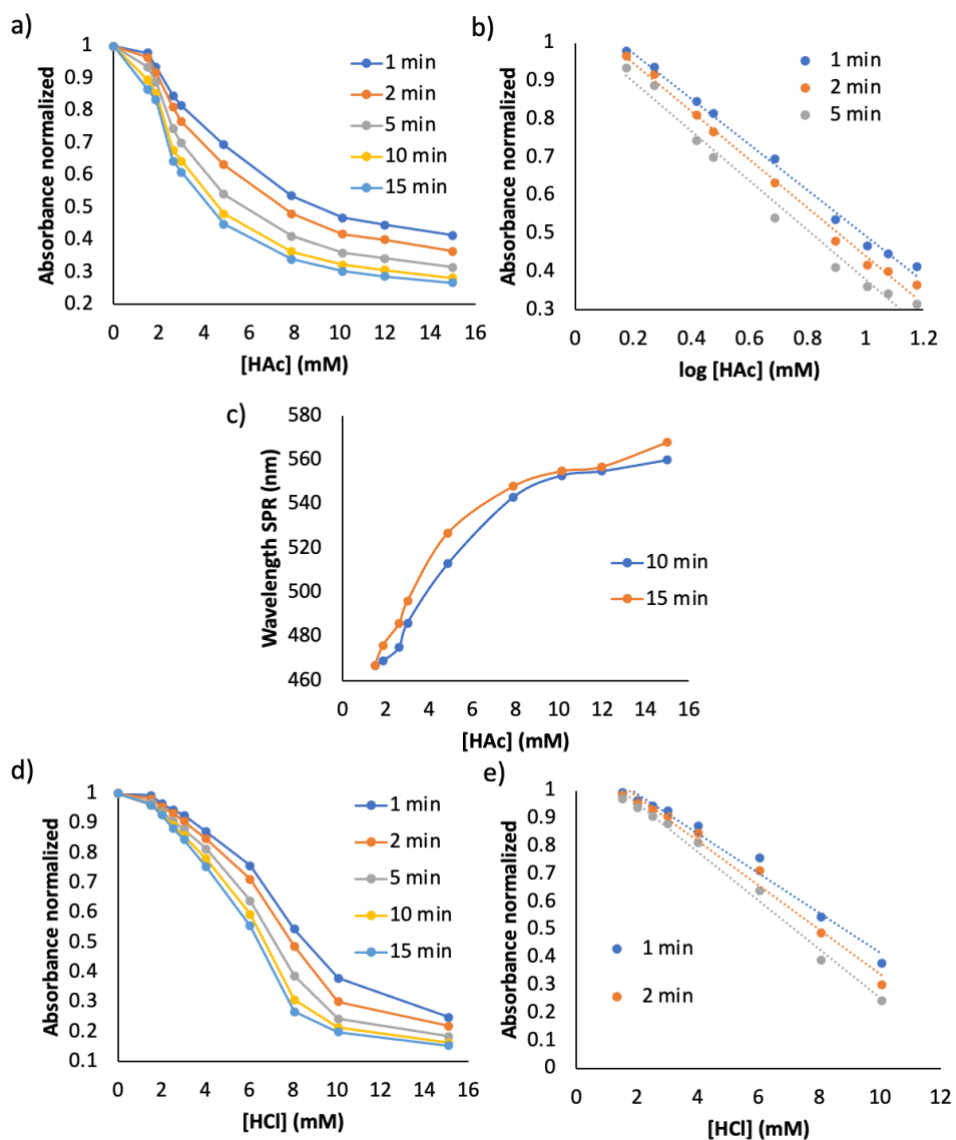


**Figure 72:** Normalized absorbance values at various times with the concentration of a) HAc, b) its log of AgNPs diluted 1/4 ( $5 \mu\text{g}\cdot\text{mL}^{-1}$ ) and c) evolution of the wavelength of the second plasmon maximum in the UV-vis spectra at 10 and 15 min of its preparation. d) and e) correspond to the influence of hydrochloric acid.

Mainly, the application of AF4-UV-Vis-DLS provides new information about transformations that analytes induce in NPs and aid to fix the experimental variables, which must be controlled for obtaining reliable results. Besides, taking into account the great discrimination capacity of AF4 for explaining transformations generated in aqueous dispersions of NPs, their use could increase assay sensitivity if necessary. Note that the dispersions assayed by AF4 corresponded to the lower concentrations tested by UV-vis spectroscopy (see Figure 71 and Figure 72 for comparison). In this sense, establishing the equation of the AF4 calibration graphs for plasmonic assays is outside the goal of this study.

#### **4.1.3.2 Monitoring plasmonic assays by IT-SPME-miniaturized LC-DAD**

##### *4.1.3.2.1 Nanoparticle assessment*

Several target analytes of different nature were chosen to study the aggregation profiles of the several assayed NPs by UV-vis spectrometry. Figure 73 a - d shows the aggregation profiles obtained as a function of time for some commercial NPs by adding HAc. For the same capping and size, AgNPs provided more sensitivity than AuNPs for HAc aggregation (see Figure 73.a and b). When the two type of noble NPs were employed together the responses were additive as it can be seen in Figure 73.c. Spermine was also assayed, but no aggregation was obtained at levels assayed for these kinds of NPs. The extension of aggregation depended on the capping of AuNPs for the same size as it can be seen in Figure 73.b and d.

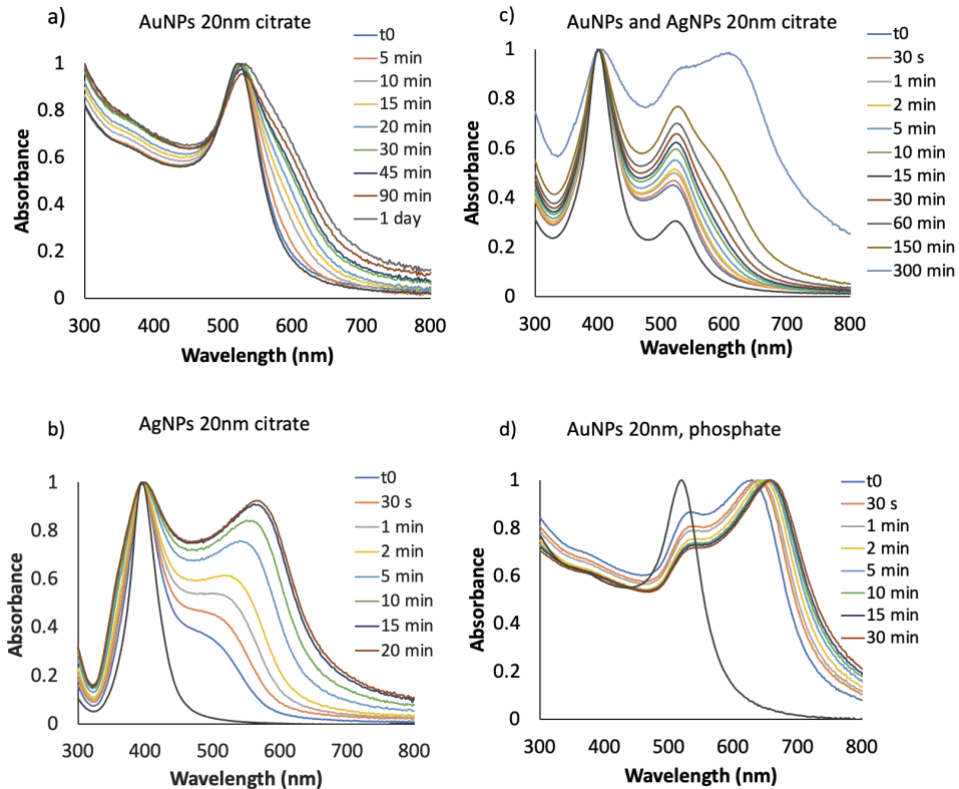


**Figure 73:** Aggregation profiles due to HAC as a function of time of: a) citrate capped AuNPs 20 nm diluted (1/4) in HAC 10% (v/v); b) citrate capped AgNPs 20 nm diluted (1/2) in HAC 0.2% (v/v); c) a mixture of citrate capped AuNPs and AgNPs 20 nm diluted (1/4) in HAC 0.7 % (v/v); d) and phosphate capped AgNPs 20 nm diluted (1/4) in HAC 0.2 % (v/v), obtained by UV-vis spectroscopic measurements.

The aggregation profiles obtained by UV-vis spectroscopy for each group of naked AuNPs as a function of successive additions of HAC and SPN are shown in Figure 74 and Figure 75, respectively. It should be noted that concentration levels for HAC was up to mM to observe aggregation effects by it for naked AuNPs (I). As can be seen, in Figure 74.a, aggregation was not observed at concentration level up to 0.8 mM of HAC, which meant they remained stable upon the addition of HAC. However, at higher concentration level, we observed aggregation as a linear function of the concentration level of HAC, resulting in an interval up to 2mM (Figure 74.c). AuNPs(II) group aggregated with a different profile than AuNPs(I) group. As can be seen, in Figure 74.b and d, these NPs were aggregated at

concentration lower than 0.4 mM of HAc and the saturation was reached up 1.2 mM. Therefore, in terms of plasmonic assays, AuNPs(I) and AuNPs(II) could be used to monitor interaction with  $[H^+]$ , depending on their concentration levels.

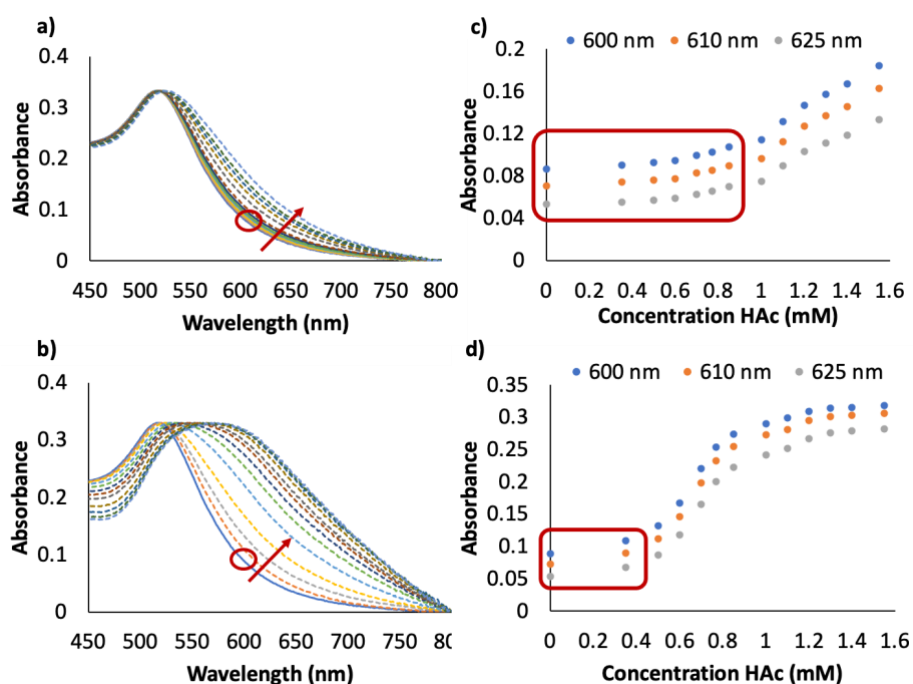


**Figure 74:** Aggregation profiles as a function of HAc concentrations by using UV-vis spectroscopy for (a) AuNPs(I) and (b) AuNPs(II) [Continuous line: no aggregation; dotted line: aggregation]. Working  $[H^+]$  concentration intervals, expressed as  $[H^+]$ , for each (c) AuNPs(I) and (d) AuNPs(II).

The behavior of naked AuNPs(I) and AuNPs(II) showed significant differences for SPN, these can be seen by comparing Figure 75.a and b. Working concentration interval for SPN was up to  $40 \mu\text{g}\cdot\text{L}^{-1}$  for AuNPs(II), meanwhile for AuNPs(I) was up to  $250 \mu\text{g}\cdot\text{L}^{-1}$ , see Figure 75.c and d, respectively. Indeed, signal saturation was reached at different concentration levels depending on the AuNPs used. These results can be correlated with the different chromatographic profiles obtained for AuNPs(I) and AuNPs(II). The AuNPs with predominant polarized distribution provided the lower aggregation concentration interval, however, AuNPs showing both effects (see Figure 52) (polarized and non-polarized) provided

extended aggregation concentration intervals, which corresponded to AuNPs(I). AuNPs(I), in presence of HAC at concentration up to 0.8 mM can be suitable to monitor other analytes (see Figure 74.c), since these concentrations did not aggregated NPs.

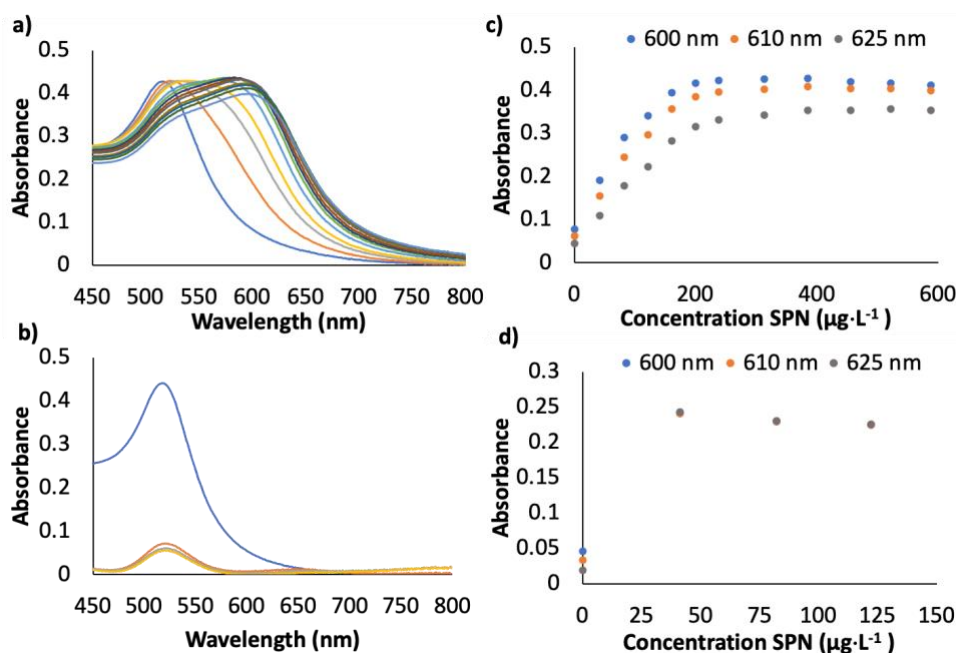


**Figure 75:** Aggregation profiles as a function of SPN concentrations by UV-vis spectroscopic measurements for a) naked AuNPs(I) and b) naked AuNPs(II). Working SPN concentration intervals for c) AuNPs(I) and d) AuNPs(II).

Hence, these results indicated that AuNPs(I) were suitable to monitor SPN and  $[H^+]$ , however AuNPs(II), would not be suitable to monitor SPN, and only interaction with  $[H^+]$  can be studied as commercial citrate capped AuNPs 20 nm, both of them with similar chromatographic profiles. IT-SPME coupled to miniaturized LC is a powerful tool for establishing the suitability of a given batch to carry out a given plasmonic assay as it is demonstrated here employing less than 10 min.



*4.1.3.2.2 Analysis of spermine and different acids by IT-SPME-miniaturized LC-DAD*

The next step was to evaluate the use of the IT-SPME-CapLC-DAD and IT-SPME-NanoLC-DAD for developing plasmonic assays. Figure 76 and Figure 77 depict the variation of naked AuNPs(I) as a function of the addition of SPN and HAC. The addition of SPN or HAC to a dispersion of naked AuNPs(I) gave rise to the aggregation of AuNPs, that was observed by means of the color change from red to blue purple (Figure 76.a). Figure 76.b shows a scheme of the separation achieved in the IT-SPME capillary in accordance with the two populations, polarized and non-polarized provided for each batch dispersion. These assays are based on the absence of a competitive organic capping on the naked gold nanoparticles and together with the high affinity of the amine groups for the nanoparticle surface for spermine [47]. As can be seen in Figure 77.a and b, the successive analyte additions resulted in changes in area of the two peaks and in the ratio between the two peaks for spermine additions. The variation of the spectra profile for chromatographic peak at 3 min showed that the decrease in the peak area was directly related with the variation of the LSPR signal due to aggregation of AuNPs since it was observed the band shift depending on the SPN concentration in the sample (see Figure 77.a, insets). As can be seen, the first chromatographic peak did not response to the SPN concentration. At low SPN concentration, aggregation was only observed in the peak corresponding to nonpolarized AuNPs. At concentrations higher than  $66 \mu\text{g}\cdot\text{L}^{-1}$ , the first peak also decreases.

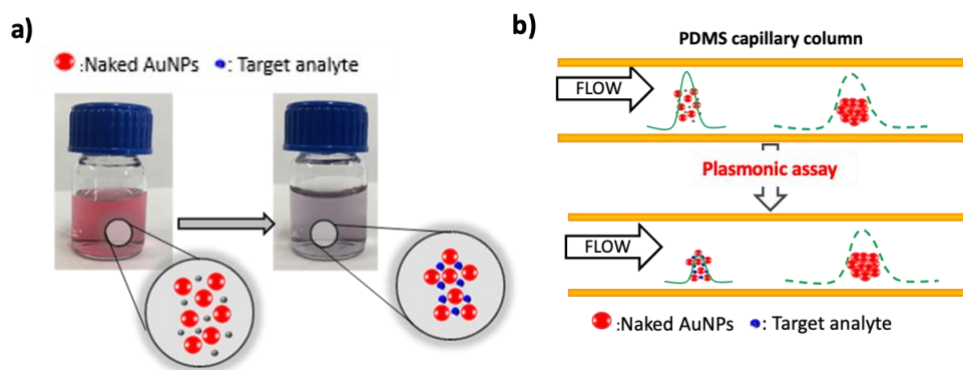


**Figure 76:** a) Schematic representation of the visual inspection, b) Variation of the chromatographic profiles inside of the capillary column in presence of target analyte.

Sensitivity of the assay by IT-SPME-CapLC-DAD was higher than that achieved by spectrophotometric measurements (see Figure 75.a and c, and Figure 77.a). Figure 77.a showed a progressive aggregation as a function of the SPN concentration ( $41$ ,  $66$  and  $82 \mu\text{g}\cdot\text{L}^{-1}$ ), which gave rise to a good discrimination of SPN concentrations (Figure 77.a, inset). This aggregation was also observed in the decrease of the chromatographic peak at  $t_r = 3.1$  min, which corresponded to the signal provided for non-polarized AuNPs in the bulk distribution. Moreover, it must be highlighted that it was possible to correlate the SPN concentration and the chromatographic area of this second peak. This fact can mean that non-polarized NP population is responsible of aggregation due to SPN. The linear regression equation was  $\text{Area} = (670 \pm 54) + (-7600 \pm 700)[\text{SPN}]$ ;  $R^2 = 0.99$ . It should be remarked that peak area was defined and calculated integrating the first and second chromatographic peak from their respective baselines to the inflection point corresponding to the coelution of both NPs populations.

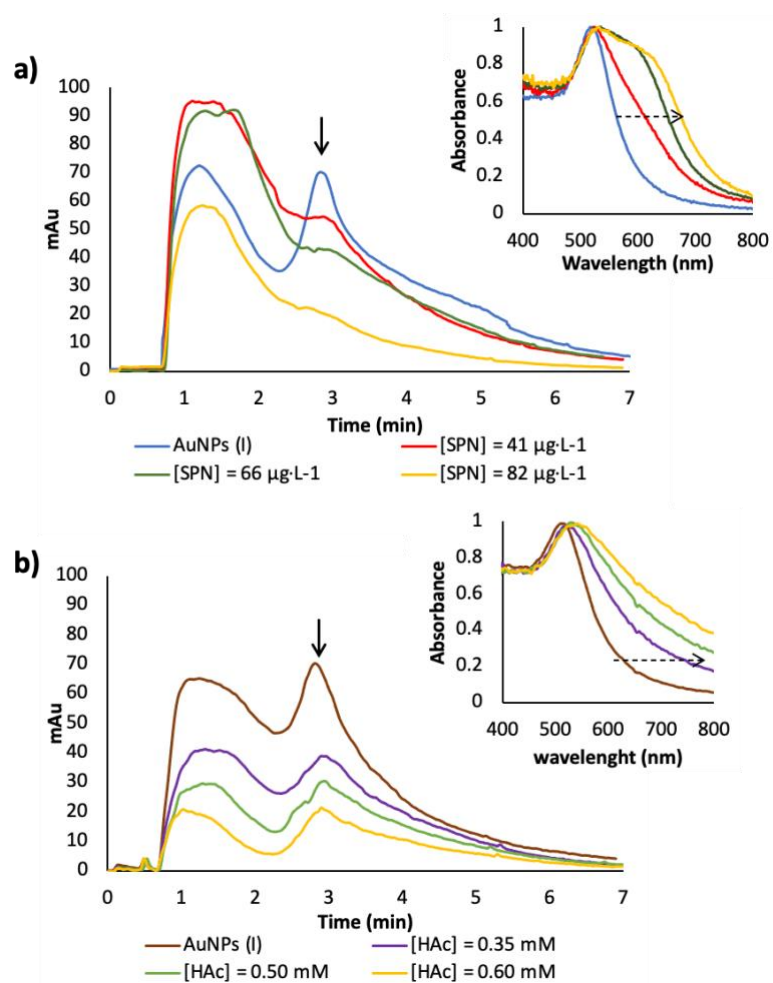


**Figure 77:** a) Chromatograms obtained for naked AuNPs(I) as a function of the added concentration of SPN [ $41 \mu\text{g}\cdot\text{L}^{-1}$  in red,  $66 \mu\text{g}\cdot\text{L}^{-1}$  in green and  $82 \mu\text{g}\cdot\text{L}^{-1}$  in yellow]; and b) chromatograms obtained for AuNPs(I) as function of the added concentration of HAc [0.35 mM in purple, 0.50 mM in green and 0.60 mM in yellow]. Insets: variation of the LSPR band of the chromatographic peak at  $t_r = 3.0$  min with the successive additions of target analyte.

Figure 77.b shows the variation of the chromatographic profiles as a function of the added concentration of HAc (0.35, 0.50 and 0.6 mM). It was observed that under the experimental conditions, both chromatographic signals decreased as a function of the added acid and their ratio remains unchanged, and this decrease was correlated with the HAc concentration. The same study was

carried out by using naked AuNPs(II). Figure 78 shows the chromatographic profiles of AuNPs(II) as a function of different additions of SPN (a) and HAC (b).

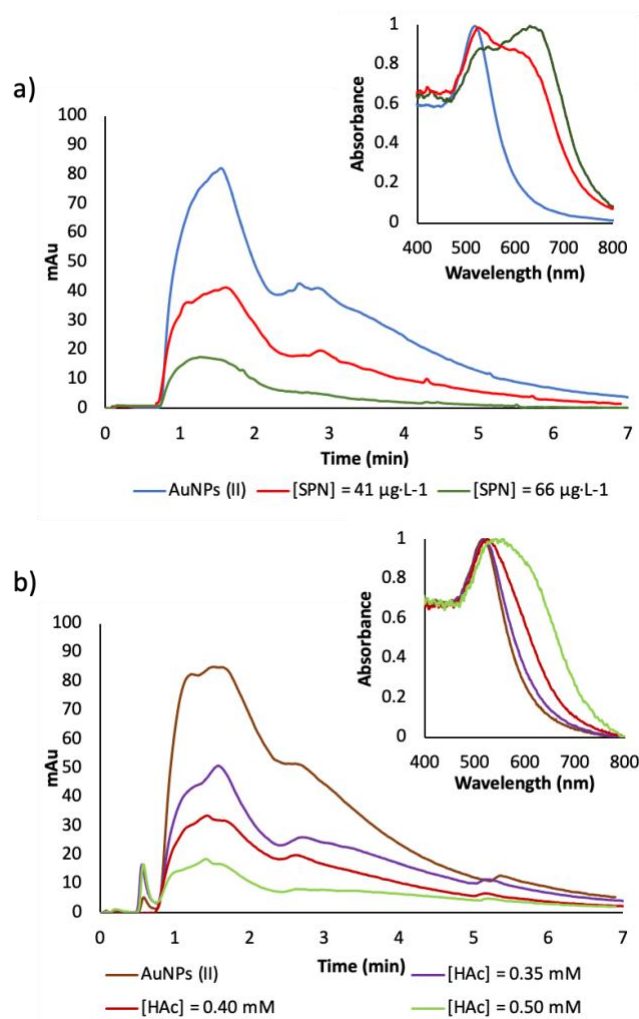


**Figure 78:** Chromatograms obtained for AuNPs(II) as function of the added concentration of a) SPN [ $41 \mu\text{g}\cdot\text{L}^{-1}$  in red and  $66 \mu\text{g}\cdot\text{L}^{-1}$  in green] and b) HAC [0.35 mM in purple, 0.40 mM in red and 0.50 mM in green]. Insets: variation of the LSPR band of the chromatographic peak at  $t_r = 3.0$  min with the successive additions of target analyte.

Contrary to the results obtained with AuNPs(I), monitoring of the plasmonic assay evolution using AuNPs(II) for SPN was not possible since in this case (Figure 78.a for spermine), the working concentration interval was shortened, since

AuNPs(II) were completely aggregated by adding low SPN concentrations (41 and 66  $\mu\text{g}\cdot\text{L}^{-1}$ ). Thus, these NPs were limited to be applied for this plasmonic assay since the concentration discrimination was very poor. Acidity analysis with AuNPs(II) provided aggregation upon the addition of HAC at different levels of concentration (0.35, 0.40 and 0.50 mM) (Figure 78.b). The kinetic aggregation was accelerated at pH acidic values since it helps to promote electrostatic bridging between different NPs and depends not only on the pH but also on the counterion [347,348]. To demonstrate this effect in the naked AuNPs, the influence of different acids was studied (HAC, phosphoric acid and hydrochloric acid) by measuring the decrease of the peak area as a function of the  $[\text{H}^+]$  for each acid. The results indicated a linear correlation between peak area and  $[\text{H}^+]$  concentration for the three acids ( $R^2 = 0.99$ , 0.99 and 0.999 for  $\text{CH}_3\text{COOH}$ ,  $\text{H}_3\text{PO}_4$  and  $\text{HCl}$ , respectively). However, the slopes were  $- 8600 \pm 800 \text{ mM}$ ,  $- 1700 \pm 200 \text{ mM}$  and  $- 556 \pm 17 \text{ mM}$  for  $\text{CH}_3\text{COOH}$ ,  $\text{H}_3\text{PO}_4$  and  $\text{HCl}$ , respectively. This suggested that, at least under the experimental conditions of this work, aggregation is produced by a decrease on the  $\zeta$ -potential and this decrease bridged of one nanoparticle to another by cross-linking inducing the aggregation. To demonstrate this, Z-potential of three different batches of AuNPs before and after the aggregation was measured. The values before aggregation were  $- 37 \pm 1$ ,  $- 36.3 \pm 0.1$  and  $- 34 \pm 1 \text{ mV}$ , for the three batches analyzed. After the addition of  $\text{CH}_3\text{COOH}$ , these values decreased to  $- 19 \pm 3$ ,  $- 22 \pm 1$  and  $- 19 \pm 1 \text{ mV}$ , for the three batches, respectively. The counterion imparting the strongest repulsive inter-particle interaction due to a higher charge density facilitated the dispersion stability, and therefore the lowest slope. It should be noted, that this effect was only observed in acidic conditions, since the addition of the corresponding salts ( $\text{CH}_3\text{COONa}$ ,  $\text{Na}_2\text{HPO}_4$  and  $\text{KCl}$ ), did not show variation on the signal.

Commercial NPs with different capping, citrate and phosphate, were assayed by aggregation from HAC. As it can be seen in Figure 79.a and b, different plasmonic bands were obtained in function of the capping for both, IT-SPME-NanoLC-DAD and UV-vis spectroscopy (see Figure 73.a and d). The kinetic of the process was slower for citrate capped AuNPs than for phosphate capped AuNPs 20 nm as discussed in the previous section. Using citrate AgNPs 20 nm the sensitivity of the assay for acetic was increased markedly as Figure 79.c and d show. These figures give the chromatograms and the spectra registered at the maximum of the two peaks for AgNPs and aggregated AgNPs adding 35 mM HAC. The spectra are in

accordance with the kinetic obtained by UV-vis spectroscopy (see Figure 73.b). However, the sensitivity achieved by naked AuNPs was the best (see Figure 74).

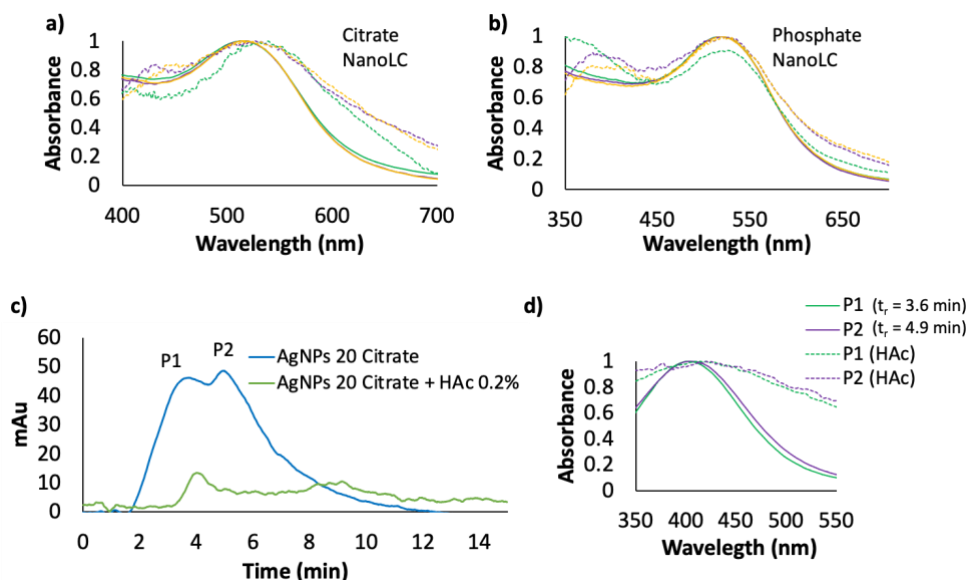


**Figure 79:** Aggregation profiles of AuNPs 20 nm a) citrate capping and b) phosphate capping diluted 1/4 with ultrapure water by acetic acid 1.75 M; the normalized spectra were obtained at the maximum of the two chromatographic peaks. c) Chromatographic profiles of citrate capped AgNPs 20 nm diluted 1/4 with ultrapure water and their aggregation adding acetic acid 35 mM. d) Normalized spectra at the maximum of the two chromatographic peaks of AgNPs 20 nm diluted 1:4 with ultrapure water and their aggregation by ITSPME-NanoLC-DAD.

An intermediate sensitivity was obtained if mixtures of AuNPs and AgNPs are used as it can be derived from Figure 80.a and b, being the concentration of acid acetic used 116 mM. The chromatograms were obtained at 400 and 530 nm corresponding to the plasmonic bands of AgNPs and AuNPs, respectively. From these studies it is derived that the aggregation assay can be optimized in function on the need concentration of HAc to test.

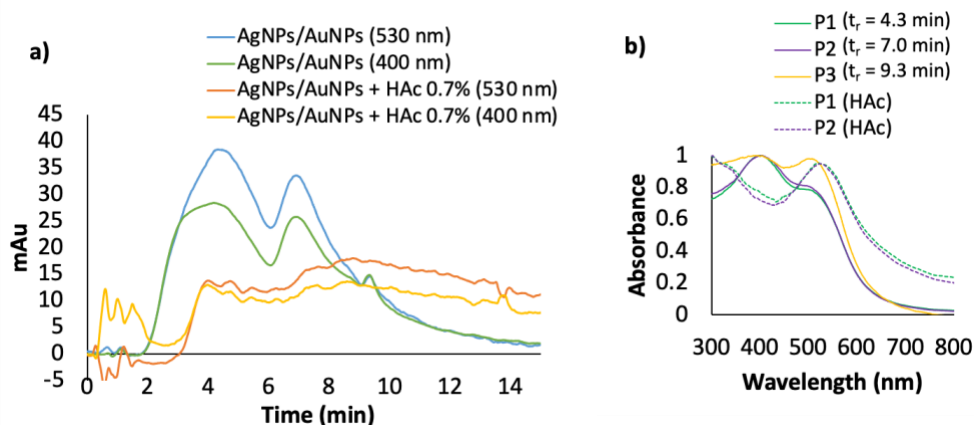


**Figure 80:** a) Chromatographic profiles of citrate capped AgNPs 20 nm and AuNPs 20 nm diluted 1/4 with ultrapure water and their aggregation adding acetic acid 116 mM. b) Normalized spectra at the maximum of the three chromatographic peaks of AgNPs 20 nm and AuNPs 20 nm diluted 1/4 with ultrapure water and their aggregation by IT-SPME-NanoLC-DAD.

To evaluate the practical application of the chromatographic method to monitor plasmonic assays, urine samples of healthy volunteers and cancer patients were analyzed following the assay described in our previous study to determine spermine (SPN) by Uv-vis spectroscopy [47]. It should be remarked that SPN has been used as cancer biomarker in urine samples in previous studies. This plasmonic assay is based on the SPN extraction by SPE with HAc (see Section 3.3.4.1.1). Therefore, contribution of both compounds must be taken into account. Extracted analyte was then added to the AuNPs dispersion in order to obtain the LSR analytical signal through the chromatographic analysis. Moreover, this assay was carried out for healthy volunteers and for cancer patients in order to study the variation in the chromatographic profiles.

Figure 81 shows the chromatographic profiles when urine samples from healthy volunteer sample (Figure 81.a) and cancer patient sample (Figure 81.b) were processed. As can be seen, chromatographic profiles allowed detecting differences in the SPN content in healthy volunteers compared with cancer patients, since aggregation in the former were lower and any change in the ratio of the two chromatographic peaks was obtained. The variation of profiles was related with the SPN concentration in each type of sample which was correlated to the

presence of the cancerous processes [47]. In this previous study, it was demonstrated that SPN can be used as a biomarker of cancerous processes and can be selectively detected by aggregation of naked AuNPs, after an SPE step to extract the amine.

In order to understand the differences with UV-vis measurements, the same samples were analyzed with UV-vis spectrophotometry (Figure 81.c and d for healthy and cancer patients, respectively). In this assay, urine for healthy volunteer and patient was added to AuNPs(I) and the spectroscopy signal was recorded for 3 min in intervals of 20 s.

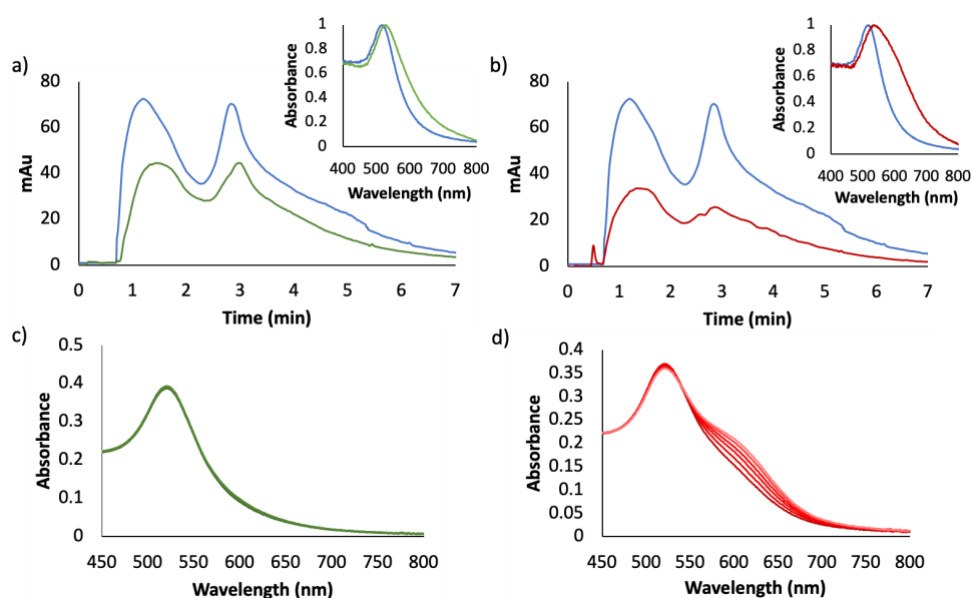


**Figure 81:** Chromatographic profiles of AuNPs(I) for a) healthy volunteer sample and b) cancer patient sample. Insets: LSPR band variation for the chromatographic peak at  $t_r = 3.0$  min. Kinetic spectroscopy study for 3 min in intervals of 20 s for c) healthy volunteers and d) cancer patients.

As above mentioned, spectroscopic signal provided a lower sensitivity than chromatographic signal. Indeed, aggregation for healthy volunteer was not observed, even at reaction time comparable with the retention times obtained in the chromatographic system (Figure 81.a). In the case of cancer patients, the aggregation was observed as a function of the contact time when using



spectroscopy, but with lower sensitivity compared with the analytical response reached with chromatography.

Finally, quantification of SPN in the cancer patient sample by using IT-SPME-CapLC-DAD was evaluated. Figure 82 shows the chromatographic profiles for AuNPs(I), acid extract and SPN at different concentration level was added and the variation when the SPN was performed (see Section 3.3.4.1.1). As can be seen, the addition of AuNPs to a urine sample induced AuNPs aggregation, its response can be quantified and therefore, the SPN concentration in urine sample can be estimated. SPN can be estimated by taking as analytical response the difference between blank signal ( $t_r = 3.1$  min) and the signal of the SPN spikes. The results indicated a linear correlation  $\text{Area} = (-3 \pm 8) + (8400 \pm 500)[\text{SPN}]$ ;  $R^2 = 0.9969$ . Finally, using this equation, the SPN concentration in urine can be estimated, and it was  $83 \mu\text{g}\cdot\text{L}^{-1}$ . This result was in agreement with the results given in the previous work [47].

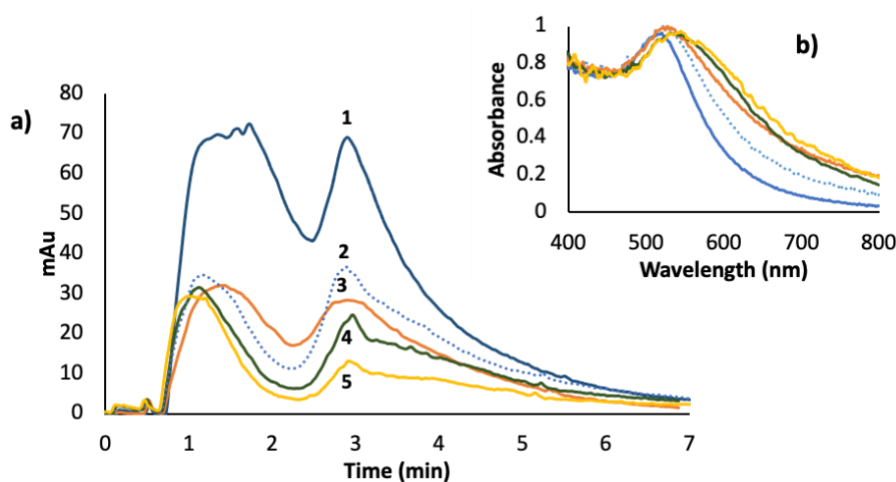


**Figure 82:** a) Chromatographic profiles obtained for 1: AuNPs(I), 2: blanc acidic extract (HAc), 3: urine sample, 4: urine sample spiked with  $16 \mu\text{g}\cdot\text{L}^{-1}$  of SPN and 5: urine sample spiked with  $26 \mu\text{g}\cdot\text{L}^{-1}$  of SPN. (b) UV spectra corresponding to peak chromatogram at 3 min.

- Conclusions

In this section, the potential of AF4-UV-vis-DLS and IT-SPME-miniaturized LC-DAD for assessment of noble MNPs for developing reliable plasmonic assays is demonstrated.

In the case of AF4-UV-vis-DLS, it showed to be a potential tool to monitor variations in aqueous dispersions of MNPs, useful for understanding plasmonic assays and carrying out them properly. Hence, plasmonic assays for hydrochloric and acetic acids were carried out obtaining suitable results and providing new information about transformations that analytes induce in MNPs.

IT-SPME-miniaturized LC-DAD takes also advantage of the LSPR of naked AuNPs as analytical signal to monitor plasmonic assays. This new tool provides better sensitivity and selectivity for developing plasmonic tests than UV-vis spectrometry. The fundamentals of the method rely on the interactions of NPs with the extractive phase immobilized inside of the IT-SPME capillary. The results indicated that these interactions gave rise to a characteristic chromatographic profile based on two chromatographic peaks, which are related with polarized and non-polarized populations in the bulk dispersion. The ratio of the two peaks conditioned their application in plasmonic assays. Commercial and naked NPs were assayed and SPN and [H<sup>+</sup>]-induced assays have been tested as targets. It is demonstrated that the chromatographic profile of a given NP dispersion, carried out in less than 10 min, assures its utility in a given plasmonic assay.

To demonstrate the practical application as a proof of concept, urine samples from different cancer patients have been analyzed, since SPN has been proposed as a cancer biomarker, with successful results. Both, naked AuNPs suitability for this assay developed in Ref. [47] by UV-vis spectroscopy and the assay developing, were carried out by the new tool proposed. Particularly, the key advantage of the employment of this separation-based method is the enhancement of the sensitivity of the previous urine assay and the potential application to isolate different phenomena that influence the LSPR signal.

## 4.2 CARBON NANOMATERIALS: CARBON BLACK

In this section, CB was characterized as analyte in solid CB bulk samples and CB dispersions using polymeric and biological dispersants by AF4-UV-vis-DLS. Size and composition distributions were studied under different experimental conditions. Moreover, CB response were analysed in different real water samples as a stability application example to study the influence of dispersive media in environmental analysis due to the growing concern about this nanoscale in the environment.

Similarly, a sample preparation method for CB extraction from soil matrices was developed taking into account the important presence of this material in environment terrestrial samples due to their wide variety of applications that use it. The CB extraction efficiency was evaluated through the study of the dispersive extraction efficiency using the same dispersants and analytical technique exposed above for their characterization.

### 4.2.1 Characterization of CB

Characterization of solid CB bulk samples (N326, N550, and N722) was performed by SEM, TEM, and Raman spectroscopy. TEM microscope was used to estimate the average core size of these nanoparticles. The measurements revealed particles sizes of 40, 69, and 72 nm for N326, N550, and N722, respectively. These results were in concordance with the specific surface area values given by the manufacturer. As it was expected, N550 and N722 showed a similar specific surface area (SSA) and SSA for N326 was higher, which was correlated with a smaller particle size.

The particle size obtained by TEM measurements also correlated with the size obtained by SEM analysis. Figure 83 shows the micrographs obtained with SEM for N326, N550, and N722, respectively. The morphology of particles was similar and aggregates of spheroidal and ellipsoidal primary particles were present in all cases.

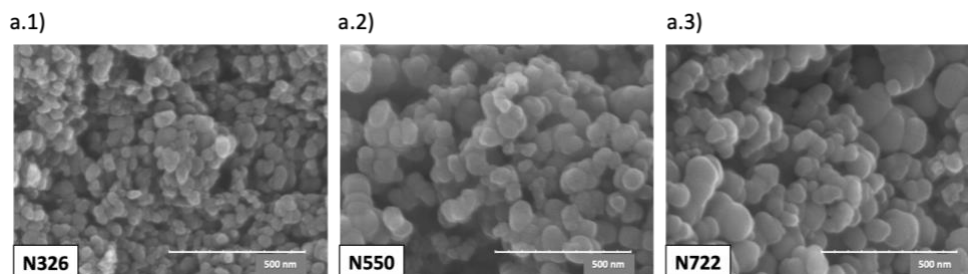


**Figure 83:** SEM micrographs of (a.1) N326, (a.2) N550, and (a.3) N722.

Different Raman bands were observed in the analysis of the N326 sample. The presence of bands at  $1300\text{ cm}^{-1}$  (D1) and  $2950\text{ cm}^{-1}$  (D1 + G) was in agreement with the CB structure. Moreover, the band D3 at  $1500\text{ cm}^{-1}$  corresponded to amorphous carbon. In particular, band D3 can be related to the amount of  $\text{sp}^3$  carbon between  $\text{sp}^2$  carbon rings, and the D4 band was attributed to hydrocarbon components or aliphatic moieties grafted (Figure 84). Similar bands were observed for samples N550 and N722, corroborating possible CB structures.

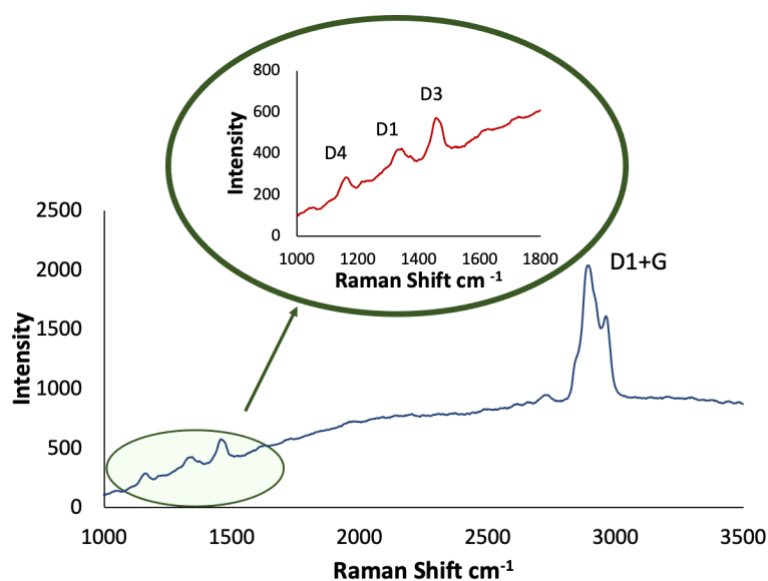


**Figure 84:** Raman spectra of CB N326. The inset shows the characteristic Raman bands between  $1000$  and  $1500\text{ cm}^{-1}$ .

Due to the great applicability of this C-NM, it is necessary obtain stable CB dispersions. Moreover, taking into account some scenarios where CB can be an analyte of interest, both polymeric and biological dispersants were studied. Figure 85.a and b show the optical microscope images of CB dispersions in each dispersant, respectively. This technique was used for characterizing the bulk dispersion; particularly, self-assembly droplets within the  $\mu\text{m}$  interval constitute its external structure in the case of a biological dispersant, which contained a surfactant in its composition, Tween 80, too.

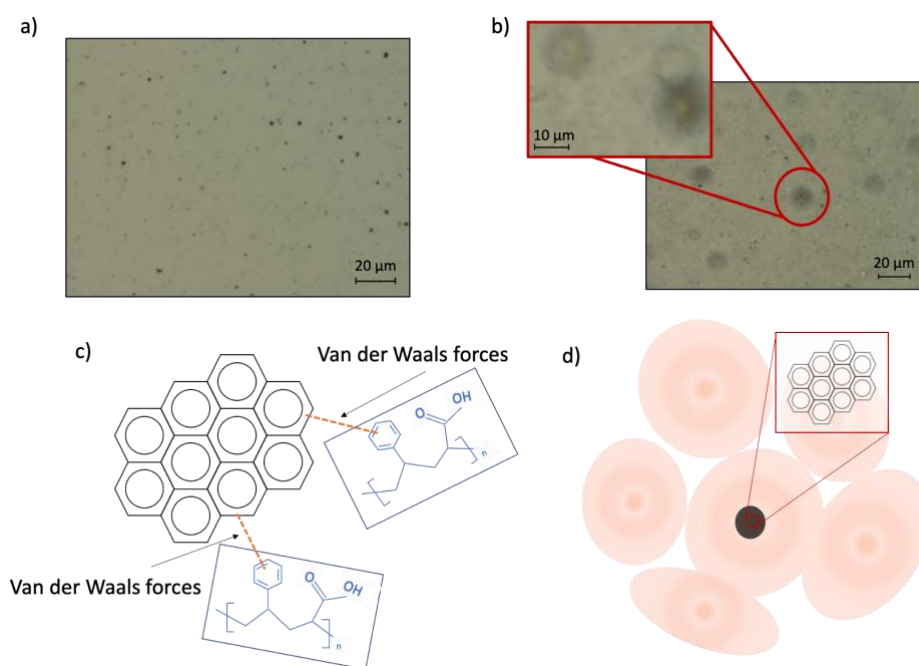


**Figure 85:** Optical microscope images of CB dispersions in a) polymeric and b) biological dispersants. Mechanism involved in the dispersion of CB using c) polymeric dispersant and d) biological dispersant.

In this study, a mixture of acrylic acid and styrene was used as a polymeric dispersant since it has been demonstrated to be used as a dispersant that can confer stability and low viscosity to the dispersion. The mechanism involved is schematized in Figure 85.c. The structure was a random copolymer containing polar and nonpolar moieties. As the polar part, acrylic acid provided solubility in water. Other monomers acting as nonpolar parts, such as styrene, bind with

nanomaterials mainly through van der Waals forces. Hydrogen bonds between carboxyl groups present in the material surface and polymer were also done. When a dispersant contains both polar and nonpolar components such as these considered, it can stabilize CB particles in water, working as a type of surfactant. Pigment dispersion was usually stabilized in water via the electrostatic repulsion of charges.

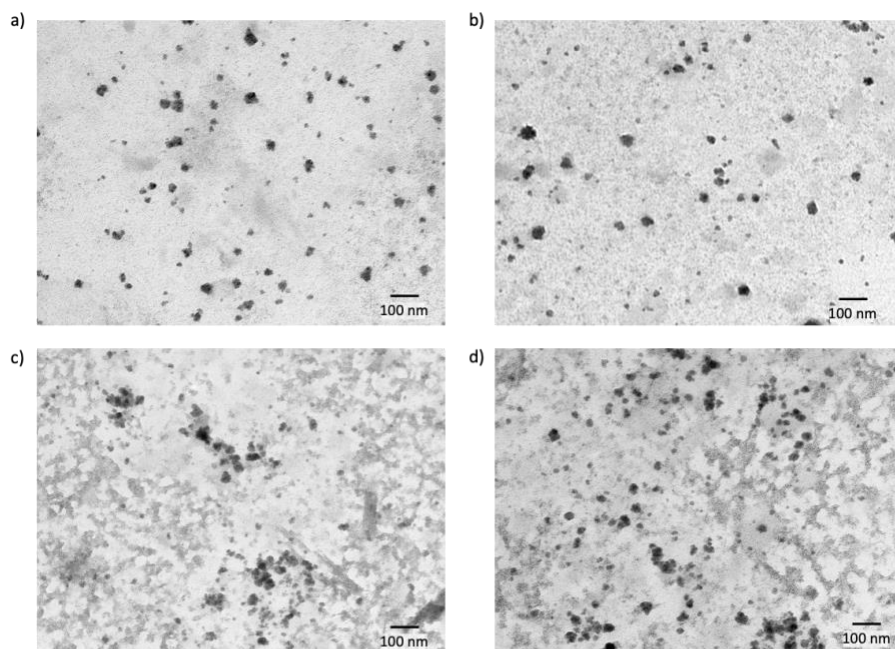
On the other hand, the biological dispersant studied in this study is based on a cell culture media. This dispersant was a high ionic strength solution, buffered at physiological pH and containing different proteins or nutrients, Tween 80 and supplemented with L-alanyl-L-glutamine dipeptide in one of the two studied media. These compounds contribute to the CB capping, mainly proteins. The self-assembly droplets provided an external environment for CB capping, and the schematic diagram is shown in Figure 85.d. It should be noted that these structures were not observed in the case of polymeric dispersant.

A TEM analysis was carried out to establish the different CB structures present in both dispersions. Moreover, AF4-DLS measurements were performed at different concentration levels in order to test linearity for quantitation purposes and study the main size populations. Sample N326 was selected as the target analyte.

The structure size of CB dispersions had a significant impact on the nanomaterial properties. Typically, primary particles combined to form aggregates of different sizes and agglomerates. As can be seen in Figure 86, TEM images allowed the observation of different forms of aggregates and agglomerates in the bulk dispersions. For the polymeric dispersant, Figure 86.a and b show primary particles dispersed individually. Meanwhile, Figure 86.c and d show several aggregates with linear, spherical, and ramified forms present in the polymeric dispersion.

Similarly, the biological dispersion showed a variety of structures. In Figure 86.e, the dispersion of different individual particles can be observed. Figure 86.f and g show some linear, spherical, and elliptic structure forms. Meanwhile, in Figure 86.h, a spherical agglomerate with a size larger than 200 nm composed of different individual particles is observed.

Polymeric dispersant



Biological dispersant

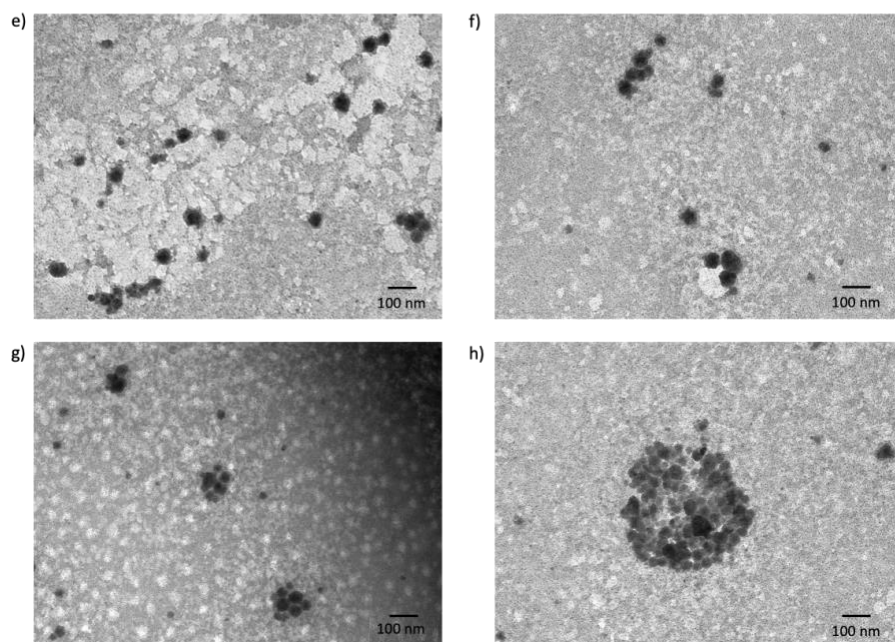


**Figure 86:** TEM images of CB structures in (a, b, c and d) polymeric dispersions; and (e, f, g and h) biological dispersions.

Using the polymeric dispersant, different CB dispersions from sample N326 were prepared and analyzed using the AF4-DLS system using a cross-flow of  $0.5 \text{ mL}\cdot\text{min}^{-1}$  and in batch DLS. Figure 87.a shows the obtained fractograms, which provided a linear relationship between peak area versus concentration with a satisfactory regression coefficient ( $R^2 = 0.99$ ). In terms of peak characteristics, a symmetric well-defined profile was obtained. Table 31 shows the width at half-height and the tailing factor for each dispersant. The calculated tailing factor for the polymeric dispersant was 1.64 and it can be correlated with the level of monodispersity provided. TEM micrographs were in agreement with the results since mainly homogeneous particles can be observed (core size of 40 nm) (Figure 87.b).

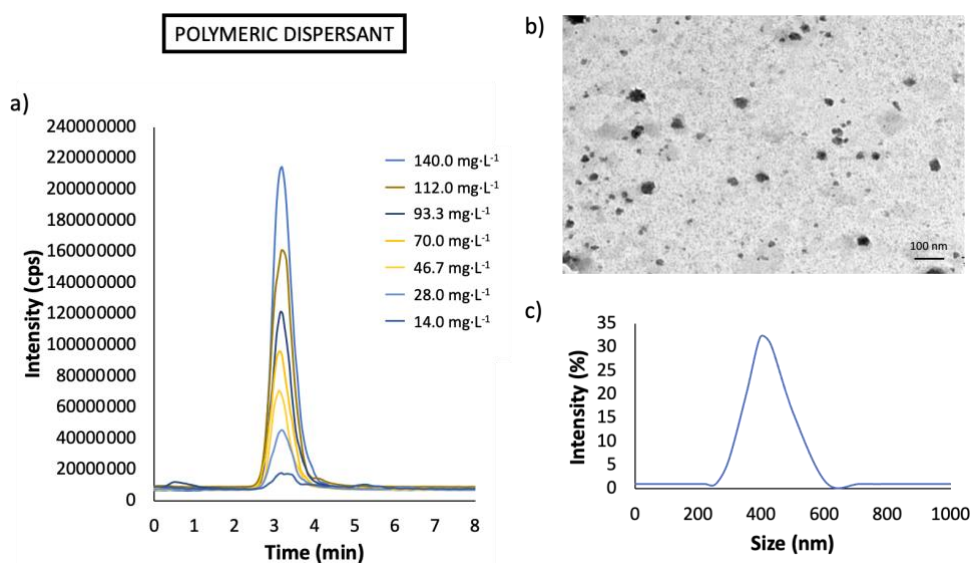


**Figure 87:** Results obtained for CB dispersion from simple N326 prepared in polymeric dispersant. a) DLS-fractograms at different concentration levels. b) TEM image of CB dispersion. c) Histogram – DLS measurement in batch.



**Table 31:** Peak, physical and analytical parameters for sample N326 in polymeric dispersant and biological supplemented dispersant.

PARAMETERS	DISPERSANTS	
	Polymeric	Biological
<b>Peak</b>		
Width half-height, $W_{1/2}$ (min)	0.63	0.82
Tailoring factor	1.64	4.9
<b>Physical</b>		
DH (nm) (DLS)	404±4	175±4
DH (nm) (AF4-DLS)	387±6	175±3
$Z_{\text{potential}}$ (mV)	23±2	-19±1
<b>Analytical</b>		
Sensitivity ( $\text{mg}^{-1}\cdot\text{L}$ )	$(1.5\pm 0.8)\cdot 10^6$	$(1.22\pm 0.07)\cdot 10^7$
LOD ( $\text{mg}\cdot\text{L}^{-1}$ )	1.38	0.16
Precision, RSD (%)	5.0	1.7

The same study was carried out using a biological dispersant and sample N326 as the target CB too. Two biological media were studied, Tween 80 + DMEM/F-12 and Tween 80 + DMEM/F-12 supplemented with L-alanyl-L-glutamine. The resulting dispersions and their dilutions were injected in the AF4-UV-vis-DLS system using a cross-flow of  $0.5 \text{ mL}\cdot\text{min}^{-1}$  (Figure 88.a). As can be seen, the use of this dispersant also resulted in a single peak but with a higher width than that obtained with the polymeric dispersant. The tailing factor in this case was 4.9, which was attributed to a wide size distribution in the biological medium. Indeed at  $36.2 \text{ mg}\cdot\text{L}^{-1}$ , a peak shoulder was observed in the AF4-DLS peak. Figure 88.b shows TEM micrographs of CB dispersion in biological dispersant.

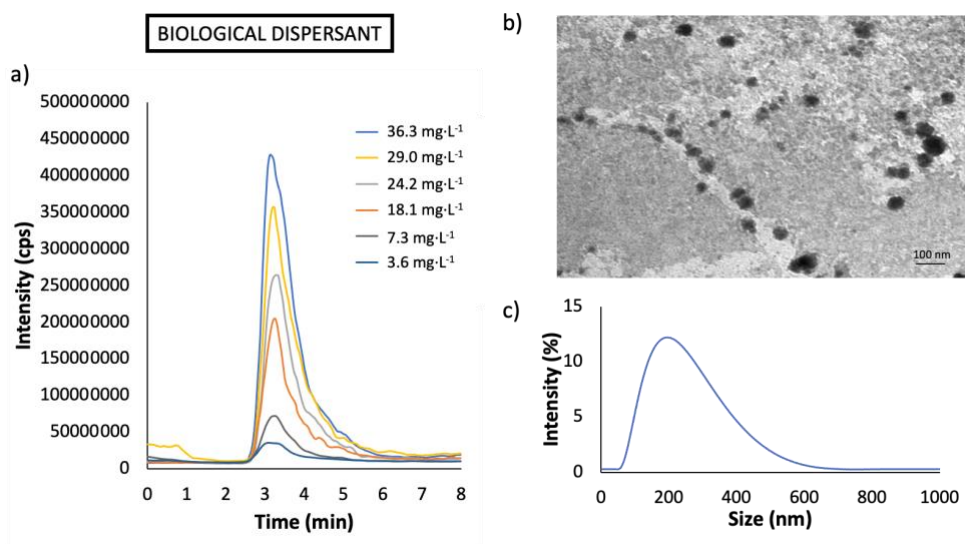


**Figure 88:** Results obtained for CB dispersion from simple N326 prepared in biological dispersant. a) DLS-fractograms at different concentration levels. b) TEM image of CB dispersion. c) Histogram – DLS measurement in batch.

Precision studies were also carried out for this purpose, and % RSD was calculated. The results obtained for three replicates showed that RSD values were lower than 5% for the CB polymeric dispersion and 1.74% for the CB biological dispersion. The precision achieved by the biological dispersant was better than that obtained by the polymeric dispersant.

Batch DLS measurements (% intensity vs particle size) are shown in Figure 87.c and Figure 88.c for both dispersions. A wider size distribution was obtained for CB in the biological medium compared with the polymeric one. Table 31 shows the DH, both from AF4-DLS and in batch DLS mode providing similar values. A single population with the calculated size is the predominant one in dispersions. The DH for CB dispersed in the biological dispersant has a value of 175 nm. Similar sizes were obtained for the cellular dispersant without the supplement (see Figure 89) although the signals of the fractograms were smaller than that obtained with the more complex cellular dispersant. For the polymeric agent, DH was 404 and 387 nm in batch and AF4-DLS, respectively, indicating a smaller dispersion capacity than that achieved by the biological dispersant.

Z-potential was also measured (see Table 31), providing positive values for the polymeric dispersant, which were in agreement with the polymer charge, and negative values for the biological dispersant related to the chemical structure of the biological medium. The cellular dispersant without a supplement provided values of Z-potential around -12 mV (see Figure 89) instead of -19 mV provided by the cellular dispersant with the L-alanyl-L-glutamine dipeptide.

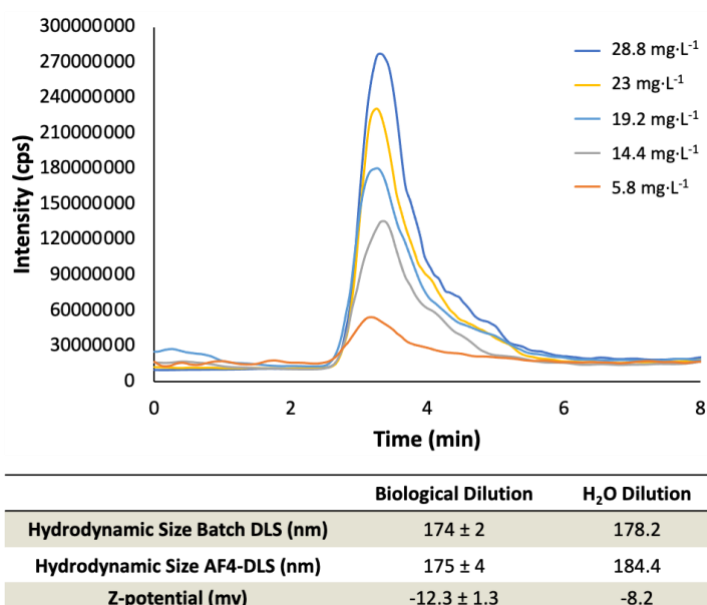


**Figure 89:** DLS-fractograms at different concentration levels obtained for CB dispersion from sample N326 prepared with cellular dispersant without supplementary compounds. DH results obtained in DLS analysis in batch and AF4 using dispersant or H<sub>2</sub>O as diluent of the CB dispersion.

Furthermore, linear calibration graphs were obtained with a satisfactory regression coefficient ( $R^2 > 0.995$ ). The slope obtained for the CB biological dispersant was  $(1.22 \pm 0.07) \cdot 10^7 \text{ mg}^{-1} \cdot \text{L}$  in a working concentration range of 3.6 to 36.3  $\text{mg} \cdot \text{L}^{-1}$ . Meanwhile, the value for the CB polymeric dispersion was  $(1.5 \pm 0.8) \cdot 10^6 \text{ mg}^{-1} \cdot \text{L}$ , in a concentration range of 14.0 to 140.0  $\text{mg} \cdot \text{L}^{-1}$ . Thus, the use of the biological dispersant gave rise to higher sensitivity. This means that detection limits for CB were lower by employing the biological dispersant. As can be seen in Table

31, LOD for the CB biological dispersion was  $0.16 \text{ mg}\cdot\text{L}^{-1}$  and for CB polymeric dispersion, it was  $1.38 \text{ mg}\cdot\text{L}^{-1}$ .

The presence of the L-alanyl-L-glutamine dipeptide in the biological medium gave rise to an increase in CB dispersion. In order to prove this, a biological medium without this additive was studied in the same working concentration range. DLS fractograms provided satisfactory regression with a slope of  $(9.9 \pm 0.3) \cdot 10^6 \text{ mg}^{-1}\cdot\text{L}$ . The results indicated that the slope was higher in the presence of L-alanyl-L-glutamine (see Table 31), which meant an increase in dispersed CB. In addition, the peak width and tailoring factor were similar in both cellular media (see Figure 89).

The stability of CB dispersion was studied for N326 CB using the biological supplemented dispersant. The slopes of the linear equation within the intervals 1.9–9.6 and 0.60–2.75  $\text{mg}\cdot\text{L}^{-1}$  were  $(1.13 \pm 0.04) \cdot 10^7$  and  $(1.15 \pm 0.08) \cdot 10^7 \text{ mg}^{-1}\cdot\text{L}$ , respectively. These results indicated that biological CB dispersion showed suitable dispersion stability in a wide concentration range since no significant differences were found. For N550 and N722, similar results were obtained.

#### 4.2.1.1 Characterization of CB mixtures by AF4

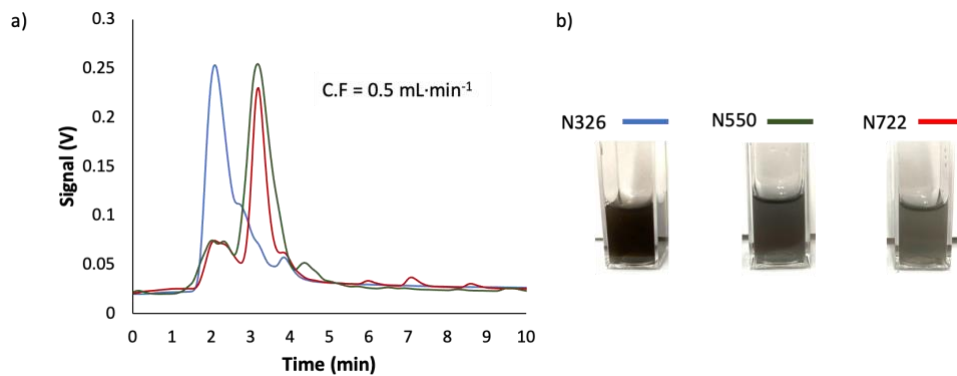
In order to evaluate CB separation with the AF4-UV-vis-DLS, three different CB samples (N326, N550, and N722) were dispersed using both dispersants, biological and polymeric, following the procedure described in Section 3.3.3.2. First, CB dispersions of the three samples were analyzed by DLS in batch mode (see Table 32). As can be seen, DH for N326 was the lowest in both dispersants, which was related to the minor core size. On the other hand, N550 exhibited the highest DH with a significant difference with respect to N722 although both of them showed a similar core size. This fact was attributed to the high oil absorption number (OAN) of sample N550, resulting in a greater capping layer of both dispersants, and thus a higher DH compared with N326 and N722.

**Table 32:** Particle size (DH) and Z-potential of different CB nanoparticles dispersions (N326, N550 and N772) using polymeric and biological dispersants (Fractograms were obtained at  $0.5 \text{ mL}\cdot\text{min}^{-1}$  except for \* at  $1.0 \text{ mL}\cdot\text{min}^{-1}$ ).

		<b>N326</b>	<b>N550</b>	<b>N722</b>
<b>POLYMERIC DISPERSANT</b>	Size Batch DLS (nm)	404.0	731.5	662.4
	Size AF4 - DLS (nm)	386.6	720.2	667.5
	Z-potential (mv)	22.6	20.4	22.9
<b>BIOLOGICAL DISPERSANT</b>	Size Batch DLS (nm)	175.5	540.6	351.8
	Size AF4 - DLS (nm)	175.4	544.1	357.2
		178.4*	538.2*	344.5*
	Z-potential (mv)	-18.8	-16.9	-17.0

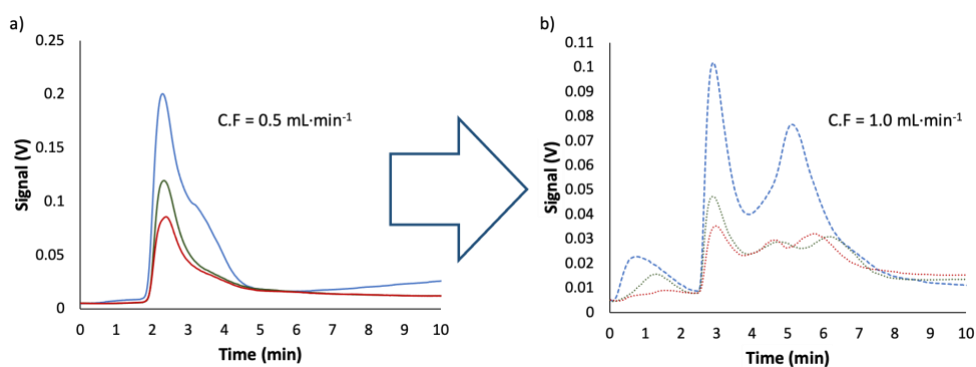
The Z-potential was also measured for CB samples, showing similar results for the different CBs. In AF4, one of the most important parameters is the cross-flow rate, which determined the resolution. In this study, two different cross-flow rates were applied to study the CB separation depending on the dispersant used.

Figure 90.a shows the fractogram for several CB samples at  $140 \text{ mg}\cdot\text{L}^{-1}$  in the polymeric dispersant at a cross-flow rate of  $0.5 \text{ mL}\cdot\text{min}^{-1}$ . N326 was identified at time 1.9 min corresponding to the void peak. Meanwhile, N550 and N722 were separated at a higher time (2.9 min). As it was expected, N550 and N722 were not resolved due to their similar particle size. For all of them, small peaks appeared in the fractograms that were compatible with aggregates or agglomerates of CB. The use of a higher cross-flow rate with the polymeric dispersant did not provide satisfactory results due to the lack of stability. Figure 90.b shows an image of each CB dispersion at the same concentration level, with their colors being directly related with the intensities obtained from AF4-DLS fractograms.



**Figure 90:** a) UV-vis fractograms obtained for polymeric CB dispersions (N326 in blue, N550 in green, and N722 in red) at cross-flow of  $0.5 \text{ mL}\cdot\text{min}^{-1}$ . b) Visual color representation of each CB biological dispersion.

Figure 91 shows the fractograms for CB biological dispersion ( $36 \text{ mg}\cdot\text{L}^{-1}$ ) for the three CB samples assayed at two cross-flow rates of  $0.5$  and  $1.0 \text{ mL}\cdot\text{min}^{-1}$ . N326 provided a peak and a shoulder at  $0.5 \text{ mL}\cdot\text{min}^{-1}$ . By using a cross-flow rate of  $1.0 \text{ mL}\cdot\text{min}^{-1}$ , suitable separation from the void peak was achieved: peaks at  $5.1$ ,  $5.7$ , and  $6.2 \text{ min}$  correspond to N326, N722, and N550, respectively. Furthermore, DH values of the three CB samples using the AF4 system for both cross-flow rates assayed were in agreement with the results provided by batch DLS measurements (see Table 32).



**Figure 91:** UV-vis fractograms obtained for biological CB dispersions (N326 in blue, N550 in green, and N722 in red) at different cross-flow rates: a)  $0.5 \text{ mL}\cdot\text{min}^{-1}$  and b)  $1.0 \text{ mL}\cdot\text{min}^{-1}$ .

### 4.2.2 Effect of time on the analytical response of CB dispersions

Figure 92 shows the % DLS fractogram signal for CB (N326) dispersion with polymeric and biological dispersants using as a reference the intensity obtained for CB dispersion at day 0 considered as a fresh dispersion.

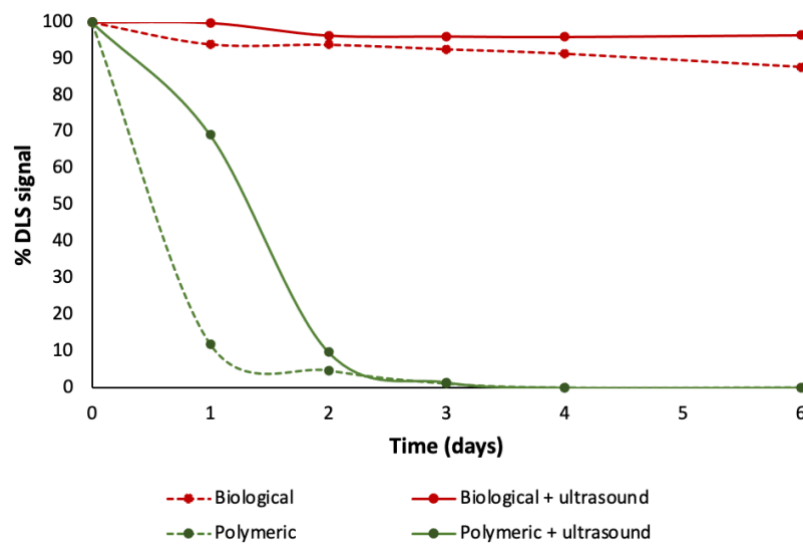


**Figure 92:** % DLS fractogram signal (using as a reference the dispersion of day 0) obtained as a function of dispersion preparation time for CB N326 with two studied dispersants: polymeric (green) and biological (red), using ultrasound (continuous line) and without ultrasound (dashed line) before injection.

As it can be seen, for the polymeric dispersant, the results indicated that the DLS fractogram decreased as a function of time. 90% of the signal was lost in 1 day, showing low stability in this dispersion medium. An ultrasound treatment of these dispersions before the injection only improved the signal reduction by 70%. Particle sizes for different CB dispersions on different days were analyzed (after the ultrasound treatment), see Table 33. For the CB polymeric dispersion, the particle size increased as the stability decreased, which corroborated the aggregation of CB.

**Table 33:** Particle size obtained with the AF4-DLS for each dispersant as a function of dispersion time after the ultrasound step.

Size (nm)	N326			
	Day 0	Day 1	Day 2	Day 6
Polymeric	386.6	432.3	2360	---
Biological	175.4	179.4	177.3	183.2

On the other hand, a stable dispersion was obtained for the CB biological dispersant since the signal was constant over time. In this case, the CB size was between 175 and 180 nm as a function of time, demonstrating the stability of CB in this dispersant.

#### 4.2.3 Influence of water matrices in CB dispersion stability

As a practical case of study, CB dispersion by dilution in several water matrices was performed taking into account the potential occurrence of these nanomaterials in the environment. For this aim, diluted dispersions were prepared with real water matrices (dilution factors of 1/2 and 1/8 for CB (N326) polymeric and biological dispersants, respectively). Table 34 shows characterization parameters for each water matrices used: conductivity, sulfate, and nitrate. As it was expected, the highest values were obtained for the waste water sample.

**Table 34:** pH, conductivity, turbidity, nitrate and sulfate values for aqueous matrices.

	pH	Conductivity ( $\mu\text{s}\cdot\text{cm}^{-1}$ )	Turbidity (NTU)	$\text{NO}_3^-$ ( $\text{mg}\cdot\text{L}^{-1}$ )	$\text{SO}_4^{2-}$ ( $\text{mg}\cdot\text{L}^{-1}$ )
Tap Water B	8.08	943	0.1526	7.32	266.25
Well Water	7.64	1091	0.2201	55.54	307.26
Waste Water	7.98	2600	0.5300	192.52	873.18

In polymeric CB dispersions, an increase in turbidity and conductivity occurred due to the presence of high amount of anions, producing a dramatic loss of dispersion stability. This effect was more remarkable for CB-diluted dispersion in



wastewater than that produced in the other water matrices, its signal being reduced up to 90% as Figure 93.a shows. When ultrapure water was used to prepare diluted dispersions, the stability of CB dispersion was not altered. In the case of CB biological dispersions, dilution with different waters did not induce a significant signal decrease (see Figure 93.b).

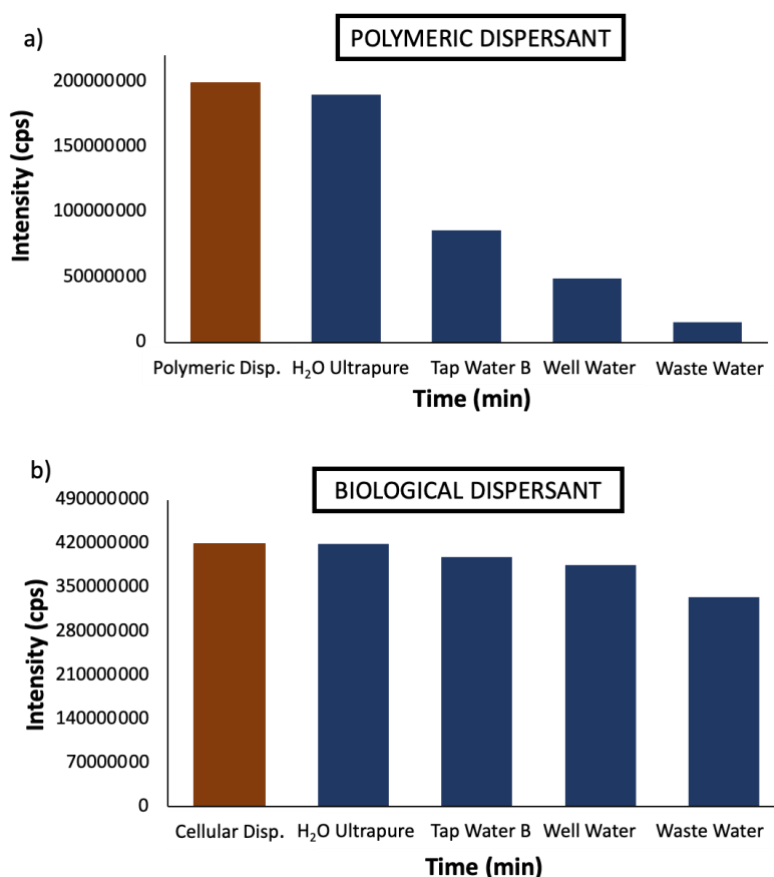


**Figure 93:** Maximum intensity obtained in DLS fractograms analysis for each CB dispersion diluted with different water matrices using a) polymeric dispersant and b) biological dispersant.

This study demonstrates the influence of the sample matrix on the stability of dispersion as a function of the CB dispersive agents. Therefore, the success in the determination of the CB size and composition distribution will depend on the analytical strategy that takes into account the dispersion performance of these compounds.

#### ***4.2.4 Isolation of CB from soils and its recovery by filter-aided procedure***

A procedure for CB isolation from soil matrices was developed. The CB isolation efficiency was evaluated through the study of the Dispersive Isolation Efficiency (D-IE) using biological and polymeric dispersants or even their sequential use. Moreover, Filter-Aided Recovery Efficiency (FA-RE) employing different membranes (fiberglass, nylon and teflon) with a wide variety of pore size (0.1 to 5  $\mu\text{m}$ ) was also studied in order to evaluate its recovery from the obtained dispersions in order to achieve a solid residue or for its re-using. Separation and quantitation of CB in dispersions were performed by field flow fractionation techniques.

##### **4.2.4.1 CB isolation from soils**

CB N326 as a target CB-NM and polymeric and biological dispersive agents were employed to study the isolation of this NM from soils and its recovery using a filter-aided procedure.

In a first step, soils samples were treated with the polymeric and biological dispersants in order to evaluate the matrix response in absence of CB. Figure 94.a and b show the AF4-DLS-fractograms obtained for mountain A soil using polymeric and biological dispersant, respectively. As it can be seen, for both dispersants, the responses were negligible. Moreover, the DH distribution did not show particles between 2.4 and 4.0 min, corresponding to the DLS-signal of CB target analyte. AF4-DLS-fractograms obtained for extraction of orchard A soil using polymeric and biological dispersants (Figure 94.c and d respectively), exhibited a similar profile compared with the mountain A soil. Mountain B and Orchard B soils were also studied and fractograms did not provide a remarkable signal (see Figure 95). These results indicated, that the different matrices did not interfere in CB fractograms.

Bearing in mind that the LODs achieved by AF4 for CB dispersions prepared from polymeric and biological dispersants are 1.38 and 0.16  $\text{mg}\cdot\text{L}^{-1}$  using area as analytical signals of fractograms, two mountain (A and B) and two orchard (A and B) soils were spiked with 2  $\text{mg}\cdot\text{g}^{-1}$  soil. Then, the spiked soils were treated with polymeric or biological dispersants employing the procedures described in Section

3.3.4.2.2 and properly diluted as this section indicated. Figure 96.a, shows the DLS fractograms obtained for CB isolated from mountain A soil using the polymeric dispersive medium. The D-IE value was 70 % as it can be seen in Table 35. On the other hand, using the biological dispersive media (Figure 96.b), D-IE was 99 %, which indicated near complete isolation of target analyte. Orchard A soil showed lower average particle size than that corresponded to mountain A soil, 230  $\mu\text{m}$  and 310  $\mu\text{m}$ , respectively, with higher particle composition percentage in the range < 100  $\mu\text{m}$ , 17.8 % and 3.94 %, respectively (see Table 36).

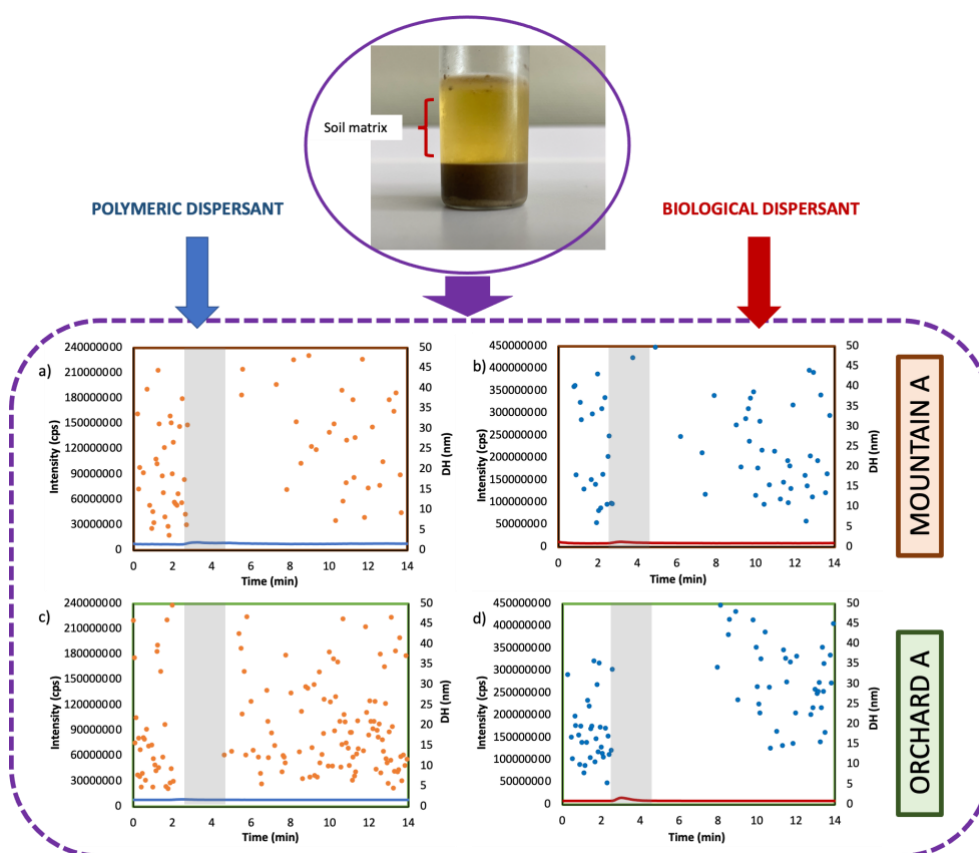


**Figure 94:** DLS-fractograms and DH obtained for soil samples. a) Mountain A soil extracted with polymeric dispersant. b) Mountain A soil extracted with biological dispersant. c) Orchard A soil extracted with polymeric dispersant. d) Orchard A soil extracted with biological dispersant.

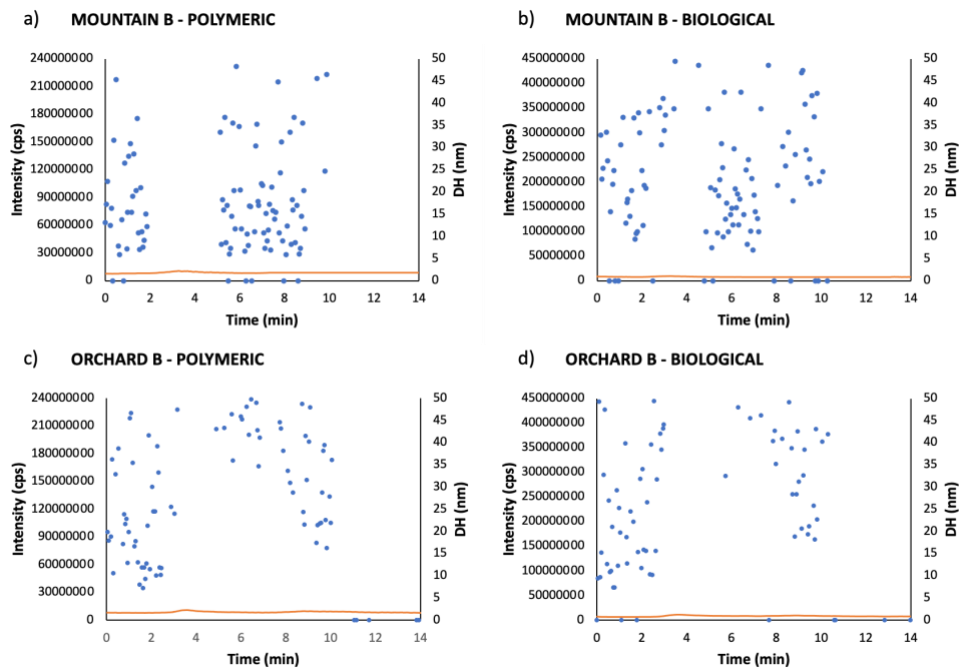


**Figure 95:** DLS-fractograms and dhydro obtained for soil samples. a) Mountain B soil extracted with polymeric dispersant. b) Mountain B soil extracted with biological dispersant. c) Orchard B soil extracted with polymeric dispersant. d) Orchard B soil extracted with biological dispersant.

In the case of CB isolated from mountain soil A, for polymeric dispersant, the average size was 399 nm (see Table 35) and zeta-potential obtained from DLS of  $19.5 \pm 1.3$  mV. In the case of biological dispersant, the values were 177 nm and  $-17.1 \pm 1.2$  mV respectively. These results indicated that the isolation mechanism for CB present in mountain A soil provided similar results than CB standard dispersions, that means that soil matrix did not induce disturb matrix effect on CB properties and stability.

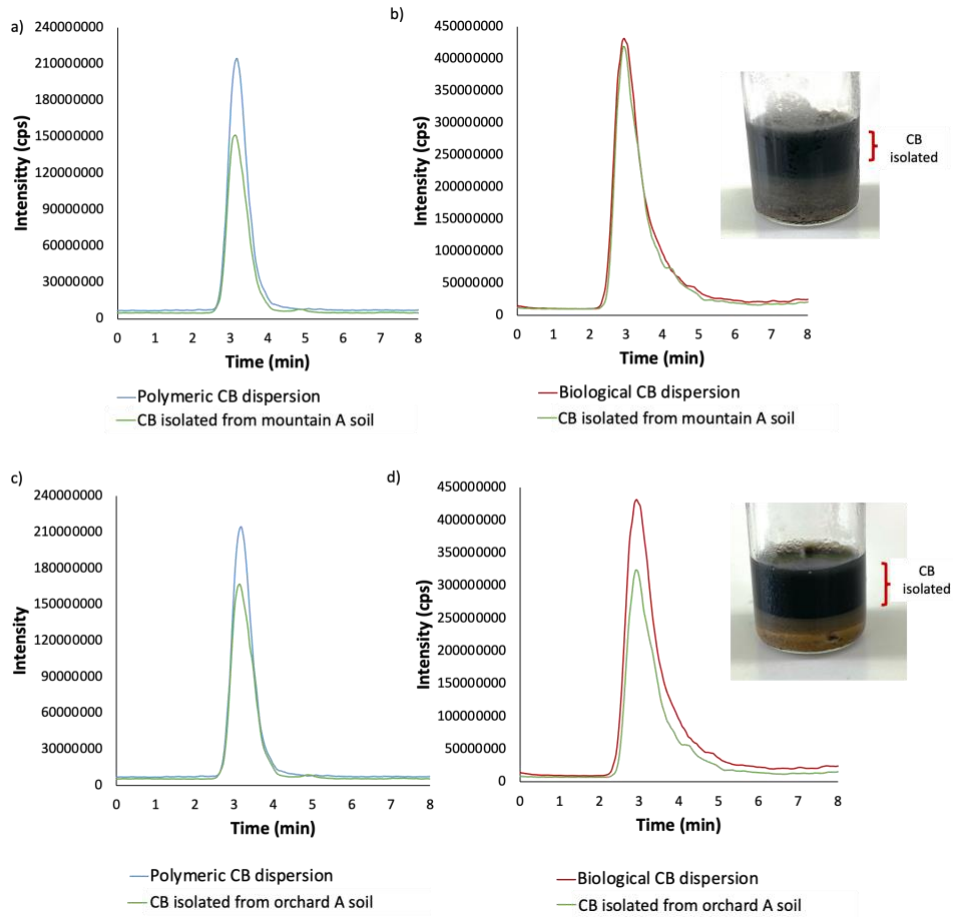


**Figure 96:** a) Fractogram for CB isolation from mountain A soil using polymeric dispersant (compared with CB bulk dispersion in the studied dispersant). b) Fractogram for CB isolation from mountain A soil using biological dispersant (compared with CB bulk dispersion in the studied dispersant). c) Fractogram for CB isolation from orchard A soil using polymeric dispersant (compared with CB bulk dispersion in the studied dispersant). d) Fractogram for CB isolation from orchard A soil using biological dispersant (compared with CB bulk dispersion in the studied dispersant).

Figure 96.c and d show the DLS fractograms obtained for CB isolation from orchard A soil using polymeric and biological dispersive media, respectively. As can be seen, the D-IE with the biological dispersant, was lower than using mountain A soil, 75 %.

Z-potentials obtained from DLS were  $3.2 \pm 1.1$  mV for polymeric dispersion and  $-2.4 \pm 0.8$  mV for biological dispersion and changes in size were also observed in reference to standard dispersions (Table 35). This fact is in accordance with possible extraction of matrix components from soil, which modified CB capping surface. As lower amount of organic matter in the soil composition (see Table 37) the lower CB isolation in the dispersion is achieved (95-99 vs 75 %), which can be related with the presence of higher amount of humic acids in mountain A in reference to orchard A, which enhanced stability of the dispersion [349]. Besides it is described that soil organic matter (SOM) was found to create unfavorable conditions for the retention [350].

**Table 35:** D-IE: isolation efficiencies after the dispersive procedure. DH obtained for CB dispersed from fractograms obtained by AF4-DLS. (\* batch DLS)

SOIL	MEDIA	DISPERSED CB FROM SOIL	
		D-EE (%)	Size (nm)
Mountain A	Polymeric	$70 \pm 2$	$399 \pm 7$ ; $404 \pm 5^*$
	Biological	$98.7 \pm 1.1$	$177 \pm 3$ ; $168 \pm 2^*$
	Sequential Polymeric-Biological	$97.9 \pm 1.9$	$182 \pm 2$
Orchard A	Polymeric	$73 \pm 2$	$380 \pm 6$ ; $391 \pm 4^*$
	Biological	$75.1 \pm 1.8$	$208 \pm 3$ ; $204 \pm 5^*$
	Sequential Polymeric-Biological	$64 \pm 2$	$213 \pm 7$
Mountain B	Polymeric	$62.9 \pm 1.4$	$409 \pm 4$
	Biological	$99.1 \pm 0.8$	$169 \pm 5$
Orchard B	Polymeric	$66 \pm 3$	$385 \pm 3$
	Biological	$96.2 \pm 1.3$	$171 \pm 4$

**Table 36:** Soil particle size composition obtained from optical microscope. Percentages (%) of each fraction for the four studied soils and estimated average size.

	< 100 $\mu\text{m}$ %	100-200 $\mu\text{m}$ %	200-300 $\mu\text{m}$ %	300-400 $\mu\text{m}$ %	> 400 $\mu\text{m}$ %	Average size ( $\mu\text{m}$ )
<b>Mountain A</b>	3.9	15.9	14.0	16.1	50.0	310
<b>Orchard A</b>	17.8	22.7	14.6	13.4	31.6	230
<b>Mountain B</b>	2.5	16.0	22.7	18.5	40.3	350
<b>Orchard B</b>	3.6	17.7	27.0	21.3	30.5	305

**Table 37:** Organic matter obtained by the gravimetric method.

Soil	Organic matter (%)
<b>Mountain A</b>	23.13
<b>Orchard A</b>	8.32
<b>Mountain B</b>	20.47
<b>Orchard B</b>	18.49

The same study was performed for mountain B and orchard B soils and isolation efficiencies after dispersion procedure were similar than those obtained for mountain A soil (see Table 35). In these three soil samples, the presence of lower percentage of particle range < 100  $\mu\text{m}$  and higher amount of organic matter near 20 % (see Table 36 and Table 37), allowed to improve the D-IE using biological dispersant.

A sequential ligand exchange study was also carried out, CB was isolated from mountain A soil using polymeric dispersant (Figure 97.a shows AF4-DLS signal obtained). Subsequently, CB settling was achieved after centrifugation and sedimentation. Polymeric dispersant was removed and CB was redispersed with the biological dispersant. As it can be seen, the separation profiles were similar to those observed with the biological dispersion and particle size and Z-potential were in concordance with initial values too. For orchard A soil (see Figure 97.b) similar

results were obtained with both dispersants, showing lower differences between initial isolation and re-isolation procedure. Thus, it was demonstrated that ligands exchange can be performed, and that soil matrix did not interfere in that capping exchanged isolation step, only a minor increase in the particle size was observed as it is reported in Table 35.

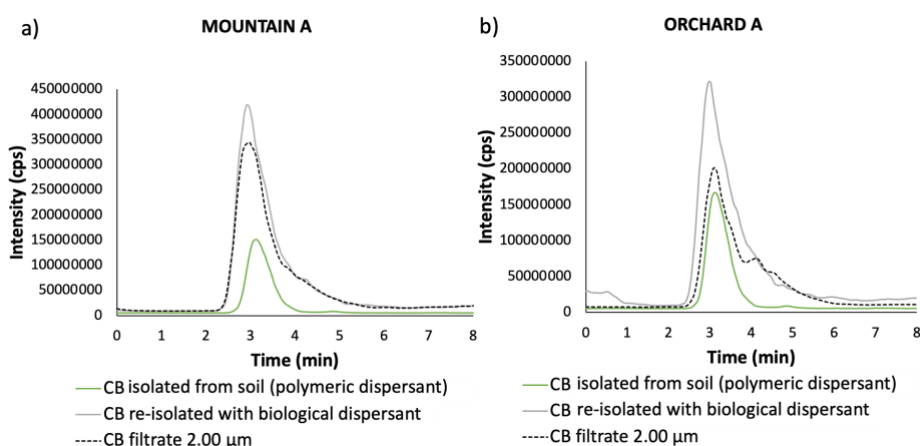


**Figure 97:** a) Ligand exchange study and filter-aided recovery assay using fiberglass 2 µm as a support (mountain A soil as matrix). b) Ligand exchange study and filter-aided recovery assay using fiberglass 2 µm as a support (orchard A soil as matrix).

As a practical application, an industrial CB based pigment paste was studied as potential pollutant of mountain A soil. Figure 98.a shows the DLS fractograms of CB isolated from soil and direct pigment paste bulk dispersion using polymeric dispersant. 88.4 % of target analyte was dispersed from soil. Average particle size was  $312 \pm 3$  nm for pigment paste isolated from soil and  $309 \pm 4$  nm for direct pigment paste standard dispersion.

In the case of the biological dispersive media, DLS fractograms can be seen in Figure 98.b. In this case, the isolation (D-IE) was quantitative and average particle size was  $106 \pm 2$  nm for direct pigment paste bulk dispersion and  $103 \pm 4$  nm for pigment paste dispersion from soil. The proposed CB isolation procedure was satisfactorily applied to soil contaminated with the pigment paste.



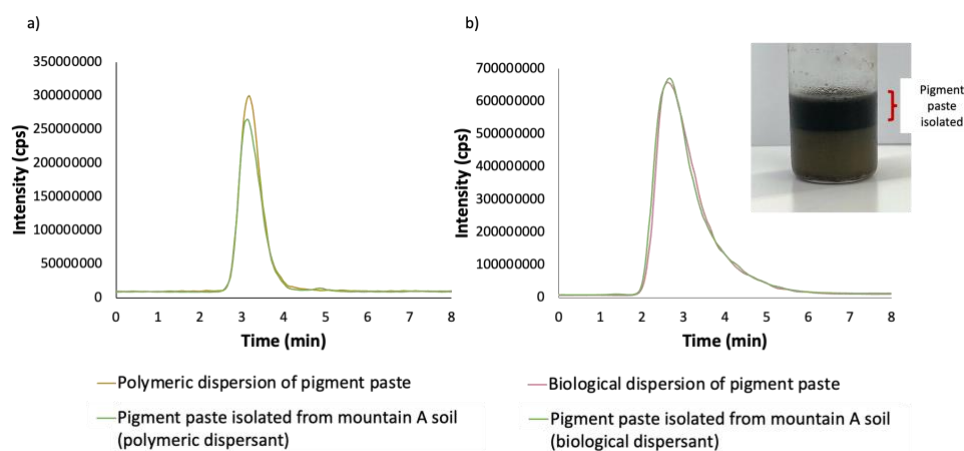


**Figure 98:** a) Fractogram for pigment paste isolation from mountain A soil using polymeric dispersant (compared with a bulk dispersion of pigment paste in the studied dispersant). b) Fractogram for pigment paste isolation from mountain A soil using biological dispersant (compared with a bulk dispersion of pigment paste in the studied dispersant).

#### 4.2.4.2 CB recovery by filter-aided extraction from the dispersion

As control experiment, the recovery efficiencies were compared with those achieved in CB dispersions directly injected in the AF4 ( $150 \text{ mg}\cdot\text{L}^{-1}$  for polymeric dispersion and  $37.5 \text{ mg}\cdot\text{L}^{-1}$  for biological dispersion). The retention of CB on the surface of the different membranes was measured by AF4-DLS. Figure 99 and Figure 100 shows the fractograms obtained after the filtration step with both dispersive media. Table 38 summarizes the FA-RE after the filter aided step obtained for each membrane. As can be seen, the amount of CB retained depended on CB hydrodynamic diameter, membrane nature and pore size and type of dispersant.

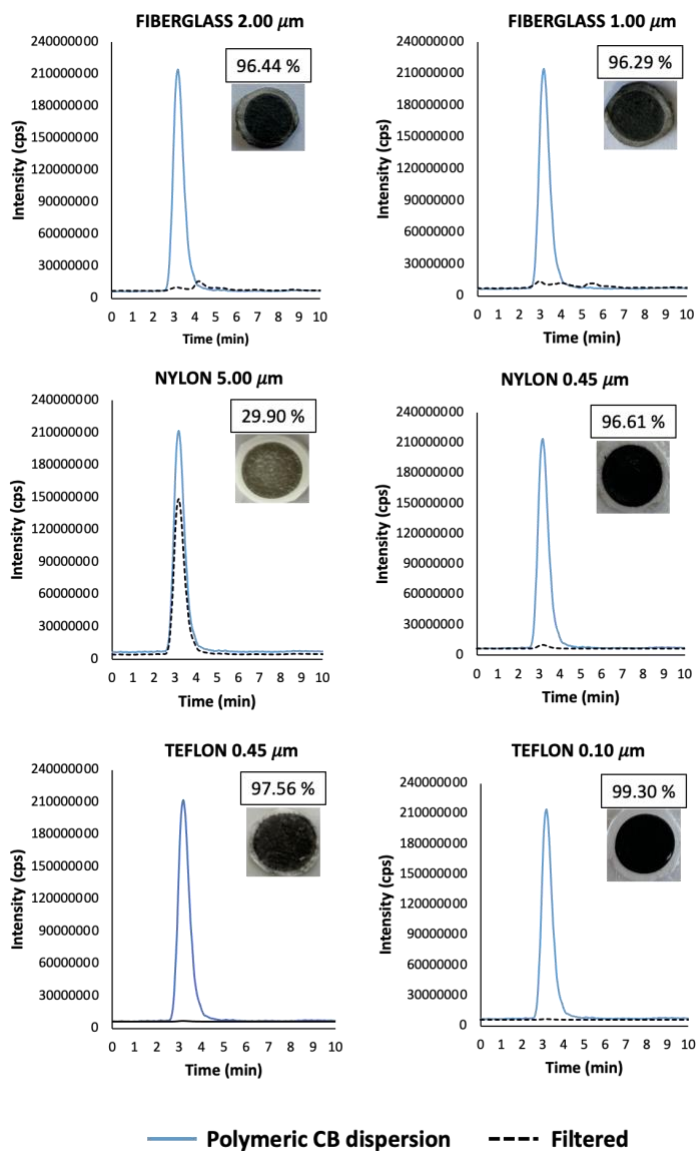


**Figure 99:** Filter based analysis of CB dispersion from sample N326 prepared with polymeric dispersant using different filters (fiberglass 2.00  $\mu\text{m}$ , fiberglass 1.00  $\mu\text{m}$ , nylon 5  $\mu\text{m}$ , nylon 0.45  $\mu\text{m}$ , teflon 0.10  $\mu\text{m}$  and teflon 0.10  $\mu\text{m}$ ).

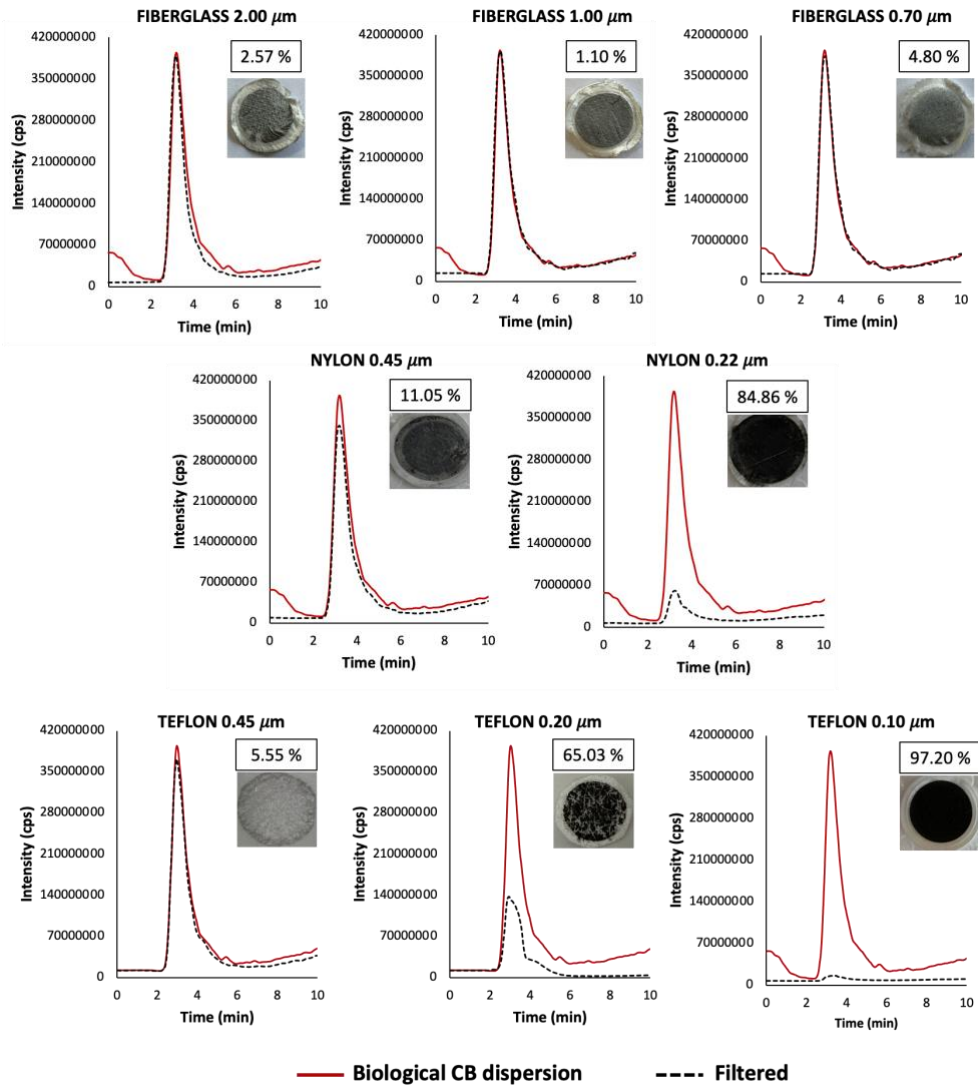


**Figure 100:** Filter based analysis of CB dispersion from sample N326 prepared with biological dispersant using different filters (fiberglass 2.00  $\mu\text{m}$ , fiberglass 1.00  $\mu\text{m}$ , fiberglass 2.00  $\mu\text{m}$ , fiberglass 0.70  $\mu\text{m}$ , nylon 0.45  $\mu\text{m}$ , nylon 0.22  $\mu\text{m}$ , teflon 0.45  $\mu\text{m}$ , teflon 0.20  $\mu\text{m}$  and teflon 0.10  $\mu\text{m}$ ).

**Table 38:** FA-RE values obtained with the filter membranes and in both dispersive media. FA- RE: Filter aided recovery efficiency.

MEMBRANE	DISPERSIVE MEDIA	
	POLYMERIC <i>FA-EE (%)</i>	BIOLOGICAL <i>FA-EE (%)</i>
Fiberglass 2.00 $\mu\text{m}$	96 $\pm$ 2	2.6 $\pm$ 0.1
Fiberglass 1.00 $\mu\text{m}$	96 $\pm$ 2	1.1 $\pm$ 0.3
Fiberglass 0.70 $\mu\text{m}$	---	4.80 $\pm$ 0.14
Nylon 5.00 $\mu\text{m}$	29.9 $\pm$ 0.6	---
Nylon 0.45 $\mu\text{m}$	96 $\pm$ 2	11.1 $\pm$ 0.7
Nylon 0.22 $\mu\text{m}$	---	84.9 $\pm$ 1.1
Teflon 0.45 $\mu\text{m}$	97 $\pm$ 2	5.6 $\pm$ 0.4
Teflon 0.20 $\mu\text{m}$	---	65.2 $\pm$ 1.4
Teflon 0.10 $\mu\text{m}$	99.1 $\pm$ 0.7	97.2 $\pm$ 2

The use of the polymeric dispersive media resulted in quantitative recovery values, except for the highest membrane pore size assayed of 5  $\mu\text{m}$ . High electrostatic interaction between the fiberglass support and the polymeric dispersant took place considering the different surface charge present to each of them, negative for filter [351,352] and positive for dispersion. In the case of nylon 0.45  $\mu\text{m}$  and teflon filters, the average particle size of dispersions (Table 35) was similar or higher than the pore size of filter generating a complete recovery.

As can be seen in Table 38 and Figure 100, the behaviour of the biological dispersion differed from that provided by the polymeric dispersions. By using fiberglass filters with pore size larger than or equal to 0.70  $\mu\text{m}$ , CB particles were poorly recovered because the hydrodynamic diameter of these particles was lower than 176 nm and electrostatic interactions between particles and filter support were negligible. Charge surface of both, CB and fiberglass material, was negative. DLS measurements of filtered solution using fiberglass 2.00  $\mu\text{m}$ , 1.00  $\mu\text{m}$  and 0.70  $\mu\text{m}$  and nylon 0.45  $\mu\text{m}$  suggested an average value of 165  $\pm$  6 nm, which is in concordance with the hydrodynamic diameter observed before filter based step.

For nylon filter 0.45  $\mu\text{m}$ , the retention was negligible, however by using nylon 0.22  $\mu\text{m}$ , retention of CB increased due to the recovery of larger particles and

the presence of electrostatical interactions that may occur between nylon material and CB dispersion with opposite charge [353]. In the case of nylon 0.22  $\mu\text{m}$  the average size obtained for the collected dispersion was  $119 \pm 4$  nm. Thereby, it can be assessed that filtration did not produce significant variations in the hydrodynamic particle size of the dispersion for filters with pore size greater than or equal to 0.45  $\mu\text{m}$ . For teflon filter, the results were in concordance with the other materials. Employing teflon 0.45  $\mu\text{m}$ , a poor efficiency was observed, but if the pore size was reduced up to 0.2  $\mu\text{m}$ , the efficiency increased taking into account the DH of CB. For this last membrane pore size, the average CB size was  $115 \pm 2$  nm. For all assays carried out without quantitative filter recovery, Z-potential analysis was measured, obtaining similar values to the initial bulk dispersion ( $-16.2 \pm 0.7$  mV). Using 0.1  $\mu\text{m}$  teflon filter, the retention was quantitative, since the hydrodynamic diameter was higher than pore size of filter.

The proposed filter-aided recovery method was evaluated using the isolated CB dispersions obtained from soil samples. Figure 101 shows the fractograms obtained after the recovery step for mountain A and orchard A soils using the studied dispersants. Subsequently, for mountain A soil, using polymeric dispersant (Figure 101.a), CB was recovered by filter-aided step, using fiberglass 2  $\mu\text{m}$  and teflon 0.10  $\mu\text{m}$  as supports. In both cases, no responses in DLS were observed at the retention times, which indicated a quantitative retention of the CB on the surface of the filter membrane. However, for biological dispersant in the same soil matrix, the CB FA-RE provided quantitative values only with teflon 0.10  $\mu\text{m}$  as Table 39 shows, and as previously established for CB standard dispersions.

Indeed, for orchard A soil, the same study was carried out. Using fiberglass 2  $\mu\text{m}$  as a support, the FA-RE was 52% (see Table 39) due to the presence of matrix components that induced CB capping modification changing the retention behaviour (Figure 101.c and d). The polymeric dispersion showed similar results. It should be noted that FA-RE was indirectly estimated by measuring CB in the filtered solution by AF4-DLS.

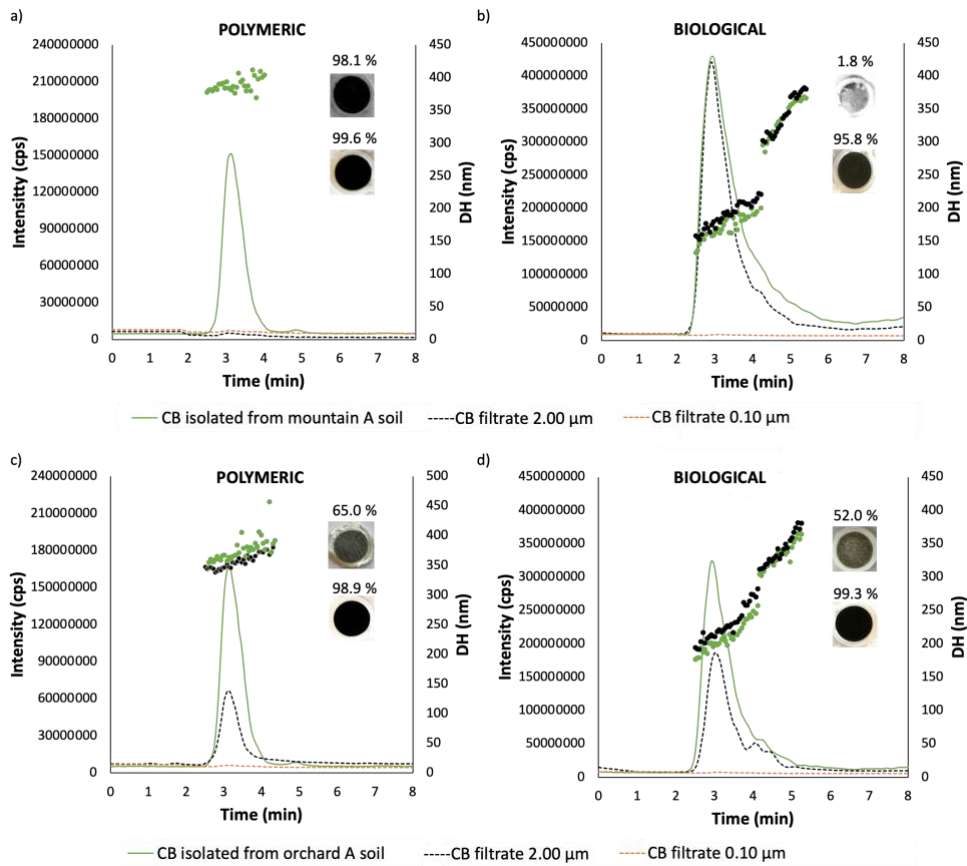


**Figure 101:** In green: fractograms for CB isolation from different soils using the studied dispersants. Dotted lines: AF4-DLS signal of filtrate using fiberglass 2  $\mu\text{m}$  (black) and teflon 0.10  $\mu\text{m}$  (orange). a) Study using mountain A soil and polymeric dispersant. b) Study using mountain A soil and biological dispersant. c) Study using orchard A soil and polymeric dispersant. d) Study using orchard A soil and biological dispersant. The inserts corresponded to recovered CB from dispersions by fiberglass 2.00  $\mu\text{m}$ , and teflon 0.10  $\mu\text{m}$  filters for all dispersions.

**Table 39:** FA-RE: efficiencies after the isolation and subsequent filter aided recovery. Hydrodynamic sizes obtained for CB dispersion residue after filter-aided recovery. (Fiberglass 2  $\mu\text{m}$  and teflon 0.10  $\mu\text{m}$  were studied) using polymeric and biological dispersive agents.

SOIL	MEDIA	EXTRACTED CB Fiberglass 2.00 $\mu\text{m}$		EXTRACTED CB Teflon 0.10 $\mu\text{m}$		REDISPERSION from filter Teflon 0.10 $\mu\text{m}$
		FA-EE (%)	Size (nm)	FA-EE (%)	Size (nm)	% Redispersion
Mount. A	<i>Polymeric</i>	98.1 $\pm$ 2.1	---	99.6 $\pm$ 0.4	---	57 $\pm$ 2
	<i>Biological</i>	1.8 $\pm$ 0.2	186 $\pm$ 3	95.8 $\pm$ 0.8	---	77 $\pm$ 5
	<i>Sequential Polymeric- Biological</i>	9.7 $\pm$ 0.6	180 $\pm$ 3	---	---	---
Orchard A	<i>Polymeric</i>	65 $\pm$ 3	367 $\pm$ 6	98.9 $\pm$ 1.1	---	52 $\pm$ 2
	<i>Biological</i>	52 $\pm$ 1.8	218 $\pm$ 5	99.3 $\pm$ 0.5	---	70 $\pm$ 3
	<i>Sequential Polymeric- Biological</i>	48.1 $\pm$ 1.1	222 $\pm$ 4	---	---	---

As it was expected, teflon 0.10  $\mu\text{m}$ , provided quantitatively FA-RE. Table 39 shows FA-RE values for CB dispersions obtained from soils. Percentages of redispersion capacity obtained from solid CB retained in filters are also depicted. These results indicated that the CB extracted can be re-used in two forms: retained in the filter or as dispersion. Filter-aided step was also carried out in the sequential ligand exchange study and similar results than those provided by the biological dispersant were obtained (Table 39 and Figure 97).

Pigment paste isolated from mountain soil A was treated by filter-aided recovery method (Figure 102.a and b). Subsequently, the FA-RE using fiberglass 2  $\mu\text{m}$  and teflon 0.10  $\mu\text{m}$  filters in polymeric dispersant (Figure 102.a) indicated quantitative recovery.

As it was expected, for pigment paste isolated dispersion using biological dispersant (Figure 102.b), retention of target analyte in fiberglass 2  $\mu\text{m}$  was

negligible, (FA-RE very low, 2.15%) in accordance with the hydrodynamic size of particles. Meanwhile, using teflon 0.10  $\mu\text{m}$  filter, a fraction of CB was retained, however, a residual CB concentration was detected in the filtered solution (48.02%) due to the presence of a CB distribution with a  $d_{\text{hydro}} = 90 \pm 5 \text{ nm}$ , which was not retained in the membrane.

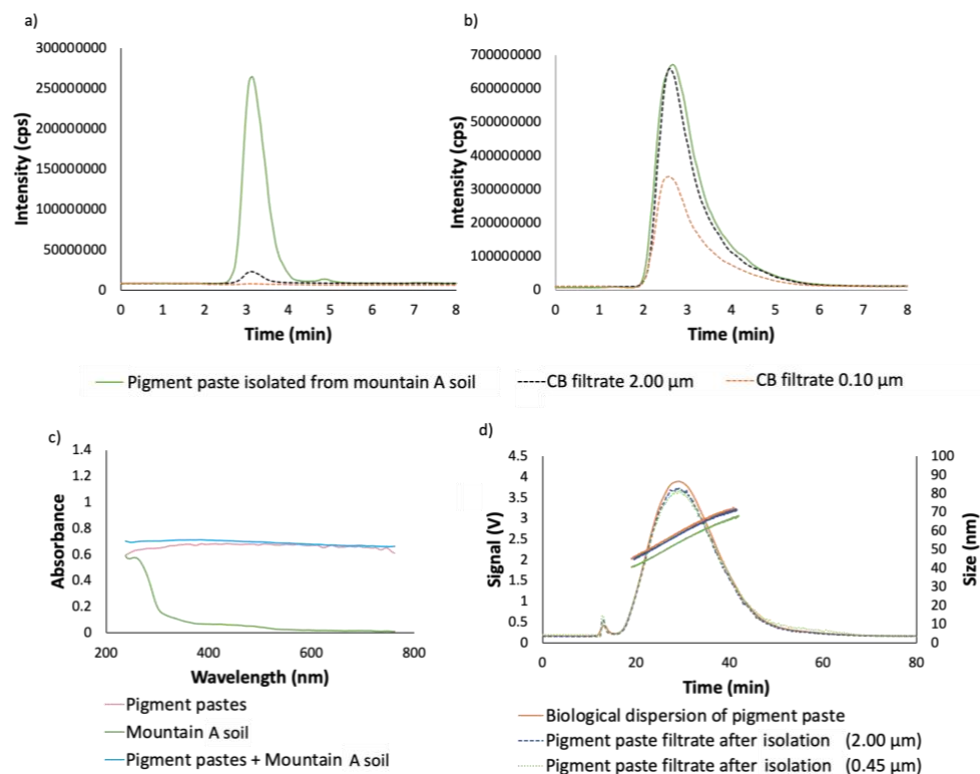


**Figure 102:** a) Fractogram for pigment paste isolation from mountain A soil using polymeric dispersant (green). Dotted lines: AF4-DLS signal of filtrate using fiberglass 2  $\mu\text{m}$  (black) and teflon 0.10  $\mu\text{m}$  (orange). b) Fractogram for pigment paste isolation from mountain A soil using biological dispersant (green). Dotted lines: AF4-DLS signal of filtrate using fiberglass 2  $\mu\text{m}$  (black) and teflon 0.10  $\mu\text{m}$  (orange). c) Diffuse reflectance: absorbance of the samples (pigment paste, mountain A soil and pigment paste isolated from soil). d) Fractogram for pigment paste dispersion using biological dispersant by SdF3-MALS (red). Dotted lines: SdF3-MALS signals of pigment paste filtrate dispersion after isolation using fiberglass 2  $\mu\text{m}$  (blue) and nylon 0.45  $\mu\text{m}$  (green) (isolation from mountain soil). Size distribution (radius of each sample).



SdF3-MALS was also used for measuring dispersions, LOD achieved by this technique was  $1.29 \text{ mg}\cdot\text{L}^{-1}$ . Figure 103, shows the SdF3-fractograms obtained for mountain A (a) and orchard A (b) soils dispersions without target analyte prepared using biological dispersant. As can be seen, mountain soil processed by dispersive and filter-aided steps using fiberglass  $2.00 \mu\text{m}$  and nylon  $0.45 \mu\text{m}$  provided negligible signals and hydrodynamic average radius (RH) of  $77 \pm 5 \text{ nm}$  and  $56 \pm 3 \text{ nm}$ , respectively. For orchard soil, the dispersion with fiberglass  $0.45 \mu\text{m}$  not showed significant signal as in the case of mountain soil and the hydrodynamic radius obtained was  $(82 \pm 3 \text{ nm})$ . Using nylon  $2.00 \mu\text{m}$  as filter membrane, an average hydrodynamic radius of  $101 \pm 4 \text{ nm}$  was calculated. Those results are in accordance with those shown in Figure 94 obtained by AF4-DLS.

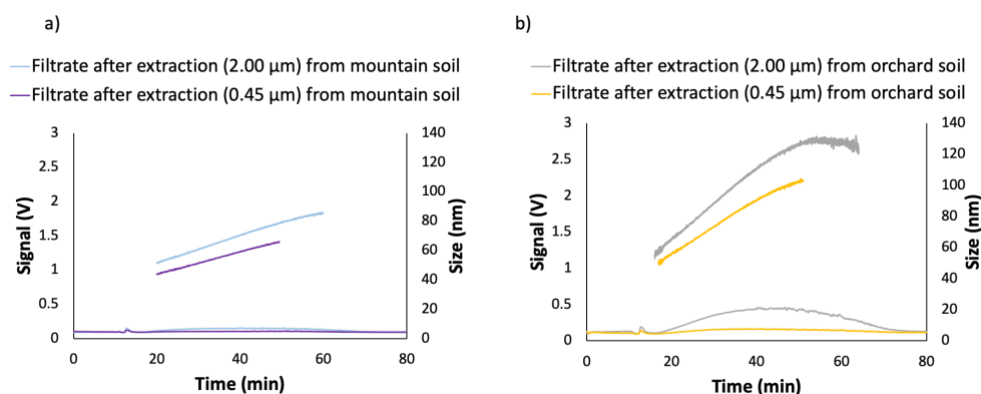


**Figure 103:** SdF3-MALS-fractograms and size distribution (radius) obtained for soil filtrate after extraction without target analyte. a) Mountain A soil filtrate after extraction (biological dispersant). b) Orchard A soil filtrate after extraction (biological dispersant).

Figure 104.a shows the SdF3-fractogram obtained for biological CB bulk dispersion, well defined distribution was achieved with average hydrodynamic radius of  $99 \pm 5 \text{ nm}$ . Following the proposed procedure, CB isolated and filtered dispersion from mountain A and orchard A soil was tested using biological dispersant as dispersive media. Results showed that D-IE of CB dispersion was quantitative for mountain A soil as matrix ( $\text{RH} = 97 \pm 3 \text{ nm}$ ). FA-RE was negligible using fiberglass  $2.00 \mu\text{m}$  and nylon  $0.45 \mu\text{m}$  as filter membranes (Figure 104.a).

As in the case of mountain A soil, SdF3-MALS analysis was carried out for orchard A soil. Figure 104.b shows the SdF3-fractograms. The FA-RE were higher than those achieved with the mountain A soil. FA-RE with fiberglass 2.00  $\mu\text{m}$  membrane was 55.2%. For nylon 0.45  $\mu\text{m}$  membranes, FA-RE was significantly higher than for other assays (76.7%). In both cases, RH were constant for the particle distribution at  $t_r = 28.7$  min: Sizes were  $98 \pm 5$  nm and  $96.3 \pm 1.4$  nm for fiberglass 2.00  $\mu\text{m}$  and nylon 0.45  $\mu\text{m}$ , respectively. However, fiberglass 2.00  $\mu\text{m}$  provided a wide distribution around  $t_r = 46 - 60$  min. This signal was obtained by a contribution between compounds extracted directly from soil and target analyte with RH of  $174.1 \pm 0.9$  nm. Those results are similar to those given in Figure 101.

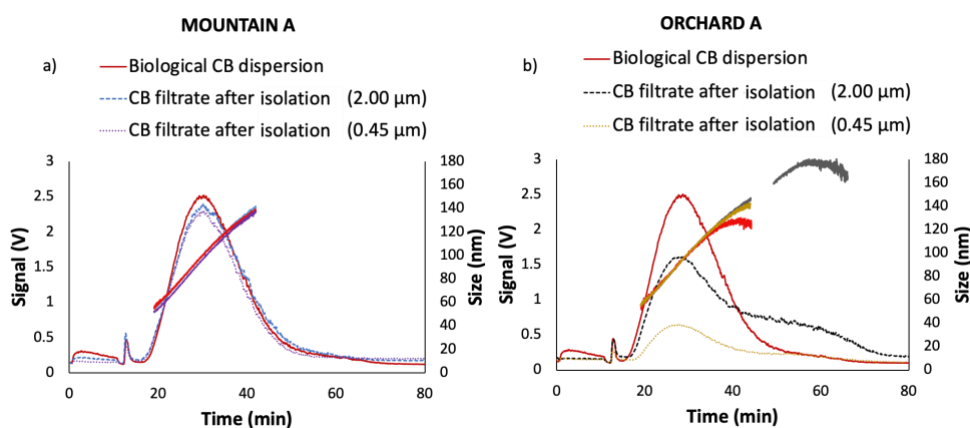


**Figure 104:** Fractograms for CB dispersion using biological dispersant by SdF3-MALS (red). Dotted lines: SdF3-MALS signals of CB filtrate dispersion after isolation using fiberglass 2  $\mu\text{m}$  and nylon 0.45  $\mu\text{m}$  (isolation from mountain soil). Size distribution (radius of each sample). a) For mountain A soil matrix and b) for orchard A soil matrix.

CB based pigment paste bulk dispersion and the filtered solution after recovery step from mountain A soil using biological dispersant were also analysed by SdF3-MALS. Fractograms obtained are shown in Figure 102.d. As in the case of CB dispersion for this matrix, isolation was quantitative and filter-aided recovery step not produce significant retention on the membrane. The average RH obtained were  $58.3 \pm 1.8$  nm for pigment paste bulk dispersion,  $59 \pm 4$  nm for pigment paste isolated and filtered with fiberglass 2.00  $\mu\text{m}$  and  $50.2 \pm 0.9$  for pigment paste isolated and filtered with nylon 0.45  $\mu\text{m}$ . As can be seen, the recovery values and

hydrodynamic sizes obtained with SdF3-MALS were in concordance with results observed with AF4-DLS.

In order to characterize and quantify the CB obtained by filter-aided recovery method in teflon membranes (0.10  $\mu\text{m}$ ), Diffuse Reflectance (DR) was used by measuring the membrane surface. DR, measured as absorbance, can be observed in Figure 102.c and Figure 105.a and b.

As can be seen, for mountain A soil, the signal for a CB standard biological dispersion was similar to the signal of CB recovered from soil, which can be related with a quantitative dispersion of the NM (Figure 105.a). CB concentration was estimated by measuring the absorbance at 650 nm. For orchard A soil, the signal of CB isolated and filter-aided recovered from soil was slightly lower than the CB recovered from standard dispersion (Figure 105.b). This fact can be explain taking into account the lower D-IE as can be observe in AF4-DLS analysis (see Figure 96.d).

DR measurements of the membrane surface (teflon 0.10  $\mu\text{m}$ ) was also measured to evaluate the concentration and FA-RE in pigment paste sample. Responses of mountain A soil dispersion recovery and direct pigment paste bulk dispersion after the filter aided step can be seen in Figure 102.c. Absorbance spectra showed comparative signals for recovered CB from pigment paste in soil and CB from standard pigment paste dispersion. However, these values were significantly lower than the recovered signal of CB dispersion directly measured at the same concentration level, according to the limited retention on the filter support.

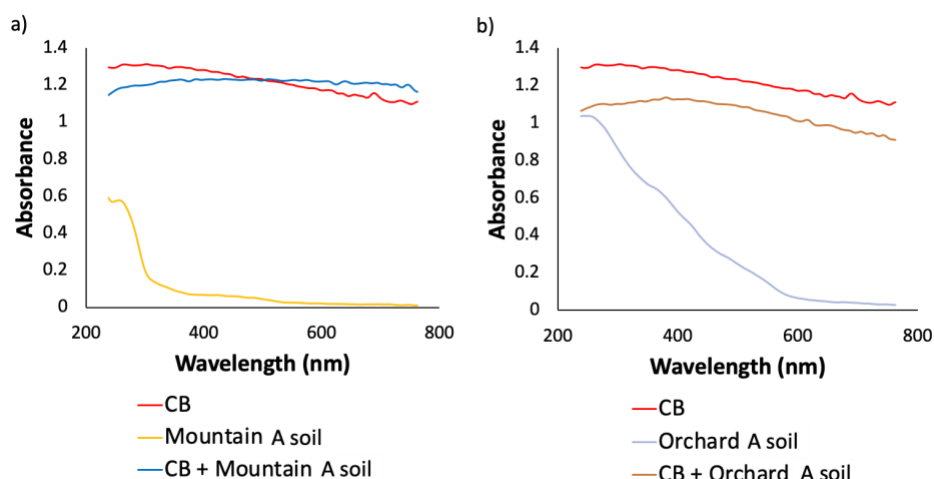


**Figure 105:** a) Diffuse reflectance study for CB isolated from mountain soil and recovered using teflon membrane 0.10  $\mu\text{m}$  (CB directly recovered (red), soil extract recovered (yellow) and CB isolated from soil and recovered (blue). b) Diffuse reflectance study for CB isolated from orchard soil and recovered using teflon membrane 0.10  $\mu\text{m}$  (CB directly recovered (red), soil extract recovered (grey) and CB isolated from soil and recovered (brown).

Table 40 shows the concentration values estimated after the CB isolation and filter-aided recovery step using teflon 0.10  $\mu\text{m}$ . The concentration was established by using the previously calculated calibration curve  $A = (0.027 \pm 0.002) [\text{CB}] + (0.09 \pm 0.06)$ ;  $R^2 = 0.9$ , and  $\text{LOD} = 0.25 \text{ mg}\cdot\text{L}^{-1}$ . (Estimated as  $3 \cdot \text{sblank} / \text{slope}$ ). The results obtained are in accordance with those provided by dispersion measurements by AF4-DLS.

**Table 40:** CB concentration and % recovery in different matrices calculated on the surface of the filter membrane.

CB isolated and fiber recovered	Concentration ( $\text{mg}\cdot\text{L}^{-1}$ )	Recovery (%)
Mountain A soil	$37.3 \pm 0.6$	$99 \pm 2$
Orchard A soil	$29.6 \pm 0.5$	$79.4 \pm 1.6$
Pigment paste in mountain A soil	$20.4 \pm 0.3$	$54.5 \pm 1.1$

- Conclusions

In this study, polymeric and biological dispersants were studied in order to evaluate their capability to disperse CB nanomaterials. The dispersion mechanism proposed showed that polymeric dispersion was achieved through van der Waals forces between nanomaterials and copolymers used, while the biological dispersant formed capping with biomolecules, mainly amino acids, around CB providing better dispersion stability than the polymeric dispersant. AF4-DLS fractograms showed a linear relationship between signal versus concentration. Moreover, the hydrodynamic sizes were analyzed by DLS, both coupled to AF4 and in batch mode, obtaining comparable values. However, the hydrodynamic size showed significant differences in the function of dispersant used for all CB samples assayed, which was related with their different capacities of dispersion. Smaller sizes were obtained and higher amounts of CB were dispersed using biological dispersants, which were improved in a biological medium supplemented with a dipeptide. Good linear calibration graphs were obtained too. Precision studies were also carried out, and the obtained RSD values were lower than 5% for all dispersants.

A stability test with time was carried out, and the results indicated that the biological dispersant allowed dispersions with suitable stability that remained at least for a week, compared with a lack of stability of the polymeric dispersion. A study of CB dispersion stability in several real environmental waters was carried out. The dispersion stability was dependent of the composition of each water matrix, which showed a greater effect in the case of polymeric dispersion.

Moreover, a procedure based on a dispersive media for CB isolation from soil samples was proposed by the first time. AF4 on-line coupled to DLS detector and SdF3 coupled to MALS were employed to study and evaluate the process. Four different soils (two mountains and two orchard soils) were used. DLS fractograms provided quantitative results for mountain A and B, and orchard B soils using biological dispersant. In the case of orchard A soil, the D-IE was less quantitative 75 %. For polymeric dispersant the isolation was near 70%. The different performance between used soils can be related with the lower particle sizes of orchard A soil and the higher concentration of organic matter present in mountain A and B, and orchard B soils which can improve the CB dispersion stability.

In the case of filter-aided process for CB recovery from achieved dispersions, the results indicated that particle size is a key parameter, which depended on the dispersive agent used. But also, surface charges must be considered in order to achieve a good recovery. Therefore, the mechanisms governing this filter approach were steric hindrance and electrostatic interactions. Polymeric dispersions resulted in quantitative recoveries except for nylon 5  $\mu\text{m}$ , however, for biological FA-EE up to 10% was achieved using membranes with pore size  $> 0.45 \mu\text{m}$ . These results can be explained considering hydrodynamic size and Z-potential. Recovered studies were also carried out for isolated CB dispersions from soils using two types of filters. For teflon 0.10  $\mu\text{m}$  filters, the recovery was completely in all scenarios according to the hydrodynamic size of particles. Results obtained with SdF3-MALS were in concordance with values observed with AF4-DLS. Moreover, diffuse reflectance results were used for quantify the CB recovery in teflon membranes 0.10  $\mu\text{m}$  supporting the quantitative isolation too.

The use of pigment paste as a CB sample provided suitable NM isolation in mountain soils in accordance with previous results. In this case, the average hydrodynamic size was near 100 nm which produced a minor recovery in teflon 0.10  $\mu\text{m}$  filter.

The comparison of AF4-DLS and SdF3-MALS has demonstrated the potential of these techniques to evaluate CB isolation from matrices of environmental interest.

Therefore, it is proposed that the FFF techniques coupled to UV-vis, DLS and MALS may become a valuable tool for rapid characterization, isolation evaluation, determination and stability studies of CB dispersions in polymeric and biological dispersants.

### 4.3 SILICA NANOMATERIALS

In this section, different silica based NMs with different sizes and structures were analysed by AF4-DLS in order to advance of the knowledge of this technique as a reliable tool for the characterization of this ENM. SiO<sub>2</sub>NPs, SiO<sub>2</sub> extracted from rice straw ashes ( $\mu$ -SiO<sub>2</sub>) and halloysite nanotubes (HNTs) were employed. Their dispersions were carried out and analysed, optimizing the size distribution separation.

For SiO<sub>2</sub> extracted from rice straw ashes, their functionalization and applicability as adsorbent tool for reduces the nitrate concentration in waters was evaluated. The ability to scale-up the synthesis was studied according to the principles of green chemistry using renewable sources, minimizing reagents, number of steps, and energy consumption, and energy consumption, and preventing waste by recycling. Adsorption studies were also carried out and compared with those corresponding to a commercial resin.

#### ***4.3.1 Characterization of silica based materials by SEM and FTIR-ATR.***

The different silica based materials were characterized by FTIR-ATR technique. Spectra are showed in Figure 106.a - d, providing different structural information. Vibration band between 780 - 810 cm<sup>-1</sup> was related with symmetric bending mode of Si - O. Meanwhile, the band between 1030 - 1110 cm<sup>-1</sup> was assigned to major asymmetric stretching of Si - O - Si [354]. Both bands were observed in all the studied samples. For HNT material, the bands correlated with Al<sub>2</sub>OH-stretching (3647 and 3610 cm<sup>-1</sup>) and the single Al<sub>2</sub>OH-bending (912 cm<sup>-1</sup>) were also observed [355].

The surface morphology and size of silica based materials were studied by scanning electron microscopy (SEM). Solid SiO<sub>2</sub>NPs provided core size particles around 19 nm, but the Figure 106.e shows also agglomerates of NPs, which can be compatible with a string-of-pearls-type morphology [356]. SiO<sub>2</sub>NPs with hydroxyl modification pretreatment are given in Figure 107.a. As it can be seen, the modification did not produce changes in the particle morphology being similar to that shown in Figure 106.e.

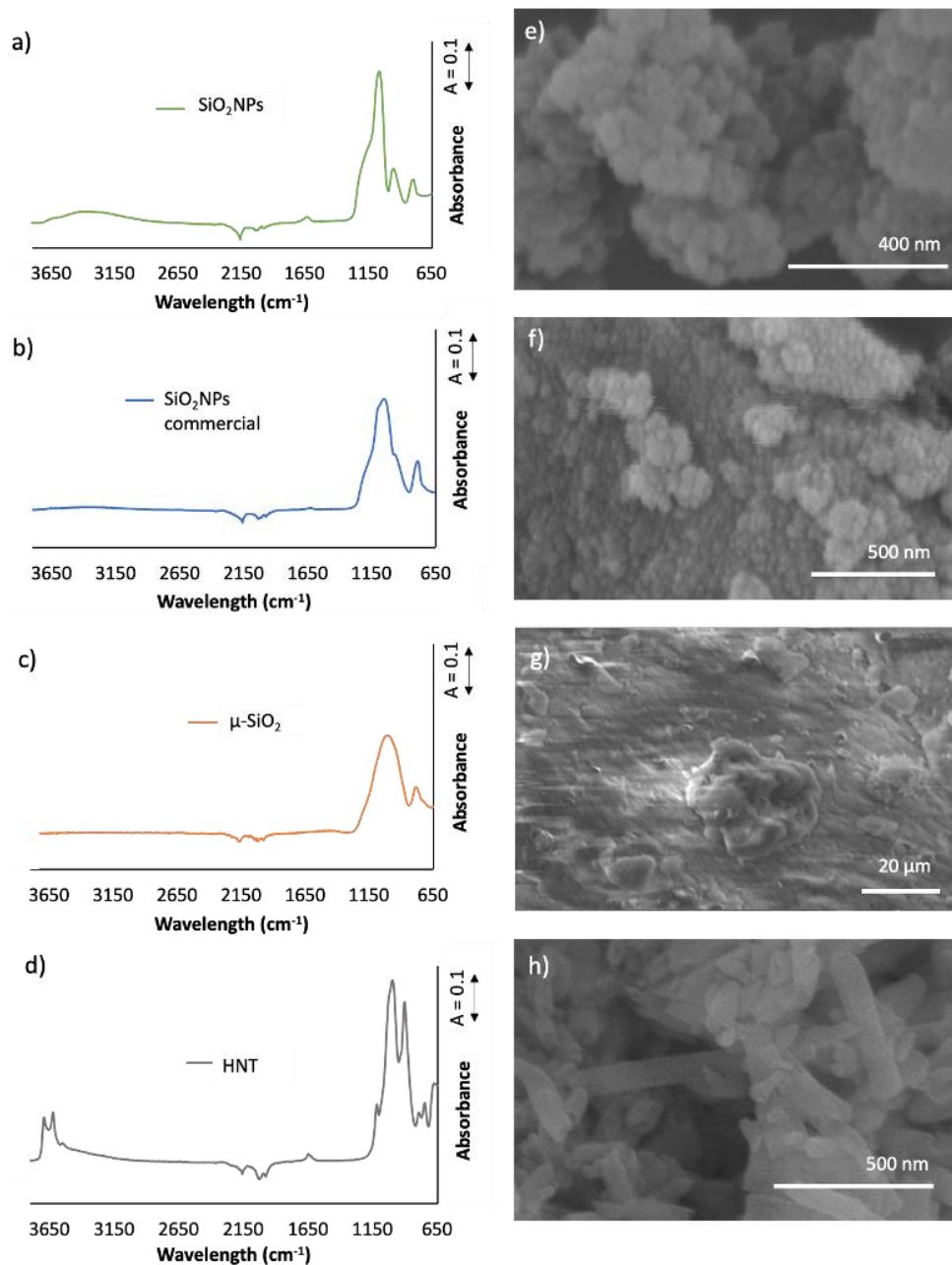


**Figure 106:** FTIR-ATR spectra of a) SiO<sub>2</sub>NPs, b) commercial SiO<sub>2</sub>NPs CL30, c) extracted μ-SiO<sub>2</sub>NPs from rice straw ashes and d) HNT. SEM images of e) SiO<sub>2</sub>NPs; f) commercial SiO<sub>2</sub>NPs CL30, g) extracted μ-SiO<sub>2</sub>NPs from rice straw ashes and h) HNT.



Commercial SiO<sub>2</sub>NPs dispersions provided spherical particle shapes with homogenous distribution. For CL30 (Figure 106.f) the average size observed was 13.52 nm. In both cases, results were in concordance with core size values provided by the manufacturer.

The morphology of the  $\mu$ -SiO<sub>2</sub> material extracted from rice straw ashes was also characterized.  $\mu$ -SiO<sub>2</sub> material was grinded and sieving obtaining different size fractions: particles < 100  $\mu$ m (30%), particles of 100 - 200  $\mu$ m (15%), particles of 200 - 300  $\mu$ m (12%), particles of 300 - 400  $\mu$ m (13%) and particles > 400  $\mu$ m (39%). The fraction containing particles < 100  $\mu$ m was analyzed by SEM. The image is showed in Figure 106.g. A heterogeneous size distribution was obtained. The extracted modified  $\mu$ -SiO<sub>2</sub> was also analysed and SEM image is observed in Figure 107.b. As can be seen, a porous material was obtained after amino modification of the  $\mu$ -SiO<sub>2</sub> while the  $\mu$ -SiO<sub>2</sub> showed a smooth surface. Finally, Figure 106.h shows HNT with average length of 0.2 - 0.5  $\mu$ m and diameter of 40 – 50 nm. Structure of modified HNT can be seen in Figure 107.c, which revealed similar size after hydroxyl pretreatment.

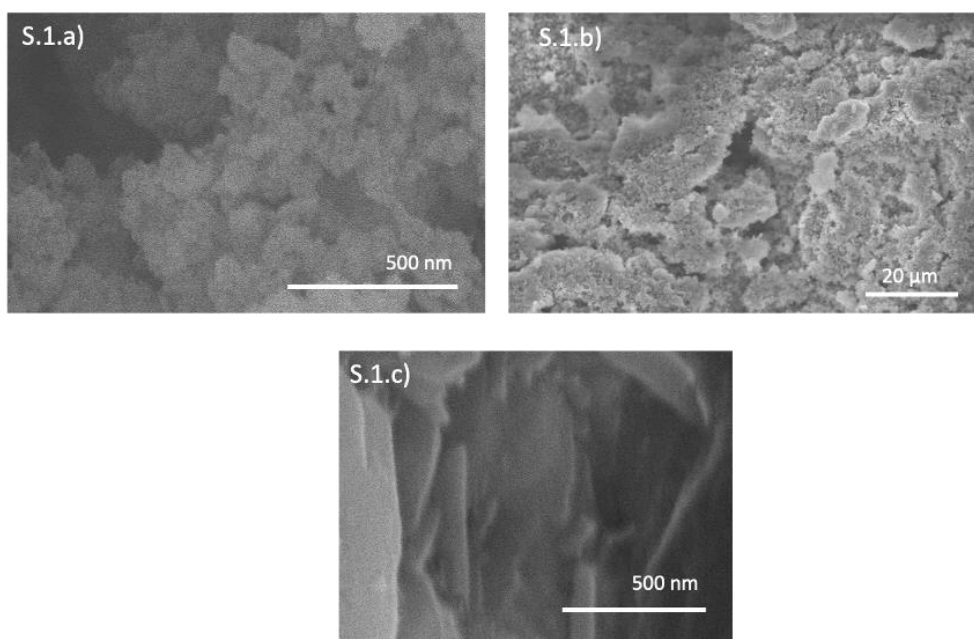


**Figure 107:** SEM images of a) SiO<sub>2</sub>NPs modified with KOH solution, b) modified extracted  $\mu$ -SiO<sub>2</sub> from rice straw ashes and c) modified HNT

Moreover, the elemental analysis was carried out (Table 41). The SiO<sub>2</sub> structure was confirmed by SEM/EDX analysis for all silica samples, which showed a relation 1:2 regards silica and oxygen atoms. LUDOX TM40 commercial SiO<sub>2</sub>NPs dispersion, exhibited a low percentage of sodium corresponding to the counterion used to carry out the SiO<sub>2</sub> NPs stabilization. In the case of LUDOX CL30, the presence of aluminum revealed its use as a modifier to carry out cationic SiO<sub>2</sub>NPs subsequently stabilization.

μ-SiO<sub>2</sub> material obtained from rice straw ashes shows a high number of elements in their composition, according to the different synthesis steps developed, such as the use of NaOH for the silicate extraction process of the ashes, H<sub>2</sub>SO<sub>4</sub> for the precipitation of silica gel and N probably from ashes. For HNT, the main elements were: silica, oxygen and aluminum as reflected in their intrinsic structure [219].

**Table 41:** Elemental composition of different silica based materials analysed expressed respect Si content.

	Relative atom content	
	O/Si	Others
SiO <sub>2</sub> NPs (TM40). <sup>a</sup>	2.00	0.05 Na/Si
SiO <sub>2</sub> NPs (CL30). <sup>b</sup>	2.19	0.02 Al/Si
SiO <sub>2</sub> NPs	2.08	---
μ-SiO <sub>2</sub> material	2.04	0.12 Na/Si; 0.04 S/Si; 0.04 N/Si
HNT	4.19	1.03 Al/Si

<sup>a</sup> Commercial SiO<sub>2</sub>NPs with anionic grade

<sup>b</sup> Commercial SiO<sub>2</sub>NPs with cationic grade

### 4.3.2 Characterization of SiO<sub>2</sub>NPs by AF4-DLS

Tween 20, Triton X-100 and KOH were tested as dispersants of solid NPs of 19 nm of core size. Using Tween 20 0.10 %, Triton X-100 0.10 % and Triton X-100 0.01 %, the particles sedimented to the bottom quickly. However, with KOH 14.5 mM, satisfactory dispersibility was achieved in accordance with the approach to impart charge to the silica surface, which keeps the particles from aggregating and gelling [357]. Considering these results, KOH was selected.

Several AF4-DLS elution programs were used (Table 18) and the corresponding fractograms for a dispersion 0.25 % (m/v) were given in Figure 108.a. The detector and injection flows remained constant at  $0.5 \text{ mL}\cdot\text{min}^{-1}$  for all programs. Moreover, the injection time was 1.5 min and transition time was 1 min. Correct separation was performed with the program that used initial cross-flow of  $0.75 \text{ mL}\cdot\text{min}^{-1}$  and elution with power x3 (Table 18, Silica – program 4).

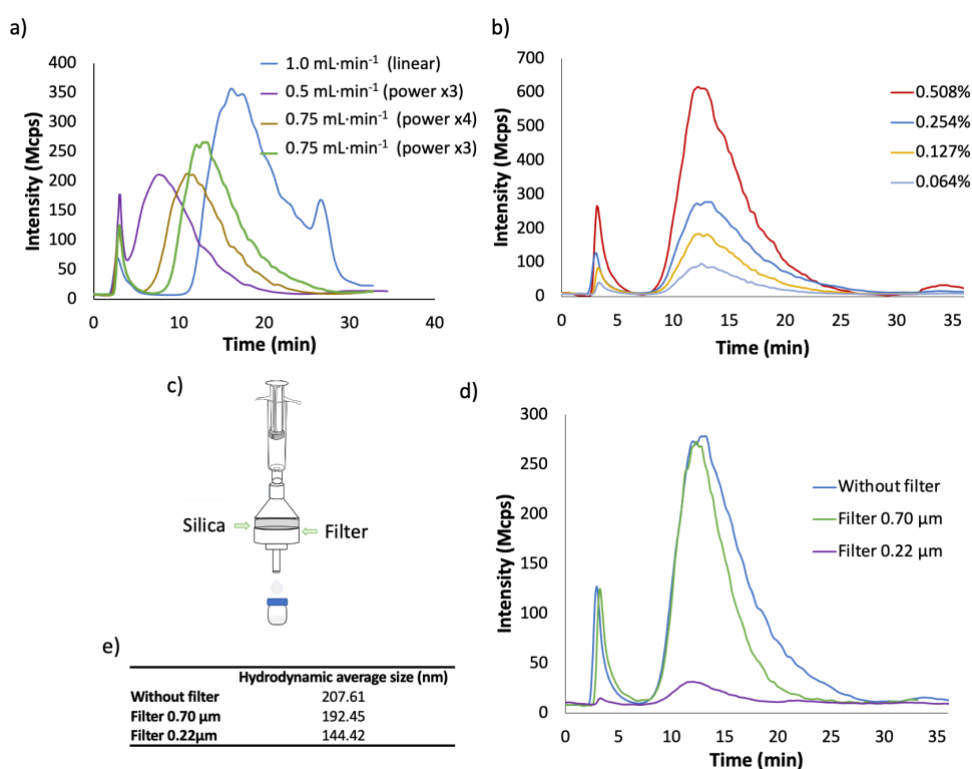


**Figure 108:** a) Fractograms obtained for each elution program used. b) Fractograms obtained for  $\text{SiO}_2\text{NPs}$  dispersion as a function of the concentration: 0.508 % (red), 0.254 % (blue), 0.127 % (yellow) and 0.064% (grey). c) Schematic representation of the filtering process. d) Fractograms obtained for each filtering using two filter membranes: fiberglass  $0.70 \mu\text{m}$  (green) and nylon  $0.22 \mu\text{m}$  (purple). Comparison with directly injected sample (blue). e) Hydrodynamic size values obtained for each samples studied:  $\text{SiO}_2\text{NPs}$ , filtering with fiberglass  $0.70 \mu\text{m}$  and filtering with nylon  $0.22 \mu\text{m}$ .

By using the program selected, several dispersions at different concentrations levels were processed, in all cases the achieved retention times of the fractograms were the same, and the hydrodynamic diameter was of  $209 \pm 4$  nm. Higher sizes and less dispersibility was obtained working at pH 9 with KOH (see Figure 109). Figure 108.b shows the fractograms registered at different  $\text{SiO}_2\text{NPs}$  concentrations. As can be seen, linear calibration graph was obtained with suitable regression coefficient ( $R^2 = 0.9893$ ) and RSD of 1.6 %. Limit of detection was evaluated and the value obtained was  $1.5 \text{ mg}\cdot\text{L}^{-1}$ .

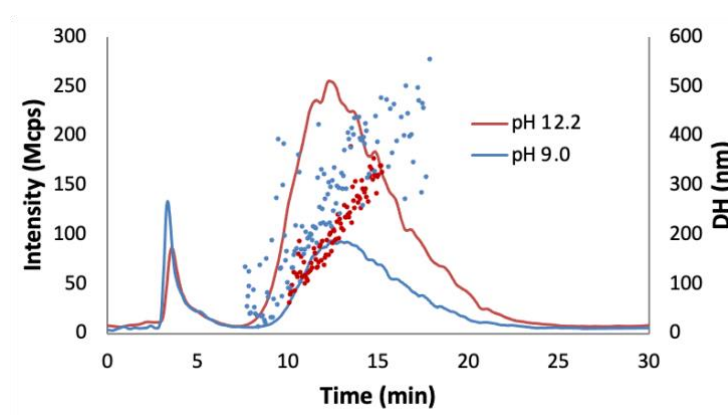


**Figure 109:** DLS fractograms obtained for  $\text{SiO}_2\text{NPs}$  dispersions carried out using KOH solution at pH 12.2 (red) and pH 9.0 (blue). Size distribution included.

Due to the high hydrodynamic size obtained in reference to the SEM measurements given in Section 4.3.1 for the silica particle, a dispersion was filtered (Figure 108.c) and the filtrate was collected and injected in the AF4-DLS. Fractograms obtained for each filter are depicted in Figure 108.d. As it can be seen, sample injected without filter treatment showed a higher polydispersity compared with filtered dispersions. Using fiberglass filter membrane of  $0.70 \mu\text{m}$ ,  $\text{SiO}_2\text{NPs}$  particle distribution shift towards lower retention times and low average size although the intensity of the DLS signal was similar. Assay with nylon filters of  $0.22 \mu\text{m}$  similar to the calculated hydrodynamic size provided an increasing retention of particles in the filter (Figure 108.e). Similar sizes were given in [282]. These sizes can be due to the dispersion of string-of-pearls of silica [356].

Commercial SiO<sub>2</sub>NPs dispersions were also studied using the AF4-DLS. Firstly, the elution program was optimized (Table 18). In all programs, the detector flow and injection flow remained constant at 0.5 mL·min<sup>-1</sup>. Moreover, the injection time was 1.5 min and 1 min as transition time. As can be seen in Figure 110.a, cross-flows with initial values lower than 1 mL·min<sup>-1</sup> (Silica - programs 5 and 6 of Table 18) did not provide suitable separations. Similarly, using programs with conditions higher than 3 mL·min<sup>-1</sup> (Silica - program 8 of Table 18), the peaks obtained were too wide and the retention time were so much high.

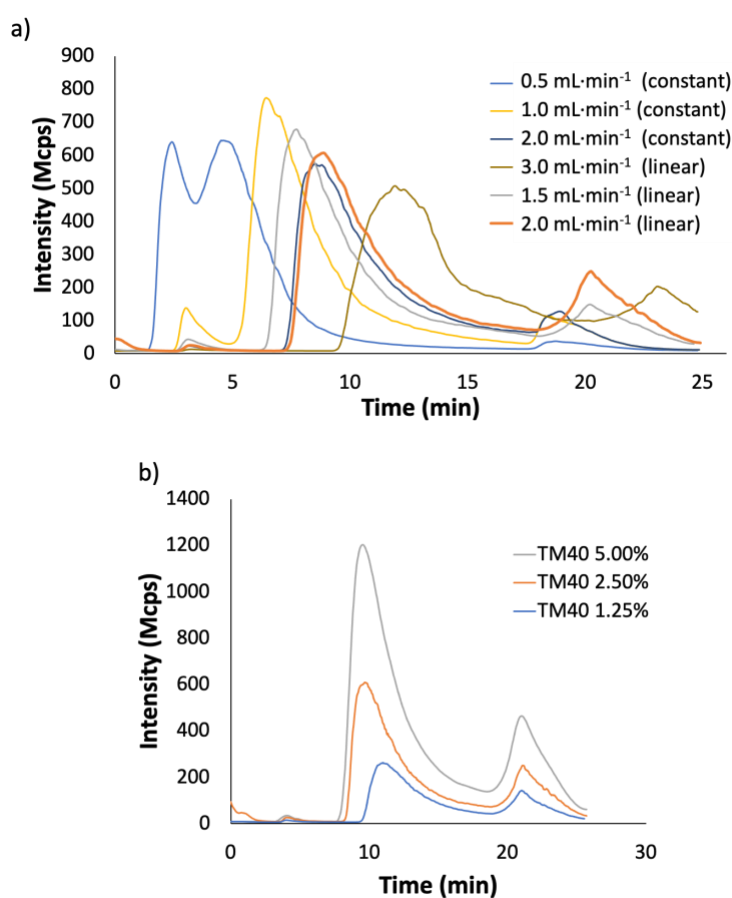


**Figure 110:** a) Fractograms obtained for each elution program used. b) Fractograms obtained for SiO<sub>2</sub>NPs dispersion TM40 at three concentration levels: 5.00 % (grey), 2.50 % (orange), 1.25 % (blue).

Employing initial cross-flows between 1.5 and 2 mL·min<sup>-1</sup> (Silica - programs 7, 9 and 10 of Table 18), the separation achieved was suitable, obtaining defined peaks with  $t_r$  in the interval 6 – 9.5 min. Moreover, in these cases, a second peak was observed at  $t_r = 19 – 21$  min, corresponding to aggregates and high particles in the dispersion. Thus, Silica - program 10 of Table 18, was selected as method to analyse all dispersions, according to the higher sensitivity obtained for larger particles compared to the other tested programs. Different concentrations (5.00 %, 2.50 % and 1.25 %) of commercial SiO<sub>2</sub>NPs dispersion TM40 were analysed. Figure 110.b shows the fractograms registered. As can be seen, commercial SiO<sub>2</sub>NPs dispersions provided satisfactory correlation ( $R^2 = 0.9985$ ). Moreover, limit detection was calculated and the value obtained was higher than obtained for solid SiO<sub>2</sub>NPs dispersions (7.2 mg·L<sup>-1</sup>). Precision studies were also carried out, for this purpose relative standard deviation (% RSD) was calculated. The results obtained for three replicates showed that RSD values were lower than 2.7%. The sizes registered were in accordance with the core size (22 nm). The hydrodynamic diameters for the first peak were 25.44 nm, 25.89 nm and 29.31 nm for the concentrations of 5.00 %, 2.50 % and 1.25 % respectively. In the case of second peak, the sizes were 61.24 nm, 62.47 nm and 59.78 nm respectively, corresponding to the aggregates in SiO<sub>2</sub>NPs distribution.

Commercial SiO<sub>2</sub>NPs dispersions at concentration of 1.25 % with different sizes and stabilization conditions were analysed following the method described. Figure 111.a shows the fractograms obtained and the hydrodynamic size values using two different analytical techniques (AF4-DLS and directly DLS in batch). Regarding commercial SiO<sub>2</sub>NPs samples with particle core size of 22 nm, two different compounds were used to carry out stable dispersions, NaOH and NH<sub>4</sub>OH. Samples TM40 and TM50, which contain Na<sup>+</sup> as counter ion, showed defined distributions with retention time of 10.91 and 11.22 min respectively. The hydrodynamic sizes obtained by AF4-DLS were 29.31 for TM40 and 30.32 for TM50. In this case, sensitivity obtained with TM40 was better than that achieved with TM50 for the same concentration since sample TM40 is preserved in the fridge. For samples with core size of 22 nm and containing NH<sub>4</sub><sup>+</sup> as counter ion, AS40 was analysed and fractogram showed a high hydrodynamic size (37.56 nm) according to the size increase of counter ion used in this dispersion.

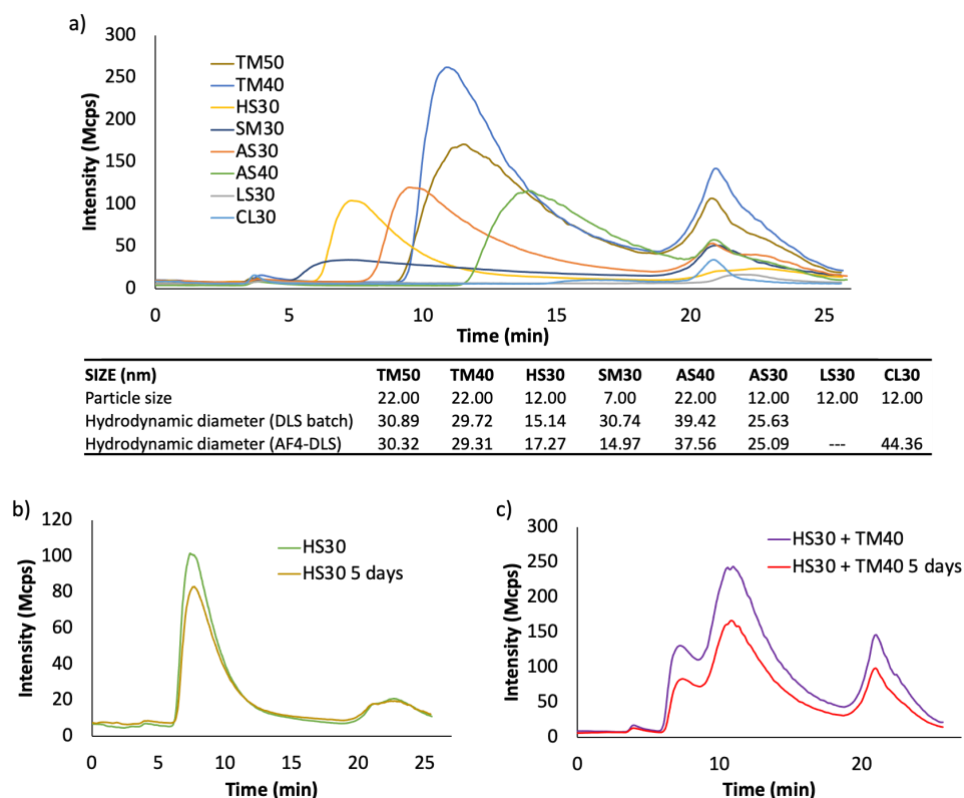


**Figure 111:** a) Fractograms of eight different commercial  $\text{SiO}_2\text{NPs}$  dispersions with different sizes and stability conditions. Values of core size of each commercial  $\text{SiO}_2\text{NPs}$  dispersion and hydrodynamic diameters obtained by AF4-DLS and direct DLS batch analysis. b) Stability study as a function of dilution preparation time for commercial  $\text{SiO}_2\text{NPs}$  dispersion HS30 1.25%. c) Separation of mixture commercial  $\text{SiO}_2\text{NPs}$  dispersion HS30 and TM40 1.25%. Stability study as a function of mixture preparation time

Commercial  $\text{SiO}_2\text{NPs}$  dispersions with core size of 12 nm were carried out using NaOH,  $\text{NH}_4\text{OH}$  and HCl as stabilizer compounds. Fractograms obtained for samples HS30 and AS30 provided suitable distributions with hydrodynamic size obtained by AF4-DLS of 17.27 nm and 25.09 nm respectively which are correlated with the counter ions added to the dispersions,  $\text{Na}^+$  for HS30 and  $\text{NH}_4^+$  for AS30. Study of sample CL30, which used HCl as stabilizer, provided a fractogram with negligible distribution at  $t_r = 16.5$  min with hydrodynamic diameter of 44.36 nm. In the case of sample LS30, which contain  $\text{Na}^+$  as counter ion at pH 8, the fractogram

obtained did not provide a defined distribution because charge density of colloidal SiO<sub>2</sub>NPs at pH < 8 was not enough at concentration higher than 10 %.

Commercial SiO<sub>2</sub>NPs dispersions with particle core size of 7 nm were also tested. Sample SM30 with Na<sup>+</sup> as counter ion was analysed and fractogram obtained showed a wide peak which was correlated with polydisperse distribution. For this sample, the average hydrodynamic size obtained was 14.97 nm. Remarkably, in all studied SiO<sub>2</sub>NPs samples a peak at  $t_r = 20.9$  min was observed corresponding to the presence of SiO<sub>2</sub>NPs aggregates with average particle size of 60 nm.

Batch size measurements obtained showed similar sizes that the hydrodynamic size observed by AF4, with the exception of sample SM30. For this commercial SiO<sub>2</sub>NPs dispersion, size values obtained with the two analytical techniques used were different, 14.97 for AF4-DLS and 30.74 nm for DLS batch. This difference can be explained considering the wide polydispersity of sample and the presence of aggregates that can be modified the sizes values obtained in analysis DLS batch where the distribution separation was not performed.

Stability study with time was also performed for diluted dispersions. Figure 111.b shows the fractograms of sample HS30 (1.25 %) 5 days after the dilution preparation. As it can be seen, a decrease is observed in the particle distribution. This effect was associated with a loss of stability of particle dispersed, which can generate solid aggregates that settle. Likewise, separation of samples HS30 and TM40 was resolved and the stability study with time was carried out (Figure 111.c). The results obtained were in agreement with the effect observed for individual analysis.

Thus, commercial SiO<sub>2</sub>NPs dispersions provided hydrodynamic diameters lower than SiO<sub>2</sub>NPs dispersions obtained from solid SiO<sub>2</sub>NPs. This effect can be attributed to the dispersion of aggregates in the second case. Moreover, the high hydrodynamic diameters induced the use of lower cross flows, showing an inverse relationship between cross flow and hydrodynamic diameter in order to get and adequate separation.



### 4.3.3 Characterization of HNT by AF4-DLS

Alkaline solution was not a good dispersant of HNTs. Accordingly different dispersants such as salts, ionic liquids and surfactants were employed to study the stability of these dispersions as a function of preparation time. Moreover, different preparation methods were tested. Figure 112 shows the stability study as a function of time for HNTs using three dispersants, their combinations and three stirring techniques. The turbidity was registered and results revealed that the use of surfactants such as Tween 20 and Triton X-100 provided the best stability. Furthermore, comparison of the different stirring techniques allowed select Ultra-Turrax as the best method for obtain stable HNT dispersions.

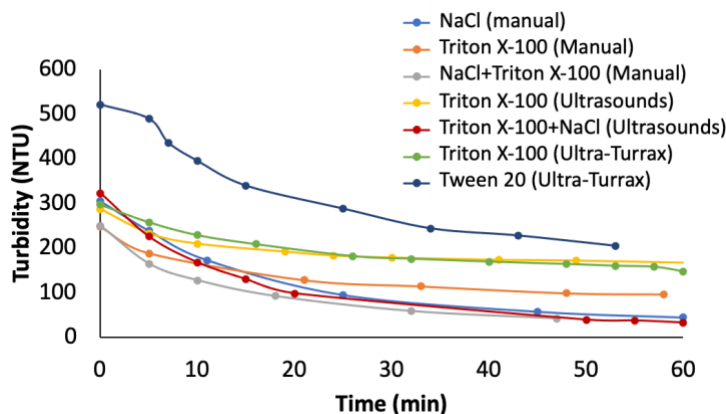


**Figure 112:** Stability study of HNT dispersion using different dispersants and techniques

As regards the modified HNT with hydroxide groups, the study of dispersion stability as a function of preparation time was also carried out. In this case, all dispersions were performed using Ultra-Turrax as a stirring method accordingly the results obtained in previous analysis. As can be seen in Figure 113, ionic liquids and salts provided lower stabilities than those obtained in surfactants. Thereby, Tween 20 was selected as suitable dispersant for further experiments.

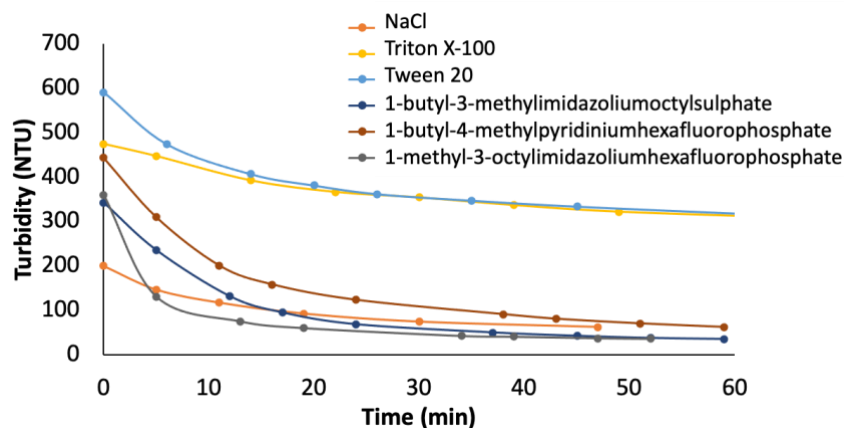


**Figure 113:** Stability study of HNT modified dispersion using different dispersants.

Hybrid pigments HNT-alizarine (AZ-HNT) and modified-HNT alizarine (AZ-mod-HNT) were characterized using optical microscopy. As can be seen in Figure 114.a, optical images provided the surface morphology. In the case of AZ-HNT and AZ-mod-HNT (Figure 114.a.2 and a.3), pinkish raspberry colour indicated the presence of pigment on the surface, however, HNT without treatment did not show that colour change (Figure 114.a.1). AF4-DLS technique was applied. Using elution program 4 for silica (Table 18), HNT dispersions were analysed. Figure 114.b shows the fractograms obtained for HNT modified at different concentration levels. As can be seen, size distribution was separated satisfactory and correlation calculated using the different concentrations tested was successful. Regression coefficient obtained was  $R^2 = 0.9925$ . Moreover, the detection limit was estimated and the value obtained was  $4.7 \text{ mg}\cdot\text{L}^{-1}$ . Along the same method, AZ-HNT and AZ-mod-HNT were studied. As noted in Figure 114.c, the presence of pigment in the surface of HNT produced an increase in the average hydrodynamic size that can be noted with broader size distribution with regard to HNT without treatment. Likewise, modification of surface with hydroxide groups also generated a higher diameter value as can be seen in the fractograms and attached table.

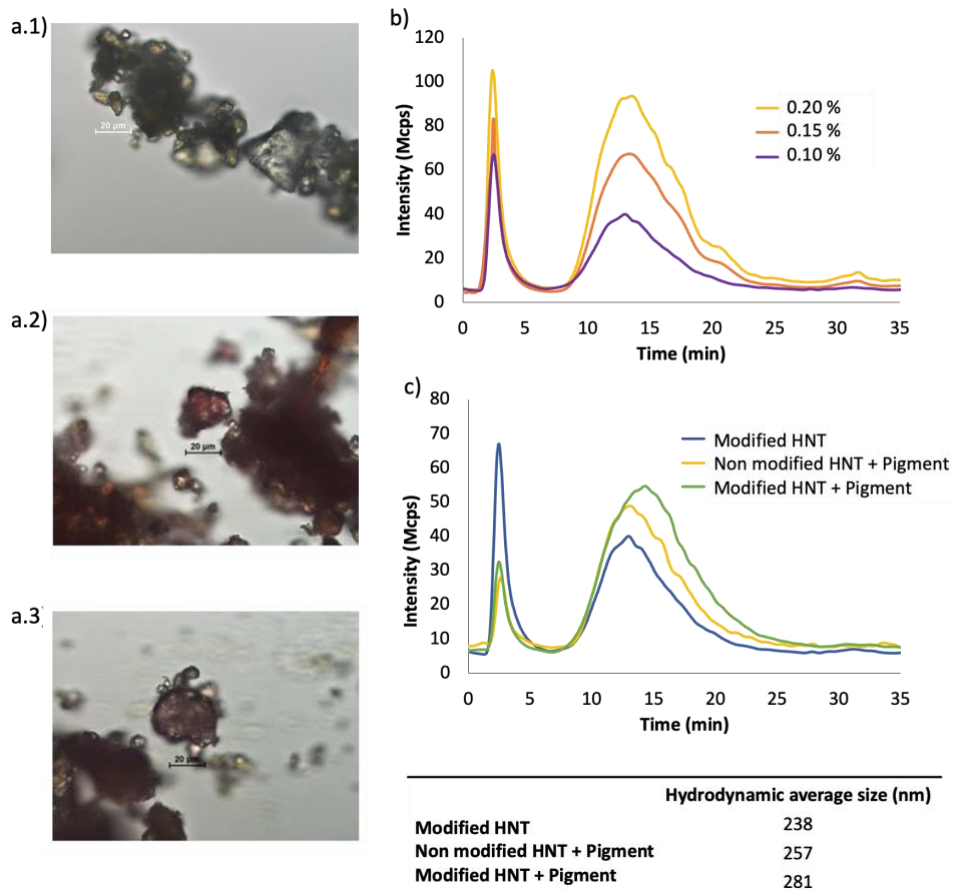


**Figure 114:** a) Optical microscopy images: 1) HNT without treatment, magnification x100; 2) Hybrid pigment AZ-HNT, magnification x50; 3) Hybrid pigment HNT modified with alizarine, magnification x50. b) Fractograms obtained for HNT modified with hydroxide groups dispersion at three concentration levels: 0.20 % (yellow), 0.15 % (orange), 0.10 % (purple). c) Study of different HNT dispersions samples at concentration of 0.10 %: HNT modified in blue, HNT non modified with pigment in yellow and HNT modified with pigment in green. Hydrodynamic average size of each dispersions analysed.

#### ***4.3.4 $\mu$ -SiO<sub>2</sub> obtained from rice straw ashes. Characterization and applicability as adsorbent material***

##### **4.3.4.1 Optimization of the amino-silica synthesis and scale up possibilities**

The selected method for the synthesis of the silica from rice straw ashes was the neutralization method with H<sub>2</sub>SO<sub>4</sub> acid until pH 7 due to it is one of the most used methods for silica synthesis, so improvements applied through greener synthesis could be implemented widely and faster than using other methodologies. Silicic acid concentration greater than the solubility limit of silica leads to its polymerization and precipitation [10]. Chemical and structural characteristics of the silica such as porosity and particle size are affected by factors such as reactant concentrations, temperature, time of stirring and addition of reagents for functionalizing or impregnating the silica surface.

Firstly, the assays were carried out using small quantities in the lab or small scale and then, it was moving to higher amount as it can be seen in Table 16 named scale-up. The quantities used at small scale were accommodated to the conditions of the process at higher scale and the results obtained, as well as the problems or limitations found, were resolved at lab scale and then, moved to higher scale in order to avoid wastes and reduce economic costs.

The studied parameters for obtaining the modified silica were the amounts of water, ammonia, APTES and ethanol, all of them expressed per g of silica (see Table 16) and, also, the time required for the synthesis. We selected APTES because is greener than ternary and quaternary ammonium tags. Water well samples were employed in order to provide a more realistic nitrate adsorption values, due to natural waters contained other anions (as sulphate, phosphate, bicarbonate, iodide), which can affect the adsorption capacity of the material as demonstrated in following sections. The assays were carried out on the fixed-bed column in flow mode (see Figure 26.b) at lab-scale. Adsorption values were calculated considering the amount of nitrate retained at each point assayed until achieving the initial concentration of nitrate (Table 42). The intercept, slope and determination coefficient of the calibration graph used for obtaining the nitrate concentration were:  $b_0 \pm sb_0 = 0.04 \pm 0.05$ ;  $b_1 \pm sb_1$  (mL· $\mu$ g<sup>-1</sup>) =  $0.053 \pm 0.01$  and  $R^2 = 0.996$ , respectively.

**Table 42:** Adsorption capacity of different synthesis of silica until achieving the nitrate initial concentration for well water.

Assay	A1	A2	A3	A4	A5	A6	A7	A8	A9	A10	A11
Adsorption (mg·g <sup>-1</sup> silica)	1.27	0.4	0.61	0.62	0.56	1.9	3.05	3.35	4.11	5.09	3.67

Assay	A12	A13	A14	A15	A16	A17	A18	A19	A20	A21	A22
Adsorption (mg·g <sup>-1</sup> silica)	4.64	4.8	4.9	5.6	2.5	0.9	8.5	10.5	8.5	6.8	3.8

Assay	A23	A24	A25	A26	A27	A28	A29	A30	A31	A32
Adsorption (mg·g <sup>-1</sup> silica)	0.97	2	1.2	3.7	3.5	3.11	4.6	4.9	4.8	8.5

The adsorption capacities of the amino-silica for well water obtained by procedure 1 varied from 0.5 to 1.3 mg nitrate·g<sup>-1</sup> modified silica as it can be seen in the assays A1-A5 of Table 16 and Table 42, while for procedure 2 provided adsorptions varying from 3.7 to 5.6 mg·g<sup>-1</sup> at lab scale (A10-A15). Therefore, procedure 2 produced amino-modified silica with higher capacity of adsorption at lab scale level (Table 16 and Table 42). Other advantages of the use of procedure 2 is the reduction of time from 6.5 h, required for procedure 1, to 1.5 h. This is because in procedure 1 a previous step for dispersion and rehydration of the SiO<sub>2</sub> (5 h) is needed, and in procedure 2 the precipitation and functionalization were carried out in one step (1.5 h).

Another parameter is the amount of APTES used per g of silica. It was observed that an increment of amount of APTES in the synthesis, increased the adsorption capacity of the amino-silica especially for the procedure 1 as Table 16 and Table 42 indicates (A6-A9). Using more than two times the amount of APTES per g of silica produced adsorbents with increased capacity of adsorption.

For procedure 2, it was observed the same trend at lab scale, two layers achieved almost double adsorption capacity as results of A18-A21 indicated (see Table 16 and Table 42). We can also see how using the procedure 1, the capacity

adsorption ( $4.1 \text{ mg}\cdot\text{g}^{-1}$  of nitrate for A9) for 5 layers is the same as one layer for the amino-modified silica by procedure 2 (see A10-A15 in Table 16 and Table 42). These results demonstrated that procedure 2 was more effective not only for obtaining the first modification also for its second modification. Procedure 2 achieved the highest adsorption, which was around  $10 \text{ mg nitrates}\cdot\text{g}^{-1}$  in only two layers for well water samples. Note that the minimum amount of APTES giving good results was  $3.3 \text{ g}\cdot\text{g}^{-1}$  de silica (Table 16 and Table 42).

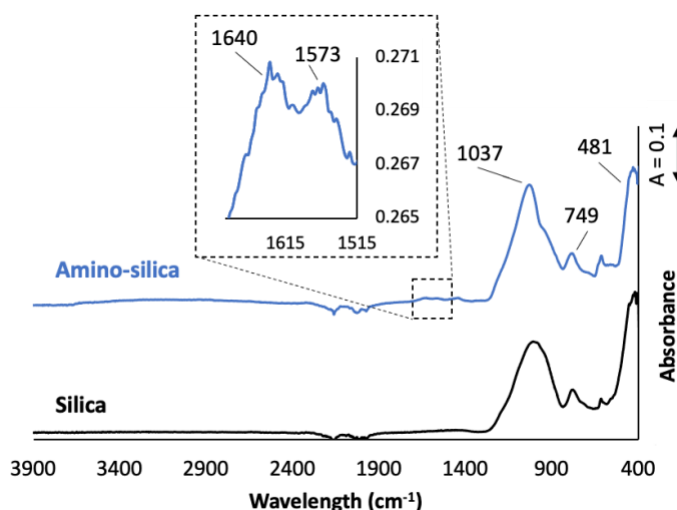
For scaling-up, several syntheses (A22-A32 of Table 16 and Table 42) were carried out considering the results at lab scale and similar conclusions were established. Procedure 2 (A29-A32) gave the best results by employing the same reagent proportions than those optimized at lab scale (A10-A13, A20). These results indicated a good scalability of the conditions established at lab.

Ammonia is used as a catalyst in the sol-gel reaction to incorporate the APTES to the silica, but this reaction can be carried out using acid as a catalyst too. In procedure 2, both steps, precipitation and modification, were made in one step and the medium for silica modification become acid due to the presence of sulfuric acid. Therefore, we tested the possibility to avoid ammonia in the procedure by considering that the sulfuric acid can act as a catalyst. The modified silica obtained by this method showed similar adsorption to that obtained in presence of ammonia, see A15 and A10-13 in Table 16 and Table 42.

Finally, standing on our idea of development of a green method of synthesis, we go a step further and we tested the possibility of reuse the medium of reaction of silica modification (ethanol, water and remaining APTES) for new synthesis or for the modification of already modified silica. For new synthesis the results were discrete as A17 and A23 synthesis show in Table 16 and Table 42 for lab and large scales. A second layer modification carried out with recycled medium gave similar adsorption than non-recycled or fresh medium, see A20 assay of Table 16 and Table 42, which gave similar values of adsorption than A18-19. Therefore, the recycled medium can be used for increasing the adsorption of modified silica by adding layers without consuming more reagent/solvents and without generation of more wastes.

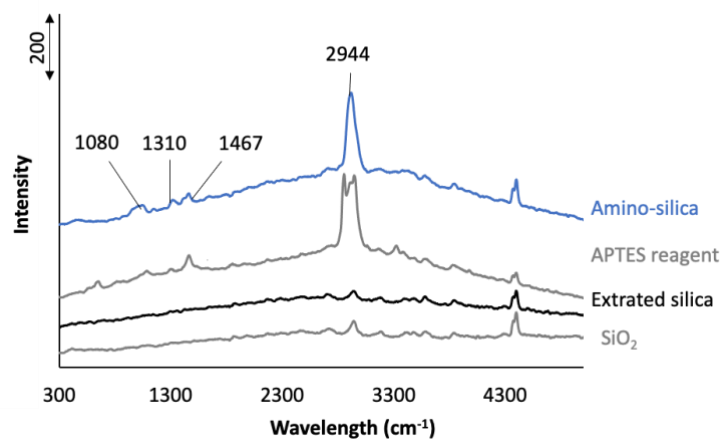
#### 4.3.4.2 Characterization of $\mu$ -SiO<sub>2</sub> material and their amino modification

Figure 115 shows the infrared spectra obtained for the silica and modified silica. In both spectra it can be seen the vibration bands at 481 and 795 cm<sup>-1</sup>, which are attributed to the deformation and regular stretching Si - O, respectively and the band at 1037 cm<sup>-1</sup> was assigned to the major asymmetric stretching of Si - O - Si [354]. Amino-functionalized silica shows two bands in the region 1650-1580 cm<sup>-1</sup>, that were not observed on silica spectrum, and corresponded to N - H bending vibration of primary amine. These bands are indicative of a successfully incorporation of amino groups on the silica by its functionalization with APTES [354].



**Figure 115:** FTIR spectra of extracted silica and amino-silica.

Figure 116 shows Raman spectra of extracted silica, amino-silica, APTES and a commercial silica (SiO<sub>2</sub> mesh X). The incorporation of APTES on silica surface to obtain amino-silica can be confirmed by the presence of characteristic bands such as very strong band at 2944 cm<sup>-1</sup> assigned to the asymmetric stretching of CH<sub>2</sub>, a strong band at 1467 cm<sup>-1</sup> indicating the Si - CH<sub>2</sub> bond [358], a band at 1310 cm<sup>-1</sup> attributed to NH<sub>2</sub> [359], and a band at 1080 cm<sup>-1</sup> assigned to Si - O - C [360].



**Figure 116:** Raman spectra of amino-silica, APTES reagent, extracted silica and commercial silica.

The specific surface and pore size distribution and the total volume of the porous of several obtained amino-silica samples were analyzed by BET. The surface areas for the different silica were in the range of 194 to 75  $\text{m}^2\cdot\text{g}^{-1}$  (Table 43), which is in accordance to the method of preparation used by precipitation [361]. Amino-silica analyzed showed a porous size lower than 20 nm, compatible with a mesoporous material [362–364].

**Table 43:** Physical properties and adsorption of modified and unmodified silica.

Sample	BET surface area ( $\text{m}^2\cdot\text{g}^{-1}$ )	Total pore volume ( $\text{cm}^3\cdot\text{g}^{-1}$ )	Pore size BET (nm)
Amino-silica <sup>a</sup>	194	0.470	15.85
Amino-silica <sup>a</sup>	144	0.312	8.65
Amino-silica <sup>b</sup>	92	0.210	14.02
Amino-silica <sup>c</sup>	75	0.121	6.55

<sup>a</sup> One layer amino-silica at lab scale.

<sup>b</sup> Two layer amino-silica at lab scale.

<sup>c</sup> One layer amino-functionalized obtained at higher scale.



The activation of modified silica was carried out with HCl 1 M (see Section 3.3.4.1.2). After activation, amino-silica was analyzed by SEM/EDX (Figure 117) and elemental analysis. Activated amino-silica retained chloride (Figure 117.a) on its surface. The activated adsorbent was used for removal nitrate from the well water and after adsorption was analyzed by SEM/EDX and elemental analysis too. Figure 117.b shows an increase of the percentage of oxygen and a decrease of the percentage of chloride (from 4.43 to 0.00%) with respect to Figure 117.a, which is indicative of the adsorption of nitrate on the adsorbent surface. These results suggested that the adsorption of the nitrate can be produced by ionic exchange as expected, nitrate anions displaced chlorine anions during the adsorption process (see Figure 118).

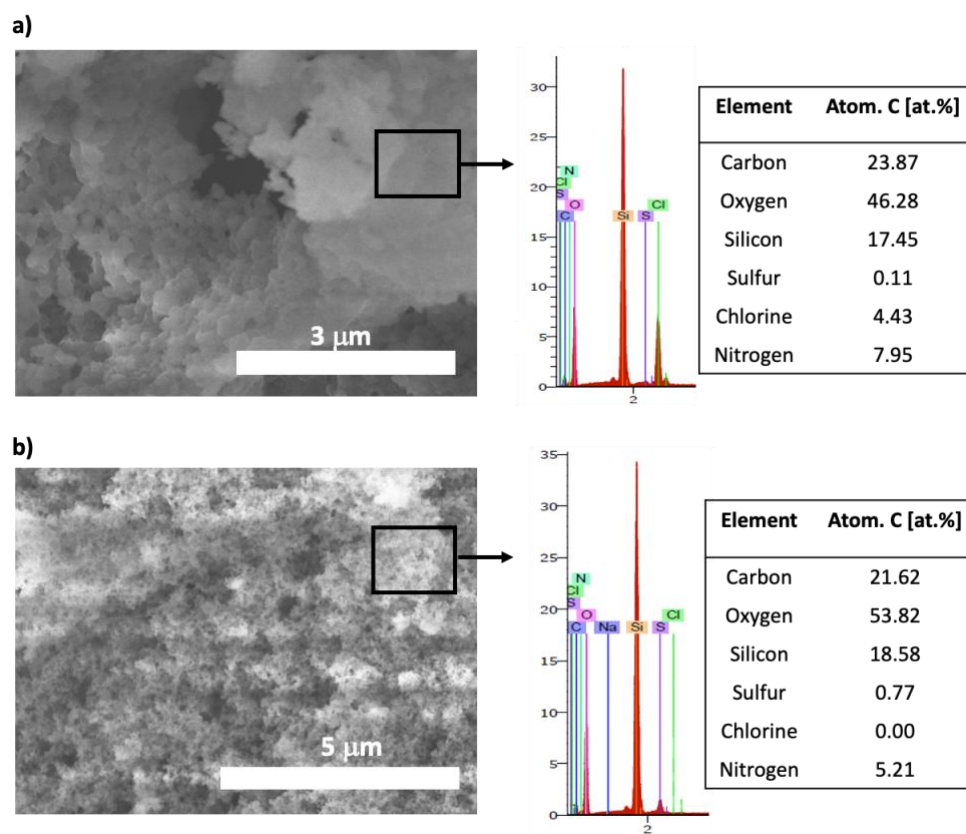


**Figure 117:** SEM images/EDX micrograph of activated amino-silica a) before and b) after adsorption of nitrates.

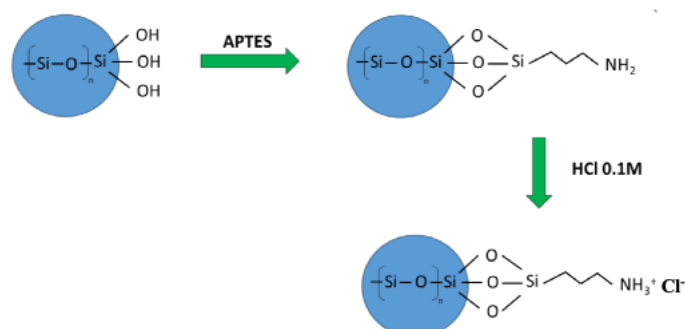


**Figure 118:** Activated form of the modified silica as an anionic exchanger.

Furthermore,  $\mu\text{-SiO}_2$  from rice ashes and their sub-products modified with aminosilane compound were analysed by AF4-DLS under the experimental conditions of Silica - Program 2 (Table 18). Fractograms obtained are shown in Figure 119.a and b. For directly extracted  $\mu\text{-SiO}_2$  from ashes, two specific size distributions were observed. The presence of larger particles than a certain size limit produce that they exhibit negligible diffusion, but are elevated to a finite distance against the channel wall by hydrodynamic lift forces. In this case, the center of larger particles is exposed to a faster stream line than that of smaller ones, and therefore, larger particles migrate faster. This effect is referred to as the steric mode of retention [365]. Thus, the first size distribution observed corresponded to an average hydrodynamic size of 4063.5 nm, meanwhile the second one was referred to a distribution with average size of 773.8 nm. In this case, the regression coefficient and RSD were calculated obtaining values of 0.9782 and 2.5%, respectively. Moreover, the LOD was evaluated and the value obtained was  $2.9 \text{ mg}\cdot\text{L}^{-1}$ .

Regarding the modified extracted  $\mu\text{-SiO}_2$ , similar results were observed. Predominant distribution was detected at  $t_r = 2.37 \text{ min}$  which hydrodynamic average size was  $2.7 \mu\text{m}$ . Distributions observed at higher retention times showed lower hydrodynamic size between 694.4 nm and 217.6 nm. In this case, the steric effect appeared to be the driving force although separation was not satisfactory due to the possible transition between steric and normal mode [366].

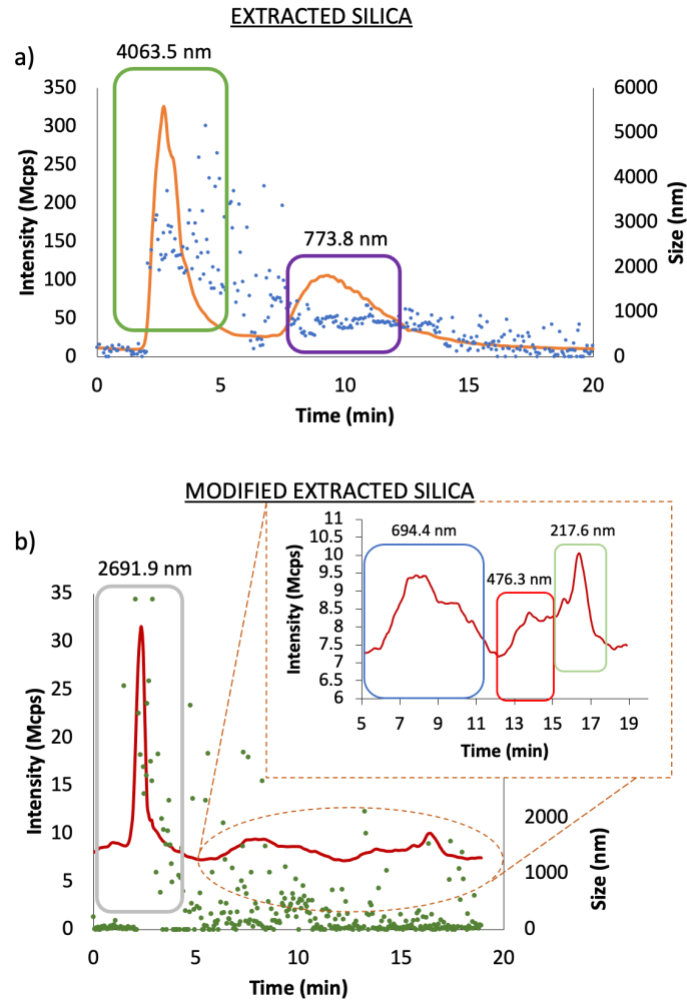


**Figure 119:** a) Fractogram and size distribution of extracted silica from ashes. b) Fractogram and size distribution of modified extracted silica from ashes.

#### 4.3.4.3 Absorption of nitrate in $\mu$ -SiO<sub>2</sub> from rice straw ashes

The effect of time on adsorption of the active modified silica was studied in a batch system (see Section 3.3.4.1.2). The removal efficiency increased up to 10 min reaching 85–90%. Then, the removal efficiency remained stable until 30 min and after 120 min, decreased to values below 30%.

To investigate the behaviour of nitrate adsorption in flow mode, adsorption was studied using the proposed device shown in Figure 26.b. A given amount of silica was placed into a column and continuous flow of a nitrate solution pumped with a peristaltic pump. The optimal conditions of the system according to the bed height and flow rate were studied. The effect of the amino-silica bed height on nitrate adsorption in fixed-bed column was investigated using different heights (see Section 3.3.4.1.3) at a constant flow rate of  $5 \text{ mL}\cdot\text{min}^{-1}$  for a standard solution containing  $26 \mu\text{g}\cdot\text{mL}^{-1}$  of nitrate. The removal efficiency is shown in Figure 120.a. From this figure, it can be observed that efficiency removal increased by increasing the bed height from 1.25 to 2.3 cm and then, remained constant. Therefore, the optimal taking up of adsorbent into the column result is about one fifth of the total column.

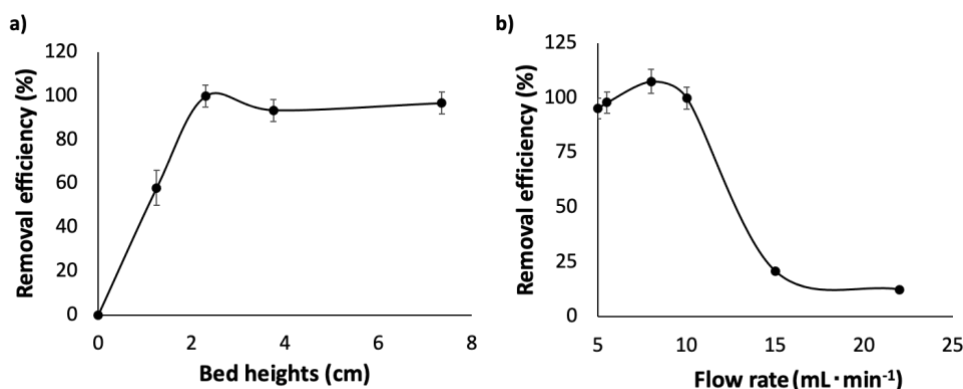


**Figure 120:** a) Effect of bed heights (cm) and b) Effect of flow rate on removal efficiency of nitrate by the amino-silica in fixed-bed column system. (n= 3).

The effect of flow rate was examined between  $5$  and  $25 \text{ mL}\cdot\text{min}^{-1}$  at a constant nitrate concentration of  $26 \mu\text{g}\cdot\text{mL}^{-1}$  and  $2.3 \text{ cm}$  of bed height (Figure 120.b). The results indicated that the removal efficiency of nitrate was not significantly influenced by the flow range assayed up to  $10 \text{ mL}\cdot\text{min}^{-1}$ . Nitrate adsorption by amino silica is affected by insufficient contact time between the adsorbent and the nitrate in the column at the higher flows assayed as it can be seen in Figure 120.b.

Figure 121 shows the experimental and theoretical values for the adsorption of nitrate with a quantity of 0.25 g of modified silica A12 (see Table 16, Table 42 and Figure 26.b) at a temperature of 25 °C (see Section 3.3.4.1.3) for several standards of nitrate between 0 and 120  $\mu\text{g}\cdot\text{mL}^{-1}$ . The  $b$ ,  $q_m$ ,  $n$ ,  $K_f$  values and the coefficient of determination ( $R^2$ ) for Langmuir and Freundlich isotherms are given in Table 44. The coefficient of determination indicated that the adsorption was fitted better by the Langmuir model ( $R^2 = 0.99$ ) than by the Freundlich model ( $R^2 = 0.97$ ). This behaviour suggested that a monolayer adsorption of nitrate onto the surface of amino-silica was achieved [367,368]. The maximum adsorption capacity ( $q_m$ ) by Langmuir model was determined as 68.5  $\text{mg}\cdot\text{g}^{-1}$  of modified silica.

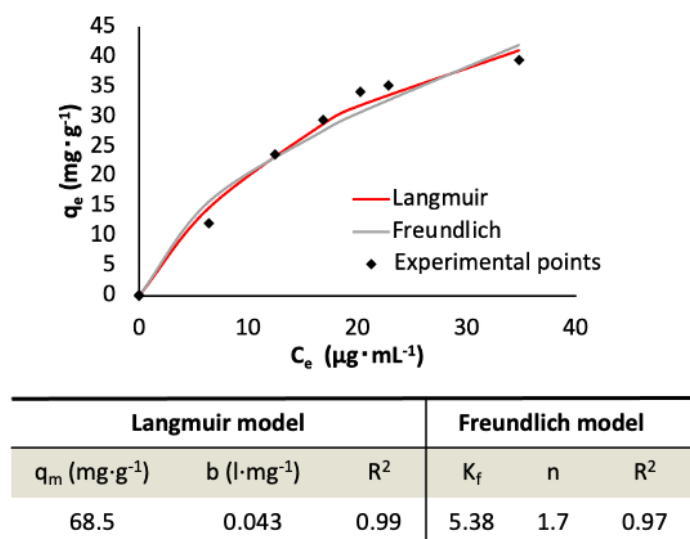


**Figure 121:** Experimental and theoretical adsorption isotherm of nitrate anion on modified silica at several concentrations assayed between 0 and 120  $\mu\text{g}\cdot\text{mL}^{-1}$ , and Langmuir and Freundlich models for nitrate anion removal.

In general, the adsorption capacity expressed as  $q_m$  obtained was in the range of other adsorbents reported as Table 44 shows. The material obtained in this work shows some advantages over the new materials proposed recently shown in Table 44. It shows a high adsorption capacity expressed as Langmuir  $q_m$  in a shorter time, besides its synthesis used as raw material (extracted silica) a by-product generated from the rice straw. On the other hand, the modification process

is carried out under standard conditions of pH and temperature. In addition, APTES as a modifier is more environmentally friendly product than tertiary and quaternary amines.

**Table 44:** Parameters for the optimization of the amino-silica synthesis and its adsorption capacity.

Adsorbent	Langmuir $q_m$ ( $\text{mg}\cdot\text{g}^{-1}$ )	Initial concentration ( $\mu\text{g}\cdot\text{mL}^{-1}$ )	Contact time (min)	T ( $^{\circ}\text{C}$ )	Ref.
DMDAC-Silica gel	39.3	100	180	30	[369]
NN-MCM-41	38.6	30-250	120	25	[370]
SBA-15	136	10-1000	180	30	[371]
RSi-bPEI	116	50	90	-	[371]
Amino-silica	68.5	25-120	30	25	Our synthesis

The dynamic adsorption process is important in the characterization of porous materials (see Table 43), it is studied by breakthrough curves, which indicates the adsorption concentration in the effluent at the outlet of a fixed-bed adsorbent [372].

A bed height of 2.3 cm was used in a column at 25  $^{\circ}\text{C}$  (see Figure 26.b), a standard solution of 40  $\mu\text{g}\cdot\text{mL}^{-1}$  of nitrate was passed through at a flow rate of 5  $\text{mL}\cdot\text{min}^{-1}$  (0.25 g of synthesis A12 of Table 16 and Table 42 was used). Breakthrough curve was fitted well to sigmoidal-type mathematical models, namely, Thomas and Yan models (Equations (H) and (I), respectively) and the adsorption capacity was calculated based on the fitting results, see Figure 122.

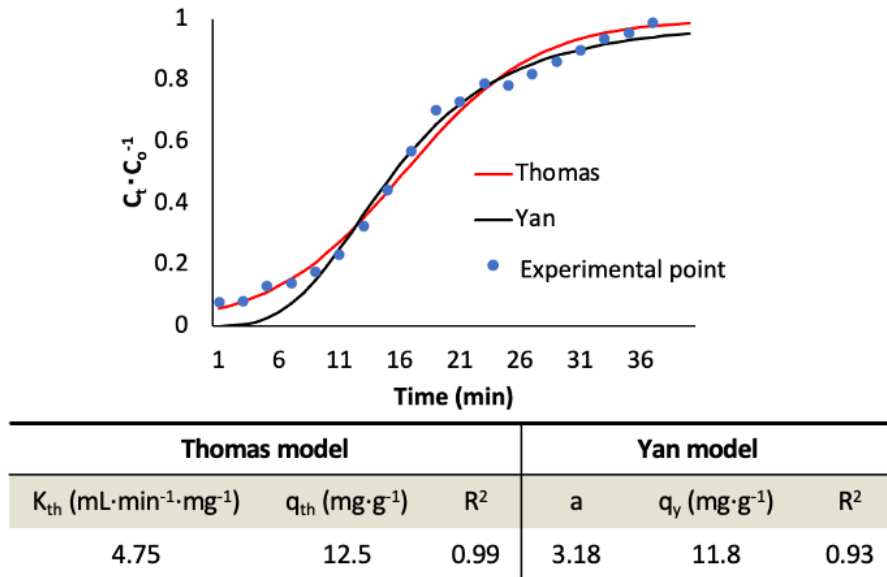


**Figure 122:** Experimental breakthrough curve for modified silica and Thomas and Yan models for nitrate anion removal.

According to the coefficient of determinations of Thomas ( $R^2 = 0.99$ ) and Yan ( $R^2 = 0.93$ ) models, the adsorption behaviour is more in line with the Thomas model, which accepts Langmuir adsorption and desorption kinetics and no axial dispersion [373]. The quantity of nitrate uptake predicted by this model was  $12.5 \text{ mg}\cdot\text{g}^{-1}$  for the standard solution assayed (see Figure 122).

#### 4.3.4.4 In-flow nitrate adsorption in standards and well water samples

A well water sample containing nitrate in a concentration of  $45 \mu\text{g}\cdot\text{mL}^{-1}$  was analyzed by using the proposed device shown in Figure 26.b at lab scale, and the results were compared with the adsorption capacity values obtained using a nitrate standard solution of  $45 \mu\text{g}\cdot\text{mL}^{-1}$ . For these experiments one layer (A14 in Table 16 and Table 42) and two layer (A18 in Table 16 and Table 42) modified amino-silica were employed. The results showed in Figure 123 provided adsorption capacity values calculated as the amount of nitrate retained until achieving the concentration of the standard solution for one-layer silica and two-layer of silica, being  $8.3$  and  $15.2 \text{ mg}\cdot\text{g}^{-1}$ , respectively. It can be seen that amino-silica that has

been modified two times achieved almost double adsorption capacity than the amino-silica modified once.

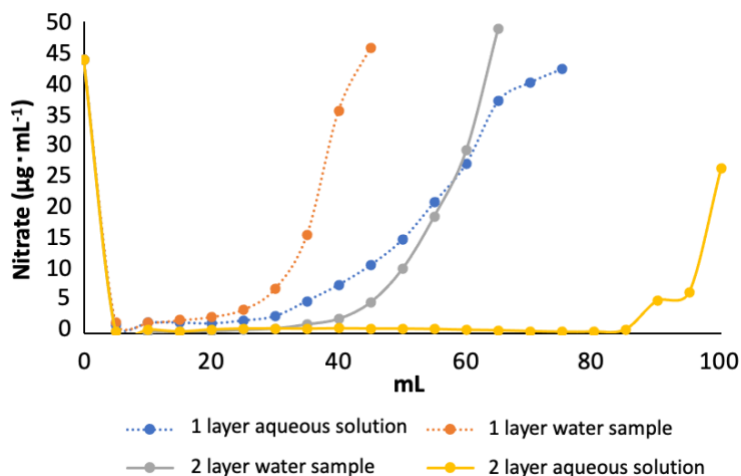
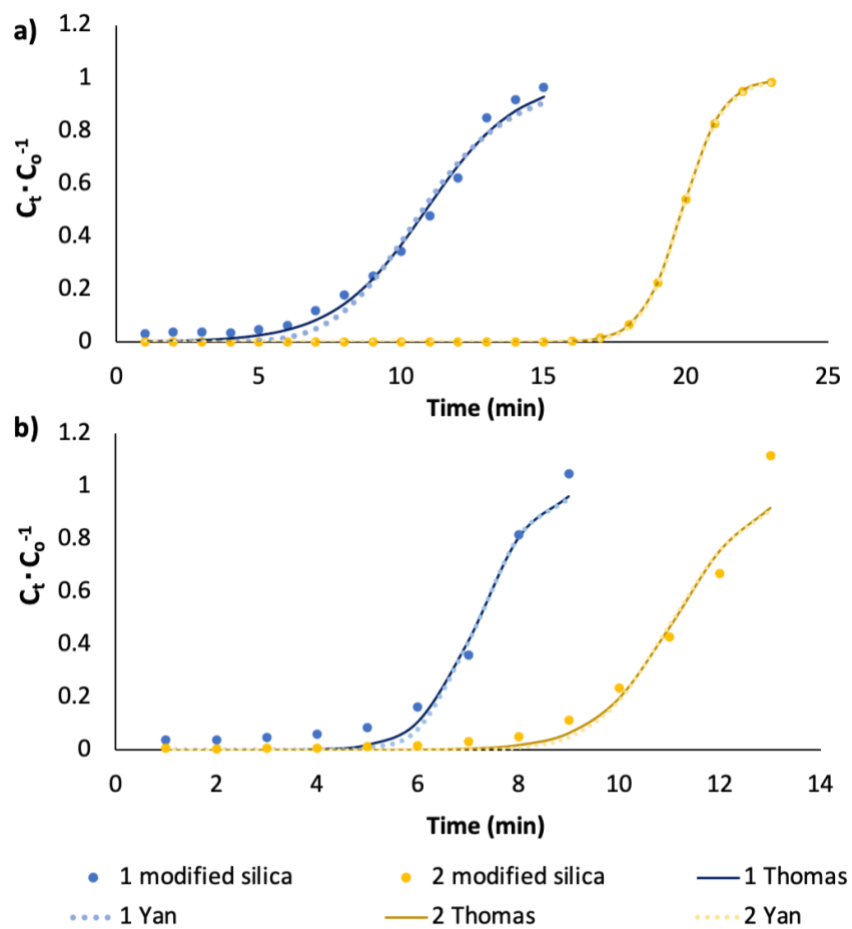


**Figure 123:** Adsorption of nitrates in aqueous solution of  $45 \mu\text{g}\cdot\text{mL}^{-1}$  and samples of water for one- and two-layer silica. Nitrate concentration vs mL of processed water.

According to the adsorption capacity values of amino-silica in well water sample, it can be seen that the adsorption capacity decreased obtaining  $4.9$  and  $8.5 \text{ mg}\cdot\text{g}^{-1}$  for one-layer silica and two-layer of silica, respectively (see Table 16 and Table 42). This decrease can be produced due to the presence of other anions in water samples, which can negatively influence the adsorption processes of nitrates. A multicomponent standard containing  $45 \mu\text{g}\cdot\text{mL}^{-1}$  of nitrate and other anions at concentration levels similar to those present in the well sample was tested using the two-layer silica. The adsorption capacity obtained for nitrate was  $10 \text{ mg}\cdot\text{g}^{-1}$ , this value supported the lower adsorption values obtained in the well water in reference to nitrate standards and the mechanisms of the adsorption (see Figure 118).

Figure 124 shows the Thomas and Yan models which are in accordance with those shown in Figure 122 for A12 synthesis of Table 16 and Table 42 by working with a standard solution. Similar results were obtained by using these models than estimating the nitrate adsorption by point by point from the results given in Figure 123.





Sample	Layers	Thomas model			Yan model		
		$k_{th}$ ( $\text{mL}\cdot\text{min}^{-1}\cdot\text{mg}^{-1}$ )	$q_{th}$ ( $\text{mg}\cdot\text{g}^{-1}$ )	$R^2$	a	$q_y$ ( $\text{mg}\cdot\text{g}^{-1}$ )	$R^2$
Standard	1	14.44	9.34	0.99	6.82	9.41	0.98
	2	32.77	17.10	0.99	28.24	17.40	0.99
Water	1	40.97	6.20	0.98	13.55	6.30	0.97
	2	29.40	9.56	0.96	14.31	9.70	0.95

**Figure 124:** Experimental breakthrough curve for modified silica analysis of Thomas and Yan models. 1 (one layer), 2 (two layer) a) standard of  $45 \mu\text{g}\cdot\text{mL}^{-1}$  and b) sample of water.

The mean value for nitrate adsorption provided by A10- A15 synthesis of Table 16 and Table 42 was  $4.7 \pm 0.6 \text{ mg}\cdot\text{g}^{-1}$  silica for well water, providing a good precision. Similar values of precision were obtained for large scale, nitrate adsorption provided by synthesis A28-A31 shown in Table 16 and Table 42 were  $4.8 \pm 0.3 \text{ mg}\cdot\text{g}^{-1}$  silica.

The regeneration performance of the modified silica with sodium hydroxide (see Section 3.3.4.1.3) was assayed with well water. The treatment was effective processing the sample for 10 min. Three cycles were assayed and the absorption values were  $90 \pm 10\%$  of that achieved in a single use. This experiment shows that the modified silica can be reused at least three times.

The same amount of active silica and a commercial resin (0.25 g) was used for studying adsorption of nitrate in a well water sample containing  $53 \mu\text{g}\cdot\text{mL}^{-1}$  of nitrate. Active silica removes a higher percentage of nitrates from the water as it is shown in Figure 125. In the interval 0.5 to 22.0 min, the nitrate concentration is  $1 \mu\text{g}\cdot\text{mL}^{-1}$  if modified silica was used as adsorbent, meanwhile for the resin nitrate concentration was near  $38 \mu\text{g}\cdot\text{mL}^{-1}$ . The adsorption kinetics is faster for silica than for resin as can be Figure 125.

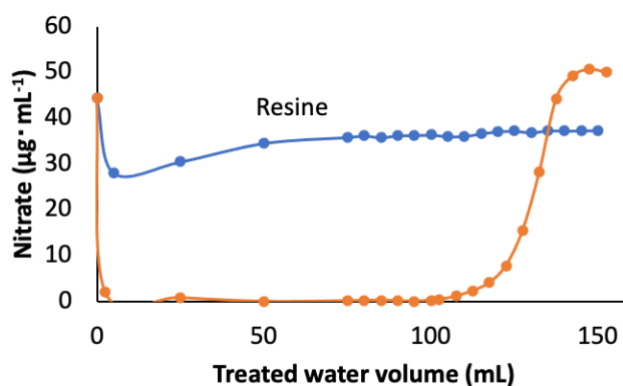


**Figure 125:** Continuous monitoring of nitrate concentration for a well water sample by using activated silica and a commercial resin.

#### **4.3.4.5 Sustainability of the process in comparison with other methods**

The principles of green chemistry were introduced in the early 1990's and articulate the objective of reducing (and/or eliminating) negative environmental impacts by decreasing waste or increasing efficiency of chemical processes or syntheses [374].

The topics of greener syntheses, environmental applications and biological toxicity were reviewed by Lehman and Larsen [375] in the case of zeolite and mesoporous silica nanomaterials. Our method at large scale was compared with industrial traditional methods and recently published works about green adsorbents. Some characteristics of those methods are summarized in Table 45. One sustainable characteristic of our method was the use of silicate from agro-waste making the process greener. Another difference is that in the same step of silica precipitation, APTES and ethanol were added to obtain amino-functionalized silica adsorbent.

Compared with the green methods reported, we can see that the use of agricultural residue as a source of silica is not new, especially for rice husk which was used as a source of silica [376], in contrast our method proposes the use of straw rice which can solve the problem of the air contamination by its burning. Respect to the green characteristics of proposed method compared to the others; the time is 8 h while in most of them required 24 h, only one method is proposed employing 3 h but, in contrast, it required higher temperatures (200 °C). In addition, our method allows recycling the medium of reaction to carry out several layers of modified silica.

**Table 45:** Comparison of traditional methods in industry (in grey), new green lab-scale methods (in white) with our green large-scale methods for synthesis of modified silica. Some of these materials were used as adsorbents.

Silica source/ Ref.	Reagent	Solvent	Synthesis conditions		By-product	Silica type	Application
			T (h)	T (°C)			
TEOS [364]	Pluronic	water	44+6	44-100, 500	Alcohol, NOx, CO <sub>2</sub> , Na <sub>2</sub> SO <sub>4</sub>	Mesoporous SBA-15	-
TEOS [377]	Dodecyl- amine	water, ethanol	18+6	20, 500	No reported	Mesoporous HMS	-
TEOS [378]	CTAB, NH <sub>3</sub>	Water, ethanol	3+6+6	20, 200, 600	No reported	Mesoporous silica MS	-
Silicate [362]	CTAB, ammonia	water	0.5+ 168	20, 500	Ethanol, NOx, CO <sub>2</sub> ,	Mesoporous MCM-41	-
Silicate [379]	H <sub>2</sub> SO <sub>4</sub>	water	3+5	35-80	Na <sub>2</sub> SO <sub>4</sub>	Precipitated industrial gel	-
TEOS [370]	CTAB, APTES	toluene	>96+6	110, 540	No reported	Mesoporous MCM-41	Removal nitrates
Agro-waste ash [380]	NaOH, H <sub>2</sub> SO <sub>4</sub>	water	24+12	Drying, rt aging	Na <sub>2</sub> SO <sub>4</sub>	Silica xerogel	-
Rice Husk ash [381]	APTES	Toluene, in N <sub>2</sub>	24	90-100	Ethanol	amorphous silica	Removal humic acid
Ash rice and clay [382]	APTES	water	3	25-200	Ethanol	powder (size: 10-800 nm)	Water disinfection
Rice straw ash (our synthesis)	NaOH, H <sub>2</sub> SO <sub>4</sub> , APTES	Water, ethanol recycled	6+2	90, rt	Na <sub>2</sub> SO <sub>4</sub> , Ethanol	Amino-silica mesoporous	Remove nitrate in waters

- Conclusions

In this work, different silica nanomaterials with different sizes and shapes have been characterized and analysed by AF4-DLS in order to evaluate the complementary information given by this technique. Firstly, solid SiO<sub>2</sub>NPs were dispersed using and hydroxide treatment and analysed by AF4 employed an initial cross flow of 0.75 mL·min<sup>-1</sup>. The sizes values obtained were 150 – 200 nm. In order to evaluate the dispersion influence in SiO<sub>2</sub>NPs fractogram profiles, eight different commercial SiO<sub>2</sub>NPs dispersions with different sizes and stability conditions were tested. The elution program was optimized and the best conditions was achieved with an initial cross flow of 2.00 mL·min<sup>-1</sup>. For silica nanomaterials analysis with other shapes and sizes in micro and nano scale, HNTs was selected. For this material, their functionalization with pigments was also evaluated.

Finally, μ-SiO<sub>2</sub> obtained from rice straw ashes and their modification with amino-functionalized groups was characterized as an example of silica micro material, obtained average hydrodynamic diameters up to 4 μm. The use of this material can solve the problem of the air contamination by its burning in the field. For this reason, in this study, the μ-SiO<sub>2</sub> sub-product from rice straw ashes was obtained and used for adsorption of nitrate from water. Two methods were studied for amino-silica synthesis and the procedure employing silicate permitted to carry out the modification with APTES in only one step and saving time, 1.5 h vs 6.5 h (including a step for silica crystallization previously to modify it) and at room temperature. We selected APTES because is more sustainable than ternary and quaternary ammonium tags. It is possible to re-use the reaction medium in order to improve the adsorption capacity by generating several layers.

Amino-silica showed a porous size lower than 20 nm, compatible with a mesoporous material. It shows a high adsorption capacity expressed as Langmuir qm in a short time. We demonstrated that the synthesis at lab is scalable by a factor around 100 employing only 2 h. Adsorption studies of nitrate in standards and real well waters at lab scale and scaling-up provided similar results. Adsorption values near to 15 mg·g<sup>-1</sup> for nitrate standards and 8.5 mg·g<sup>-1</sup> for well water were obtained until achieving the initial nitrate concentration. Experimental breakthrough curves fitted to Thomas model gave similar results for adsorption capacities. The adsorption capacity of silica was higher than that achieved by a commercial resin used for potable water treatment.

The scaled-up method was compared with industrial traditional methods and recently published works about green adsorbents. One sustainable characteristic of our method was the use of silicate from agro-waste making the process greener. Another difference is that in the same step of silica precipitation, APTES and ethanol were added to obtain amino-functionalized silica adsorbent. The time is 8 h (6 h for obtaining the silica from rice straw ashes and 2 h for amino-silica product) while in most of the reported methods required 24 h, only one method is proposed employing 3 h but, in contrast, it required higher temperatures (200 °C) and it is for water disinfection. In addition, our method allows recycling the medium of reaction.

## **CHAPTER 5: CONCLUSIONS**





The present Thesis has been focused to establish new knowledge for characterization, determination and use of NMs from two different approaches, as analytes and analytical tools. AuNPs, AgNPs, CB and several silica based micro- and nanomaterials have been studied using spectroscopic, image and separation techniques. Image and spectroscopic techniques provide valuable information about NMs and their changes. However, these studied techniques only provide a partial characterization. Focusing in the separation techniques, field flow fractionation and in-tube SPME miniaturized liquid chromatographic have been deeply evaluated and proposed for NMs characterization. These techniques show an especial relevance because provide complementary characteristic information about NMs allowing the understanding of their performance. Table 46 shows a summary of the approaches applied and analytical techniques used for each NM.

**Table 46:** Approaches applied and analytical techniques used for each NM studied.

	AuNPs	AgNPs	CB	Silica based NMs
<b><i>NMs approaches</i></b>				
Analyte	✓	✓	✓	✓
Tool	✓	✓		✓
<b><i>Spectroscopic techniques</i></b>				
DLS, UV-vis, FTIR, Raman, DR	✓	✓	✓	✓
<b><i>Image techniques</i></b>				
SEM, TEM, optical microscope	✓	✓	✓	✓
<b><i>Separation technique</i></b>				
Field flow fractionation (UV-vis, DLS, MALS)	✓	✓	✓	✓
IT-SPME-miniaturized LC (UV-vis)	✓	✓		

### ***As analytes***

The uses and applications of NMs has increased considerably in the last years. Subsequently, their presence in different samples, such as industrial, cosmetics, food, medical, biological and environmental matrices have also

increased, which produce the need to develop different analytical techniques in order to determine and to characterize them. Sizes, morphology, structure and dispersion stability are crucial properties, which should be evaluated. Table 47 summarized the parameters evaluated and techniques used for characterizing each NM studied here.

**Table 47:** Measured properties, techniques employed and parameters evaluated for each NMs characterized.

Analyte	Properties measured	Techniques	Parameters evaluated
<b>AuNPs</b>	- Absorbance (SPR band) - Size	- AF4-UV-vis-DLS - IT-SPME-CapLC - IT-SPME-NanoLC - SEM/TEM	- Size and particle distribution - Dispersion stability with time
<b>AgNPs</b>	- Absorbance (SPR band) - Size	- AF4-UV-vis-DLS - IT-SPME-CapLC - IT-SPME-NanoLC - SEM/TEM - Optical microscope - UV-vis - DLS	- Size and particle distribution - Dispersion stability with time - Dispersion stability in different waters - Capture in soils
<b>CB</b>	- Absorbance - Size - Vibrational modes	- AF4-UV-vis-DLS - SdF3-MALS - Raman - SEM/TEM - Optical microscope - DR - DLS	- Size distribution in polymeric and biological dispersants - Structural characterization - Dispersion mechanisms - Dispersion stability with time - Dispersion stability in different waters - Isolation from soils
<b>Silica based materials</b>	- Absorbance - Size - Vibrational modes	- AF4-DLS - SEM - IR - Optical microscope	- Structural characterization - Size distribution (wide range of sizes nm to $\mu\text{m}$ )

**MNPs** such as AuNPs and AgNPs have been characterized and determined in this Thesis as analytes focusing in their characteristic SPR band. Dispersions of these NMs have been evaluated in order to establish their particle and size distribution using two separation techniques, IT-SPME-miniaturized LC-DAD and AF4-UV-vis-DLS. The potential of IT-SPME-miniaturized LC-DAD MNPs have been demonstrated for assessment of MNPs dispersions by the first time. Results showed two particle distributions corresponding to polarized and non-polarized populations in the bulk dispersion, which separation was explained by means of size exclusion and hydrophobic effect, respectively.

AF4-UV-vis-DLS showed that there is an effective variation in the number of NPs dispersed as a function of time, this variation was attributed to their dissolution in aqueous diluted dispersion. Comparing the different citrate MNPs studied, results showed that the dependence of the signal with time was more intense for AgNPs than for AuNPs, which can be correlated with its low stability. Moreover, related to particle size, it is shown that the decrease in the signal was higher for bigger MNPs. In all cases, the hydrodynamic diameter was constant.

For AgNPs, a stability study in several water matrices was carried out using AF4 technique. This study provided knowledge to understand the possible behaviour of AgNPs in the environment for short times (up to 180 min). Results were compatible with the aggregation of AgNPs, a change in the SPR band and a size growth with time were observed. Aggregation kinetics depended on the type of water. Several sizes were obtained in the function of the water which determined the color of AgNPs. The higher effect was observed using tap water compared with the other water matrices. Regarding with the mechanism of action involve in the procedure, ionic strength could induce the NPs aggregation. However, dissolved organic matter and halides could provide the NPs stabilization and passivation, respectively. Thus, it was demonstrated that AF4-UV-vis technique provides relevant information for characterizing the aggregation process of MNPs in the different water matrices studied with respect other analytical techniques.

A quantitative study of the capacity of different soils to capture these AgNPs by combining on-line IT-SPME, miniaturized LC and measuring the change of SPR band were done here. Results showed that AgNPs adsorption on a given soil was mainly affected by the amount of organic matter and secondary, by properties such as the soil particle size, pH, conductivity (EC) and oxidation/reduction

potential (Eh). Moreover, it was observed that the presence of compounds extracted from soil matrix could affect the AgNPs retention. This study represents a step forward in understanding of AgNPs when exposed to complex environmental scenarios and a valuable one taking into account the reduced number of studies of NPs in solid matrices.

**CB** dispersions were carried out using polymeric and biological dispersants, considering the possible matrices and applications where this NM is used. The dispersive capability was evaluated and the dispersion mechanisms for each dispersant were proposed. AF4-UV-vis-DLS was used as analytical technique. The hydrodynamic sizes obtained, showed significant differences taking into account the dispersant used. Polymeric dispersant provided higher hydrodynamic diameters with lower stability, however, using biological dispersant, the hydrodynamic size was lower and the stability enhanced considerably. Biological dispersant allowed to obtain dispersions with suitable stability for a week, compared with the lower stability observed for polymeric dispersions. The dilution of the polymeric dispersion with different real water matrices produced a dramatic loss of dispersion stability, this effect being negligible in the case of biological dispersions.

Moreover, it is interesting to note that a deeper knowledge about CB dispersions is demanded in both research and industrial applications. The stability of aqueous dispersions of CB NPs is still problematic at an industrial level, especially for those applications that require smaller particles, for example, rubber and pigment industries, due to their greater surface area.

Focusing in the CB greater applicability and possible presence in environmental samples during their lifecycle, a sample pretreatment procedure based on dispersive media was developed to evaluate CB isolation in soil samples by the first time. Moreover, a filter-aided step was applied in order to evaluate the possible CB recovery. Soil samples contaminated with CB were studied, the NM isolation depended on the matrix composition, obtaining a possible relationship between organic matter percentage and particle composition of soils with the procedure efficiency. Soils with higher amount of organic matter and lower particle sizes, showed better CB dispersion efficiencies using biological dispersant.

For filter-aided recovery step, different membranes were tested using polymeric and biological CB dispersion. Teflon 0.10  $\mu\text{m}$  provided better results for CB recovery. Diffuse reflectance was employed for quantify the CB recovered. To evaluate the practical application, a soil sample contaminated with a CB-based pigment paste was analysed achieving quantitative dispersive isolations for biological dispersant, showing that the proposed methodology is a promising tool for sample preparation in CB environmental analysis. AF4-DLS and SdF3-MALS were used as analytical techniques, providing satisfactory results.

**Silica based materials** were studied by AF4 in order to complete the information provided by other analytical techniques. Different silica materials from nanometers to micrometers were analyzed for evaluated the high variety of available sizes. Moreover, different shapes such as silica NPs or HNTs were also characterized.

Dispersions of solid  $\text{SiO}_2$ NPs were carried out and characterized by AF4-DLS. The hydrodynamic sizes values were obtained. Moreover, different commercial  $\text{SiO}_2$ NPs dispersions with different nm sizes and stability conditions were also analyzed. In this case, the hydrodynamic diameters were lower confirming the presence of possible aggregates in the first  $\text{SiO}_2$ NPs dispersions analyzed. For silica NMs with other shapes, HNTs was selected. For this material, its functionalization with pigments was also evaluated.

Finally,  $\mu\text{-SiO}_2$  obtained from rice straw ashes and their modification with amino-functionalized groups were characterized as an example of silica micro material, obtained average hydrodynamic diameters up to 4  $\mu\text{m}$ .

### ***As analytical tools***

NMs also can be employed as tools in order to enhance and perform novel analytical process in different research fields. In this approach, AuNPs, AgNPs and  $\mu\text{-SiO}_2$  obtained from rice straw ashes have been used as sensors or sorbents in this Thesis. Table 48 summarized the different roles as tools of the NMs studied, focusing in the kind of analyte determined, the matrices and the techniques used.

**Table 48:** NMs studied as analytical tools: analyte determined, matrices and techniques employed for characterization.

NMs	Analyte determined	Matrices	Technique	Analytical tool
AuNPs	- Spermine - HAc - HCl - H <sub>3</sub> PO <sub>4</sub>	- Urine - Aqueous matrix	- IT-SPME-CapLC - IT-SPME-NanoLC - UV-vis - AF4-UV-vis-DLS	Detection / sensor
AgNPs	- HAc - HCl	- Aqueous matrix	- IT-SPME-CapLC - IT-SPME-NanoLC - UV-vis - AF4-UV-vis-DLS	Detection / sensor
$\mu$ - SiO <sub>2</sub> from rice straw ashes	- Nitrate	- Well water	- UV-vis - IR - SEM - BET technique - Optical microscope	Sample preparation / adsorbent material

**MNPs** shows a specific SPR band which is applied as analytical response for a wide number of chemical sensors and biosensors. Different plasmonic assays using AuNPs and AgNPs were developed in order to monitor NPs aggregation induced by interaction with several analytes like acids and SPN, which allowed their quantification. Urine samples were used to determine SPN as a cancer biomarker as a proof of concept of the analytical tool developed. As analytical techniques, IT-SPME-miniaturized LC-DAD and AF4-UV-vis-DLS were employed. These new tools provide better sensitivity and selectivity for developing plasmonic tests than UV-vis spectroscopy.

**$\mu$ -SiO<sub>2</sub> from rice straw ashes** was obtained and modified with amino compound in order to obtain a useful sub-product for reducing nitrate content in waters. It was demonstrated that the silica synthesis developed at lab was scalable more than a hundred times with good results in standards and real well waters. The

scaled-up method was compared with industrial traditional methods and recently published works, which showed a considerably advantages for our synthesis, such as to allow the recycling of the reaction medium, the use of silicate from agro-waste making the process greener, and the unified of the all procedure in one step reducing the total time synthesis.

Moreover, this strategy can palliate negative effects of the agriculture waste practices on the environment which can produce water resources pollution by the excessive use of fertilizers or an increase of harmful gases concentration in the atmosphere due to the open burning of rice straw.

Taking into account the different results obtained in this Thesis, it can be seen that the applicability of NMs have increased considerably in the last years. Moreover, their presence in different scenarios and matrices is growing showing the need of new knowledge.

Nowadays, there are many analytical achievements in the use of nanomaterials as tools in the development of new analytical processes, with special incidence in sample treatment. However, the detection and determination of NMs in complex samples (environmental, biological or industrial) is still very limited, and the systematic validation of the corresponding methods to be incorporated in routine/control laboratories is far from reality today. For this reason, in order to obtain a complete comprehension of their performance and activity, its necessary carries out a characterization, determination and evaluation of NMs taking into account their particular properties and developing new analytical methodologies that complement the existing ones.

According their toxicity, as conclusion so far is that, even though NMs are not per se dangerous, there still is scientific uncertainty about the safety of NMs in many aspects and therefore the safety assessment of the substances must be done on a case-by-case basis. New methodologies are also necessary in order to complete the knowledge of this materials from the point of view of toxicology.

Thus, in this Thesis, it has been possible to develop the study of these NMs as analytes, taking into account different parameters that can affect their properties (dispersion time, environmental conditions, mixtures, presence in different matrices, etc.) with the aim of characterizing and evaluating them to

ensure their correct performance in different analytical tools. In addition, the analytical methodologies developed have contributed to complete the existing knowledge regarding these NMs and can use as a starting point for future lines of research.



## REFERENCES



- 
- [1] F. Albalawi, M.Z. Hussein, S. Fakurazi, M.J. Masarudin, Engineered nanomaterials: The challenges and opportunities for nanomedicines, *Int. J. Nanomedicine*. 16 (2021). <https://doi.org/10.2147/IJN.S288236>.
- [2] E.R. Bandala, M. Berli, Engineered nanomaterials (ENMs) and their role at the nexus of Food, Energy, and Water, *Mater. Sci. Energy Technol.* 2 (2019). <https://doi.org/10.1016/j.mset.2018.09.004>.
- [3] F. Laborda, E. Bolea, G. Cepriá, M.T. Gómez, M.S. Jiménez, J. Pérez-Arantegui, J.R. Castillo, Detection, characterization and quantification of inorganic engineered nanomaterials: A review of techniques and methodological approaches for the analysis of complex samples, *Anal. Chim. Acta.* 904 (2016). <https://doi.org/10.1016/j.aca.2015.11.008>.
- [4] R.A. Yokel, R.C. MacPhail, Engineered nanomaterials: Exposures, hazards, and risk prevention, *J. Occup. Med. Toxicol.* 6 (2011). <https://doi.org/10.1186/1745-6673-6-7>.
- [5] N. Phogat, S.A. Khan, S. Shankar, A.A. Ansary, I. Uddin, Fate of inorganic nanoparticles in agriculture, *Adv. Mater. Lett.* 7 (2016). <https://doi.org/10.5185/amlett.2016.6048>.
- [6] J.R. Lead, G.E. Batley, P.J.J. Alvarez, M.N. Croteau, R.D. Handy, M.J. McLaughlin, J.D. Judy, K. Schirmer, Nanomaterials in the environment: Behavior, fate, bioavailability, and effects—An updated review, *Environ. Toxicol. Chem.* 37 (2018). <https://doi.org/10.1002/etc.4147>.
- [7] Y. Wang, A. Hu, Carbon quantum dots: Synthesis, properties and applications, *J. Mater. Chem. C* 2 (2014). <https://doi.org/10.1039/c4tc00988f>.
- [8] A. Gupta, S. Dubey, M. Mishra, Unique Structures, Properties and Applications of Dendrimers, *J. Drug Deliv. Ther.* 8 (2018). <https://doi.org/10.22270/jddt.v8i6-s.2083>.
- [9] P.H.C. Camargo, K.G. Satyanarayana, F. Wypych, Nanocomposites: Synthesis, structure, properties and new application opportunities, *Mater. Res.* 12 (2009). <https://doi.org/10.1590/S1516-14392009000100002>.
- [10] E.D.E.R. Hyde, A. Seyfaee, F. Neville, R. Moreno-Atanasio, Colloidal Silica Particle Synthesis and Future Industrial Manufacturing Pathways: A Review, *Ind. Eng. Chem. Res.* 55 (2016). <https://doi.org/10.1021/acs.iecr.6b01839>.
- [11] D. Ziental, B. Czarczynska-Goslinska, D.T. Mlynarczyk, A. Glowacka-Sobotta, B. Stanisz, T. Goslinski, L. Sobotta, Titanium dioxide nanoparticles: Prospects and applications in medicine, *Nanomaterials*. 10 (2020). <https://doi.org/10.3390/nano10020387>.

- [12] E. Caballero-Díaz, M. Valcárcel Cases, Analytical methodologies for nanotoxicity assessment, *TrAC Trends Anal. Chem.* 84 (2016). <https://doi.org/10.1016/j.trac.2016.03.007>.
- [13] COM, European Commission. Internal Market, Industry, Entrepreneurship and SMEs, A New Circ. Econ. Action Plan a Clean. More Compet. Eur. (2020) 1–19.
- [14] R. Stoika, Basic Principles of Nanotoxicology, *Biomed. Nanomater.*, (2022), pp 171-195. [https://doi.org/10.1007/978-3-030-76235-3\\_7](https://doi.org/10.1007/978-3-030-76235-3_7).
- [15] V. Vishwakarma, S.S. Samal, N. Manoharan, Safety and Risk Associated with Nanoparticles - A Review, *J. Miner. Mater. Charact. Eng.* 09 (2010). <https://doi.org/10.4236/jmmce.2010.95031>.
- [16] H. Bahadar, F. Maqbool, K. Niaz, M. Abdollahi, Toxicity of nanoparticles and an overview of current experimental models, *Iran. Biomed. J.* 20 (2016). <https://doi.org/10.7508/ibj.2016.01.001>.
- [17] L. Chen, R.A. Yokel, B. Hennig, M. Toborek, Manufactured aluminum oxide nanoparticles decrease expression of tight junction proteins in brain vasculature, *J. Neuroimmune Pharmacol.* 3 (2008). <https://doi.org/10.1007/s11481-008-9131-5>.
- [18] S.M. Hussain, K.L. Hess, J.M. Gearhart, K.T. Geiss, J.J. Schlager, In vitro toxicity of nanoparticles in BRL 3A rat liver cells, *Toxicol. Vitro.* 19 (2005). <https://doi.org/10.1016/j.tiv.2005.06.034>.
- [19] M.T. Zhu, W.Y. Feng, B. Wang, T.C. Wang, Y.Q. Gu, M. Wang, Y. Wang, H. Ouyang, Y.L. Zhao, Z.F. Chai, Comparative study of pulmonary responses to nano- and submicron-sized ferric oxide in rats, *Toxicology.* 247 (2008). <https://doi.org/10.1016/j.tox.2008.02.011>.
- [20] I.L. Gunsolus, C.L. Haynes, Analytical Aspects of Nanotoxicology, *Anal. Chem.* 88 (2016). <https://doi.org/10.1021/acs.analchem.5b04221>.
- [21] T.A. Qiu, P.L. Clement, C.L. Haynes, Linking nanomaterial properties to biological outcomes: analytical chemistry challenges in nanotoxicology for the next decade, *Chem. Commun.* 54 (2018). <https://doi.org/10.1039/c8cc06473c>.
- [22] Handbook of Nanomaterials in Analytical Chemistry, (2020). <https://doi.org/10.1016/c2018-0-00945-7>.
- [23] F.S. Ligler, H.S. White, Nanomaterials in analytical chemistry, *Anal. Chem.* 85 (2013). <https://doi.org/10.1021/ac403331m>.
- [24] F. Valentini, G. Palleschi, Nanomaterials and analytical chemistry, *Anal. Lett.* 41 (2008). <https://doi.org/10.1080/00032710801912805>.

- [25] S.I. Kaya, A. Cetinkaya, S.A. Ozkan, Green analytical chemistry approaches on environmental analysis, *Trends Environ. Anal. Chem.* 33 (2022). <https://doi.org/10.1016/j.teac.2022.e00157>.
- [26] Á.I. López-Lorente, M. Valcárcel, The third way in analytical nanoscience and nanotechnology: Involvement of nanotools and nanoanalytes in the same analytical process, *TrAC Trends Anal. Chem.* 75 (2016). <https://doi.org/10.1016/j.trac.2015.06.011>.
- [27] K.A.D. Guzmán, M.R. Taylor, J.F. Banfield, Environmental risks of nanotechnology: National nanotechnology initiative funding, 2000-2004, *Environ. Sci. Technol.* 40 (2006). <https://doi.org/10.1021/es0515708>.
- [28] Z. Ahmad, S.A. Shah, I. Khattak, H. Ullah, A.A. Khan, R.A. Shah, S.A. Khan, S.B. Khan, Melia Azedarach impregnated Co and Ni zero-valent metal nanoparticles for organic pollutants degradation: validation of experiments through statistical analysis, *J. Mater. Sci. Mater. Electron.* 31 (2020). <https://doi.org/10.1007/s10854-020-04250-5>.
- [29] L. Chekli, B. Bayatsarmadi, R. Sekine, B. Sarkar, A.M. Shen, K.G. Scheckel, W. Skinner, R. Naidu, H.K. Shon, E. Lombi, E. Donner, Analytical characterisation of nanoscale zero-valent iron: A methodological review, *Anal. Chim. Acta.* 903 (2016). <https://doi.org/10.1016/j.aca.2015.10.040>.
- [30] S.B. Yaqoob, R. Adnan, R.M. Rameez Khan, M. Rashid, Gold, Silver, and Palladium Nanoparticles: A Chemical Tool for Biomedical Applications, *Front. Chem.* 8 (2020). <https://doi.org/10.3389/fchem.2020.00376>.
- [31] N.K. Younis, J.A. Ghoubaira, E.P. Bassil, H.N. Tantawi, A.H. Eid, Metal-based nanoparticles: Promising tools for the management of cardiovascular diseases, *Nanomedicine Nanotechnology, Biol. Med.* 36 (2021). <https://doi.org/10.1016/j.nano.2021.102433>.
- [32] H. Hinterwirth, S.K. Wiedmer, M. Moilanen, A. Lehner, G. Allmaier, T. Waitz, W. Lindner, M. Lämmerhofer, Comparative method evaluation for size and size-distribution analysis of gold nanoparticles, *J. Sep. Sci.* 36 (2013). <https://doi.org/10.1002/jssc.201300460>.
- [33] D.C. Hone, P.I. Walker, R. Evans-Gowing, S. FitzGerald, A. Beeby, I. Chambrier, M.J. Cook, D.A. Russell, Generation of cytotoxic singlet oxygen via phthalocyanine-stabilized gold nanoparticles: A potential delivery vehicle for photodynamic therapy, *Langmuir.* 18 (2002). <https://doi.org/10.1021/la0256230>.
- [34] S.H. Lee, B.H. Jun, Silver nanoparticles: Synthesis and application for nanomedicine, *Int. J. Mol. Sci.* 20 (2019). <https://doi.org/10.3390/ijms20040865>.

- [35] L. Xu, Y.Y. Wang, J. Huang, C.Y. Chen, Z.X. Wang, H. Xie, Silver nanoparticles: Synthesis, medical applications and biosafety, *Theranostics*. 10 (2020). <https://doi.org/10.7150/thno.45413>.
- [36] E. Hutter, D. Maysinger, Gold nanoparticles and quantum dots for bioimaging, *Microsc. Res. Tech.* 74 (2011). <https://doi.org/10.1002/jemt.20928>.
- [37] J. Kneipp, H. Kneipp, W.L. Rice, K. Kneipp, Optical probes for biological applications based on surface-enhanced Raman scattering from indocyanine green on gold nanoparticles, *Anal. Chem.* 77 (2005). <https://doi.org/10.1021/ac050109v>.
- [38] P. Proposito, L. Burratti, I. Venditti, Silver nanoparticles as colorimetric sensors for water pollutants, *Chemosensors*. 8 (2020). <https://doi.org/10.3390/CHEMOSENSORS8020026>.
- [39] L. Calzolari, F. Franchini, D. Gilliland, F. Rossi, Protein-nanoparticle interaction: Identification of the ubiquitin-gold nanoparticle interaction site, *Nano Lett.* 10 (2010). <https://doi.org/10.1021/nl101746v>.
- [40] M. Carbone, D.T. Donia, G. Sabbatella, R. Antiochia, Silver nanoparticles in polymeric matrices for fresh food packaging, *J. King Saud Univ. - Sci.* 28 (2016). <https://doi.org/10.1016/j.jksus.2016.05.004>.
- [41] P.P. Pompa, G. Vecchio, A. Galeone, V. Brunetti, S. Sabella, G. Maiorano, A. Falqui, G. Bertoni, R. Cingolani, In Vivo toxicity assessment of gold nanoparticles in *Drosophila melanogaster*, *Nano Res.* 4 (2011). <https://doi.org/10.1007/s12274-011-0095-z>.
- [42] C. Noël, J.C. Simard, D. Girard, Gold nanoparticles induce apoptosis, endoplasmic reticulum stress events and cleavage of cytoskeletal proteins in human neutrophils, *Toxicol. Vitro*. 31 (2016). <https://doi.org/10.1016/j.tiv.2015.11.003>.
- [43] N. Durán, W.R. Rolim, M. Durán, W.J. Fávaro, A.B. Seabra, Nanotoxicology of silver nanoparticles: Toxicity in animals and humans., *Quim. Nova*. 42 (2019). <https://doi.org/10.21577/0100-4042.20170318>.
- [44] O. Barash, N. Peled, U. Tisch, P.A. Bunn, F.R. Hirsch, H. Haick, Classification of lung cancer histology by gold nanoparticle sensors, *Nanomedicine Nanotechnology, Biol. Med.* 8 (2012). <https://doi.org/10.1016/j.nano.2011.10.001>.
- [45] C. Fang, R. Dharmarajan, M. Megharaj, R. Naidu, Gold nanoparticle-based optical sensors for selected anionic contaminants, *TrAC Trends Anal. Chem.* 86 (2017). <https://doi.org/10.1016/j.trac.2016.10.008>.
- [46] K. Shrivastava, N. Nirmalkar, S.S. Thakur, M.K. Deb, S.S. Shinde, R. Shankar, Sucrose

- capped gold nanoparticles as a plasmonic chemical sensor based on non-covalent interactions: Application for selective detection of vitamins B1 and B6 in brown and white rice food samples, *Food Chem.* 250 (2018). <https://doi.org/10.1016/j.foodchem.2018.01.002>.
- [47] N. Jornet-Martínez, M. González-Béjar, Y. Moliner-Martínez, P. Campíns-Falcó, J. Pérez-Prieto, Sensitive and selective plasmonic assay for spermine as biomarker in human urine, *Anal. Chem.* 86 (2014). <https://doi.org/10.1021/ac404165j>.
- [48] T.M. Benn, P. Westerhoff, Nanoparticle silver released into water from commercially available sock fabrics, *Environ. Sci. Technol.* 42 (2008). <https://doi.org/10.1021/es7032718>.
- [49] L. Pan, Y.T. Liu, X.M. Xie, X.D. Zhu, Coordination-driven hierarchical assembly of silver nanoparticles on MoS<sub>2</sub> nanosheets for improved lithium storage, *Chem. - An Asian J.* 9 (2014). <https://doi.org/10.1002/asia.201301690>.
- [50] Z. Li, Z. Wang, J. Khan, M.K. Lagasse, K.S. Suslick, Ultrasensitive Monitoring of Museum Airborne Pollutants Using a Silver Nanoparticle Sensor Array, *ACS Sensors.* 5 (2020). <https://doi.org/10.1021/acssensors.0c00583>.
- [51] Y. Shang, M. Kamrul Hasan, G.J. Ahammed, M. Li, H. Yin, J. Zhou, Applications of nanotechnology in plant growth and crop protection: A review, *Molecules.* 24 (2019). <https://doi.org/10.3390/molecules24142558>.
- [52] C.C. Fernandez, A.R. Sokolonski, M.S. Fonseca, D. Staniscic, D.B. Araújo, V. Azevedo, R.D. Portela, L. Tasic, Applications of silver nanoparticles in dentistry: Advances and technological innovation, *Int. J. Mol. Sci.* 22 (2021). <https://doi.org/10.3390/ijms22052485>.
- [53] R. Asadi Dokht Lish, S.A. Johari, M. Sarkheil, I.J. Yu, On how environmental and experimental conditions affect the results of aquatic nanotoxicology on brine shrimp (*Artemia salina*): A case of silver nanoparticles toxicity, *Environ. Pollut.* 255 (2019). <https://doi.org/10.1016/j.envpol.2019.113358>.
- [54] S.S.D. Kumar, N.K. Rajendran, N.N. Houreld, H. Abrahamse, Recent advances on silver nanoparticle and biopolymer-based biomaterials for wound healing applications, *Int. J. Biol. Macromol.* 115 (2018). <https://doi.org/10.1016/j.ijbiomac.2018.04.003>.
- [55] I.M. Chung, I. Park, K. Seung-Hyun, M. Thiruvengadam, G. Rajakumar, Plant-Mediated Synthesis of Silver Nanoparticles: Their Characteristic Properties and Therapeutic Applications, *Nanoscale Res. Lett.* 11 (2016). <https://doi.org/10.1186/s11671-016-1257-4>.
- [56] G. FRENS, Controlled Nucleation for the Regulation of the Particle Size in

- Monodisperse Gold Suspensions, *Nat. Phys. Sci.* 241 (1973). <https://doi.org/10.1038/physci241020a0>.
- [57] J. Turkevich, P.C. Stevenson, J. Hillier, A study of the nucleation and growth processes in the synthesis of colloidal gold, *Discuss. Faraday Soc.* 11 (1951). <https://doi.org/10.1039/DF9511100055>.
- [58] M. Brust, M. Walker, D. Bethell, D.J. Schiffrin, R. Whyman, Synthesis of thiol-derivatised gold nanoparticles in a two-phase liquid-liquid system, *J. Chem. Soc. Chem. Commun.* 7 (1994). <https://doi.org/10.1039/C39940000801>.
- [59] K. Aslan, V.H. Pérez-Luna, Surface modification of colloidal gold by chemisorption of alkanethiols in the presence of a nonionic surfactant, *Langmuir.* 18 (2002). <https://doi.org/10.1021/la025795x>.
- [60] J.M. Abad, S.F.L. Mertens, M. Pita, V.M. Fernández, D.J. Schiffrin, Functionalization of thioctic acid-capped gold nanoparticles for specific immobilization of histidine-tagged proteins, *J. Am. Chem. Soc.* 127 (2005). <https://doi.org/10.1021/ja042717i>.
- [61] N.Y. Stozhko, M.A. Bukharinova, E.I. Khamzina, A. V Tarasov, Electrochemical Properties of Phytosynthesized Gold Nanoparticles for Electrosensing, (2022) 1–19.
- [62] S. Jadoun, R. Arif, N.K. Jangid, R.K. Meena, Green synthesis of nanoparticles using plant extracts: a review, *Environ. Chem. Lett.* 19 (2021). <https://doi.org/10.1007/s10311-020-01074-x>.
- [63] S. Irvani, H. Korbekandi, S. V. Mirmohammadi, B. Zolfaghari, Synthesis of silver nanoparticles: Chemical, physical and biological methods, *Res. Pharm. Sci.* 9 (2014).
- [64] M. Rafique, M.S. Rafique, U. Kalsoom, A. Afzal, S.H. Butt, A. Usman, Laser ablation synthesis of silver nanoparticles in water and dependence on laser nature, *Opt. Quantum Electron.* 51 (2019). <https://doi.org/10.1007/s11082-019-1902-0>.
- [65] P.B. Khodke, R.R. Popat, P. V. Burakale, P.P. Chinchole, V.N. Shrikhande, Silver nanoparticles - A review, *Res. J. Pharm. Technol.* 10 (2017). <https://doi.org/10.5958/0974-360X.2017.00321.3>.
- [66] H. Barani, B. Mahltig, Microwave-Assisted Synthesis of Silver Nanoparticles: Effect of Reaction Temperature and Precursor Concentration on Fluorescent Property, *J. Clust. Sci.* 33 (2022). <https://doi.org/10.1007/s10876-020-01945-x>.
- [67] A. Roy, O. Bulut, S. Some, A.K. Mandal, M.D. Yilmaz, Green synthesis of silver nanoparticles: Biomolecule-nanoparticle organizations targeting antimicrobial activity, *RSC Adv.* 9 (2019). <https://doi.org/10.1039/c8ra08982e>.
- [68] R.H. Ahmed, D.E. Mustafa, Green synthesis of silver nanoparticles mediated by



- traditionally used medicinal plants in Sudan, *Int. Nano Lett.* 10 (2020). <https://doi.org/10.1007/s40089-019-00291-9>.
- [69] S. Kaabipour, S. Hemmati, A review on the green and sustainable synthesis of silver nanoparticles and one-dimensional silver nanostructures, *Beilstein J. Nanotechnol.* 12 (2021). <https://doi.org/10.3762/BJNANO.12.9>.
- [70] B. Khodashenas, H.R. Ghorbani, Synthesis of silver nanoparticles with different shapes, *Arab. J. Chem.* 12 (2019). <https://doi.org/10.1016/j.arabjc.2014.12.014>.
- [71] D.A. Lomelí-Rosales, A. Zamudio-Ojeda, S.A. Cortes-Llamas, G. Velázquez-Juárez, One-step synthesis of gold and silver non-spherical nanoparticles mediated by Eosin Methylene Blue agar, *Sci. Rep.* 9 (2019). <https://doi.org/10.1038/s41598-019-55744-0>.
- [72] M. Laurence Budlayan, J. Phyrre Lagare-Oracion, L. Dela Rosa, M. Joy Rodriguez, R.Y. Capangpangan, J. Manigo, A. Alguno, E. Austria, S. Arco, J. Patricio, A Facile Route in Controlling the Optical Absorbance of Polyvinylpyrrolidone-Capped Silver Nanoparticles Via Chemical Reduction Technique, *IOP Conf. Ser. Mater. Sci. Eng.* 925 (2020). <https://doi.org/10.1088/1757-899X/925/1/012050>.
- [73] S. Franco-Ulloa, G. Tatulli, S.L. Bore, M. Moglianetti, P.P. Pompa, M. Cascella, M. De Vivo, Dispersion state phase diagram of citrate-coated metallic nanoparticles in saline solutions, *Nat. Commun.* 11 (2020). <https://doi.org/10.1038/s41467-020-19164-3>.
- [74] M. Yaseen, M. Humayun, A. Khan, M. Usman, H. Ullah, A.A. Tahir, H. Ullah, Preparation, functionalization, modification, and applications of nanostructured gold: A critical review, *Energies.* 14 (2021). <https://doi.org/10.3390/en14051278>.
- [75] D. Horinek, DLVO Theory, *Encycl. Appl. Electrochem.*, (2014). [https://doi.org/10.1007/978-1-4419-6996-5\\_7](https://doi.org/10.1007/978-1-4419-6996-5_7).
- [76] I. Ielo, G. Rando, F. Giacobello, S. Sfameni, A. Castellano, M. Galletta, D. Drommi, G. Rosace, M.R. Plutino, Synthesis, chemical–physical characterization, and biomedical applications of functional gold nanoparticles: A review, *Molecules.* 26 (2021). <https://doi.org/10.3390/molecules26195823>.
- [77] R. Singh, P. Thakur, A. Thakur, H. Kumar, P. Chawla, J. V. Rohit, R. Kaushik, N. Kumar, Colorimetric sensing approaches of surface-modified gold and silver nanoparticles for detection of residual pesticides: a review, *Int. J. Environ. Anal. Chem.* 101 (2021). <https://doi.org/10.1080/03067319.2020.1715382>.
- [78] M. Sabela, S. Balme, M. Bechelany, J.M. Janot, K. Bisetty, A Review of Gold and Silver Nanoparticle-Based Colorimetric Sensing Assays, *Adv. Eng. Mater.* 19 (2017). <https://doi.org/10.1002/adem.201700270>.

- [79] B. Casteleiro, J.M.G. Martinho, J.P.S. Farinha, Encapsulation of gold nanoclusters: Stabilization and more, *Nanoscale*. 13 (2021). <https://doi.org/10.1039/d1nr04939a>.
- [80] J. Tournebize, A. Boudier, A. Sapin-Minet, P. Maincent, P. Leroy, R. Schneider, Role of gold nanoparticles capping density on stability and surface reactivity to design drug delivery platforms, *ACS Appl. Mater. Interfaces*. 4 (2012). <https://doi.org/10.1021/am3012752>.
- [81] J. Heo, H. Cho, J. Lee, Surfactant-free nanoparticle–DNA complexes with ultrahigh stability against salt for environmental and biological sensing, *Analyst*. 139 (2014). <https://doi.org/10.1039/c4an01271b>.
- [82] A. Elbakry, A. Zaky, R. Liebl, R. Rachel, A. Goepferich, M. Breunig, Layer-by-layer assembled gold nanoparticles for sirna delivery, *Nano Lett.* 9 (2009). <https://doi.org/10.1021/nl9003865>.
- [83] M. Chanana, P. Rivera-gil, M.A. Correa-Duarte, L.M. Liz-Marzán, W.J. Parak, Physicochemical properties of protein-coated gold nanoparticles in biological fluids and cells before and after proteolytic digestion, *Angew. Chemie - Int. Ed.* 52 (2013) 4179–4183. <https://doi.org/10.1002/anie.201208019>.
- [84] S. Ip, C.M. MacLaughlin, N. Gunari, G.C. Walker, Phospholipid membrane encapsulation of nanoparticles for surface-enhanced raman scattering, *Langmuir*. 27 (2011). <https://doi.org/10.1021/la200212c>.
- [85] M.M. Khalaf, H.M. Abd El-Lateef, I.M.A. Mohamed, M.E.A. Zaki, A. Toghan, Facile synthesis of gold-nanoparticles by different capping agents and their anticancer performance against liver cancer cells, *Colloids Interface Sci. Commun.* 44 (2021). <https://doi.org/10.1016/j.colcom.2021.100482>.
- [86] Y. Nangia, N. Wangoo, S. Sharma, J.S. Wu, V. Dravid, G.S. Shekhawat, C. Raman Suri, Facile biosynthesis of phosphate capped gold nanoparticles by a bacterial isolate *Stenotrophomonas maltophilia*, *Appl. Phys. Lett.* 94 (2009). <https://doi.org/10.1063/1.3141519>.
- [87] L.C. Lopes, D. Lima, A.C. Mendes Hacke, B.S. Schweigert, G.N. Calaça, F.F. Simas, R.P. Pereira, M. Iacomini, A.G. Viana, C.A. Pessôa, Gold nanoparticles capped with polysaccharides extracted from pineapple gum: Evaluation of their hemocompatibility and electrochemical sensing properties, *Talanta*. 223 (2021). <https://doi.org/10.1016/j.talanta.2020.121634>.
- [88] A.A. Omolaja, B. Pearce, S.I. Omoruyia, J.A. Badmus, E. Ismail, J. Marnewick, S. Botha, M. Benjeddou, O.E. Ekpob, A.A. Hussein, The potential of chalcone-capped gold nanoparticles for the management of diabetes mellitus, *Surfaces and Interfaces*. 25 (2021). <https://doi.org/10.1016/j.surfin.2021.101251>.

- [89] M. Vanin dos Santos Lima, G. Beloni de Melo, L. Gracher Teixeira, C. Grella Miranda, P.H. Hermes de Araújo, C. Sayer, R. Porto Ineu, F.V. Leimann, O. Hess Gonçalves, Green synthesis of silver nanoparticles using *Ilex paraguariensis* extracts: antimicrobial activity and acetylcholinesterase modulation in rat brain tissue, *Green Chem. Lett. Rev.* 15 (2022) 126–136. <https://doi.org/10.1080/17518253.2021.2024896>.
- [90] A. Syafiuddin, Salmiati, M.R. Salim, A. Beng Hong Kueh, T. Hadibarata, H. Nur, A Review of Silver Nanoparticles: Research Trends, Global Consumption, Synthesis, Properties, and Future Challenges, *J. Chinese Chem. Soc.* 64 (2017). <https://doi.org/10.1002/jccs.201700067>.
- [91] M.N. Aktara, S. Nayim, N.K. Sahoo, M. Hossain, The synthesis of thiol-stabilized silver nanoparticles and their application towards the nanomolar-level colorimetric recognition of glutathione, *New J. Chem.* 43 (2019). <https://doi.org/10.1039/c9nj01360a>.
- [92] H. Alsubaie, Z. Zaheer, E.S. Aazam, Role of ionic surfactants on the nucleation and growth of silver nanoparticles, *J. Mol. Liq.* 341 (2021). <https://doi.org/10.1016/j.molliq.2021.117309>.
- [93] A.M. El Badawy, K.G. Scheckel, M. Suidan, T. Tolaymat, The impact of stabilization mechanism on the aggregation kinetics of silver nanoparticles, *Sci. Total Environ.* 429 (2012). <https://doi.org/10.1016/j.scitotenv.2012.03.041>.
- [94] D.I. Saragih, D.C.V. Arifin, B. Rusdianto, S. Suyanta, S.J. Santosa, Synthesis of silver nanoparticles using tyrosine as reductor and capping agent, *Key Eng. Mater.* 840 (2020). <https://doi.org/10.4028/www.scientific.net/kem.840.360>.
- [95] E.E.L. Tanner, S. V. Sokolov, N.P. Young, R.G. Compton, DNA capping agent control of electron transfer from silver nanoparticles, *Phys. Chem. Chem. Phys.* 19 (2017). <https://doi.org/10.1039/c7cp01721a>.
- [96] V. Kulikouskaya, K. Hileuskaya, A. Kraskouski, I. Kozerozhets, E. Stepanova, I. Kuzminski, L. You, V. Agabekov, Chitosan-capped silver nanoparticles: A comprehensive study of polymer molecular weight effect on the reaction kinetic, physicochemical properties, and synergetic antibacterial potential, *SPE Polym.* (2022). <https://doi.org/10.1002/pls2.10069>.
- [97] J. Tashkhourian, O. Sheydaei, Chitosan capped silver nanoparticles as colorimetric sensor for the determination of iron(III), *Anal. Bioanal. Chem. Res.* 4 (2017). <https://doi.org/10.22036/abcr.2017.69942.1127>.
- [98] T.M.D. Dang, T.T.T. Le, E. Fribourg-Blanc, M.C. Dang, Influence of surfactant on the preparation of silver nanoparticles by polyol method, *Adv. Nat. Sci. Nanosci.*

- Nanotechnol. 3 (2012). <https://doi.org/10.1088/2043-6262/3/3/035004>.
- [99] T. Yu, Q. Wei, Plasmonic molecular assays: Recent advances and applications for mobile health, *Nano Res.* 11 (2018). <https://doi.org/10.1007/s12274-018-2094-9>.
- [100] Y.C. Yeh, B. Creran, V.M. Rotello, Gold nanoparticles: Preparation, properties, and applications in bionanotechnology, *Nanoscale.* 4 (2012). <https://doi.org/10.1039/c1nr11188d>.
- [101] C.M. Cobley, S.E. Skrabalak, D.J. Campbell, Y. Xia, Shape-controlled synthesis of silver nanoparticles for plasmonic and sensing applications, *Plasmonics.* 4 (2009). <https://doi.org/10.1007/s11468-009-9088-0>.
- [102] K.L. Kelly, E. Coronado, L.L. Zhao, G.C. Schatz, The optical properties of metal nanoparticles: The influence of size, shape, and dielectric environment, *J. Phys. Chem. B.* 107 (2003). <https://doi.org/10.1021/jp026731y>.
- [103] Y.J. Ahn, Y.G. Gil, Y.J. Lee, H. Jang, G.J. Lee, A dual-mode colorimetric and SERS detection of hydrogen sulfide in live prostate cancer cells using a silver nanoplate-coated paper assay, *Microchem. J.* 155 (2020). <https://doi.org/10.1016/j.microc.2020.104724>.
- [104] N. Jornet-Martínez, L. Hakobyan, A.I. Argente-García, C. Molins-Legua, P. Campíns-Falcó, Nylon-Supported Plasmonic Assay Based on the Aggregation of Silver Nanoparticles: In Situ Determination of Hydrogen Sulfide-like Compounds in Breath Samples as a Proof of Concept, *ACS Sensors.* 4 (2019). <https://doi.org/10.1021/acssensors.9b01019>.
- [105] M. Yarbakht, M. Nikkhah, Unmodified gold nanoparticles as a colorimetric probe for visual methamphetamine detection, *J. Exp. Nanosci.* 11 (2016). <https://doi.org/10.1080/17458080.2015.1100333>.
- [106] S. Guo, E. Wang, Synthesis and electrochemical applications of gold nanoparticles, *Anal. Chim. Acta.* 598 (2007). <https://doi.org/10.1016/j.aca.2007.07.054>.
- [107] P. V. Kamat, Photophysical, photochemical and photocatalytic aspects of metal nanoparticles, *J. Phys. Chem. B.* 106 (2002). <https://doi.org/10.1021/jp0209289>.
- [108] K.G. Thomas, P. V. Kamat, Chromophore-Functionalized Gold Nanoparticles, *Acc. Chem. Res.* 36 (2003). <https://doi.org/10.1021/ar030030h>.
- [109] S. Hong, X. Li, Optimal size of gold nanoparticles for surface-enhanced Raman spectroscopy under different conditions, *J. Nanomater.* 2013 (2013). <https://doi.org/10.1155/2013/790323>.
- [110] Y. Wang, H. Wei, B. Li, W. Ren, S. Guo, S. Dong, E. Wang, SERS opens a new way in

- aptasensor for protein recognition with high sensitivity and selectivity, 48 Chem. Commun. (2007). <https://doi.org/10.1039/b709492b>.
- [111] S. Nie, S.R. Emory, Probing single molecules and single nanoparticles by surface-enhanced Raman scattering, *Science*. 275 (1997). <https://doi.org/10.1126/science.275.5303.1102>.
- [112] R.J. Dijkstra, W.J.J.M. Scheenen, N. Dam, E.W. Roubos, J.J. ter Meulen, Monitoring neurotransmitter release using surface-enhanced Raman spectroscopy, *J. Neurosci. Methods*. 159 (2007). <https://doi.org/10.1016/j.jneumeth.2006.06.017>.
- [113] L.A. Dykman, N.G. Khlebtsov, Immunological properties of gold nanoparticles, *Chem. Sci*. 8 (2017). <https://doi.org/10.1039/c6sc03631g>.
- [114] R. Saenmuangchin, A. Siripinyanond, Flow field-flow fractionation for hydrodynamic diameter estimation of gold nanoparticles with various types of surface coatings, *Anal. Bioanal. Chem*. 410 (2018). <https://doi.org/10.1007/s00216-018-1284-3>.
- [115] S.J. Park, S.Y. Lee, History and structure of carbon fibers, *Springer Ser. Mater. Sci*. 210 (2014). [https://doi.org/10.1007/978-94-017-9478-7\\_1](https://doi.org/10.1007/978-94-017-9478-7_1).
- [116] G. Speranza, Carbon nanomaterials: Synthesis, functionalization and sensing applications, *Nanomaterials*. 11 (2021). <https://doi.org/10.3390/nano11040967>.
- [117] A. Kausar, Contemporary applications of carbon black-filled polymer composites: An overview of essential aspects, *J. Plast. Film Sheeting*. 34 (2018). <https://doi.org/10.1177/8756087917725773>.
- [118] M.J. Yee, N.M. Mubarak, E.C. Abdullah, M. Khalid, R. Walvekar, R.R. Karri, S. Nizamuddin, A. Numan, Carbon nanomaterials based films for strain sensing application—A review, *Nano-Structures and Nano-Objects*. 18 (2019). <https://doi.org/10.1016/j.nanoso.2019.100312>.
- [119] F. Arduini, S. Cinti, V. Mazzaracchio, V. Scognamiglio, A. Amine, D. Moscone, Carbon black as an outstanding and affordable nanomaterial for electrochemical (bio)sensor design, *Biosens. Bioelectron*. 156 (2020). <https://doi.org/10.1016/j.bios.2020.112033>.
- [120] T. Hüffer, S. Wagner, T. Reemtsma, T. Hofmann, Sorption of organic substances to tire wear materials: Similarities and differences with other types of microplastic, *TrAC Trends Anal. Chem*. 113 (2019). <https://doi.org/10.1016/j.trac.2018.11.029>.
- [121] Y. Fan, G.D. Fowler, M. Zhao, The past, present and future of carbon black as a rubber reinforcing filler – A review, *J. Clean. Prod*. 247 (2020). <https://doi.org/10.1016/j.jclepro.2019.119115>.

- [122] T.A. Silva, F.C. Moraes, B.C. Janegitz, O. Fatibello-Filho, D. Ganta, Electrochemical biosensors based on nanostructured carbon black: A review, *J. Nanomater.* 2017 (2017). <https://doi.org/10.1155/2017/4571614>.
- [123] I. Chaudhuri, C. Fruijtier-Pöllöth, Y. Ngiewih, L. Levy, Evaluating the evidence on genotoxicity and reproductive toxicity of carbon black: a critical review, *Crit. Rev. Toxicol.* 48 (2018). <https://doi.org/10.1080/10408444.2017.1391746>.
- [124] J. Bae, W. Kim, K. Rah, E.C. Jung, S. Lee, Application of flow field-flow fractionation (FIFFF) for size characterization of carbon black particles in ink, *Microchem. J.* 104 (2012). <https://doi.org/10.1016/j.microc.2012.04.007>.
- [125] T. Myojo, M. Ono-Ogasawara, Review; risk assessment of aerosolized SWCNTs, MWCNTs, fullerenes and carbon black, *KONA Powder Part. J.* 2018 (2018). <https://doi.org/10.14356/kona.2018013>.
- [126] Z.O. Kyjovska, A.M.Z. Boisen, P. Jackson, H. Wallin, U. Vogel, K.S. Hougaard, Daily sperm production: Application in studies of prenatal exposure to nanoparticles in mice, *Reprod. Toxicol.* 36 (2013). <https://doi.org/10.1016/j.reprotox.2012.12.005>.
- [127] O. Fichera, L. Alpan, J. Laloy, T. Tabarrant, U. Uhrner, Q. Ye, J. Mejia, J.M. Dogné, S. Lucas, Characterization of water-based paints containing titanium dioxide or carbon black as manufactured nanomaterials before and after atomization, *Appl. Nanosci.* 9 (2019). <https://doi.org/10.1007/s13204-019-01030-4>.
- [128] K. Kim, S. Lee, W. Kim, Characterization of carbon black nanoparticles using asymmetrical flow field-flow fractionation (AsFIFFF), *Anal. Sci. Technol.* 32 (2019). <https://doi.org/10.5806/AST.2019.32.3.77>.
- [129] K.M. White, C.S. Palenik, Toner Particles as Forensic Evidence: Microanalytical Characterization of Known Toner and Recognition of Toner in Environmental Samples, *J. Forensic Sci.* 65 (2020). <https://doi.org/10.1111/1556-4029.14501>.
- [130] L. Vieira Jodar, L.O. Orzari, T. Storti Ortolani, M.H.M.T. Assumpção, F.C. Vicentini, B.C. Janegitz, Electrochemical Sensor Based on Casein and Carbon Black for Bisphenol A Detection, *Electroanalysis.* 31 (2019). <https://doi.org/10.1002/elan.201900176>.
- [131] R. Sakthivel, S. Kubendhiran, S.M. Chen, P. Ranganathan, S.P. Rwei, Functionalized Carbon Black Nanospheres Hybrid with MoS<sub>2</sub> Nanoclusters for the Effective Electrocatalytic Reduction of Chloramphenicol, *Electroanalysis.* 30 (2018). <https://doi.org/10.1002/elan.201800070>.
- [132] N. Debnath, V. Panwar, T. Roy, M. Saha, K. Pal, Improved dispersion of carbon black in ABS/PANI blend through its acid functionalization and addition of nanoclay, thereby enhancing mechanical and thermal properties, *Polym. Bull.* 77 (2020).

<https://doi.org/10.1007/s00289-019-02979-6>.

- [133] M. Sandomierski, T. Buchwald, B. Strzemiecka, A. Voelkel, Carbon black modified with 4-hydroxymethylbenzenediazonium salt as filler for phenol-formaldehyde resins and abrasive tools, *J. Appl. Polym. Sci.* 137 (2020). <https://doi.org/10.1002/app.48160>.
- [134] J. Kim, G. Kim, S.Y. Kim, S. Lee, Y. Kim, J. Lee, J. Kim, Y.C. Jung, J. Kwon, H. Han, Fabrication of highly flexible electromagnetic interference shielding polyimide carbon black composite using hot-pressing method, *Compos. Part B Eng.* 221 (2021). <https://doi.org/10.1016/j.compositesb.2021.109010>.
- [135] J. Bott, A. Störmer, R. Franz, Migration of nanoparticles from plastic packaging materials containing carbon black into foodstuffs, *Food Addit. Contam. - Part A Chem. Anal. Control. Expo. Risk Assess.* 31 (2014). <https://doi.org/10.1080/19440049.2014.952786>.
- [136] S. Yu, Z. Tang, S. Fang, S. Wu, B. Guo, Polyrhodanine mediated interface in natural rubber/carbon black composites toward ultralow energy loss, *Compos. Part A Appl. Sci. Manuf.* 149 (2021). <https://doi.org/10.1016/j.compositesa.2021.106589>.
- [137] K. Xu, Y.X. Liu, X.F. Wang, S.W. Li, J.M. Cheng, Combined toxicity of functionalized nano-carbon black and cadmium on *Eisenia fetida* coelomocytes: The role of adsorption, *J. Hazard. Mater.* 398 (2020). <https://doi.org/10.1016/j.jhazmat.2020.122815>.
- [138] K.M. Bendtsen, A. Brostrøm, A.J. Koivisto, I. Koponen, T. Berthing, N. Bertram, K.I. Kling, M. Dal Maso, O. Kangasniemi, M. Poikkimäki, K. Loeschner, P.A. Clausen, H. Wolff, K.A. Jensen, A.T. Saber, U. Vogel, Airport emission particles: Exposure characterization and toxicity following intratracheal instillation in mice, *Part. Fibre Toxicol.* 16 (2019). <https://doi.org/10.1186/s12989-019-0305-5>.
- [139] K. Xu, X. Wang, C. Lu, Y. Liu, D. Zhang, J. Cheng, Toxicity of three carbon-based nanomaterials to earthworms: Effect of morphology on biomarkers, cytotoxicity, and metabolomics, *Sci. Total Environ.* 777 (2021). <https://doi.org/10.1016/j.scitotenv.2021.146224>.
- [140] L. Canesi, C. Ciacci, M. Betti, R. Fabbri, B. Canonico, A. Fantinati, A. Marcomini, G. Pojana, Immunotoxicity of carbon black nanoparticles to blue mussel hemocytes, *Environ. Int.* 34 (2008). <https://doi.org/10.1016/j.envint.2008.04.002>.
- [141] A.K. Pal, I. Aalaei, S. Gadde, P. Gaines, D. Schmidt, P. Demokritou, D. Bello, High resolution characterization of engineered nanomaterial dispersions in complex media using tunable resistive pulse sensing technology, *ACS Nano.* 8 (2014). <https://doi.org/10.1021/nn502219q>.

- [142] F.Z. Koudri, I. Moulefera, S. Bahoussi, A. Belmokhtar, A. Benyoucef, Development of hybrid materials based on carbon black reinforced poly(2-methoxyaniline): preparation, characterization and tailoring optical, thermal and electrochemical properties, *Colloid Polym. Sci.* 299 (2021). <https://doi.org/10.1007/s00396-021-04837-2>.
- [143] Z. Xiao, L.B. Kong, S. Ruan, X. Li, S. Yu, X. Li, Y. Jiang, Z. Yao, S. Ye, C. Wang, T. Zhang, K. Zhou, S. Li, Recent development in nanocarbon materials for gas sensor applications, *Sensors Actuators, B Chem.* 274 (2018). <https://doi.org/10.1016/j.snb.2018.07.040>.
- [144] J. Xu, J. Yu, W. He, J. Huang, J. Xu, G. Li, Wet compounding with pyrolytic carbon black from waste tyre for manufacture of new tyre – A mini review, *Waste Manag. Res.* 39 (2021). <https://doi.org/10.1177/0734242X211004746>.
- [145] A. Geng, Q. Zhong, C. Mei, L. Wang, L. Xu, L. Gan, Applications of Wet-Functionalized Graphene in Rubber Composites, *Prog. Chem.* 31 (2019). <https://doi.org/10.7536/PC180817>.
- [146] D. Veeman, M.V. Shree, P. Sureshkumar, T. Jagadeesha, L. Natrayan, M. Ravichandran, P. Paramasivam, Sustainable Development of Carbon Nanocomposites: Synthesis and Classification for Environmental Remediation, *J. Nanomater.* 2021 (2021). <https://doi.org/10.1155/2021/5840645>.
- [147] S. Karki, M.B. Gohain, D. Yadav, P.G. Ingole, Nanocomposite and bio-nanocomposite polymeric materials/membranes development in energy and medical sector: A review, *Int. J. Biol. Macromol.* 193 (2021). <https://doi.org/10.1016/j.ijbiomac.2021.11.044>.
- [148] M. Parthasarathy, Challenges and emerging trends in toner waste recycling: A review, *Recycling.* 6 (2021). <https://doi.org/10.3390/recycling6030057>.
- [149] T. Yan, Z. Wang, Z.J. Pan, Flexible strain sensors fabricated using carbon-based nanomaterials: A review, *Curr. Opin. Solid State Mater. Sci.* 22 (2018). <https://doi.org/10.1016/j.cossms.2018.11.001>.
- [150] T.M.B.F. Oliveira, F.W.P. Ribeiro, C.P. Sousa, G.R. Salazar-Banda, P. de Lima-Neto, A.N. Correia, S. Morais, Current overview and perspectives on carbon-based (bio)sensors for carbamate pesticides electroanalysis, *TrAC Trends Anal. Chem.* 124 (2020) 115779. <https://doi.org/10.1016/j.trac.2019.115779>.
- [151] F.S. Bierkandt, L. Leibrock, S. Wagener, P. Laux, A. Luch, The impact of nanomaterial characteristics on inhalation toxicity, *Toxicol. Res.* 7 (2018). <https://doi.org/10.1039/c7tx00242d>.
- [152] I. Basinas, A.S. Jiménez, K.S. Galea, M. Van Tongeren, F. Hurley, A systematic review



- of the routes and forms of exposure to engineered nanomaterials, *Ann. Work Expo. Heal.* 62 (2018). <https://doi.org/10.1093/annweh/wxy048>.
- [153] C. Teng, C. Jiang, S. Gao, X. Liu, S. Zhai, Fetotoxicity of nanoparticles: Causes and mechanisms, *Nanomaterials*. 11 (2021). <https://doi.org/10.3390/nano11030791>.
- [154] A. Kausar, Polyurethane Composite Foams in High-Performance Applications: A Review, *Polym. - Plast. Technol. Eng.* 57 (2018). <https://doi.org/10.1080/03602559.2017.1329433>.
- [155] L. Fulcheri, N. Probst, G. Flamant, F. Fabry, E. Grivei, X. Bourrat, Plasma processing: A step towards the production of new grades of carbon black, *Carbon*. 40 (2002). [https://doi.org/10.1016/S0008-6223\(01\)00169-5](https://doi.org/10.1016/S0008-6223(01)00169-5).
- [156] C.O. Okoye, I. Jones, M. Zhu, Z. Zhang, D. Zhang, Manufacturing of carbon black from spent tyre pyrolysis oil – A literature review, *J. Clean. Prod.* 279 (2021). <https://doi.org/10.1016/j.jclepro.2020.123336>.
- [157] R.J. Mccunney, H.J. Muranko, C.M. Long, A.K. Hamade, P.A. Valberg, P. Morfeld, *Carbon Black*, John Wiley & Sons, Volume 5, (2012).
- [158] D. Sahu, G.M. Kannan, R. Vijayaraghavan, Carbon black particle exhibits size dependent toxicity in human monocytes, *Int. J. Inflamm.* 2014 (2014). <https://doi.org/10.1155/2014/827019>.
- [159] M.J. Wang, C.A. Gray, S.A. Reznick, K. Mahmud, Y. Kutsovsky, *Carbon Black*, John Wiley & Son, (2003).
- [160] K.E. Lewis, G.D. Parfitt, Stability of non-aqueous dispersions: Part 3 - Rate of coagulation of Sterling MTG in Aerosol OT + n-heptane solutions, *Trans. Faraday Soc.* 62 (1966). <https://doi.org/10.1039/TF9666201652>.
- [161] V.L. Kononenko, J.K. Shimkus, J.C. Giddings, M.N. Myers, Feasibility studies on photophoretic effects in field-flow fractionation of particles, *J. Liq. Chromatogr. Relat. Technol.* 20 (1997). <https://doi.org/10.1080/10826079708005600>.
- [162] M. Wissler, Graphite and carbon powders for electrochemical applications, *J. Power Sources*. 156 (2006). <https://doi.org/10.1016/j.jpowsour.2006.02.064>.
- [163] W. Kwon, J.M. Kim, S.W. Rhee, Electrocatalytic carbonaceous materials for counter electrodes in dye-sensitized solar cells, *J. Mater. Chem. A*. 1 (2013). <https://doi.org/10.1039/c2ta00360k>.
- [164] J. Beniak, P. Krizan, M. Matus, Conductive material properties for fdm additive manufacturing, *MM Sci. J.* 2020 (2020). [https://doi.org/10.17973/MMSJ.2020\\_03\\_2019135](https://doi.org/10.17973/MMSJ.2020_03_2019135).

- [165] S.A. Goetz, D.T. Nguyen, A.P. Esser-Kahn, Surface modification of carbon black nanoparticles enhances photothermal separation and release of CO<sub>2</sub>, *Carbon*. 105 (2016). <https://doi.org/10.1016/j.carbon.2016.03.053>.
- [166] G. Ibáñez-Redín, T.A. Silva, F.C. Vicentini, O. Fatibello-Filho, Effect of carbon black functionalization on the analytical performance of a tyrosinase biosensor based on glassy carbon electrode modified with dihexadecylphosphate film, *Enzyme Microb. Technol.* 116 (2018). <https://doi.org/10.1016/j.enzmictec.2018.05.007>.
- [167] D. Leistenschneider, K. Zürbes, C. Schneidermann, S. Grätz, S. Oswald, K. Wegner, B. Klemmed, L. Giebeler, A. Eychmüller, L. Borchardt, Mechanochemical Functionalization of Carbon Black at Room Temperature, *C*. 4 (2018). <https://doi.org/10.3390/c4010014>.
- [168] X. Li, F. Forouzandeh, A.J. Kakanat, F. Feng, D.W.H. Banham, S. Ye, D.Y. Kwok, V. Birss, Surface Characteristics of Microporous and Mesoporous Carbons Functionalized with Pentafluorophenyl Groups, *ACS Appl. Mater. Interfaces*. 10 (2018). <https://doi.org/10.1021/acsami.7b13880>.
- [169] M.K. Mun, L.W. Ho, J.W. Park, D.S. Kim, G.Y. Yeom, D.W. Kim, Hydrophobic surface treatment of carbon black nanoparticles in isopropyl alcohol solution using He/SF<sub>6</sub> atmospheric plasma jet, *J. Nanosci. Nanotechnol.* 17 (2017). <https://doi.org/10.1166/jnn.2017.15173>.
- [170] S. Eris, Z. Daşdelen, F. Sen, Enhanced electrocatalytic activity and stability of monodisperse Pt nanocomposites for direct methanol fuel cells, *J. Colloid Interface Sci.* 513 (2018). <https://doi.org/10.1016/j.jcis.2017.11.085>.
- [171] A.N. Mohan, M. B, Surface modified graphene/SnO<sub>2</sub> nanocomposite from carbon black as an efficient disinfectant against *Pseudomonas aeruginosa*, *Mater. Chem. Phys.* 232 (2019). <https://doi.org/10.1016/j.matchemphys.2019.04.074>.
- [172] D. Pantea, H. Darmstadt, S. Kaliaguine, C. Roy, Electrical conductivity of conductive carbon blacks: Influence of surface chemistry and topology, *Appl. Surf. Sci.* 217 (2003). [https://doi.org/10.1016/S0169-4332\(03\)00550-6](https://doi.org/10.1016/S0169-4332(03)00550-6).
- [173] N. Probst, E. Grivei, Structure and electrical properties of carbon black, *Carbon*. 40 (2002). [https://doi.org/10.1016/S0008-6223\(01\)00174-9](https://doi.org/10.1016/S0008-6223(01)00174-9).
- [174] J. ping Song, K. yan Tian, L. xiang Ma, W. Li, S. chune Yao, The effect of carbon black morphology to the thermal conductivity of natural rubber composites, *Int. J. Heat Mass Transf.* 137 (2019). <https://doi.org/10.1016/j.ijheatmasstransfer.2019.03.078>.
- [175] Y. Fukunaga, Y. Fujii, S. Inada, Y. Tsumura, M. Asada, M. Naito, N. Torikai, Dispersion

- state of carbon black in polystyrene produced with different dispersion media and its effects on composite rheological properties, *Polym. J.* 51 (2019). <https://doi.org/10.1038/s41428-018-0149-0>.
- [176] S. Subramanian, G. Øye, Aqueous carbon black dispersions stabilized by sodium lignosulfonates, *Colloid Polym. Sci.* 299 (2021). <https://doi.org/10.1007/s00396-021-04840-7>.
- [177] S. Shukla, S. Bhattacharjee, A.Z. Weber, M. Secanell, Experimental and Theoretical Analysis of Ink Dispersion Stability for Polymer Electrolyte Fuel Cell Applications, *J. Electrochem. Soc.* 164 (2017). <https://doi.org/10.1149/2.0961706jes>.
- [178] B. Szadkowski, A. Marzec, M. Zaborski, Use of carbon black as a reinforcing nano-filler in conductivity-reversible elastomer composites, *Polym. Test.* 81 (2020). <https://doi.org/10.1016/j.polymertesting.2019.106222>.
- [179] K. Liu, B. Wan, An SDS-PAGE based method for the quantification of carbon black in biological samples, *Analyst.* 145 (2020). <https://doi.org/10.1039/D0AN00046A>.
- [180] H. Li, X. Chen, D. Shen, F. Wu, R. Pleixats, J. Pan, Functionalized silica nanoparticles: Classification, synthetic approaches and recent advances in adsorption applications, *Nanoscale.* 13 (2021). <https://doi.org/10.1039/d1nr04048k>.
- [181] B.O. Alan, M. Barisik, Size and roughness dependent temperature effects on surface charge of silica nanoparticles, *Colloids Surfaces A Physicochem. Eng. Asp.* 629 (2021). <https://doi.org/10.1016/j.colsurfa.2021.127407>.
- [182] S. Varshney, A. Nigam, S.J. Pawar, N. Mishra, Structural, optical, cytotoxic, and anti-microbial properties of amorphous silica nanoparticles synthesised via hybrid method for biomedical applications, *Mater. Technol.* (2021). <https://doi.org/10.1080/10667857.2021.1959190>.
- [183] D. Du, Y. Jiang, J. Feng, L. Li, J. Feng, Facile synthesis of silica aerogel composites via ambient-pressure drying without surface modification or solvent exchange, *Vacuum.* 173 (2020). <https://doi.org/10.1016/j.vacuum.2019.109117>.
- [184] I.A. Rahman, V. Padavettan, Synthesis of Silica nanoparticles by Sol-Gel: Size-dependent properties, surface modification, and applications in silica-polymer nanocomposites a review, *J. Nanomater.* 2012 (2012). <https://doi.org/10.1155/2012/132424>.
- [185] D. Napierska, L.C.J. Thomassen, D. Lison, J.A. Martens, P.H. Hoet, The nanosilica hazard: Another variable entity, *Part. Fibre Toxicol.* 7 (2010). <https://doi.org/10.1186/1743-8977-7-39>.
- [186] T.H. Liou, C.C. Yang, Synthesis and surface characteristics of nanosilica produced

- from alkali-extracted rice husk ash, *Mater. Sci. Eng. B Solid-State Mater. Adv. Technol.* 176 (2011). <https://doi.org/10.1016/j.mseb.2011.01.007>.
- [187] G.A. Silva, Introduction to nanotechnology and its applications to medicine, *Surg. Neurol.* 61 (2004). <https://doi.org/10.1016/j.surneu.2003.09.036>.
- [188] F. Akhter, A.A. Rao, M.N. Abbasi, S.A. Wahocho, M.A. Mallah, H. Anees-ur-Rehman, Z.A. Chandio, A Comprehensive Review of Synthesis, Applications and Future Prospects for Silica Nanoparticles (SNPs), *Silicon.* (2022). <https://doi.org/10.1007/s12633-021-01611-5>.
- [189] M. Rezaeian, H. Afjoul, A. Shamloo, A. Maleki, N. Afjoul, Green synthesis of silica nanoparticles from olive residue and investigation of their anticancer potential, *Nanomedicine.* 16 (2021). <https://doi.org/10.2217/nnm-2021-0040>.
- [190] N. Surayah Osman, N. Sapawe, Waste Material As an Alternative Source of Silica Precursor in Silica Nanoparticle Synthesis-A Review, *Mater. Today Proc.* 19 (2019). <https://doi.org/10.1016/j.matpr.2019.11.132>.
- [191] A. Luthfiah, Y. Deawati, M. Lutfi Firdaus, I. Rahayu, D.R. Eddy, Silica from natural sources: A review on the extraction and potential application as a supporting photocatalytic material for antibacterial activity, *Sci. Technol. Indones.* 6 (2021). <https://doi.org/10.26554/sti.2021.6.3.144-155>.
- [192] S.N. Ishmah, M.D. Permana, M.L. Firdaus, D.R. Eddy, Extraction of Silica from Bengkulu Beach Sand using Alkali Fusion Method, *PENDIPA J. Sci. Educ.* 4 (2020). <https://doi.org/10.33369/pendipa.4.2.1-5>.
- [193] P.N.E. Diagboya, E.D. Dikio, Silica-based mesoporous materials; emerging designer adsorbents for aqueous pollutants removal and water treatment, *Microporous Mesoporous Mater.* 266 (2018). <https://doi.org/10.1016/j.micromeso.2018.03.008>.
- [194] K.L. Kadam, L.H. Forrest, W.A. Jacobson, Rice straw as a lignocellulosic resource: Collection, processing, transportation, and environmental aspects, *Biomass and Bioenergy.* 18 (2000). [https://doi.org/10.1016/S0961-9534\(00\)00005-2](https://doi.org/10.1016/S0961-9534(00)00005-2).
- [195] L.B. McCusker, F. Liebau, G. Engelhardt, Nomenclature of structural and compositional characteristics of ordered microporous and mesoporous materials with inorganic hosts: (IUPAC recommendations 2001), *Pure Appl. Chem.* 73 (2001). <https://doi.org/10.1351/pac200173020381>.
- [196] R.K. Iler, The chemistry of silica: solubility, polymerization, colloid and surface properties, and biochemistry, *Lavoisierfr.* (1979). <https://doi.org/10.1002/ange.19800920433>.

- [197] L. Tosheva, V.P. Valtchev, Nanozeolites: Synthesis, crystallization mechanism, and applications, *Chem. Mater.* 17 (2005). <https://doi.org/10.1021/cm047908z>.
- [198] The IUPAC Compendium of Chemical Terminology, (2019). <https://doi.org/10.1351/goldbook>.
- [199] A. van Blaaderen, A.P.M. Kentgens, Particle morphology and chemical microstructure of colloidal silica spheres made from alkoxysilanes, *J. Non. Cryst. Solids.* 149 (1992). [https://doi.org/10.1016/0022-3093\(92\)90064-Q](https://doi.org/10.1016/0022-3093(92)90064-Q).
- [200] W. Vogelsberger, J. Schmidt, F. Roelofs, Dissolution kinetics of oxidic nanoparticles: The observation of an unusual behaviour, *Colloids Surfaces A Physicochem. Eng. Asp.* 324 (2008). <https://doi.org/10.1016/j.colsurfa.2008.03.032>.
- [201] L.T. Zhuravlev, Concentration of Hydroxyl Groups on the Surface of Amorphous Silicas, *Langmuir.* 3 (1987). <https://doi.org/10.1021/la00075a004>.
- [202] C.O. Metin, L.W. Lake, C.R. Miranda, Q.P. Nguyen, Stability of aqueous silica nanoparticle dispersions, *J. Nanoparticle Res.* 13 (2011). <https://doi.org/10.1007/s11051-010-0085-1>.
- [203] T. Gholami, M. Salavati-Niasari, M. Bazarganipour, E. Noori, Synthesis and characterization of spherical silica nanoparticles by modified Stöber process assisted by organic ligand, *Superlattices Microstruct.* 61 (2013). <https://doi.org/10.1016/j.spmi.2013.06.004>.
- [204] B. Strachota, M. Šlouf, L. Matějka, Tremendous reinforcing, pore-stabilizing and response-accelerating effect of in situ generated nanosilica in thermoresponsive poly(N-isopropylacrylamide) cryogels, *Polym. Int.* 66 (2017). <https://doi.org/10.1002/pi.5406>.
- [205] L. Larreal de Hernandez, L. Anez-Borges, T. Woignier, A. Hafidi Alaoui, S. Calas-Etienne, F. Despetis, L. Bonnet, B. Colaiocco, S. Tahir, P. Dieudonné-George, Surface and porous textural properties of silica–wollastonite composites prepared by sol-gel process, *J. Sol-Gel Sci. Technol.* 90 (2019). <https://doi.org/10.1007/s10971-018-4874-9>.
- [206] P. Kaliyappan, A. Paulus, J. D’Haen, P. Samyn, Y. Uytendhouwen, N. Hafezkhiani, A. Bogaerts, V. Meynen, K. Elen, A. Hardy, M.K. Van Bael, Probing the impact of material properties of core-shell SiO<sub>2</sub>@TiO<sub>2</sub>spheres on the plasma-catalytic CO<sub>2</sub>dissociation using a packed bed DBD plasma reactor, *J. CO<sub>2</sub> Util.* 46 (2021). <https://doi.org/10.1016/j.jcou.2021.101468>.
- [207] M.E. Ali, M.M. Rahman, T.S. Dhahi, M. Kashif, M.S. Sarkar, W.J. Basirun, S.B.A. Hamid, S.K. Bhargava, M. Ramadan, Nanostructured Materials: Bioengineering Platforms for Sensing Nucleic Acids, *Encycl. Smart Mater.* (2022).

- <https://doi.org/10.1016/b978-0-12-815732-9.00154-6>.
- [208] A. Ballester-Caudet, L. Hakobyan, Y. Moliner-Martinez, C. Molins-Legua, P. Campíns-Falcó, Ionic-liquid doped polymeric composite as passive colorimetric sensor for meat freshness as a use case, *Talanta*. 223 (2021). <https://doi.org/10.1016/j.talanta.2020.121778>.
- [209] D. Saber, M.A. Abd El-baky, M.A. Attia, Advanced Fiber Metal Laminates Filled with Silicon Dioxide Nanoparticles with Enhanced Mechanical Properties, *Fibers Polym.* 22 (2021). <https://doi.org/10.1007/s12221-021-0192-x>.
- [210] S. Sprenger, Epoxy resin composites with surface-modified silicon dioxide nanoparticles: A review, *J. Appl. Polym. Sci.* 130 (2013). <https://doi.org/10.1002/app.39208>.
- [211] D.G. Gomes, J.C. Pieretti, W.R. Rolim, A.B. Seabra, H.C. Oliveira, Advances in nano-based delivery systems of micronutrients for a greener agriculture, *Adv. Nano-Fertilizers Nano-Pesticides Agric.* (2021, pp 111-143). <https://doi.org/10.1016/b978-0-12-820092-6.00005-7>.
- [212] H. Huang, W. Feng, Y. Chen, J. Shi, Inorganic nanoparticles in clinical trials and translations, *Nano Today*. 35 (2020). <https://doi.org/10.1016/j.nantod.2020.100972>.
- [213] P.N. Minoofar, B.S. Dunn, J.I. Zink, Multiply doped nanostructured silicate sol-gel thin films: Spatial segregation of dopants, energy transfer, and distance measurements, *J. Am. Chem. Soc.* 127 (2005). <https://doi.org/10.1021/ja045185e>.
- [214] J.A. García-Calzón, M.E. Díaz-García, Synthesis and analytical potential of silica nanotubes, *TrAC Trends Anal. Chem.* 35 (2012). <https://doi.org/10.1016/j.trac.2012.01.003>.
- [215] Y. Zou, Y. Hu, Z. Shen, L. Yao, D. Tang, S. Zhang, S. Wang, B. Hu, G. Zhao, X. Wang, Application of aluminosilicate clay mineral-based composites in photocatalysis, *J. Environ. Sci.* 115 (2022). <https://doi.org/10.1016/j.jes.2021.07.015>.
- [216] A.C. Lopes, P. Martins, S. Lanceros-Mendez, Aluminosilicate and aluminosilicate based polymer composites: Present status, applications and future trends, *Prog. Surf. Sci.* 89 (2014). <https://doi.org/10.1016/j.progsurf.2014.08.002>.
- [217] S. Pavlidou, C.D. Pappaspyrides, A review on polymer-layered silicate nanocomposites, *Prog. Polym. Sci.* 33 (2008). <https://doi.org/10.1016/j.progpolymsci.2008.07.008>.
- [218] L.F. Atyaksheva, I.A. Kasyanov, Halloysite, Natural Aluminosilicate Nanotubes: Structural Features and Adsorption Properties (A Review), *Pet. Chem.* 61 (2021).

- <https://doi.org/10.1134/S0965544121080119>.
- [219] M. Massaro, G. Lazzara, R. Noto, S. Riela, Halloysite nanotubes: a green resource for materials and life sciences, *Rend. Lincei*. 31 (2020). <https://doi.org/10.1007/s12210-020-00886-x>.
- [220] G. Zhuang, F. Rodrigues, Z. Zhang, M.G. Fonseca, P. Walter, M. Jaber, Dressing protective clothing: stabilizing alizarin/halloysite hybrid pigment and beyond, *Dye. Pigment*. 166 (2019). <https://doi.org/10.1016/j.dyepig.2019.03.006>.
- [221] P. Yuan, D. Tan, F. Annabi-Bergaya, Properties and applications of halloysite nanotubes: Recent research advances and future prospects, *Appl. Clay Sci*. 112–113 (2015). <https://doi.org/10.1016/j.clay.2015.05.001>.
- [222] Y. Yang, Y. Chen, F. Leng, L. Huang, Z. Wang, W. Tian, Recent advances on surface modification of halloysite nanotubes for multifunctional applications, *Appl. Sci*. 7 (2017). <https://doi.org/10.3390/app7121215>.
- [223] M.C. Chao, H.P. Lin, C.Y. Mou, Controlling the morphology and mesostructural orderness of the mesoporous silica nanoparticles, *Chem. Lett*. 33 (2004). <https://doi.org/10.1246/cl.2004.672>.
- [224] B.G. Trewyn, C.M. Whitman, V.S.Y. Lin, Morphological control of room-temperature ionic liquid templated mesoporous silica nanoparticles for controlled release of antibacterial agents, *Nano Lett*. 4 (2004). <https://doi.org/10.1021/nl048774r>.
- [225] S. Rahmani, J.O. Durand, C. Charnay, L. Lichon, M. Férid, M. Garcia, M. Gary-Bobo, Synthesis of mesoporous silica nanoparticles and nanorods: Application to doxorubicin delivery, *Solid State Sci*. 68 (2017). <https://doi.org/10.1016/j.solidstatesciences.2017.04.003>.
- [226] R. Narayan, U.Y. Nayak, A.M. Raichur, S. Garg, Mesoporous silica nanoparticles: A comprehensive review on synthesis and recent advances, *Pharmaceutics*. 10 (2018). <https://doi.org/10.3390/pharmaceutics10030118>.
- [227] F. Yan, X. Lin, B. Su, Vertically ordered silica mesochannel films: Electrochemistry and analytical applications, *Analyst*. 141 (2016). <https://doi.org/10.1039/c6an00146g>.
- [228] J. He, S. Fujikawa, T. Kunitake, A. Nakao, Preparation of porous and nonporous silica nanofilms from aqueous sodium silicate, *Chem. Mater*. 15 (2003). <https://doi.org/10.1021/cm034253d>.
- [229] V. Urbanova, A. Walcarius, Vertically-aligned mesoporous silica films, *Zeitschrift Fur Anorg. Und Allg. Chemie*. 640 (2014). <https://doi.org/10.1002/zaac.201300442>.

- [230] Q. Abbas, Understanding the UV-Vis Spectroscopy for Nanoparticles, *J. Nanomater. Mol. Nanotechnol.* 8 (2019). <https://doi.org/10.4172/2324-8777.1000268>
- [231] A. Reza, A.S. M. Noor, M. Maarof, Application of Surface Plasmon Resonance Based on a Metal Nanoparticle, *Plasmon. Princ. Appl.* (2012). <https://doi.org/10.5772/51219>.
- [232] V. Amendola, R. Pilot, M. Frasconi, O.M. Maragò, M.A. Iati, Surface plasmon resonance in gold nanoparticles: A review, *J. Phys. Condens. Matter.* 29 (2017). <https://doi.org/10.1088/1361-648X/aa60f3>.
- [233] M. Abdolkarimi-Mahabadi, A. Bayat, A. Mohammadi, Use of UV-Vis Spectrophotometry for Characterization of Carbon Nanostructures: a Review, *Theor. Exp. Chem.* 57 (2021). <https://doi.org/10.1007/s11237-021-09687-1>.
- [234] A.R. Barron, Physical methods in chemistry and nano science, *Open Stax.* (2012).
- [235] J. Cao, T. Sun, K.T.V. Grattan, Gold nanorod-based localized surface plasmon resonance biosensors: A review, *Sensors Actuators, B Chem.* 195 (2014). <https://doi.org/10.1016/j.snb.2014.01.056>.
- [236] C.F. Phelps, Dynamic light scattering, with application to chemistry, biology and physics, *Biochem. Educ.* 5 (1977). [https://doi.org/10.1016/0307-4412\(77\)90025-5](https://doi.org/10.1016/0307-4412(77)90025-5).
- [237] I. Alghoraibi, C. Soukkaie, R. Zein, A. Alahmad, J.G. Walter, M. Daghestani, Aqueous extract of *Eucalyptus camaldulensis* leaves as reducing and capping agent in biosynthesis of silver nanoparticles, *Inorg. Nano-Metal Chem.* 50 (2020). <https://doi.org/10.1080/24701556.2020.1728315>.
- [238] G. Arya, R.M. Kumari, N. Gupta, A. Kumar, R. Chandra, S. Nimesh, Green synthesis of silver nanoparticles using *Prosopis juliflora* bark extract: reaction optimization, antimicrobial and catalytic activities, *Artif. Cells, Nanomedicine Biotechnol.* 46 (2018). <https://doi.org/10.1080/21691401.2017.1354302>.
- [239] S. Khademi, A. Shakeri-Zadeh, R. Solgi, H. Azimian, H. Ghadiri, Observation of targeted gold nanoparticles in nasopharyngeal tumour nude mice model through dual-energy computed tomography, *IET Nanobiotechnology.* 15 (2021). <https://doi.org/10.1049/nbt2.12035>.
- [240] Y. Bo, J. Cui, Y. Cai, S. Xu, Preparation and characterization of poly(methyl methacrylate) and poly(maleic anhydride-co-diallyl phthalate) grafted carbon black through  $\gamma$ -ray irradiation, *Radiat. Phys. Chem.* 119 (2016). <https://doi.org/10.1016/j.radphyschem.2015.11.005>.
- [241] B. Bocca, E. Sabbioni, I. Mičetić, A. Alimonti, F. Petrucci, Size and metal composition characterization of nano- and microparticles in tattoo inks by a combination of



- analytical techniques, *J. Anal. At. Spectrom.* 32 (2017). <https://doi.org/10.1039/c6ja00210b>.
- [242] W. Zhang, Y. Wang, Z. Li, W. Wang, H. Sun, M. Liu, Synthesis and Characterization of Hyaluronic Acid Modified Colloidal Mesoporous Silica Nanoparticles, *IOP Conf. Ser. Mater. Sci. Eng.* 275 (2018). <https://doi.org/10.1088/1757-899X/275/1/012009>.
- [243] Y. Wang, H. Gong, W. Wang, H. Sun, M. Liu, Synthesis and characterization of amino-terminated polyethylene glycol functionalized mesoporous silica nanoparticles, *Adv. Intell. Syst. Comput* (2016). <https://doi.org/10.2991/icmia-16.2016.15>.
- [244] S. Betancur, J.C. Carmona, N.N. Nassar, C.A. Franco, F.B. Cortés, Role of Particle Size and Surface Acidity of Silica Gel Nanoparticles in Inhibition of Formation Damage by Asphaltene in Oil Reservoirs, *Ind. Eng. Chem. Res.* 55 (2016). <https://doi.org/10.1021/acs.iecr.6b01187>.
- [245] J. Maya-Cornejo, R. Carrera-Cerritos, D. Sebastián, J. Ledesma-García, L.G. Arriaga, A.S. Aricò, V. Baglio, PtCu catalyst for the electro-oxidation of ethanol in an alkaline direct alcohol fuel cell, *Int. J. Hydrogen Energy.* 42 (2017). <https://doi.org/10.1016/j.ijhydene.2017.07.226>.
- [246] C. Di Dong, C.W. Chen, C.M. Hung, Preparing carbon-black-coated magnetite nanoparticles: Fabrication, characterization, and heterogeneous persulfate oxidation of methylene blue, *Desalin. Water Treat.* 63 (2017). <https://doi.org/10.5004/dwt.2017.0316>.
- [247] V.G. Milt, S. Ivanova, O. Sanz, M.I. Domínguez, A. Corrales, J.A. Odriozola, M.A. Centeno, Au/TiO<sub>2</sub> supported on ferritic stainless steel monoliths as CO oxidation catalysts, *Appl. Surf. Sci.* 270 (2013). <https://doi.org/10.1016/j.apsusc.2012.12.159>.
- [248] M. Rajabzadeh, R. Khalifeh, H. Eshghi, A. Hafizi, Design and synthesis of CuO@SiO<sub>2</sub> multi-yolk@shell and its application as a new catalyst for CO<sub>2</sub> fixation reaction under solventless condition, *J. Ind. Eng. Chem.* 89 (2020). <https://doi.org/10.1016/j.jiec.2020.06.020>.
- [249] J. Seo, D. Cha, K. Takanabe, J. Kubota, K. Domen, Electrodeposited ultrafine NbO<sub>x</sub>, ZrO<sub>x</sub>, and TaO<sub>x</sub> nanoparticles on carbon black supports for oxygen reduction electrocatalysts in acidic media, *ACS Catal.* 3 (2013). <https://doi.org/10.1021/cs400525u>.
- [250] A. Rautela, J. Rani, M. Debnath (Das), Green synthesis of silver nanoparticles from *Tectona grandis* seeds extract: characterization and mechanism of antimicrobial action on different microorganisms, *J. Anal. Sci. Technol.* 10 (2019). <https://doi.org/10.1186/s40543-018-0163-z>.

- [251] S. Shankar, A.A. Oun, J.W. Rhim, Preparation of antimicrobial hybrid nano-materials using regenerated cellulose and metallic nanoparticles, *Int. J. Biol. Macromol.* 107 (2018). <https://doi.org/10.1016/j.ijbiomac.2017.08.129>.
- [252] N.I. Hulkoti, T.C. Taranath, Biosynthesis of nanoparticles using microbes-A review, *Colloids Surfaces B Biointerfaces.* 121 (2014). <https://doi.org/10.1016/j.colsurfb.2014.05.027>.
- [253] M.F. Smiechowski, V.F. Lvovich, Characterization of non-aqueous dispersions of carbon black nanoparticles by electrochemical impedance spectroscopy, *J. Electroanal. Chem.* 577 (2005). <https://doi.org/10.1016/j.jelechem.2004.11.015>.
- [254] L. Ejenstam, A. Swerin, J. Pan, P.M. Claesson, Corrosion protection by hydrophobic silica particle-polydimethylsiloxane composite coatings, *Corros. Sci.* 99 (2015). <https://doi.org/10.1016/j.corsci.2015.06.018>.
- [255] P.J. Wibawa, M. Nur, M. Asy'ari, H. Nur, SEM, XRD and FTIR analyses of both ultrasonic and heat generated activated carbon black microstructures, *Heliyon.* 6 (2020). <https://doi.org/10.1016/j.heliyon.2020.e03546>.
- [256] E.A. Grulke, S.B. Rice, J.C. Xiong, K. Yamamoto, T.H. Yoon, K. Thomson, M. Saffaripour, G.J. Smallwood, J.W. Lambert, A.J. Stromberg, R. Macy, N.J. Briot, D. Qian, Size and shape distributions of carbon black aggregates by transmission electron microscopy, *Carbon.* 130 (2018). <https://doi.org/10.1016/j.carbon.2018.01.030>.
- [257] K. Tiede, A.B.A. Boxall, S.P. Tear, J. Lewis, H. David, M. Hassellöv, Detection and characterization of engineered nanoparticles in food and the environment, *Food Addit. Contam. - Part A Chem. Anal. Control. Expo. Risk Assess.* 25 (2008). <https://doi.org/10.1080/02652030802007553>.
- [258] R.A. González-Fuenzalida, Y. Moliner-Martínez, C. Molins-Legua, V. Parada-Artigues, J. Verdú-Andrés, P. Campins-Falcó, New Tools for Characterizing Metallic Nanoparticles: AgNPs, A Case Study, *Anal. Chem.* 88 (2016). <https://doi.org/10.1021/acs.analchem.5b04751>.
- [259] T. Ito, L. Sun, M.A. Bevan, R.M. Crooks, Comparison of nanoparticle size and electrophoretic mobility measurements using a carbon-nanotube-based coulter counter, dynamic light scattering, transmission electron microscopy, and phase analysis light scattering, *Langmuir.* 20 (2004). <https://doi.org/10.1021/la049524t>.
- [260] R.A. González-Fuenzalida, Y. Moliner-Martínez, C. Molins-Legua, P. Campins-Falcó, Miniaturized liquid chromatography coupled on-line to in-tube solid-phase microextraction for characterization of metallic nanoparticles using plasmonic measurements. A tutorial, *Anal. Chim. Acta.* 1045 (2019). <https://doi.org/10.1016/j.aca.2018.07.073>.

- [261] J. McClements, M. Zhang, N. Radacsi, V. Koutsos, Measuring the interactions between carbon black nanoparticles and latex thin films in aqueous media using AFM force spectroscopy, *Colloids Surfaces A Physicochem. Eng. Asp.* 603 (2020). <https://doi.org/10.1016/j.colsurfa.2020.124920>.
- [262] J.B. Langford, I.S. Lurie, Use of micro, capillary, and nano liquid chromatography for forensic analysis, *J. Sep. Sci.* 45 (2022). <https://doi.org/10.1002/jssc.202100631>.
- [263] C.L. Arthur, J. Pawliszyn, Solid Phase Microextraction with Thermal Desorption Using Fused Silica Optical Fibers, *Anal. Chem.* 62 (1990). <https://doi.org/10.1021/ac00218a019>.
- [264] K. Mizuno, H. Kataoka, Analysis of urinary 8-isoprostane as an oxidative stress biomarker by stable isotope dilution using automated online in-tube solid-phase microextraction coupled with liquid chromatography-tandem mass spectrometry, *J. Pharm. Biomed. Anal.* 112 (2015). <https://doi.org/10.1016/j.jpba.2015.04.020>.
- [265] S.L. Wang, S. Hu, H. Xu, Analysis of aldehydes in human exhaled breath condensates by in-tube SPME-HPLC, *Anal. Chim. Acta.* 900 (2015). <https://doi.org/10.1016/j.aca.2015.10.018>.
- [266] A. Masiá, Y. Moliner-Martinez, M. Muñoz-Ortuño, Y. Pico, P. Campíns-Falcó, Multiresidue analysis of organic pollutants by in-tube solid phase microextraction coupled to ultra-high performance liquid chromatography-electrospray-tandem mass spectrometry, *J. Chromatogr. A.* 1306 (2013). <https://doi.org/10.1016/j.chroma.2013.07.019>.
- [267] M.E. Schimpf, K. Caldwell, J.C. Giddings, *Field flow fractionation handbook*, Wiley-Interscience, (2000).
- [268] G. Lespes, V. De Carsalade Du Pont, Field-flow fractionation for nanoparticle characterization, *J. Sep. Sci.* 45 (2022). <https://doi.org/10.1002/jssc.202100595>.
- [269] A.I. Ivaneev, M.S. Ermolin, P.S. Fedotov, S. Faucher, G. Lespes, Sedimentation Field-flow Fractionation in Thin Channels and Rotating Coiled Columns: From Analytical to Preparative Scale Separations, *Sep. Purif. Rev.* 50 (2021). <https://doi.org/10.1080/15422119.2020.1784940>.
- [270] S. Tadjiki, M.D. Montañó, S. Assemi, A. Barber, J. Ranville, R. Beckett, Measurement of the Density of Engineered Silver Nanoparticles Using Centrifugal FFF-TEM and Single Particle ICP-MS, *Anal. Chem.* 89 (2017). <https://doi.org/10.1021/acs.analchem.7b00652>.
- [271] A.Y. Jassim, J. Wang, K.W. Chung, F. Loosli, A. Chanda, G.I. Scott, M. Baalousha, Comparative assessment of the fate and toxicity of chemically and biologically

- synthesized silver nanoparticles to juvenile clams, *Colloids Surfaces B Biointerfaces*. 209 (2022). <https://doi.org/10.1016/j.colsurfb.2021.112173>.
- [272] M.V. Taboada-López, D. Bartczak, S. Cuello-Núñez, H. Goenaga-Infante, P. Bermejo-Barrera, A. Moreda-Piñeiro, F4-UV-ICP-MS for detection and quantification of silver nanoparticles in seafood after enzymatic hydrolysis, *Talanta*. 232 (2021). <https://doi.org/10.1016/j.talanta.2021.122504>.
- [273] D. Itabashi, R. Murao, S. Taniguchi, K. Mizukami, H. Takagi, M. Kimura, Determination of size distribution of nanoparticles using asymmetric flow field-flow fractionation (AF4), *ISIJ Int.* 60 (2020). <https://doi.org/10.2355/isijinternational.ISIJINT-2019-387>.
- [274] J. Lee, E.S. Goda, J. Choi, J. Park, S. Lee, Synthesis and characterization of elution behavior of nonspherical gold nanoparticles in asymmetrical flow field-flow fractionation (AsF4FFF), *J. Nanoparticle Res.* 22 (2020). <https://doi.org/10.1007/s11051-020-04987-4>.
- [275] R. Drexel, V. Sogne, M. Dinkel, F. Meier, T. Klein, Asymmetrical flow field-flow fractionation for sizing of gold nanoparticles in suspension, *J. Vis. Exp.* 2020 (2020). <https://doi.org/10.3791/61757>.
- [276] B. Bocca, B. Battistini, F. Petrucci, Silver and gold nanoparticles characterization by SP-ICP-MS and AF4-FFF-MALS-UV-ICP-MS in human samples used for biomonitoring, *Talanta*. 220 (2020). <https://doi.org/10.1016/j.talanta.2020.121404>.
- [277] S. López-Sanz, N.R. Fariñas, R. del C.R. Martín-Doimeadios, Á. Ríos, Analytical strategy based on asymmetric flow field flow fractionation hyphenated to ICP-MS and complementary techniques to study gold nanoparticles transformations in cell culture medium, *Anal. Chim. Acta.* 1053 (2019). <https://doi.org/10.1016/j.aca.2018.11.053>.
- [278] F. Giorgi, J.M. Curran, D. Gilliland, R. La Spina, M. Whelan, E.A. Patterson, Limitations of Nanoparticles Size Characterization by Asymmetric Flow Field-Fractionation Coupled with Online Dynamic Light Scattering, *Chromatographia*. 84 (2021). <https://doi.org/10.1007/s10337-020-03997-7>.
- [279] V. Nischwitz, N. Gottselig, A. Missong, E. Klumpp, M. Braun, Extending the capabilities of field flow fractionation online with ICP-MS for the determination of particulate carbon in latex and charcoal, *J. Anal. At. Spectrom.* 33 (2018). <https://doi.org/10.1039/c8ja00101d>.
- [280] W. Kim, J. Bae, C.H. Eum, J. Jung, S. Lee, Study on dispersibility of thermally stable carbon black particles in ink using asymmetric flow field-flow fractionation (AsF4FFF), *Microchem. J.* 142 (2018). <https://doi.org/10.1016/j.microc.2018.06.035>.

- [281] Y.H. Park, W.S. Kim, D.W. Lee, Size analysis of industrial carbon blacks by sedimentation and flow field-flow fractionation, *Anal. Bioanal. Chem.* 375 (2003). <https://doi.org/10.1007/s00216-002-1722-z>.
- [282] S. Han, J. Choi, Y. Yoo, E.C. Jung, S. Lee, Size Monitoring in the Synthesis of Silica Nanoparticles Using Asymmetrical Flow Field-Flow Fractionation (AF4), *Bull. Korean Chem. Soc.* 37 (2016). <https://doi.org/10.1002/bkcs.10675>.
- [283] H. Kato, A. Nakamura, H. Banno, Determination of number-based size distribution of silica particles using centrifugal field-flow fractionation, *J. Chromatogr. A.* 1602 (2019). <https://doi.org/10.1016/j.chroma.2019.05.055>.
- [284] C. Contado, J. Mejia, O. Lozano García, J.P. Piret, E. Dumortier, O. Toussaint, S. Lucas, Physicochemical and toxicological evaluation of silica nanoparticles suitable for food and consumer products collected by following the EC recommendation Field- and Flow-based Separations, *Anal. Bioanal. Chem.* 408 (2016). <https://doi.org/10.1007/s00216-015-9101-8>.
- [285] E. Alasonati, T. Caebergs, J. Pétry, N. Sebaihi, P. Fiscaro, N. Feltin, Size measurement of silica nanoparticles by Asymmetric Flow Field-Flow Fractionation coupled to Multi-Angle Light Scattering: A comparison exercise between two metrological institutes, *J. Chromatogr. A.* 1638 (2021). <https://doi.org/10.1016/j.chroma.2020.461859>.
- [286] B. Li, S.L. Chua, A.L. Ch'ng, D. Yu, S.P. Koh, H. Phang, P.K.T. Chiew, An effective approach for size characterization and mass quantification of silica nanoparticles in coffee creamer by AF4-ICP-MS, *Anal. Bioanal. Chem.* 412 (2020). <https://doi.org/10.1007/s00216-020-02770-x>.
- [287] M.S. McKee, J. Filser, Impacts of metal-based engineered nanomaterials on soil communities, *Environ. Sci. Nano.* 3 (2016). <https://doi.org/10.1039/c6en00007j>.
- [288] J.D. Judy, J.M. Unrine, P.M. Bertsch, Evidence for biomagnification of gold nanoparticles within a terrestrial food chain, *Environ. Sci. Technol.* 45 (2011). <https://doi.org/10.1021/es103031a>.
- [289] A. Braun, E. Klumpp, R. Azzam, C. Neukum, Transport and deposition of stabilized engineered silver nanoparticles in water saturated loamy sand and silty loam, *Sci. Total Environ.* 535 (2015). <https://doi.org/10.1016/j.scitotenv.2014.12.023>.
- [290] M. Hoppe, R. Mikutta, J. Utermann, W. Duijnsveld, G. Guggenberger, Retention of sterically and electrosterically stabilized silver nanoparticles in soils, *Environ. Sci. Technol.* 48 (2014). <https://doi.org/10.1021/es5026189>.
- [291] H. Ebrahimzadeh, N. Tavassoli, M.M. Amini, Y. Fazaeli, H. Abedi, Determination of

- very low levels of gold and palladium in wastewater and soil samples by atomic absorption after preconcentration on modified MCM-48 and MCM-41 silica, *Talanta*. 81 (2010). <https://doi.org/10.1016/j.talanta.2010.02.007>.
- [292] M. Grzelczak, J. Pérez-Juste, P. Mulvaney, L.M. Liz-Marzán, Shape control in gold nanoparticle synthesis, *Chem. Soc. Rev.* 37 (2008). <https://doi.org/10.1039/b711490g>.
- [293] S.E. Lohse, N.S. Abadeer, M. Zoloty, J.C. White, L.A. Newman, C.J. Murphy, Nanomaterial Probes in the Environment: Gold Nanoparticle Soil Retention and Environmental Stability as a Function of Surface Chemistry, *ACS Sustain. Chem. Eng.* 5 (2017). <https://doi.org/10.1021/acssuschemeng.7b02622>.
- [294] A.D. Maynard, R.J. Aitken, T. Butz, V. Colvin, K. Donaldson, G. Oberdörster, M.A. Philbert, J. Ryan, A. Seaton, V. Stone, S.S. Tinkle, L. Tran, N.J. Walker, D.B. Warheit, Safe handling of nanotechnology, *Nature*. 444 (2006). <https://doi.org/10.1038/444267a>.
- [295] E. Navarro, A. Baun, R. Behra, N.B. Hartmann, J. Filser, A.J. Miao, A. Quigg, P.H. Santschi, L. Sigg, Environmental behavior and ecotoxicity of engineered nanoparticles to algae, plants, and fungi, *Ecotoxicology*. 17 (2008). <https://doi.org/10.1007/s10646-008-0214-0>.
- [296] A.L. Rodd, M.A. Creighton, C.A. Vaslet, J.R. Rangel-Mendez, R.H. Hurt, A.B. Kane, Effects of surface-engineered nanoparticle-based dispersants for marine oil spills on the model organism *Artemia franciscana*, *Environ. Sci. Technol.* 48 (2014). <https://doi.org/10.1021/es500892m>.
- [297] N. Seiler, J.G. Delcros, J.P. Moulinoux, Polyamine transport in mammalian cells. An update, *Int. J. Biochem. Cell Biol.* 28 (1996). [https://doi.org/10.1016/1357-2725\(96\)00021-0](https://doi.org/10.1016/1357-2725(96)00021-0).
- [298] K. Igarashi, K. Kashiwagi, Modulation of cellular function by polyamines, *Int. J. Biochem. Cell Biol.* 42 (2010). <https://doi.org/10.1016/j.biocel.2009.07.009>.
- [299] U. Bachrach, Polyamines as markers of malignancy, *Prog. Drug Res.* 39 (1992). [https://doi.org/10.1007/978-3-0348-7144-0\\_2](https://doi.org/10.1007/978-3-0348-7144-0_2).
- [300] B.E.K. Klein, J.A. McElroy, R. Klein, K.P. Howard, K.E. Lee, Nitrate-nitrogen levels in rural drinking water: Is there an association with age-related macular degeneration?, *J. Environ. Sci. Heal. - Part A Toxic/Hazardous Subst. Environ. Eng.* 48 (2013). <https://doi.org/10.1080/10934529.2013.823323>.
- [301] K.M. Wollin, H.H. Dieter, Toxicological guidelines for monocyclic nitro-, amino- and aminonitroaromatics, nitramines, and nitrate esters in drinking water, *Arch. Environ. Contam. Toxicol.* 49 (2005). <https://doi.org/10.1007/s00244-004-0112-2>.

- [302] S. Gao, C. Li, C. Jia, H. Zhang, Q. Guan, X. Wu, J. Wang, M. Lv, Health risk assessment of groundwater nitrate contamination: a case study of a typical karst hydrogeological unit in East China, *Environ. Sci. Pollut. Res.* 27 (2020). <https://doi.org/10.1007/s11356-019-07075-w>.
- [303] M. Donner, R. Gohier, H. de Vries, A new circular business model typology for creating value from agro-waste, *Sci. Total Environ.* 716 (2020). <https://doi.org/10.1016/j.scitotenv.2020.137065>.
- [304] A.J. Frank, N. Cathcart, K.E. Maly, V. Kitaev, Synthesis of silver nanoprisms with variable size and investigation of their optical properties: A first-year undergraduate experiment exploring plasmonic nanoparticles, *J. Chem. Educ.* 87 (2010). <https://doi.org/10.1021/ed100166g>.
- [305] J.E. Millstone, S.J. Hurst, G.S. Métraux, J.I. Cutler, C.A. Mirkin, Colloidal gold and silver triangular nanoprisms, *Small.* 5 (2009). <https://doi.org/10.1002/smll.200801480>.
- [306] B. Katana, D. Takács, E. Csapó, T. Szabó, A. Jamnik, I. Szilagyi, Ion Specific Effects on the Stability of Halloysite Nanotube Colloids - Inorganic Salts versus Ionic Liquids, *J. Phys. Chem. B.* 124 (2020). <https://doi.org/10.1021/acs.jpcc.0c07885>.
- [307] X. Guo, J. Wang, Comparison of linearization methods for modeling the Langmuir adsorption isotherm, *J. Mol. Liq.* 296 (2019). <https://doi.org/10.1016/j.molliq.2019.111850>.
- [308] A.K. Singh, Nanoparticle Ecotoxicology, *Eng. Nanoparticles*, (2016). <https://doi.org/10.1016/b978-0-12-801406-6.00008-x>.
- [309] M.A.E. de Franco, C.B. de Carvalho, M.M. Bonetto, R. de Pelegrini Soares, L.A. Féris, Diclofenac removal from water by adsorption using activated carbon in batch mode and fixed-bed column: Isotherms, thermodynamic study and breakthrough curves modeling, *J. Clean. Prod.* 181 (2018). <https://doi.org/10.1016/j.jclepro.2018.01.138>.
- [310] H. Radnia, A.A. Ghoreyshi, H. Younesi, M. Masomi, K. Pirzadeh, Adsorption of Fe(II) from aqueous phase by chitosan: Application of physical models and artificial neural network for prediction of breakthrough, *Int. J. Eng. Trans. B Appl.* 26 (2013). <https://doi.org/10.5829/idosi.ije.2013.26.08b.06>.
- [311] P. Serra-Mora, N. Jornet-Martinez, Y. Moliner-Martinez, P. Campíns-Falcó, In tube-solid phase microextraction-nano liquid chromatography: Application to the determination of intact and degraded polar triazines in waters and recovered struvite, *J. Chromatogr. A.* 1513 (2017). <https://doi.org/10.1016/j.chroma.2017.07.053>.

- [312] L. Calzolari, D. Gilliland, C.P. García, F. Rossi, Separation and characterization of gold nanoparticle mixtures by flow-field-flow fractionation, *J. Chromatogr. A*. 1218 (2011). <https://doi.org/10.1016/j.chroma.2011.01.017>.
- [313] A.R. Jochem, G.N. Ankah, L.A. Meyer, S. Elsenberg, C. Johann, T. Kraus, Colloidal Mechanisms of Gold Nanoparticle Loss in Asymmetric Flow Field-Flow Fractionation, *Anal. Chem.* 88 (2016). <https://doi.org/10.1021/acs.analchem.6b02397>.
- [314] Y. jie Chang, Y. hsin Shih, C.H. Su, H.C. Ho, Comparison of three analytical methods to measure the size of silver nanoparticles in real environmental water and wastewater samples, *J. Hazard. Mater.* 322 (2017). <https://doi.org/10.1016/j.jhazmat.2016.03.030>.
- [315] Y. Yang, C.L. Long, H.P. Li, Q. Wang, Z.G. Yang, Analysis of silver and gold nanoparticles in environmental water using single particle-inductively coupled plasma-mass spectrometry, *Sci. Total Environ.* 563–564 (2016). <https://doi.org/10.1016/j.scitotenv.2015.12.150>.
- [316] R. Baiee, Z. Liu, L. Li, Understanding the stability and durability of laser-generated Ag nanoparticles and effects on their antibacterial activities, *Adv. Nat. Sci. Nanosci. Nanotechnol.* 10 (2019). <https://doi.org/10.1088/2043-6254/ab2e6e>.
- [317] R.A. González-Fuenzalida, Y. Moliner-Martínez, M. González-Béjar, C. Molins-Legua, J. Verdú-Andres, J. Pérez-Prieto, P. Campins-Falcó, In situ colorimetric quantification of silver cations in the presence of silver nanoparticles, *Anal. Chem.* 85 (2013). <https://doi.org/10.1021/ac402822d>.
- [318] M.G. Espinoza, M.L. Hinks, A.M. Mendoza, D.P. Pullman, K.I. Peterson, Kinetics of halide-induced decomposition and aggregation of silver nanoparticles, *J. Phys. Chem. C*. 116 (2012). <https://doi.org/10.1021/jp3011926>.
- [319] X. Li, J.J. Lenhart, H.W. Walker, Dissolution-accompanied aggregation kinetics of silver nanoparticles, *Langmuir*. 26 (2010). <https://doi.org/10.1021/la101768n>.
- [320] M. Tejamaya, I. Römer, R.C. Merrifield, J.R. Lead, Stability of citrate, PVP, and PEG coated silver nanoparticles in ecotoxicology media, *Environ. Sci. Technol.* 46 (2012). <https://doi.org/10.1021/es2038596>.
- [321] M. Baalousha, Y. Nur, I. Römer, M. Tejamaya, J.R. Lead, Effect of monovalent and divalent cations, anions and fulvic acid on aggregation of citrate-coated silver nanoparticles, *Sci. Total Environ.* 454–455 (2013). <https://doi.org/10.1016/j.scitotenv.2013.02.093>.
- [322] J.-P. Hsu, B.-T. Liu, Effect of Particle Size on Critical Coagulation Concentration, *J. Colloid Interface Sci.* 198 (1998). <https://doi.org/10.1006/jcis.1997.5275>.



- [323] P.C. Hiemenz, R. Rajagopalan, Principles of colloid and surface chemistry., Marcel Dekker, (1997).
- [324] D.C. António, C. Cascio, Jakšić, D. Jurašin, D.M. Lyons, A.J.A. Nogueira, F. Rossi, L. Calzolari, Assessing silver nanoparticles behaviour in artificial seawater by mean of AF4 and spICP-MS, *Mar. Environ. Res.* 111 (2015). <https://doi.org/10.1016/j.marenvres.2015.05.006>.
- [325] J. Bot, A., Benites, The Soil Importance of Soil Inorganic Matter Key to Drought-Resistant Soil and Sustained Food an Production, Food and Agriculture Organization of the United Nations, (2005).
- [326] G.P. Gillman, L.C. Bell, Soil solution studies on weathered soils from tropical north queensland, *Aust. J. Soil Res.* 16 (1978). <https://doi.org/10.1071/SR9780067>.
- [327] A.K. Alva, M.E. Sumner, W.P. Miller, Relationship between ionic strength and electrical conductivity for soil solutions, *Soil Sci.* 152 (1991). <https://doi.org/10.1097/00010694-199110000-00001>.
- [328] Y. Liang, S.A. Bradford, J. Simunek, H. Vereecken, E. Klumpp, Sensitivity of the transport and retention of stabilized silver nanoparticles to physicochemical factors, *Water Res.* 47 (2013). <https://doi.org/10.1016/j.watres.2013.02.025>.
- [329] Y. Liang, S.A. Bradford, J. Simunek, M. Heggen, H. Vereecken, E. Klumpp, Retention and remobilization of stabilized silver nanoparticles in an undisturbed loamy sand soil, *Environ. Sci. Technol.* 47 (2013). <https://doi.org/10.1021/es402046u>.
- [330] O. Furman, S. Usenko, B.L.T. Lau, Relative importance of the humic and fulvic fractions of natural organic matter in the aggregation and deposition of silver nanoparticles, *Environ. Sci. Technol.* 47 (2013). <https://doi.org/10.1021/es303275g>.
- [331] V.L. Pachapur, A. Dalila Larios, M. Cledón, S.K. Brar, M. Verma, R.Y. Surampalli, Behavior and characterization of titanium dioxide and silver nanoparticles in soils, *Sci. Total Environ.* 563–564 (2016). <https://doi.org/10.1016/j.scitotenv.2015.11.090>.
- [332] C.M. Park, J. Heo, N. Her, K.H. Chu, M. Jang, Y. Yoon, Modeling the effects of surfactant, hardness, and natural organic matter on deposition and mobility of silver nanoparticles in saturated porous media, *Water Res.* 103 (2016). <https://doi.org/10.1016/j.watres.2016.07.022>.
- [333] O. Sagee, I. Dror, B. Berkowitz, Transport of silver nanoparticles (AgNPs) in soil, *Chemosphere.* 88 (2012). <https://doi.org/10.1016/j.chemosphere.2012.03.055>.
- [334] J.F. Liu, J.B. Chao, R. Liu, Z.Q. Tan, Y.G. Yin, Y. Wu, G. Bin Jiang, Cloud point extraction

- as an advantageous preconcentration approach for analysis of trace silver nanoparticles in environmental waters, *Anal. Chem.* 81 (2009). <https://doi.org/10.1021/ac900918e>.
- [335] D.M. Mitrano, A. Barber, A. Bednar, P. Westerhoff, C.P. Higgins, J.F. Ranville, Silver nanoparticle characterization using single particle ICP-MS (SP-ICP-MS) and asymmetrical flow field flow fractionation ICP-MS (AF4-ICP-MS), *J. Anal. At. Spectrom.* 27 (2012). <https://doi.org/10.1039/c2ja30021d>.
- [336] K. Tiede, A.B.A. Boxall, D. Tiede, S.P. Tear, H. David, J. Lewis, A robust size-characterisation methodology for studying nanoparticle behaviour in “real” environmental samples, using hydrodynamic chromatography coupled to ICP-MS, *J. Anal. At. Spectrom.* 24 (2009). <https://doi.org/10.1039/b822409a>.
- [337] J. Liu, G. Jiang, *Silver nanoparticles in the environment*, Springer, (2015). <https://doi.org/10.1007/978-3-662-46070-2>.
- [338] Y. Hashimoto, S. Takeuchi, S. Mitsunobu, Y.S. Ok, Chemical speciation of silver (Ag) in soils under aerobic and anaerobic conditions: Ag nanoparticles vs. ionic Ag, *J. Hazard. Mater.* 322 (2017). <https://doi.org/10.1016/j.jhazmat.2015.09.001>.
- [339] G. Cornelis, C. DooletteMadeleine Thomas, M.J. McLaughlin, J.K. Kirby, D.G. Beak, D. Chittleborough, Retention and Dissolution of Engineered Silver Nanoparticles in Natural Soils, *Soil Sci. Soc. Am. J.* 76 (2012). <https://doi.org/10.2136/sssaj2011.0360>.
- [340] M. Li, P. Wang, F. Dang, D.M. Zhou, The transformation and fate of silver nanoparticles in paddy soil: effects of soil organic matter and redox conditions, *Environ. Sci. Nano.* 4 (2017). <https://doi.org/10.1039/c6en00682e>.
- [341] G. Cornelis, L. Pang, C. Doolette, J.K. Kirby, M.J. McLaughlin, Transport of silver nanoparticles in saturated columns of natural soils, *Sci. Total Environ.* 463–464 (2013). <https://doi.org/10.1016/j.scitotenv.2013.05.089>.
- [342] Y. Yin, Z.Y. Li, Z. Zhong, B. Gates, Y. Xia, S. Venkateswaran, Synthesis and characterization of stable aqueous dispersions of silver nanoparticles through the Tollens process, *J. Mater. Chem.* 12 (2002). <https://doi.org/10.1039/b107469e>.
- [343] J.L. Axson, D.I. Stark, A.L. Bondy, S.S. Capracotta, A.D. Maynard, M.A. Philbert, I.L. Bergin, A.P. Ault, Rapid Kinetics of Size and pH-Dependent Dissolution and Aggregation of Silver Nanoparticles in Simulated Gastric Fluid, *J. Phys. Chem. C.* 119 (2015). <https://doi.org/10.1021/acs.jpcc.5b03634>.
- [344] S.K. Mwilu, A.M. El Badawy, K. Bradham, C. Nelson, D. Thomas, K.G. Scheckel, T. Tolaymat, L. Ma, K.R. Rogers, Changes in silver nanoparticles exposed to human synthetic stomach fluid: Effects of particle size and surface chemistry, *Sci. Total*

- Environ. 447 (2013). <https://doi.org/10.1016/j.scitotenv.2012.12.036>.
- [345] T.C. Prathna, N. Chandrasekaran, A. Mukherjee, Studies on aggregation behaviour of silver nanoparticles in aqueous matrices: Effect of surface functionalization and matrix composition, *Colloids Surfaces A Physicochem. Eng. Asp.* 390 (2011). <https://doi.org/10.1016/j.colsurfa.2011.09.047>.
- [346] J. Liu, R.H. Hurt, Ion release kinetics and particle persistence in aqueous nano-silver colloids, *Environ. Sci. Technol.* 44 (2010). <https://doi.org/10.1021/es9035557>.
- [347] C.J. Bueno-Alejo, C. D'Alfonso, N.L. Pacioni, M. González-Béjar, M. Grenier, O. Lanzalunga, E.I. Alarcon, J.C. Scaiano, Ultraclean derivatized monodisperse gold nanoparticles through laser drop ablation customization of polymorph gold nanostructures, *Langmuir*. 28 (2012). <https://doi.org/10.1021/la3010689>.
- [348] G. Palazzo, G. Valenza, M. Dell'Aglio, A. De Giacomo, On the stability of gold nanoparticles synthesized by laser ablation in liquids, *J. Colloid Interface Sci.* 489 (2017). <https://doi.org/10.1016/j.jcis.2016.09.017>.
- [349] Y. Han, G. Hwang, S. Park, A. Gomez-Flores, E. Jo, I.C. Eom, M. Tong, H.J. Kim, H. Kim, Stability of carboxyl-functionalized carbon black nanoparticles: the role of solution chemistry and humic acid, *Environ. Sci. Nano.* 4 (2017). <https://doi.org/10.1039/c6en00530f>.
- [350] J. Lohwacharin, S. Takizawa, P. Punyapalakul, Carbon black retention in saturated natural soils: Effects of flow conditions, soil surface roughness and soil organic matter, *Environ. Pollut.* 205 (2015). <https://doi.org/10.1016/j.envpol.2015.05.036>.
- [351] A. Bismarck, A.R. Boccaccini, E. Egia-Ajuriagojeaskoa, D. Hülsenberg, T. Leutbecher, Surface characterization of glass fibers made from silicate waste: Zeta-potential and contact angle measurements, *J. Mater. Sci.* 39 (2004). <https://doi.org/10.1023/B:JMSC.0000011493.26161.a6>.
- [352] Z. Xu, S. Mahalingam, J.L. Rohn, G. Ren, M. Edirisinghe, Physio-chemical and antibacterial characteristics of pressure spun nylon nanofibres embedded with functional silver nanoparticles, *Mater. Sci. Eng. C.* 56 (2015). <https://doi.org/10.1016/j.msec.2015.06.003>.
- [353] D. Dong, Fiberglass Surface and Its Electrokinetic Properties, *Int. Nonwovens J.* os-8 (1999). <https://doi.org/10.1177/1558925099os-800218>.
- [354] V.H. Le, C.N.H. Thuc, H.H. Thuc, Synthesis of silica nanoparticles from Vietnamese rice husk by sol-gel method, *Nanoscale Res. Lett.* 8 (2013). <https://doi.org/10.1186/1556-276x-8-58>.
- [355] C. Li, Y. Zhao, T. Zhu, Y. Li, J. Ruan, G. Li, Effective solvent-free oxidation of

- cyclohexene to allylic products with oxygen by mesoporous etched halloysite nanotube supported Co<sup>2+</sup>, *RSC Adv.* 8 (2018). <https://doi.org/10.1039/c7ra11245a>.
- [356] A.K. Brewer, A.M. Striegel, Characterizing string-of-pearls colloidal silica by multidetector hydrodynamic chromatography and comparison to multidetector size-exclusion chromatography, off-line multiangle static light scattering, and transmission electron microscopy, *Anal. Chem.* 83 (2011). <https://doi.org/10.1021/ac103314c>.
- [357] M.F. Sorna-Gowri, V.; Almeida, L.; Amorim, T.; Carneiro, T.; Soutp, A.P.; Esteves, Novel copolymer for SiO<sub>2</sub> nanoparticles dispersion, *J. Appl. Polym. Sci.* 124 (2012). [doi.org/10.1002/app.35068](https://doi.org/10.1002/app.35068).
- [358] Y. Sun, M. Yanagisawa, M. Kunimoto, M. Nakamura, T. Homma, Depth profiling of APTES self-assembled monolayers using surface-enhanced confocal Raman microspectroscopy, *Spectrochim. Acta - Part A Mol. Biomol. Spectrosc.* 184 (2017). <https://doi.org/10.1016/j.saa.2017.04.036>.
- [359] A.F. Jaramillo, R. Baez-Cruz, L.F. Montoya, C. Medinam, E. Pérez-Tijerina, F. Salazar, D. Rojas, M.F. Melendrez, Estimation of the surface interaction mechanism of ZnO nanoparticles modified with organosilane groups by Raman Spectroscopy, *Ceram. Int.* 43 (2017). <https://doi.org/10.1016/j.ceramint.2017.06.027>.
- [360] A.A.R. De Oliveira, V. Ciminelli, M.S.S. Dantas, H.S. Mansur, M.M. Pereira, Acid character control of bioactive glass/polyvinyl alcohol hybrid foams produced by sol-gel, *J. Sol-Gel Sci. Technol.* 47 (2008). <https://doi.org/10.1007/s10971-008-1777-1>.
- [361] S. V. Patwardhan, Biomimetic and bioinspired silica: Recent developments and applications, *Chem. Commun.* 47 (2011). <https://doi.org/10.1039/c0cc05648k>.
- [362] J.S. Beck, J.C. Vartuli, W.J. Roth, M.E. Leonowicz, C.T. Kresge, K.D. Schmitt, C.T.W. Chu, D.H. Olson, E.W. Sheppard, S.B. McCullen, J.B. Higgins, J.L. Schlenker, A New Family of Mesoporous Molecular Sieves Prepared with Liquid Crystal Templates, *J. Am. Chem. Soc.* 114 (1992). <https://doi.org/10.1021/ja00053a020>.
- [363] V.B. Cashin, D.S. Eldridge, A. Yu, D. Zhao, Surface functionalization and manipulation of mesoporous silica adsorbents for improved removal of pollutants: A review, *Environ. Sci. Water Res. Technol.* 4 (2018). <https://doi.org/10.1039/c7ew00322f>.
- [364] D. Zhao, J. Feng, Q. Huo, N. Melosh, G.H. Fredrickson, B.F. Chmelka, G.D. Stucky, Triblock copolymer syntheses of mesoporous silica with periodic 50 to 300 angstrom pores, *Science.* 279 (1998). <https://doi.org/10.1126/science.279.5350.548>.
- [365] H. Dou, Y.J. Lee, E.C. Jung, B.C. Lee, S. Lee, Study on steric transition in asymmetrical flow field-flow fractionation and application to characterization of high-energy

- material, *J. Chromatogr. A.* 1304 (2013). <https://doi.org/10.1016/j.chroma.2013.06.051>.
- [366] Y.B. Kim, J.S. Yang, M.H. Moon, Investigation of steric transition with field programming in frit inlet asymmetrical flow field-flow fractionation, *J. Chromatogr. A.* 1576 (2018). <https://doi.org/10.1016/j.chroma.2018.09.036>.
- [367] I. Langmuir, The adsorption of gases on plane surfaces of glass, mica and platinum, *J. Am. Chem. Soc.* 40 (1918). <https://doi.org/10.1021/ja02242a004>.
- [368] V.S. Munagapati, D.S. Kim, Equilibrium isotherms, kinetics, and thermodynamics studies for congo red adsorption using calcium alginate beads impregnated with nano-goethite, *Ecotoxicol. Environ. Saf.* 141 (2017). <https://doi.org/10.1016/j.ecoenv.2017.03.036>.
- [369] J.K. Kang, S.C. Lee, S.B. Kim, Synthesis of quaternary ammonium-functionalized silica gel through grafting of dimethyl dodecyl [3-(trimethoxysilyl)propyl]ammonium chloride for nitrate removal in batch and column studies, *J. Taiwan Inst. Chem. Eng.* 102 (2019). <https://doi.org/10.1016/j.jtice.2019.05.019>.
- [370] M. Ebrahimi-Gatkash, H. Younesi, A. Shahbazi, A. Heidari, Amino-functionalized mesoporous MCM-41 silica as an efficient adsorbent for water treatment: batch and fixed-bed column adsorption of the nitrate anion, *Appl. Water Sci.* 7 (2017). <https://doi.org/10.1007/s13201-015-0364-1>.
- [371] J.K. Kang, S.B. Kim, Synthesis of quaternized mesoporous silica SBA-15 with different alkyl chain lengths for selective nitrate removal from aqueous solutions, *Microporous Mesoporous Mater.* 295 (2020). <https://doi.org/10.1016/j.micromeso.2019.109967>.
- [372] Z. Aksu, F. Gönen, Biosorption of phenol by immobilized activated sludge in a continuous packed bed: Prediction of breakthrough curves, *Process Biochem.* 39 (2004). [https://doi.org/10.1016/S0032-9592\(03\)00132-8](https://doi.org/10.1016/S0032-9592(03)00132-8).
- [373] K.H. Chu, Fixed bed sorption: Setting the record straight on the Bohart-Adams and Thomas models, *J. Hazard. Mater.* 177 (2010). <https://doi.org/10.1016/j.jhazmat.2010.01.019>.
- [374] P.T. Anastas, J.C. Warner, *Green Chemistry: Theory and Practice*, Green Chem. Theory Pract. Oxford Univ. Press. New York. (1998).
- [375] S.E. Lehman, S.C. Larsen, Zeolite and mesoporous silica nanomaterials: Greener syntheses, environmental applications and biological toxicity, *Environ. Sci. Nano.* 1 (2014). <https://doi.org/10.1039/c4en00031e>.

- [376] M. Ahmaruzzaman, V.K. Gupta, Rice husk and its ash as low-cost adsorbents in water and wastewater treatment, *Ind. Eng. Chem. Res.* 50 (2011). <https://doi.org/10.1021/ie201477c>.
- [377] P.T. Tanev, T.J. Pinnavaia, Mesoporous silica molecular sieves prepared by ionic and neutral surfactant templating: A comparison of physical properties, *Chem. Mater.* 8 (1996). <https://doi.org/10.1021/cm950549a>.
- [378] M. Šoltys, M. Balouch, O. Kašpar, M. Lhotka, P. Ulbrich, A. Zdražil, P. Kovačik, F. Štěpánek, Evaluation of scale-up strategies for the batch synthesis of dense and hollow mesoporous silica microspheres, *Chem. Eng. J.* 334 (2018). <https://doi.org/10.1016/j.cej.2017.11.026>.
- [379] D.S. Otto, W. Flörke, H.A. Graetsch, F. Brunk, L. Benda, S. Paschen, H.E. Bergna, W.O. Roberts, W.A. Welsh, D.M. Chapman, M. Ettlinger, D. Kerner, M. Maier, W. Meon, R. Schmoll, H. Gies, *Silica*, Wiley-VCH Verlag. (2007). [https://doi.org/10.1002/14356007.a23\\_583.pub3](https://doi.org/10.1002/14356007.a23_583.pub3)
- [380] V. Vaibhav, U. Vijayalakshmi, S.M. Roopan, Agricultural waste as a source for the production of silica nanoparticles, *Spectrochim. Acta - Part A Mol. Biomol. Spectrosc.* 139 (2015). <https://doi.org/10.1016/j.saa.2014.12.083>.
- [381] A. Imyim, E. Prapalimrungsi, Humic acids removal from water by aminopropyl functionalized rice husk ash, *J. Hazard. Mater.* 184 (2010). <https://doi.org/10.1016/j.jhazmat.2010.08.108>.
- [382] S.B. Kausley, R.A. Patil, (2012) Method for purifying water by contacting water with a porous rice husk ash and clay mixture and apparatus therefor. Patent WO2012025943A1.
- [383] J. Feng, Y. Tian, X. Wang, C. Luo, M. Sun, Basalt fibers functionalized with gold nanoparticles for in-tube solid-phase microextraction, *J. Sep. Sci.* 41 (2018). <https://doi.org/10.1002/jssc.201701027>.
- [384] Z. Liu, W. Zhou, C. Wang, W. Hu, Z. Chen, Cotton thread modified with ionic liquid copolymerized polymer for online in-tube solid-phase microextraction and HPLC analysis of nonsteroidal anti-inflammatory drugs, *J. Sep. Sci.* 43 (2020). <https://doi.org/10.1002/jssc.202000212>.
- [385] J. Liu, Q. Liu, L. Wei, X. Chen, Z. Li, Y. Xu, X. Gao, X. Lu, J. Zhao, A novel polyhedral oligomeric silsesquioxane-based hybrid monolith as a sorbent for on-line in-tube solid phase microextraction of bisphenols in milk prior to high performance liquid chromatography-ultraviolet detection analysis, *Food Chem.* 374 (2022). <https://doi.org/10.1016/j.foodchem.2021.131775>.
- [386] J. Feng, X. Wang, S. Han, X. Ji, C. Li, C. Luo, M. Sun, An ionic-liquid-modified

- melamine-formaldehyde aerogel for in-tube solid-phase microextraction of estrogens followed by high performance liquid chromatography with diode array detection, *Microchim. Acta.* 186 (2019). <https://doi.org/10.1007/s00604-019-3909-4>.
- [387] A. Ishizaki, H. Kataoka, Online in-tube solid-phase microextraction coupled to liquid chromatography–tandem mass spectrometry for the determination of tobacco-specific nitrosamines in hair samples, *Molecules.* 26 (2021). <https://doi.org/10.3390/molecules26072056>.
- [388] M. Sun, J. Feng, X. Ji, C. Li, S. Han, M. Sun, Y. Feng, J. Feng, H. Sun, Polyaniline/titanium dioxide nanorods functionalized carbon fibers for in-tube solid-phase microextraction of phthalate esters prior to high performance liquid chromatography–diode array detection, *J. Chromatogr. A.* 1642 (2021). <https://doi.org/10.1016/j.chroma.2021.462003>.
- [389] H.D. Ponce-Rodríguez, A.A. García-Robles, P. Sáenz-González, J. Verdú-Andrés, P. Campíns-Falcó, On-line in-tube solid phase microextraction coupled to capillary liquid chromatography–diode array detection for the analysis of caffeine and its metabolites in small amounts of biological samples, *J. Pharm. Biomed. Anal.* 178 (2020). <https://doi.org/10.1016/j.jpba.2019.112914>.
- [390] M. Sun, S. Han, H. Maloko Loussala, J. Feng, C. Li, X. Ji, J. Feng, H. Sun, Graphene oxide-functionalized mesoporous silica for online in-tube solid-phase microextraction of polycyclic aromatic hydrocarbons from honey and detection by high performance liquid chromatography–diode array detector, *Microchem. J.* 166 (2021). <https://doi.org/10.1016/j.microc.2021.106263>.
- [391] M. Mei, J. Pang, X. Huang, Q. Luo, Magnetism-reinforced in-tube solid phase microextraction for the online determination of trace heavy metal ions in complex samples, *Anal. Chim. Acta.* 1090 (2019). <https://doi.org/10.1016/j.aca.2019.09.028>.
- [392] C. Peng, S. Zhang, C. Wu, Y. Feng, D. Zhao, X. Wang, Z. Bai, In-tube solid phase microextraction and determination of ractopamine in pork muscle samples using amide group modified polysaccharide-silica hybrid monolith as sorbent prior to HPLC analysis, *Food Chem.* 355 (2021). <https://doi.org/10.1016/j.foodchem.2021.129662>.





# **ANNEX**



## A1. ABBREVIATIONS

AF4:	Asymmetrical flow field flow fractionation
AFM:	Atomic force microscope
AgNPs:	Silver nanoparticles
AuNPs:	Gold nanoparticles
BC:	Black carbon
BPA:	Bisphenol A
BPEI:	Branched polyethyleneimine
BW:	Bottled water
C-NMs:	Carbon based nanomaterials
Cap:	Capillary
CB:	Carbon black
CCC:	Critical coagulation concentration
CDs:	Carbon dots
CFs:	Carbon fibers
CNOs:	Carbon nano onions
CNS:	Carbon nanostructure
CNT:	Carbon nanotube
Cps:	Counts per second
CVC:	Chemical vapor condensation
<i>D</i> :	Translational diffusion
DAD:	Diode array detector
DH:	Hydrodynamic diameter
DLS:	Dynamic light scattering
DOM:	Dissolved organic matter
EC:	Electrical conductivity
EDS:	Energy dispersive X-ray spectroscopy
EIS:	Electrochemical impedance spectroscopy
EIF3:	Electrical field flow fractionation
$\epsilon_{max}$ :	Extinction coefficient
ENMs:	Engineered nanomaterials
FBS:	Fetal bovine serum
FFF:	Field flow fractionation
FRET:	Fluorescence resonance energy transfer
FTIR:	Fourier transform infrared spectroscopy

---

GC:	Glass carbon
GF3:	Gravitational field flow fractionation
HA:	Humic acid
HAc:	Acetic acid
HNT:	Halloysite nanotubes
IAARC:	International Agency for Research on Cancer
ICP-MS:	Inductively coupled mass spectroscopy
LC:	Liquid chromatography
LOD:	Limit of detection
MgF3:	Magnetic field flow fractionation
MNPs:	Metallic nanoparticles
MTEOS:	Tetraethylorthosilicate
MWCNT:	Multiwalled carbon nanotubes
NIR:	Near infrared range
NMs:	Nanomaterials
NO <sub>3</sub> <sup>-</sup> :	Nitrate
NPs:	Nanoparticles
OAN:	Oil absorption number
PBS:	Phosphate buffer saline
PDMS:	Polydimethylsiloxane
PET:	Photoinduced electron transfer process
QDs:	Quantum dots
RH:	Hydrodynamic radius
RSD:	Relative standard deviation
S-SiO <sub>2</sub> NPs:	Spherical silica nanoparticles
SdF3:	Sedimentation field flow fractionation
SEM:	Scanning electron microscope
SERS:	Surface-enhanced Raman spectroscopy
SiO <sub>2</sub> NPs:	Silica nanoparticles
SiNTs:	Silica nanotubes
SOM:	Soil organic matter
SPME:	Solid phase microextraction
SPR:	Surface plasmon resonance
SSA:	Specific surface area
SW:	Sea water
SWCNT:	Single walled carbon nanotubes

TEM:	Transmission electron microscope
TEOS:	Tetraethylorthosilicate
TF3:	Thermal field flow fractionation
TMB:	3,3',5,5'-tetramethylbenzidine
t <sub>r</sub> :	Retention time
TW:	Tap water
UV-vis:	Ultraviolet-visible
XPS:	X-ray photoelectron spectroscopy
XRD:	X-ray diffraction



## A2. FIGURE LIST

<b>Figure 1:</b> Publications from 2012-2021 with the topic “Nanomaterials”. Source: Web of Science, May 2022. ....	4
<b>Figure 2:</b> Percentages of use of NMs.....	4
<b>Figure 3:</b> Schematic representation of the approaches where NMs are of analytical interest.....	8
<b>Figure 4:</b> Application areas of MNPs with key words a) “Gold nanoparticles applications” 2016-2022. b) “Silver nanoparticles applications” 2016-2022. (Source: Web of Science). May 2022. ....	10
<b>Figure 5:</b> Schematic representation of the electrical double layer in a negatively charged NP.....	14
<b>Figure 6:</b> a) Schematic representation of localized SPR band. b) Normalized SPR bands of spherical AUNPs of 20, 40 and 60 nm. c) SPR bands of spherical AgNPs of 20, 40 and 60 nm .....	17
<b>Figure 7:</b> Application areas of CB-NMs. Web of Science and keywords “Carbon Black nanoparticles applications” 2016-2022.....	22
<b>Figure 8:</b> Summary of the CB synthetic processes. ....	26
<b>Figure 9:</b> Schematic diagram of CB primary particles, different configurations and aggregates/agglomerates.....	28
<b>Figure 10:</b> Different surface modified-CB and their main properties. ....	29
<b>Figure 11:</b> Different shapes of silica based NMs. ....	34
<b>Figure 12:</b> Schematic diagram to induce a) negative charge and b) positive charges in the Silica based NMs surface. ....	36
<b>Figure 13:</b> Representation of chemical structure of HNT. ....	38
<b>Figure 14:</b> In flow-through IT-SPME configuration.....	48
<b>Figure 15:</b> a) Principle of asymmetric flow field flow fractionation (AF4). b) Principle of sedimentation field flow fractionation (SdF3) .....	53
<b>Figure 16:</b> Spermine chemistry structure.....	61
<b>Figure 17:</b> a) UV-vis spectrophotometer. b) Diffuse reflection probe with integral video camera. ....	78
<b>Figure 18:</b> a) FTIR-ATR spectrophotometer. b) Raman fiber optic probe coupled to Raman spectrophotometer. ....	79
<b>Figure 19:</b> DLS system.....	80
<b>Figure 20:</b> IT-SPME CapLC system with binary capillary pump. ....	81
<b>Figure 21:</b> AF4 system equipped with UV-vis and DLS detectors. ....	82

<b>Figure 22:</b> SdF3 system equipped with a MALS detector.....	82
<b>Figure 23:</b> Optical microscope.....	83
<b>Figure 24:</b> a) Hitachi S-4100 scanning electron microscope. b) Jeol 1010 transmission electron microscope. ....	84
<b>Figure 25:</b> a) UV-vis spectra of styrene (green) and acrylic acid (purple) diluted in water at different preparation time. b) UV-vis spectra of polymer mixture (styrene and acrylic acid diluted in water) at different preparation time.....	89
<b>Figure 26:</b> Lab manifolds for testing nitrate adsorption: a) for silica activation and establishing of adsorption isotherms and b) for in flow nitrate adsorption studies and breakthrough curves.....	94
<b>Figure 27:</b> Filter-aided recovery procedure. ....	96
<b>Figure 28:</b> Off-line IT-SPME system .....	98
<b>Figure 29:</b> In-valve IT-SPME-miniaturized LC with six port valve a) in load position, b) in inject position. ....	99
<b>Figure 30:</b> Fractograms for 20, 40, 60 and 80 nm citrate-capped AuNPs aqueous dispersions (dilution 1/4).....	114
<b>Figure 31:</b> Fractograms for 20, 40 and 60 nm citrate-capped AgNPs aqueous dispersions (dilution 1/4).....	116
<b>Figure 32:</b> Fractograms of the evolution of nanoparticles dispersions over dilution preparation time for different NPs sizes a) AuNPs 20 nm, b) AuNPs 40 nm, c) AuNPs 60 nm, d) AuNPs 80 nm. ....	117
<b>Figure 33:</b> a) Variation of the peak area as a function of time for citrate-capped AuNPs. b) Variation of the DH as a function of time for citrate-capped AuNPs. c) Variation of the peak area as a function of time for citrate-capped AuNPs. d) Variation of the DH as a function of time for citrate-capped AuNPs. ....	118
<b>Figure 34:</b> Fractograms of the evolution of nanoparticles dispersions as function of dilution preparation time for different sizes a) AgNPs 20 nm, b) AgNPs 40 nm, c) AgNPs 60 nm.....	119
<b>Figure 35:</b> Study of AuNPs-PBS dispersions as function of dilution preparation time. ....	120
<b>Figure 36:</b> Mixtures of different sizes of AuNPs (dilution 1/8) and AgNPs (dilution 1/4). a) Fractograms of the evolution of 20, 40 and 80 nm AuNPs mixture; b) DLS values of AuNPs sizes, DLS spectra in green and DH distribution in red; c) fractograms of the evolution of 20, 40 and 60 nm AgNPs evolution mixture; d) DLS values of AgNPs sizes, DLS spectra in green and DH distribution in red. ....	121
<b>Figure 37:</b> a) Effect in the dilution ratio for AuNPs 60 nm with time. b) TEM micrographs for diluted dispersions of citrate-capped AuNPs (60 nm) just after their	



preparation and after 72 h. c) DH of AuNPs at different dilution times (0, 24, 48 and 72 h). .....	122
<b>Figure 38:</b> AuNPs and AgNPs dissolution TMB assay for several times of preparation of diluted dispersions from batch NPs: a) AuNPs for 0, 48 and 72 h; and b) 0, 3, 48 and 72 h. For more explanation see text.....	123
<b>Figure 39:</b> Fractograms obtained with a) UV-vis, b) DLS detectors, and c) UV-vis spectra of dispersions diluted 1/4 with ultrapure water (5 mg·L <sup>-1</sup> ) of various commercial batches of AgNPs. ....	125
<b>Figure 40:</b> Spectra of batches a) O2 and b) O1 diluted ¼ with bottled mineral water measured at several times (0.5, 1, 2, 5, 10, 15 min, the SPR band for the dilution with ultrapure water was also include, marked with *) and their fractograms (solid lines) c) and d), respectively, by using dynamic light scattering (DLS) and DH (points) measured at different times.....	128
<b>Figure 41:</b> Spectra of AgNPs batches O1 and O2 diluted 1/4 with bottled mineral water 1 and tap water measured at several times (0.5, 1, 2, 5, 10, 15 min). The SPR band for the dilution with ultrapure water was also included.....	129
<b>Figure 42:</b> Spectra of AgNPs batches M1 and M2 diluted 1/4 with bottled mineral water 1 and tap water measured at several times (0.5, 1, 2, 5, 10, 15 min). The SPR band for the dilution with ultrapure water was also included.....	130
<b>Figure 43:</b> Fractograms ( $\lambda = 395$ nm) obtained for suspensions diluted 1/4 of batches a) O2 and b) O1 with BW2 water at different times and batch O2 with water c) bottled water (BW1), d) tap water (TW), and e) sea water (SW) at different time using the DLS detector.....	131
<b>Figure 44:</b> Fractograms (solid line) and DH (points) obtained for suspension of batches a) O2 and b) O1 diluted 1/4 with BW2 water at different times using UV-vis detector. (c) Fractograms and DH for suspension of batch O2 diluted 1/4 with BW1 water at different times using the DLS signal. ....	133
<b>Figure 45:</b> Spectra of the several batches diluted 1/4 with transitional and sea waters measured at several times (9.5, 1, 2, 5, 10, 15 min). The SPR band for the dilution ultrapure water was also included.....	135
<b>Figure 46:</b> Static DLS registers for batch O2 diluted 1/4 with a) sea water (SW) and b) tap water (TW) measured at several times. Insert shows the changes in size of AgNPs with time. ....	136
<b>Figure 47:</b> Uv-vis spectra for batch O2 diluted 1/4 with a) sea water (SW) and b) tap water (TW) measured at several times. The SPR band for the dilution with ultrapure water was also included. c) Color of the suspension in SW with time.....	137

- Figure 48:** AF4 coupled in series with UV-vis and DLS detectors for batch O2 diluted 1/4 with sea (SW) water measured at several times: a) fractograms at 395 nm; b) optic images at 30 and 180 min; c) DLS fractograms at 30 and 180 min; d) fractograms at 750 nm of SW and UPW at 30 min. Cross-flow was 0.2 mL·min<sup>-1</sup>.  
..... 138
- Figure 49:** AF4 coupled in series with UV-vis and DLS detectors for batch O2 diluted 1/4 with tap (TW) water measured at 30 min: a) fractograms at 395 nm; b) DLS fractograms; c) fractograms at 750 nm of TW and UPW. Cross flow was 0.2 mL·min<sup>-1</sup>.  
..... 139
- Figure 50:** On-line IT-SPME-CapLC-DAD (inset: normalized spectra obtained at the maximum of the two chromatographic peaks) and off-line IT-SPME and AF4 results for (1/8) ultrapure water diluted dispersion of AgNPs (20 nm core; citrate capping).  
..... 141
- Figure 51:** Chromatographic profiles of commercial citrate capped MNPs. In blue: signal obtained by capillary LC; and in orange: signal obtained by nanoLC..... 143
- Figure 52:** a) Chromatographic profiles obtained for three batches of naked AuNPs corresponding to AuNPs(I). b) Chromatographic profiles obtained for three batches of naked AuNPs corresponding to AuNPs(II). Inserts: UV-vis spectra for both types of naked AuNPs..... 144
- Figure 53:** IR spectra for the four studied soils obtained by FTIR-ATR. .... 145
- Figure 54:** Chart showing the distribution of particle size in the 4 studied soils. 147
- Figure 55:** Eclipse microscope pictures for each fraction of the orchard soil after being sieved: (1) below 100 µm, (2) 100-200 µm, (3) 200-300 µm, (4) 300-400 µm and (5) above 400 µm..... 148
- Figure 56:** Characterization of the soils by optic microscope. a) Eclipse microscope image of the soil mixture sample (500 µm). Histogram of the particle size distribution obtained by: b) optic microscope (f: frequency) and c) after sieving resulting in different fractions: (1) under 100 µm, (2) 100-200 µm, (3) 200-300 µm, (4) 300-400 µm and (5) over 400 µm. .... 149
- Figure 57:** TEM histogram of 17.3 nm AgNPs showing their size distribution and TEM picture (upper-right corner). b) UV-vis spectrum of 1:8 17.3 nm AgNPs..... 151
- Figure 58:** a) UV-vis spectrum of the supernatant after contaminating soil samples with: (A) AgNPs, (SB) synthesis blank and (W) water. b) TEM picture of the supernatant contaminated with AgNPs. c) UV-vis spectra of the successive additions of AgNPs on the SB supernatant. d) UV-vis spectrum showing the SPRB of the used AgNPs synthesis. .... 152

<b>Figure 59:</b> UV-vis spectra of the supernatants of: (SB) soil-synthesis blank and (Citrate) soil-sodium citrate solution mixtures. ....	153
<b>Figure 60:</b> a) CapLC chromatograms for samples of 1/8 AgNPs: (sample U) unprocessed and (sample P) processed. b) DAD spectra for the peaks obtained in the 3 series (A, SB and W) for the 4 soils (in this case, measured in the chromatograms of the orchard soil samples). ....	154
<b>Figure 61:</b> Variation of the CapLC signals in time (0-80 min range) for the 3 series (A, SB and W) in each of the 4 soils (compost, mountain, orchard and urban). (n=2) .....	155
<b>Figure 62:</b> a) Chromatograms for: (1) 1/16 AgNPs standard, (2) 1/16 Sample A of the orchard soil and (3) a HA standard (10 mg·L <sup>-1</sup> ). b) DAD spectra for: (1-I) 1st and (1-II) 2nd chromatographic peaks of 1/16 AgNPs, (2-I) 1st and (2-II) 2nd peaks of 1/16 Sample A and (3) 1st peak of the HAs standard. c) Chromatograms obtained for AgNPs: (1w) without, and in the presence of 1% sodium thiosulfate after (1x) 40, (1y) 45 and (1z) 50 minutes of reaction. ....	156
<b>Figure 63:</b> a) IT-SPME-CapLC Calibration curve for HAs from 0 to 500 mg·L <sup>-1</sup> . b) Chromatograms obtained for [HAs] standards of: (1) 0.5, (2) 2, (3) 5, (4) 10, (5) 25 and (6) 50 mg·L <sup>-1</sup> . c) DAD spectrum for (4). ....	158
<b>Figure 64:</b> Chromatograms for (1) compost, (2) mountain, (3) orchard and (4) urban soils corresponding to: for samples A, injections a) without and b) in the presence of 1% sodium thiosulfate; for samples SB, injections c) without and d) in the presence of 1% sodium thiosulfate (note, exposure time of the samples to sodium thiosulfate: 50 min, 1/16 sample A dilutions). ....	159
<b>Figure 65:</b> Chromatograms obtained from measuring samples: a) without and b) in the presence of 1% sodium thiosulfate for different fractions of urban soil: (1) coarse fraction, (2) 300 to 400 μm, (3) 200 to 300 μm, (4) 100 to 200 μm and (5) below 100 μm (note, exposure time of the samples to sodium thiosulfate of 50 min, 1/16 sample dilutions). ....	162
<b>Figure 66:</b> a) SEM pictures of the 4 studied soils: (1) compost, (2) mountain, (3) orchard and (4) urban. ....	164
<b>Figure 67:</b> Representation of Ag amount (estimated by SEM microanalysis) vs retained AgNPs amount (estimated by the IT-SPME-CapLC-DAD method) in each soil. (n=2) .....	164
<b>Figure 68:</b> Capture % of AgNPs vs the extracted interfering compound (as mg·L <sup>-1</sup> of HAs): a) for the 4 studied soils (LSOM: low-containing SOM; HSOM: high-containing SOM); b) for different-sized fractions of the urban soil. (n=2) .....	166

- Figure 69:** Fractograms of three different batches of AgNPs 20 nm diluted 1/4 with ultrapure water ( $5 \mu\text{g}\cdot\text{mL}^{-1}$ ) with a) UV-vis detection, b) DLS detection, and c) their spectra. .... 169
- Figure 70:** UV-vis spectra recorded after 10 min. corresponding to the suspension of AgNPs in a 1/4 dilution ( $5 \mu\text{g}\cdot\text{mL}^{-1}$ ) in the presence of different concentrations of a) HAc and b) hydrochloric acid. .... 171
- Figure 71:** Fractograms with UV-vis detection corresponding to suspensions of AgNPs in a 1/4 dilution ( $5 \mu\text{g}\cdot\text{mL}^{-1}$ ) and a) 1.5 mM or c) 3 mM HAc at different times. Fractograms with DLS detection and DH corresponding to the same suspensions at different times (b and d) respectively. .... 172
- Figure 72:** Normalized absorbance values at various times with the concentration of a) HAc, b) its log of AgNPs diluted 1/4 ( $5 \mu\text{g}\cdot\text{mL}^{-1}$ ) and c) evolution of the wavelength of the second plasmon maximum in the UV-vis spectra at 10 and 15 min of its preparation. d) and e) correspond to the influence of hydrochloric acid. .... 174
- Figure 73:** Aggregation profiles due to HAc as a function of time of: a) citrate capped AuNPs 20 nm diluted (1/4) in HAc 10% (v/v); b) ) citrate capped AgNPs 20 nm diluted (1/2) in HAc 0.2% (v/v); c) a mixture of citrate capped AuNPs and AgNPs 20 nm diluted (1/4) in HAc 0.7 % (v/v); d) and phosphate capped AgNPs 20 nm diluted (1/4) in HAc 0.2 % (v/v), obtained by UV-vis spectroscopic measurements. .... 176
- Figure 74:** Aggregation profiles as a function of HAc concentrations by using UV-vis spectroscopy for (a) AuNPs(I) and (b) AuNPs(II) [Continuous line: no aggregation; dotted line: aggregation]. Working  $[\text{H}^+]$  concentration intervals, expressed as  $[\text{H}^+]$ , for each (c) AuNPs(I) and (d) AuNPs(II). .... 177
- Figure 75:** Aggregation profiles as a function of SPN concentrations by UV-vis spectroscopic measurements for a) naked AuNPs(I) and b) naked AuNPs(II). Working SPN concentration intervals for c) AuNPs(I) and d) AuNPs(II). .... 178
- Figure 76:** a) Schematic representation of the visual inspection, b) Variation of the chromatographic profiles inside of the capillary column in presence of target analyte. .... 180
- Figure 77:** a) Chromatograms obtained for naked AuNPs(I) as a function of the added concentration of SPN [ $41 \mu\text{g}\cdot\text{L}^{-1}$  in red,  $66 \mu\text{g}\cdot\text{L}^{-1}$  in green and  $82 \mu\text{g}\cdot\text{L}^{-1}$  in yellow]; and b) chromatograms obtained for AuNPs(I) as function of the added concentration of HAc [0.35 mM in purple, 0.50 mM in green and 0.60 mM in yellow]. Insets: variation of the LSPR band of the chromatographic peak at  $t_r = 3.0$  min with the successive additions of target analyte. .... 181

- Figure 78:** Chromatograms obtained for AuNPs(II) as function of the added concentration of a) SPN [ $41 \mu\text{g}\cdot\text{L}^{-1}$  in red and  $66 \mu\text{g}\cdot\text{L}^{-1}$  in green] and b) HAC [0.35 mM in purple, 0.40 mM in red and 0.50 mM in green]. Insets: variation of the LSPR band of the chromatographic peak at  $t_r = 3.0$  min with the successive additions of target analyte..... 182
- Figure 79:** Aggregation profiles of AuNPs 20 nm a) citrate capping and b) phosphate capping diluted 1/4 with ultrapure water by acetic acid 1.75 M; the normalized spectra were obtained at the maximum of the two chromatographic peaks. c) Chromatographic profiles of citrate capped AgNPs 20 nm diluted 1/4 with ultrapure water and their aggregation adding acetic acid 35 mM. d) Normalized spectra at the maximum of the two chromatographic peaks of AgNPs 20 nm diluted 1:4 with ultrapure water and their aggregation by ITSPME-NanoLC-DAD. .... 184
- Figure 80:** a) Chromatographic profiles of citrate capped AgNPs 20 nm and AuNPs 20 nm diluted 1/4 with ultrapure water and their aggregation adding acetic acid 116 mM. b) Normalized spectra at the maximum of the three chromatographic peaks of AgNPs 20 nm and AuNPs 20 nm diluted 1/4 with ultrapure water and their aggregation by IT-SPME-NanoLC-DAD..... 185
- Figure 81:** Chromatographic profiles of AuNPs(I) for a) healthy volunteer sample and b) cancer patient sample. Insets: LSPR band variation for the chromatographic peak at  $t_r = 3.0$  min. Kinetic spectroscopy study for 3 min in intervals of 20 s for c) healthy volunteers and d) cancer patients..... 186
- Figure 82:** a) Chromatographic profiles obtained for 1: AuNPs(I), 2: blanc acidic extract (HAc), 3: urine sample, 4: urine sample spiked with  $16 \mu\text{g}\cdot\text{L}^{-1}$  of SPN and 5: urine sample spiked with  $26 \mu\text{g}\cdot\text{L}^{-1}$  of SPN. (b) UV spectra corresponding to peak chromatogram at 3 min. .... 187
- Figure 83:** SEM micrographs of (a.1) N326, (a.2) N550, and (a.3) N722. .... 190
- Figure 84:** Raman spectra of CB N326. The inset shows the characteristic Raman bands between  $1000$  and  $1500 \text{ cm}^{-1}$ . .... 190
- Figure 85:** Optical microscope images of CB dispersions in a) polymeric and b) biological dispersants. Mechanism involved in the dispersion of CB using c) polymeric dispersant and d) biological dispersant..... 191
- Figure 86:** TEM images of CB structures in (a, b, c and d) polymeric dispersions; and (e, f, g and h) biological dispersions. .... 193
- Figure 87:** Results obtained for CB dispersion from simple N326 prepared in polymeric dispersant. a) DLS-fractograms at different concentration levels. b) TEM image of CB dispersion. c) Histogram – DLS measurement in batch. .... 194

---

<b>Figure 88:</b> Results obtained for CB dispersion from simple N326 prepared in biological dispersant. a) DLS-fractograms at different concentration levels. b) TEM image of CB dispersion. c) Histogram – DLS measurement in batch. ....	196
<b>Figure 89:</b> DLS-fractograms at different concentration levels obtained for CB dispersion from sample N326 prepared with cellular dispersant without supplementary compounds. DH results obtained in DLS analysis in batch and AF4 using dispersant or H <sub>2</sub> O as diluent of the CB dispersion. ....	197
<b>Figure 90:</b> a) UV-vis fractograms obtained for polymeric CB dispersions (N326 in blue, N550 in green, and N722 in red) at cross-flow of 0.5 mL·min <sup>-1</sup> . b) Visual color representation of each CB biological dispersion. ....	200
<b>Figure 91:</b> UV-vis fractograms obtained for biological CB dispersions (N326 in blue, N550 in green, and N722 in red) at different cross-flow rates: a) 0.5 mL·min <sup>-1</sup> and b) 1.0 mL·min <sup>-1</sup> . ....	200
<b>Figure 92:</b> % DLS fractogram signal (using as a reference the dispersion of day 0) obtained as a function of dispersion preparation time for CB N326 with two studied dispersants: polymeric (green) and biological (red), using ultrasound (continuous line) and without ultrasound (dashed line) before injection. ....	201
<b>Figure 93:</b> Maximum intensity obtained in DLS fractograms analysis for each CB dispersion diluted with different water matrices using a) polymeric dispersant and b) biological dispersant. ....	203
<b>Figure 94:</b> DLS-fractograms and DH obtained for soil samples. a) Mountain A soil extracted with polymeric dispersant. b) Mountain A soil extracted with biological dispersant. c) Orchard A soil extracted with polymeric dispersant. d) Orchard A soil extracted with biological dispersant. ....	205
<b>Figure 95:</b> DLS-fractograms and dhydro obtained for soil samples. a) Mountain B soil extracted with polymeric dispersant. b) Mountain B soil extracted with biological dispersant. c) Orchard B soil extracted with polymeric dispersant. d) Orchard B soil extracted with biological dispersant. ....	206
<b>Figure 96:</b> a) Fractogram for CB isolation from mountain A soil using polymeric dispersant (compared with CB bulk dispersion in the studied dispersant). b) Fractogram for CB isolation from mountain A soil using biological dispersant (compared with CB bulk dispersion in the studied dispersant). c) Fractogram for CB isolation from orchard A soil using polymeric dispersant (compared with CB bulk dispersion in the studied dispersant). d) Fractogram for CB isolation from orchard A soil using biological dispersant (compared with CB bulk dispersion in the studied dispersant). ....	207

- Figure 97:** a) Ligand exchange study and filter-aided recovery assay using fiberglass 2  $\mu\text{m}$  as a support (mountain A soil as matrix). b) Ligand exchange study and filter-aided recovery assay using fiberglass 2  $\mu\text{m}$  as a support (orchard A soil as matrix). ..... 210
- Figure 98:** a) Fractogram for pigment paste isolation from mountain A soil using polymeric dispersant (compared with a bulk dispersion of pigment paste in the studied dispersant). b) Fractogram for pigment paste isolation from mountain A soil using biological dispersant (compared with a bulk dispersion of pigment paste in the studied dispersant). ..... 211
- Figure 99:** Filter based analysis of CB dispersion from sample N326 prepared with polymeric dispersant using different filters (fiberglass 2.00  $\mu\text{m}$ , fiberglass 1.00  $\mu\text{m}$ , nylon 5  $\mu\text{m}$ , nylon 0.45  $\mu\text{m}$ , teflon 0.10  $\mu\text{m}$  and teflon 0.10  $\mu\text{m}$ ). ..... 212
- Figure 100:** Filter based analysis of CB dispersion from sample N326 prepared with biological dispersant using different filters (fiberglass 2.00  $\mu\text{m}$ , fiberglass 1.00  $\mu\text{m}$ , fiberglass 0.70  $\mu\text{m}$ , nylon 0.45  $\mu\text{m}$ , nylon 0.22  $\mu\text{m}$ , teflon 0.45  $\mu\text{m}$ , teflon 0.20  $\mu\text{m}$  and teflon 0.10  $\mu\text{m}$ ). ..... 213
- Figure 101:** In green: fractograms for CB isolation from different soils using the studied dispersants. Dotted lines: AF4-DLS signal of filtrate using fiberglass 2  $\mu\text{m}$  (black) and teflon 0.10  $\mu\text{m}$  (orange). a) Study using mountain A soil and polymeric dispersant. b) Study using mountain A soil and biological dispersant. c) Study using orchard A soil and polymeric dispersant. d) Study using orchard A soil and biological dispersant. The inserts corresponded to recovered CB from dispersions by fiberglass 2.00  $\mu\text{m}$ , and teflon 0.10  $\mu\text{m}$  filters for all dispersions. .... 216
- Figure 102:** a) Fractogram for pigment paste isolation from mountain A soil using polymeric dispersant (green). Dotted lines: AF4-DLS signal of filtrate using fiberglass 2  $\mu\text{m}$  (black) and teflon 0.10  $\mu\text{m}$  (orange). b) Fractogram for pigment paste isolation from mountain A soil using biological dispersant (green). Dotted lines: AF4-DLS signal of filtrate using fiberglass 2  $\mu\text{m}$  (black) and teflon 0.10  $\mu\text{m}$  (orange). c) Diffuse reflectance: absorbance of the samples (pigment paste, mountain A soil and pigment paste isolated from soil). d) Fractogram for pigment paste dispersion using biological dispersant by SdF3-MALS (red). Dotted lines: SdF3-MALS signals of pigment paste filtrate dispersion after isolation using fiberglass 2  $\mu\text{m}$  (blue) and nylon 0.45  $\mu\text{m}$  (green) (isolation from mountain soil). Size distribution (radius of each sample). ..... 218
- Figure 103:** SdF3-MALS-fractograms and size distribution (radius) obtained for soil filtrate after extraction without target analyte. a) Mountain A soil filtrate after

extraction (biological dispersant). b) Orchard A soil filtrate after extraction (biological dispersant). .....	219
<b>Figure 104:</b> Fractograms for CB dispersion using biological dispersant by SdF3-MALS (red). Dotted lines: SdF3-MALS signals of CB filtrate dispersion after isolation using fiberglass 2 $\mu\text{m}$ and nylon 0.45 $\mu\text{m}$ (isolation from mountain soil). Size distribution (radius of each sample). a) For mountain A soil matrix and b) for orchard A soil matrix.....	220
<b>Figure 105:</b> a) Diffuse reflectance study for CB isolated from mountain soil and recovered using teflon membrane 0.10 $\mu\text{m}$ (CB directly recovered (red), soil extract recovered (yellow) and CB isolated from soil and recovered (blue). b) Diffuse reflectance study for CB isolated from orchard soil and recovered using teflon membrane 0.10 $\mu\text{m}$ (CB directly recovered (red), soil extract recovered (grey) and CB isolated from soil and recovered (brown).....	222
<b>Figure 106:</b> FTIR-ATR spectra of a) $\text{SiO}_2\text{NPs}$ , b) commercial $\text{SiO}_2\text{NPs}$ CL30, c) extracted $\mu\text{-SiO}_2\text{NPs}$ from rice straw ashes and d) HNT. SEM images of e) $\text{SiO}_2\text{NPs}$ ; f) commercial $\text{SiO}_2\text{NPs}$ CL30, g) extracted $\mu\text{-SiO}_2\text{NPs}$ from rice straw ashes and h) HNT. ....	226
<b>Figure 107:</b> SEM images of a) $\text{SiO}_2\text{NPs}$ modified with KOH solution, b) modified extracted $\mu\text{-SiO}_2$ from rice straw ashes and c) modified HNT.....	227
<b>Figure 108:</b> a) Fractograms obtained for each elution program used. b) Fractograms obtained for $\text{SiO}_2\text{NPs}$ dispersion as a function of the concentration: 0.508 % (red), 0.254 % (blue), 0.127 % (yellow) and 0.064% (grey). c) Schematic representation of the filtering process. d) Fractograms obtained for each filtering using two filter membranes: fiberglass 0.70 $\mu\text{m}$ (green) and nylon 0.22 $\mu\text{m}$ (purple). Comparison with directly injected sample (blue). e) Hydrodynamic size values obtained for each samples studied: $\text{SiO}_2\text{NPs}$ , filtering with fiberglass 0.70 $\mu\text{m}$ and filtering with nylon 0.22 $\mu\text{m}$ . ....	229
<b>Figure 109:</b> DLS fractograms obtained for $\text{SiO}_2\text{NPs}$ dispersions carried out using KOH solution at pH 12.2 (red) and pH 9.0 (blue). Size distribution included.....	230
<b>Figure 110:</b> a) Fractograms obtained for each elution program used. b) Fractograms obtained for $\text{SiO}_2\text{NPs}$ dispersion TM40 at three concentration levels: 5.00 % (grey), 2.50 % (orange), 1.25 % (blue). ....	231
<b>Figure 111:</b> a) Fractograms of eight different commercial $\text{SiO}_2\text{NPs}$ dispersions with different sizes and stability conditions. Values of core size of each commercial $\text{SiO}_2\text{NPs}$ dispersion and hydrodynamic diameters obtained by AF4-DLS and direct DLS batch analysis. b) Stability study as a function of dilution preparation time for commercial $\text{SiO}_2\text{NPs}$ dispersion HS30 1.25%. c) Separation of mixture commercial	









---

SiO <sub>2</sub> NPs dispersion HS30 and TM40 1.25%. Stability study as a function of mixture preparation time.....	233
<b>Figure 112:</b> Stability study of HNT dispersion using different dispersants and techniques .....	235
<b>Figure 113:</b> Stability study of HNT modified dispersion using different dispersants. ....	236
<b>Figure 114:</b> a) Optical microscopy images: 1) HNT without treatment, magnification x100; 2) Hybrid pigment AZ-HNT, magnification x50; 3) Hybrid pigment HNT modified with alizarine, magnification x50. b) Fractograms obtained for HNT modified with hydroxide groups dispersion at three concentration levels: 0.20 % (yellow), 0.15 % (orange), 0.10 % (purple). c) Study of different HNT dispersions samples at concentration of 0.10 %: HNT modified in blue, HNT non modified with pigment in yellow and HNT modified with pigment in green. Hydrodynamic average size of each dispersions analysed. ....	237
<b>Figure 115:</b> FTIR spectra of extracted silica and amino-silica. ....	241
<b>Figure 116:</b> Raman spectra of amino-silica, APTES reagent, extracted silica and commercial silica. ....	242
<b>Figure 117:</b> SEM images/EDX micrograph of activated amino-silica a) before and b) after adsorption of nitrates. ....	243
<b>Figure 118:</b> Activated form of the modified silica as an anionic exchanger. ....	244
<b>Figure 119:</b> a) Fractogram and size distribution of extracted silica from ashes. b) Fractogram and size distribution of modified extracted silica from ashes. ....	245
<b>Figure 120:</b> a) Effect of bed heights (cm) and b) Effect of flow rate on removal efficiency of nitrate by the amino-silica in fixed-bed column system. (n= 3). ....	246
<b>Figure 121:</b> Experimental and theoretical adsorption isotherm of nitrate anion on modified silica at several concentrations assayed between 0 and 120 µg·mL <sup>-1</sup> , and Langmuir and Freundlich models for nitrate anion removal. ....	247
<b>Figure 122:</b> Experimental breakthrough curve for modified silica and Thomas and Yan models for nitrate anion removal.....	249
<b>Figure 123:</b> Adsorption of nitrates in aqueous solution of 45 µg·mL <sup>-1</sup> and samples of water for one- and two-layer silica. Nitrate concentration vs mL of processed water. ....	250
<b>Figure 124:</b> Experimental breakthrough curve for modified silica analysis of Thomas and Yan models. 1 (one layer), 2 (two layer) a) standard of 45 µg·mL <sup>-1</sup> and b) sample of water.....	251
<b>Figure 125:</b> Continuous monitoring of nitrate concentration for a well water sample by using activated silica and a commercial resin. ....	252



### A3. TABLE LIST

<b>Table 1:</b> Principal properties of different NMs.....	6
<b>Table 2:</b> Capping agents used in AuNPs. ....	15
<b>Table 3:</b> Capping agents used in AgNPs. ....	16
<b>Table 4:</b> Relationship between nanomaterials shape and SPR band. ....	18
<b>Table 5:</b> Uses of MNPs as colorimetric sensors in to determine different analytes. ....	19
<b>Table 6:</b> Characteristics and functions of matrices where CB can be found.....	23
<b>Table 7:</b> Reviews of “Carbon Black Nanoparticles / nanomaterials “ (2018-2021)	25
<b>Table 8:</b> Silica content present in different natural silica sources [189, 190, 191].	32
<b>Table 9:</b> Revision studies using DLS techniques for NMs characterization.....	42
<b>Table 10:</b> Column dimensions and Flow of principal LC systems.....	46
<b>Table 11:</b> Applications of IT-SPME described in the literature between 2017 – 2022. ....	49
<b>Table 12:</b> Some representative studies using FFF techniques for AuNPs and AgNPs characterization. ....	54
<b>Table 13:</b> Reviews published in the last 5 years using FFF techniques for CB separation and characterization.....	56
<b>Table 14:</b> Reports using FFF techniques for silica NMs separation and characterization .....	58
<b>Table 15:</b> Summary of reagents used in this Thesis, with their hazard pictograms, where  = Flammable (GHS02);  = Corrosive (GHS05);  = Toxic (GHS06);  =Harmful (GHS07);  =Health hazard (GHS08);  = Environmental hazard (GHS09). ....	75
<b>Table 16:</b> Parameters for the optimization of the amino-silica synthesis. ....	87
<b>Table 17:</b> Dispersant compositions and techniques used in the preparation of HNTs and HNTs modified dispersions. ....	91
<b>Table 18:</b> AF4 experimental conditions used in several works of this Thesis. (Df: detector flow rate; If: injection flow rate; Ff: focus flow rate; Cf: cross flow rate; It: injection time; Tt: transition time) .....	102
<b>Table 19:</b> SdF3 experimental conditions used for study CB dispersions and their extractions from soils. ....	109

<b>Table 20:</b> Values of RSD (%) and correlation between peak area and dilution ratio for AuNPs (20, 40, 60 and 80 nm) and AgNPs (20, 40 and 60 nm). A: ordinate and B: slope of the straight lines. ....	115
<b>Table 21:</b> Detection limits calculated for each diluted dispersion of citrate-capped AuNPs and AgNPs. ....	124
<b>Table 22:</b> Wavelength values ( $\lambda$ ) of SPB, width of the peak at half the maximum, extinction coefficient ( $\epsilon_{\max}$ ) obtained by UV-vis spectroscopy and DH for different commercial batches of AgNPs. ....	126
<b>Table 23:</b> pH, electrical conductivity (EC) and redox potential for each aqueous matrices used. Z-potentials for M and O batches of AgNPs diluted 1/4 with several water matrices. ....	127
<b>Table 24:</b> IR bands and functional groups. ....	146
<b>Table 25:</b> Soil particle size composition. Percentages (%) of each fraction for the four studied soils and estimated average size. ....	147
<b>Table 26:</b> Estimations of pH, EC and Eh for the 4 kinds of studied soils. ....	150
<b>Table 27:</b> Retention % of AgNPs quantified by IT-SPME-CapLC-DAD in the different spiked soils from both, the second peak of the chromatogram and by using the disrupting agent. ....	161
<b>Table 28:</b> Retention % of AgNPs in urban soil fractions quantified by IT-SPME-CapLC-DAD. ....	162
<b>Table 29:</b> SEM microanalysis. Elementary composition of the different soils. ....	163
<b>Table 30:</b> Wavelength values ( $\lambda$ ) of the plasmon maximum, width of the peak at half the maximum, extinction coefficient ( $\epsilon_{\max}$ ) obtained by UV-vis spectroscopy and DH by DLS for three different commercial batches of AgNPs. ....	169
<b>Table 31:</b> Peak, physical and analytical parameters for sample N326 in polymeric dispersant and biological supplemented dispersant. ....	195
<b>Table 32:</b> Particle size (DH) and Z-potential of different CB nanoparticles dispersions (N326, N550 and N772) using polymeric and biological dispersants (Fractograms were obtained at 0.5 mL·min <sup>-1</sup> except for * at 1.0 mL·min <sup>-1</sup> . ....	199
<b>Table 33:</b> Particle size obtained with the AF4-DLS for each dispersant as a function of dispersion time after the ultrasound step. ....	202
<b>Table 34:</b> pH, conductivity, turbidity, nitrate and sulfate values for aqueous matrices. ....	202
<b>Table 35:</b> D-IE: isolation efficiencies after the dispersive procedure. DH obtained for CB dispersed from fractograms obtained by AF4-DLS. (* batch DLS) ....	208

---

<b>Table 36:</b> Soil particle size composition obtained from optical microscope. Percentages (%) of each fraction for the four studied soils and estimated average size. ....	209
<b>Table 37:</b> Organic matter obtained by the gravimetric method. ....	209
<b>Table 38:</b> FA-RE values obtained with the filter membranes and in both dispersive media. FA- RE: Filter aided recovery efficiency. ....	214
<b>Table 39:</b> FA-RE: efficiencies after the isolation and subsequent filter aided recovery. Hydrodynamic sizes obtained for CB dispersion residue after filter-aided recovery. (Fiberglass 2 $\mu\text{m}$ and teflon 0.10 $\mu\text{m}$ were studied) using polymeric and biological dispersive agents. ....	217
<b>Table 40:</b> CB concentration and % recovery in different matrices calculated on the surface of the filter membrane. ....	222
<b>Table 41:</b> Elemental composition of different silica based materials analysed expressed respect Si content. ....	228
<b>Table 42:</b> Adsorption capacity of different synthesis of silica until achieving the nitrate initial concentration for well water. ....	239
<b>Table 43:</b> Physical properties and adsorption of modified and unmodified silica. ....	242
<b>Table 44:</b> Parameters for the optimization of the amino-silica synthesis and its adsorption capacity. ....	248
<b>Table 45:</b> Comparison of traditional methods in industry (in grey), new green lab-scale methods (in white) with our green large-scale methods for synthesis of modified silica. Some of these materials were used as adsorbents. ....	254
<b>Table 46:</b> Approaches applied and analytical techniques used for each NM studied. ....	259
<b>Table 47:</b> Measured properties, techniques employed and parameters evaluated for each NMs characterized. ....	260
<b>Table 48:</b> NMs studied as analytical tools: analyte determined, matrices and techniques employed for characterization. ....	264



#### A4. PhD CONTRIBUTIONS TO PUBLICATIONS

- Campíns-Falcó, P., González-Fuenzalida, R.A., **Sanjuan-Navarro, L.**, Moliner-Martínez, Y., Verdú-Andrés, J., Molins-Legua, C., Herráez-Hernández, R. Capillary LC of metallic nanoparticles coupled on line to IT-SPME: application to plasmonic assays. *Actualidad Analítica*. 60, 36-37 (2017). **Contribution 100%**
- González-Fuenzalida, R.A., **Sanjuan-Navarro, L.**, Moliner-Martínez, Y., Campíns-Falcó, P. Quantitative study of the capture of silver nanoparticles by several kinds of soils. *Science of the Total Environment*. 630, 1226-1236 (2018). **Contribution 50%**
- Moliner, C., Teruel-Juanes, R., Primaz, C.T., Badia, J.D., Bosio, B., Campíns-Falcó, P., Molins-Legua, C., Hernandez, F., **Sanjuan-Navarro, L.**, Madramany, P., Moran, J., Castro, J., Sanchis, F.J., Martinez, J.D., Hiddink, F., Ribes-Greus, A., Arato, E. Reduction of Nitrates in waste water through the valorization of rice straw: LIFE LIBERNITRATE Project. *Sustainability*. 10, 3007 (2018). **Contribution 100%**
- **Sanjuan-Navarro, L.**, Boughbina-Portolés, A., Moliner-Martínez, Y., Campíns-Falcó, P. Aqueous dilution of noble NPs bulk dispersions: modelling instability due to dissolution by AF4 and stablishing considerations for plasmonic assays. *Nanomaterials*. 10, 1802 (2020). **Contribution 100%**
- Boughbina-Portolés, A., **Sanjuan-Navarro, L.**, Moliner-Martínez, Y., Campíns-Falcó, P. Study of the stability of citrate capped AgNPs in several environmental water matrices by asymmetrical flow field flow fractionation. *Nanomaterials*. 11, 926 (2021). **Contribution 50%**
- **Sanjuan-Navarro, L.**, Cortés-Bautista, S., Moliner-Martínez, Y., Campíns-Falcó, P. In-tube solid phase microextraction coupled to miniaturized liquid chromatography for both, noble metal nanoparticles assessment and sensitive plasmonic assay development. *Analytica Chimica Acta*. 1171, 338665 (2021). **Contribution 50%**

- 
- Robles-Jimarez, H.R., **Sanjuan-Navarro, L.**, Jornet-Martínez, N., Primaz, C.T., Teruel-Juanes, R., Molins-Legua, C., Ribes-Greus, A., Campíns-Falcó, P. New silica based adsorbent material from rice straw and its in-flow applications to nitrate reduction in waters: Process sustainability and scale-up possibilities. *Science of the Total Environment*. 805, 150317 (2022). **Contribution 50%**
  - **Sanjuan-Navarro, L.**, Moliner-Martínez, Y., Campíns-Falcó, P. Characterization and Quantitation of Carbon Black Nanomaterials in Polymeric and Biological Aqueous Dispersants by Asymmetrical Flow Field Flow Fractionation. *ACS Omega*. 6(47), 31822-31830 (2021). **Contribution 100%**
  - **Sanjuan-Navarro, L.**, Moliner-Martínez, Y., Campíns-Falcó, P. The State of Art of Nanocarbon Black as Analyte of Interest in Several Matrices: A Review. *Trends in Analytical Chemistry*. (Submitted). **Contribution 100%**
  - **Sanjuan-Navarro, L.**, Moliner-Martínez, Y., Campíns-Falcó, P. Isolation of Carbon Black from soils employing a biological dispersant and its recovery by filter-aided procedure: characterization by field flow fractionation techniques. (submitted). **Contribution 100%**
  - **Sanjuan-Navarro, L.**, Moliner-Martínez, Y., Campíns-Falcó, P. Asymmetrical flow field flow fractionation for the analysis of different silica materials: from nanometers to micrometers. **Contribution 100%**
  - Primaz, C.T., Jornet-Martínez, N., **Sanjuan-Navarro, L.**, Moliner-Estopiñán, C.E., Campíns-Falcó, P., Molins-Legua, C., Ribes-Greus, A., Badía-Valiente, J.D., Teruel-Juanes, R., Gil-Castell, O., Bosio, B., Arato, E. Patent 2727673. Procedimiento de adsorción de nitratos mediante sílice modificada activa a partir de cenizas de paja de arroz. ES2727673A1 --- WO 2020/169862A1. Concession data: 24.02.2021. **Contribution 2.5%**